



HAL
open science

Dual Calorimetry for High Precision Neutrino Oscillation Measurement at JUNO Experiment

Yang Han

► **To cite this version:**

Yang Han. Dual Calorimetry for High Precision Neutrino Oscillation Measurement at JUNO Experiment. Physics [physics]. Université Paris Cité, 2020. English. NNT : 2020UNIP7188 . tel-03295420

HAL Id: tel-03295420

<https://theses.hal.science/tel-03295420>

Submitted on 22 Jul 2021

HAL is a multi-disciplinary open access archive for the deposit and dissemination of scientific research documents, whether they are published or not. The documents may come from teaching and research institutions in France or abroad, or from public or private research centers.

L'archive ouverte pluridisciplinaire **HAL**, est destinée au dépôt et à la diffusion de documents scientifiques de niveau recherche, publiés ou non, émanant des établissements d'enseignement et de recherche français ou étrangers, des laboratoires publics ou privés.



Université
de Paris

Université de Paris
École Doctorale 560 STEP'UP
Laboratoire AstroParticule et Cosmologie

Dual Calorimetry for High Precision Neutrino Oscillation Measurement at JUNO Experiment

Par Yang HAN

Thèse de doctorat de Physique de l'Univers
Dirigée par Anatael CABRERA et Antoine KOUCHNER

Présentée et soutenue publiquement le 30 Novembre 2020

Devant un jury composé de:

Marie-Hélène SCHUNE Directrice de recherche, CNRS, IJCLab	Présidente du jury
Stefano DUSINI Researcher, INFN Padova	Rapporteur
Xavier SARAZIN Directeur de recherche, CNRS, IJCLab	Rapporteur
Marco GRASSI Associate Professor, University of Padova	Examineur
Hiroshi NUNOKAWA Associate Professor, PUC-Rio	Examineur
Alessandra TONAZZO Professeur, Université de Paris	Examinatrice
Anatael CABRERA Charge de recherche, CNRS, IJCLab	Co-encadrant de thèse
Antoine KOUCHNER Professeur, Université de Paris	Directeur de thèse



Except where otherwise noted, this is work licensed under
<https://creativecommons.org/licenses/by-nc-nd/3.0/fr/>

Résumé

Depuis la découverte de la particule postulée par Pauli, le neutrino, dans les années 1950, les connaissances accumulées sur les neutrinos ont approfondi notre compréhension de l'univers. Le phénomène de l'oscillation des neutrinos est une des découvertes les plus remarquables dans les dernières décennies. Il a révélé et continue de élucider les propriétés fondamentales des neutrinos. À ce jour, la physique de l'oscillation des neutrinos est entrée dans une ère de haute précision. JUNO est une expérience de neutrinos de nouvelle génération basée sur le plus grand détecteur de scintillateur liquide au monde, visant principalement à mesurer l'oscillation des neutrinos de réacteur à haute précision. Ses perspectives principales scientifiques incluent la détermination de l'ordre de masse des neutrinos (MO) et la mesure de la moitié de tous les paramètres d'oscillation (θ_{12} , Δm_{21}^2 et Δm_{32}^2) avec une haute précision sans précédent. En tant que détecteur de scintillateur liquide de pointe, JUNO contribuera également à l'exploration des neutrinos de supernova, des neutrinos solaires, des géo-neutrinos, de la désintégration du proton, etc.

En ce qui concerne les objectifs principaux de JUNO, le point le plus critique est le contrôle de l'énergie, y compris l'exactitude et la précision, afin d'obtenir les mesures d'oscillation des neutrinos les plus précises. L'objectif du contrôle de l'énergie dans le JUNO détecteur est d'avoir une $\sim 3\%$ résolution d'énergie à 1 MeV et les erreurs systématiques de détection d'énergie inférieures à 1%. Motivé par le contrôle de l'énergie exigeant, un nouveau concept, appelée *Double Calorimétrie*, est réalisé pour la première fois à JUNO en introduisant un deuxième système de lecture (SPMT) en plus du système de lecture principale (LPMT). Ce concept apporte des perspicacités uniques pour le contrôle des erreurs systématiques grâce à la décomposition de la dégénérescence des compositions différentes de détecteur réponse, y compris les non-linéarités et la non-uniformité.

Cette thèse est consacrée au développement, pour la première fois, de la nouvelle technique d'étalonnage des détecteurs avec la Double Calorimétrie pour le contrôle de l'énergie concernant l'exactitude et la précision. La méthodologie de la nouvelle technique d'étalonnage, ainsi que ses performances prospectives seront présentées dans cette thèse. Pour la validation du matériel critique de la Double Calorimétrie, les performances de l'électronique de lecture de SPMT sont préalablement testées et validées dans cette thèse. La technique de la Double Calorimétrie développée dans cette thèse assurera les conditions de la détermination de MO intrinsèque ($\sim 3\sigma$) de JUNO et de la mesure des paramètres d'oscillation inférieur à 1%. En dehors de l'étude de MO intrinsèque de JUNO, une étude de MO synergie entre JUNO et des expériences de faisceaux de neutrinos à ligne de base longue est également réalisée dans cette thèse pour étudier la mesure possible de MO entièrement résolue ($\geq 5\sigma$). Par conséquent, cette thèse couvre plusieurs techniques nouvelles qui sont maintenant adoptées par JUNO couvrant du matériel à la physique la plus importante de JUNO.

MOTS-CLÉS : Oscillation des neutrinos, Ordre de mass des neutrinos, Scintillateur liquide, JUNO, Etalonnage, Non-linéarité de charge, Double Calorimétrie, Electronique de lecture

Abstract

Since the discovery of the Pauli's hypothetical particle, neutrino, in 1950's from the nuclear reactor, the accumulated knowledge about neutrino has deepened our understanding of the universe. The neutrino oscillation phenomenon, as one of the most remarkable discoveries in recent decades, has revealed and continues unraveling the fundamental properties of neutrinos. To date, neutrino oscillation physics has entered into a high precision era. JUNO is a new generation neutrino experiment based on the world's largest liquid scintillator detector, aiming primarily for the high precision reactor neutrino oscillation measurements. Its major scientific prospects include the neutrino *mass ordering* (MO) determination and the unprecedented precision measurement of half of all oscillation parameters (θ_{12} , Δm_{21}^2 and Δm_{32}^2). Being the state of the art liquid scintillator detector, JUNO will also contribute to the exploration of supernova neutrinos, solar neutrinos, geo-neutrinos, proton decay, etc.

Regarding the primary physics goals of JUNO, the most critical and challenging topic is the energy control including both accuracy and precision in order to achieve the most precise neutrino oscillation measurements. The goal of the energy control in the JUNO detector is to have an unprecedented $\sim 3\%$ energy resolution at 1 MeV and sub-percent energy detection systematics. Motivated by the challenging energy control, a novel design, called *Dual Calorimetry*, is implemented for the first time at JUNO by introducing a second readout (SPMT) system in addition to the main readout (LPMT) system. This design brings some unique insights for the systematics control through the breakdown of the degeneracy of different detector response compositions including non-linearities and non-uniformity.

This thesis is devoted to develop, for the first time ever, the novel detector calibration technique of the Dual Calorimetry to address the energy control in terms of both accuracy and precision. The methodology of the novel calibration technique, together with its prospect performance, i.e. sub-percent energy control, will be presented in this thesis. For the critical hardware validation of the Dual Calorimetry, the performance of the SPMT readout electronics is preliminarily tested and validated during this thesis. The Dual Calorimetry technique developed in this thesis will ensure the conditions of the $\sim 3\sigma$ JUNO intrinsic MO determination and sub-percent oscillation parameters measurement. Besides the JUNO intrinsic MO study, a MO synergy study between JUNO and long baseline neutrino beam experiments is also performed during this thesis for investigating the possible fully resolved MO measurement ($\geq 5\sigma$). Hence, this thesis covers several novel techniques that are now considered as baseline in JUNO covering from the hardware all the way to the most important physics of JUNO.

KEYWORDS: Neutrino oscillation, Neutrino mass ordering, Liquid scintillator, JUNO, Calibration, Charge non-linearity, Dual Calorimetry, Readout electronics

Acknowledgements

I would like to express my appreciation to the following people, without whom I would not accomplish this work.

First I would like to thank Anatael Cabrera for providing the excellent opportunity of doing the interesting work in the JUNO collaboration at APC and IJCLab. He provided the constant guidance and support throughout my PhD program. He always encouraged me to follow my physics intuition to think and to explore. In the meanwhile, he has been giving me valuable advice and his broad vision in neutrino physics inspired me a lot. When I started my PhD, I was fortunate in working with Marco Grassi. He was very patient to guide me in physics and the physics tools. I learned directly from him about the neutrino physics, neutrino detection, programming, etc. I enjoyed the discussions with him where I benefited a lot. I am also very grateful to Antoine Kouchner to be my supervisor. Even through I did not work with him scientifically, I could not complete my thesis without his kindness and support in administration.

I would like also to thank the JUNO colleagues, especially the calibration group at Shanghai Jiaotong University, including Feiyang Zhang, Yuanyuan Zhang, Mengjiao Xiao and Jianglai Liu. I would like to thank Feiyang in particular who directly shared his knowledge of the calibration simulation. The discussions with them inspired me to combine the traditional calibration techniques with the novel Dual Calorimetry design, and finally I could come up with the idea of the channel-wise Dual Calorimetry calibration which is the core of the thesis.

In the first half of my PhD program, I had the opportunity to work with the excellent electronics engineers, Cayetano Santos and Andrea Triossi. I would like to thank them to help me to understand the electronics and to support me for the testing of the JUNO SPMT readout electronics. In the last few month of my PhD, I had the chance to work with the renowned phenomenologist, Hiroshi Nunokawa, during his sabbatical at IJCLab. It was a great pleasure to work with him on the neutrino mass ordering synergy topic. We spent several unforgettable afternoons together with Anatael for discussion and brainstorming, and finally we achieved fruitful results.

I would like to thank again Anatael for his careful reading of the full thesis, as well as Diana Navas, Hiroshi and Marco for their careful reading of different parts. Their valuable feedback helped me to polish this thesis. I would like also to thank Stefano Dusini and Xavier Sarazin for their careful reading of the thesis as the referees, Marie-Hélène Schune for her support of the jury and Alessandra Tonazzo for her support from the doctoral school. I also want to thank my PhD monitoring committee members, Jose Busto and Santiago Pita, who have monitored my work throughout the PhD program, providing constructive suggestions. I am also very grateful to the Chinese Scholarship Council for providing my funding to study in France. In addition, I am very pleased to guide an undergraduate student, Hanyi Chen, together with Anatael. Her excellence allowed her to complete a small scientific project.

Last I want to thank my closest family for their full support of my scientific career decision at every step.

Contents

Introduction	1
1 Introduction to Neutrino Physics	4
1.1 A Brief History of Neutrino Discovery	4
1.2 Neutrinos Properties	5
1.3 Neutrino Oscillation Theory	6
1.3.1 Neutrino Oscillation in Vacuum	7
1.3.2 Matter Effects	9
1.4 Neutrino Oscillation Measurements	10
1.4.1 Solar Neutrino Oscillation	11
1.4.2 Atmospheric Neutrino Oscillations	14
1.4.3 Long Baseline Neutrino Beam Experiments	17
1.4.4 Reactor Neutrino Oscillation	19
1.4.5 Present Knowledge of Neutrino Oscillations	20
1.5 Outlook	23
2 Neutrino Physics with JUNO	26
2.1 Neutrino MO Determination at JUNO	26
2.1.1 Motivation	26
2.1.2 Reactor $\bar{\nu}_e$ Disappearance in Vacuum	28
2.1.3 Reactor Neutrino Signal	29
2.1.4 Backgrounds	31
2.1.5 Event Selection	32
2.1.6 MO Sensitivity from Spectral Analysis at JUNO	33
2.2 High Precision θ_{12} , Δm_{21}^2 and Δm_{32}^2 Measurements	37
2.3 Beyond Reactor Neutrino Oscillation	38
2.3.1 Supernova Neutrinos	38
2.3.2 Solar Neutrinos	39
2.3.3 Proton Decay	40
2.3.4 Geo-neutrinos	40
2.3.5 Other Topics	41
3 JUNO Detector	42
3.1 Liquid Scintillator	42
3.2 Readout System	44
3.2.1 LPMT Readout System	45
3.2.2 SPMT Readout System	47
3.3 Calibration	48
3.3.1 Calibration Sources	48
3.3.2 Calibration System	49
3.4 Veto Detectors	51

3.4.1	Water Cherenkov (WC) Detector	51
3.4.2	Top Tracker	51
3.5	Other Detector Related Systems	52
4	Dual Calorimetry Concept	53
4.1	JUNO Challenge and Motivation of Dual Calorimetry	53
4.2	The Principle of Dual Calorimetry	56
4.2.1	Fully Correlated Response Relation	58
4.2.2	Partially Correlated Response Relation	59
4.2.3	Uncorrelated Response Relation	61
4.2.4	Response Comparison	66
4.3	Dual Calorimetry Possible Implementations	67
4.3.1	Dual Calorimetry Calibration Channel-wise	67
4.3.2	Dual Calorimetry with Neutrino Oscillation	67
4.3.3	Other Possible Implementations	68
5	Dual Calorimetry Calibration	70
5.1	Dual Calorimetry Calibration with UV Laser Source	71
5.1.1	UV Laser Advantages in DCC	71
5.1.2	Methodology	72
5.1.3	Advantages and Challenges	77
5.2	Dual Calorimetry Calibration with Radioactive Sources	81
5.2.1	Radioactive Source Advantages in DCC	81
5.2.2	Methodology	82
5.2.3	Advantages and Challenges	87
5.2.4	Implications on Single Calorimetry	88
5.3	Dual Calorimetry Calibration Strategy and Performance	89
5.3.1	Dual Calorimetry Calibration First Stage	89
5.3.2	Dual Calorimetry Calibration Second Stage	89
5.3.3	Performance	90
5.4	SPMT in Dual Calorimetry Calibration	91
5.4.1	Direct PE Counting in SPMT Readout	91
5.4.2	Poisson Zero PE Counting in the SPMT Readout	92
5.4.3	Threshold Effect	94
5.5	Dual Calorimetry Calibration Systematics	96
5.5.1	The Poisson Statistics Effect	96
5.5.2	The PMT Charge Resolution Effect	99
5.5.3	The LPMT Effective Threshold Effect	100
5.5.4	DCC Capability with the SPMT QNL Control	102
5.5.5	The Single LPMT NU Map Effect (C_2 Correction)	103
5.5.6	Other Systematic Effects	103
5.6	Summary and Outlook	104
6	Energy Control with Dual Calorimetry Calibration	105
6.1	Energy Scale Control with DCC	106
6.1.1	Energy Scale Non-linearity	107
6.1.2	NU in Energy Scale	112
6.2	Energy Resolution Control with DCC	115
6.2.1	Energy Resolution of JUNO	115
6.2.2	QNL in Energy Resolution and DCC Control	117
6.3	Summary and Outlook	120

7	SPMT Readout Electronics Performance for Dual Calorimetry	121
7.1	ABC Board	121
7.2	ABC Version 0 Performance Test	122
7.2.1	Charge Data Stream	123
7.2.2	Discriminator Data Stream	131
7.3	Summary	134
8	Neutrino Mass Ordering Synergy between JUNO and LBνB	136
8.1	Motivation	136
8.2	Publication: Earliest Resolution to the Neutrino Mass Ordering?	136
8.3	Summary	155
	Conclusions	156
	List of Figures	162
	List of Tables	163
	Bibliography	175

Introduction

Neutrinos, as fundamental particles in the Standard Model (SM), were conjectured as massless and electrically neutral fermions. The discovery of the neutrino oscillation, manifesting as the spontaneous neutrino flavor transformation, indicates that neutrinos have non-degenerate masses, and their mass eigenstates and flavor eigenstates are mixed.

In the three generations neutrino framework, regarding the non-degenerate mass eigenstates ν_1 , ν_2 and ν_3 , at least two of them are massive. The mass ordering of ν_1 and ν_2 has been determined as $m_1 < m_2$ through the solar neutrino measurement. However, it is still unknown whether $m_1 < m_2 < m_3$ or $m_3 < m_1 < m_2$, meaning that the neutrino mass ordering (MO) remains unsolved. Neutrino oscillations are sensitive to the squared mass differences $\Delta m_{ij}^2 = m_i^2 - m_j^2$, thus being able to be used to investigate the MO as the sign of Δm_{32}^2 .

Regarding the mixture between mass eigenstates and flavor eigenstates, it can be characterized by the 3×3 PMNS (*Pontecorvo–Maki–Nakagawa–Sakata*) matrix. Under the unitary assumption, the PMNS matrix can be parameterized by three mixing angles θ_{12} , θ_{23} , θ_{13} , and one CP violation phase δ_{CP} in the case of Dirac neutrino. The current precision of θ_{12} , θ_{23} and θ_{13} is at a few percent level, as well as Δm_{21}^2 and $|\Delta m_{32}^2|$, while δ_{CP} remains unknown. The future neutrino oscillation experiments, being in the high precision measurement era, will focus on the neutrino MO determination, the CP violation phase measurement and the improvement of the precision of oscillation parameters. A brief introduction to the neutrino physics with the highlight of the neutrino oscillation physics including the historical milestones, present status and open questions is given in Chapter 1.

The Jiangmen Underground Neutrino Observatory (JUNO) is a key future experiment in the era of the high precision neutrino oscillation measurement. By means of the high precision the reactor neutrino ($\bar{\nu}_e$) oscillation measurement, JUNO pursues the determination of the MO at $\sim 3\sigma$ significance with 6 years statistics. The MO determination at JUNO is unique, as it is vacuum oscillation driven and independent of δ_{CP} and θ_{23} . The other experiments targeting the MO determination are the long baseline neutrino beam experiments and the atmospheric neutrino experiments whose MO measurements all rely on the matter effects and are affected either by δ_{CP} or θ_{23} . With the reactor neutrino measurement, JUNO can also improve the precision of three oscillation parameters θ_{12} , Δm_{21}^2 and Δm_{32}^2 to unprecedented sub-percent level, contributing to the test of the standard three generations neutrino framework.

Beyond reactor neutrinos, JUNO is capable to observe supernova neutrinos, solar neutrinos, atmospheric neutrinos, geo-neutrinos, etc. It is also sensitive to some beyond SM physics such as the search for proton decay. The rich physics potentials make JUNO to be one of the most important future neutrino experiment. The aforementioned physics topics of JUNO are reviewed in Chapter 2, focusing in particular on the high precision reactor neutrino oscillation topics.

The JUNO experimental design is driven by the neutrino MO determination. The JUNO detector is placed at ~ 53 km from two nuclear power plant complexes with equal baselines. The design of the major components of the JUNO detector is reviewed in Chapter 3. The detector is designed to have the world's largest ($\sim 20,000$ tons) liquid scintillator (LS) as the target medium for obtaining large statistics. The detection of reactor neutrinos in the LS is via the inverse beta decay reaction. For obtaining a high precision reactor neutrino energy spectrum to extract the MO and oscillation parameters information, the most critical point is the energy control. Specifically, the energy resolution is aimed to be $\sim 3\%$ at 1MeV. The stochastic term of the energy resolution requires ~ 1200 photoelectrons (PEs) yield per MeV achieved by $\sim 18,000$ 20-inch PMTs (LPMT). Meanwhile, the energy scale uncertainty and the non-stochastic term of the energy resolution both need to be controlled below 1%, which imply the precise control of the energy detection systematics.

However, for the LPMT calorimetry, it is challenging to control precisely its energy detection systematics to sub-percent level. For the reason of this challenge, on the one hand, in the reactor neutrino energy range, a single LPMT needs to handle an unprecedented vast dynamic range in the charge detection which is at least 1 order of magnitude larger than the current reactor neutrino experiments such as Daya Bay, Double Chooz, KamLAND and RENO. On the other hand, the charge detection effect, i.e. the charge non-linearity (QNL), is typically degenerated with 1.) the detector non-uniformity effect, 2.) the non-linearity effect during energy deposition in the LS and 3.) even the non-stability effect. While the QNL becomes a constraint for the experiment, it is non-trivial to perform an independent calibration of the QNL. The uncalibrated LPMT QNL, likely being the main limitation for the energy detection systematics control, could have a significant impact on the physics measurement at JUNO, which prompts this thesis to explore novel technique for the QNL control.

The JUNO 3-inch PMT (SPMT) calorimetry is introduced as the "zero" QNL reference for the LPMT calorimetry. The SPMT system contains $\sim 26,000$ PMTs designed to work mainly in the robust single PE counting mode. The SPMT and LPMT systems constitute the Dual Calorimetry design providing a unique opportunity for the breakdown of the degeneracy between the QNL effect and other systematic effects. The isolation, hence calibration, of the LPMT QNL can be achieved with the Dual Calorimetry. The overall energy control including both the energy scale and the energy resolution can be improved with the Dual Calorimetry, thus helping to realize the physics goals of JUNO.

The concept of the Dual Calorimetry design is elaborated in Chapter 4, where the basic principle of this novel design is explained in full detail. The most important implementation of the Dual Calorimetry, i.e. the channel-wise Dual Calorimetry calibration (DCC), is developed in this thesis, as will be detailed in Chapter 5 together with the prospect performance. The SPMT readout response linearity control and systematic effects of the DCC method are also addressed in Chapter 5. Then the energy control including the energy scale and the energy resolution with the DCC is addressed in Chapter 6, where a significant improvement of the QNL effect related energy control is demonstrated.

The performance of SPMT system, especially the SPMT readout electronics, is the key for the success of the Dual Calorimetry. Therefore, this thesis involves also the test of the SPMT readout electronics for the Dual Calorimetry hardware validation, which is presented in Chapter 7.

The Dual Calorimetry technique developed in this thesis ensures the conditions of the stringent energy control, thus contributing to the high precision reactor neutrino oscillation measurement at JUNO including the its intrinsic MO measurement and oscillation parameters. The JUNO intrinsic MO measurement is likely not able to resolve the MO at $\geq 5\sigma$ level. Therefore, a MO synergy study between JUNO and long baseline neutrino beam experiments is carried out during this thesis for investigating the possible earliest resolved MO measurement and the possible vacuum oscillation driven MO solution. This MO synergy study is presented in Chapter 8.

Chapter 1

Introduction to Neutrino Physics

Neutrinos are one of the basic building blocks of the universe. They are classified as one of the elementary particles in the Standard Model (SM). Neutrinos are also one of the least understood particles due to the fact that they interact very weakly with matter. Exploring the neutrino properties and interactions has been one of the most exciting activities in particle physics. From the neutrino hypothesis to the neutrino discovery and the most recent discovery of the neutrino oscillation phenomenon, an enormous amount of knowledge about neutrinos has been accumulated. This chapter aims to briefly review the basic knowledge and current status of neutrino physics, particularly focusing on the neutrino oscillation physics.

A brief overview of the neutrino history is presented in Sec.1.1, followed by the introduction of the basic properties of neutrinos in Sec.1.2. Then the neutrino oscillation physics is reviewed. In Sec.1.3, a brief theoretical description of neutrino oscillations is presented. The experimental measurements of the neutrino oscillations are addressed in Sec.1.4, together with some historical milestones and the state of the art knowledge. In the end, some of the open questions and the ongoing and future experimental effort in the neutrino field are briefly reviewed in Sec.1.5.

1.1 A Brief History of Neutrino Discovery

The history of neutrinos dates back to the end of nineteenth century along with the discovery and the study of radioactivity. In 1896, Henri Becquerel discovered the radiation coming from uranium [1, 2]. Subsequently, the radioactivity was observed by Marie and Pierre Curie from other substances such as radium and polonium [3]. In 1899, Ernest Rutherford found that the uranium radiation was complex and he described two distinct types of radiation, one that is easily absorbed, called α , and the other that is more penetrative, called β [4]. Later on, in 1902, it was demonstrated that the β radiation (or decay) was, in substance, electron. At that time, the β decay was believed to be a two-body process in which a radioactive nucleus decayed into a different nucleus emitting an electron. By applying the energy conservation law, the emitted electron should have a discrete and unique energy. However, in 1914, James Chadwick showed that the energy spectrum of the electron from β decay was continuous, which was puzzling because it suggested the possible violation of the energy conservation law [5].

The hypothesis of neutrino was introduced in 1930 by Wolfgang Pauli in order to explain the continuous energy spectrum of β decay and to rescue the energy conservation law [6]. Pauli suggested a light, neutral and spin $1/2$ particle, later on named *neutrino* by Enrico Fermi, as the third body of the β decay. Then, the continuous β decay spectrum would become understandable. In 1933, Enrico Fermi built the theory of β decay in which a neutron decays into a proton, an electron and a neutrino [7]. In 1934, Hans

Bethe and Rudolf Peierls calculated the probability of the interaction (i.e. the cross section) between a neutrino and a proton, and they found that the cross section should be extremely small resulting in an unprecedented challenge for detecting neutrinos [8], as it remains now.

More than twenty years later, in 1956, the neutrino was finally discovered by Frederick Reines and Clyde Cowan [9]. They led the detection of neutrinos from the nuclear reactor of Savannah River. The neutrino coming out of a nuclear reactor is now known as the electron antineutrino.

In 1962, the second type of neutrino, i.e. muon neutrino, was discovered from the pion decay by a team led by Melvin Schwartz, Leon Lederman and Jack Steinberger at Brookhaven National Laboratory [10]. In 1975, Martin Perl and his team discovered the third type of lepton, i.e. tau lepton, in the SLAC electron-positron collider [11]. The third type of neutrino was inferred to exist. The direct tau neutrino measurement was done in 2000 by the DONUT collaboration [12]. Three species of neutrino have been discovered up to now. And the number of *active*¹ neutrino species is constraint to be 2.9840 ± 0.0082 by the measurement of the Z boson resonance at LEP and SLC electron-positron colliders [13].

Beginning with the β decay to the neutrino hypothesis to the three species of neutrino discovery, the exploration of neutrinos and their properties has spanned the twentieth century. To this day, physicists continue to explore the mysteries of neutrinos.

1.2 Neutrinos Properties

Neutrinos are matter particles with three generations in the Standard Model of particle physics. The SM [14, 15, 16] is so far the most successful theory to describe all matter and all interactions except gravity in the universe. In order to better describe the neutrino properties, the SM is briefly reviewed with the highlight of neutrinos in this section.

The elementary particles in the SM are shown in Fig.1.1. The SM is a gauge theory under the local symmetry group $SU(3) \times SU(2) \times U(1)$. This gauge group describes the interactions and determines the number of gauge bosons as interaction carriers. It is composed of three subgroups. The $SU(3)$ leads to the quantum chromodynamics (QCD), the theory of strong interaction. Eight gluons are the mediators of the strong interaction. The $SU(2)$ is responsible for the weak interaction with W^\pm and Z bosons as interaction carriers. The $U(1)$ leads to quantum electrodynamics (QED), the theory of electromagnetic interaction, with the photon as the interaction carrier.

In the SM, quarks and leptons are the fundamental constituent of matter and they are fermions with spin 1/2 being classified into three generations. Quarks have six flavors, and they participate in all the three interactions described in the SM. The charged leptons with three flavors, i.e. e , μ and τ , participate in electromagnetic and weak interactions. Neutrinos, as the neutral leptons, also have three flavors linked to the charged lepton flavors, namely ν_e , ν_μ and ν_τ . Neutrinos are only sensitive to the weak interaction in the SM framework. All fundamental fermions, including the neutrinos, are massive, hence they are, a priori, sensitive to the gravitational interaction which is not described in the SM.

There is also a scalar boson, i.e. Higgs boson, in the SM. It is responsible for the generation of masses for weak bosons and fermions through the so called Higgs mechanism (or Brout-Englert-Higgs mechanism)[17, 18, 19]. According to the past experimental observations, neutrinos were hypothesized as massless particles in the SM. However, the

1. The opposite to *active* neutrinos are *sterile* neutrinos, i.e. possible hypothetical neutrino states that might not coupled to the Z boson.

experimentally observed neutrino flavor transformation phenomena, i.e. neutrino oscillations, imply that neutrinos are massive particles. The neutrino oscillations originate from the non-degenerate neutrino masses and the mixing between the mass eigenstates and the flavor eigenstates. In order to include the neutrino masses, the SM extension was investigated [20]. However the extension depends on the nature of neutrino (i.e. Dirac or Majorana) which remains unknown. The so called see-saw mechanism [21] is a popular model responsible for the neutrino mass generation.

In spite of the large amount of knowledge accumulated, neutrinos are still mysterious in many aspects, and many open questions remain which will be reviewed in Sec.1.5. The neutrino oscillation, as the first hint of the physics beyond the SM, is a probe to demystify some of the secrets behind the nature of neutrinos and to explore new physics.

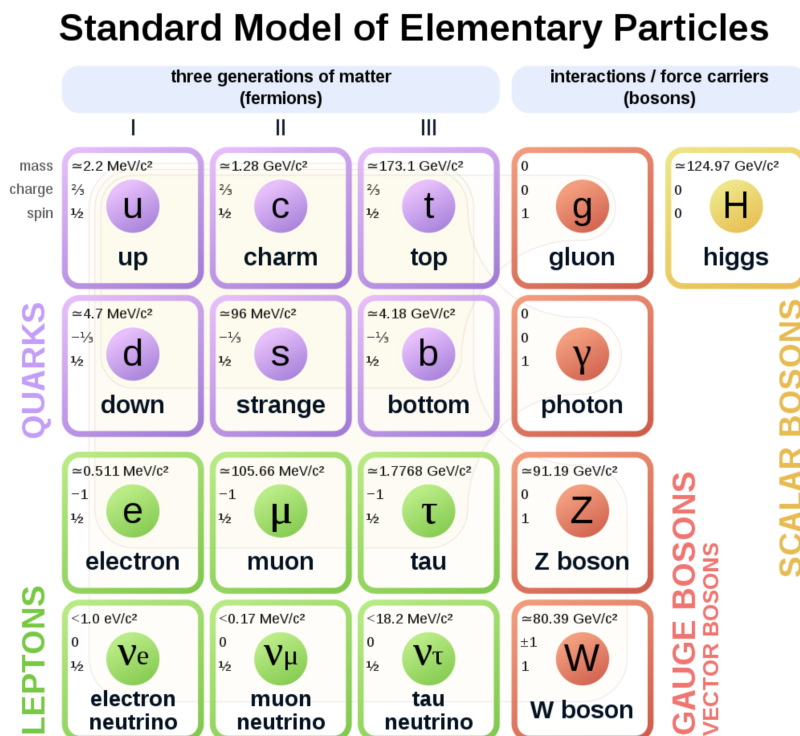


Figure 1.1 – Elementary particles in the Standard Model. Taken from [22]

1.3 Neutrino Oscillation Theory

Even though neutrinos were long thought to be massless, some early theoretical work already attempted to describe massive neutrinos, neutrino mixing and oscillations. The first idea of neutrino mass, mixing and oscillation was brought forward by Bruno Pontecorvo in 1957 in analogy with $K^0 \rightleftharpoons \bar{K}^0$ oscillation [23]. But only one type (electron-type) of neutrino was known at that time. So he described a possibility of neutrino to antineutrino oscillation i.e. $\nu \rightleftharpoons \bar{\nu}$. After the discovery of the second type of neutrino, i.e. muon neutrino (ν_μ), Pontecorvo extended his neutrino oscillation idea to two neutrinos case, i.e. $\nu_e \rightleftharpoons \nu_\mu$ oscillation [24]. In 1962, a two neutrino mixture theory had also been proposed by Ziro Maki, Masami Nakagawa and Shoichi Sakata [25]. To commemorate their pioneering work on neutrino mass, mixing and oscillation, the matrix used to describe the neutrino mixing is named as *Pontecorvo–Maki–Nakagawa–Sakata* (*PMNS*) matrix.

With the neutrino oscillation discovery and confirmation by various experiments

[26, 27, 28, 29, 30, 31, 32], to this day, the three neutrino oscillation framework has been largely studied and established both experimentally and theoretically, but some issues remain to be fully understood. The non-degenerate masses and the mixing between mass eigenstates and flavor eigenstates account for the spontaneous neutrino flavor transformations, namely neutrino oscillations. This section aims to review the theoretical description of the neutrino oscillation with the plane wave treatment¹.

1.3.1 Neutrino Oscillation in Vacuum

The lepton flavor is the label to distinguish the experimentally observed different types of neutrinos. The flavor states are the eigenstates of the weak interaction. As for the neutrino mass states, they are the eigenstates of the Hamiltonian, which obey the Schrödinger equation approximately.

In the three neutrino framework, the flavor eigenstates are denoted as $|\nu_\alpha\rangle$ with $\alpha = e, \mu, \tau$, and the mass eigenstates are denoted as $|\nu_i\rangle$ with $i = 1, 2, 3$. The mixture between them can be given by:

$$|\nu_\alpha\rangle = \sum_{i=1}^3 U_{\alpha i}^* |\nu_i\rangle, \quad (1.1)$$

where the weight U is the element of a 3×3 unitary matrix, i.e. the PMNS matrix.

Under the plane wave approximation, the mass eigenstate $|\nu_i\rangle$ evolving over time can be written as:

$$|\nu_i(t)\rangle = e^{-iE_i t} |\nu_i\rangle, \quad (1.2)$$

where E_i is the energy eigenvalue:

$$E_i = \sqrt{\vec{p}^2 + m_i^2}. \quad (1.3)$$

Thus, for a neutrino created with a definite flavor α at time $t=0$, i.e. $|\nu_\alpha(t=0)\rangle = |\nu_\alpha\rangle$, its time evolution is given by:

$$|\nu_\alpha(t)\rangle = \sum_{i=1}^3 U_{\alpha i}^* e^{-iE_i t} |\nu_i\rangle. \quad (1.4)$$

Similarly, the mass eigenstates can be expressed in terms of the superposition of the flavor eigenstates:

$$|\nu_i\rangle = \sum_{\beta=e,\mu,\tau} U_{\beta i} |\nu_\beta\rangle. \quad (1.5)$$

Substituting Eq.(1.5) into Eq.(1.4), the evolution of the flavor eigenstates with time is given by:

$$|\nu_\alpha(t)\rangle = \sum_{\beta=e,\mu,\tau} \sum_{i=1}^3 U_{\alpha i}^* e^{-iE_i t} U_{\beta i} |\nu_\beta\rangle. \quad (1.6)$$

Therefore, the eigenstate with 100% ingredient of α flavor ($\alpha = e, \mu$ or τ) at $t=0$ becomes the superposition of different flavor eigenstates at $t > 0$.

1. For simplicity, the plane wave treatment is considered here as it results the desired oscillation formula despite its defects and problems [33]. More complete and correct treatments can be performed by using the quantum mechanical wave-packet approach [34] or quantum field theory treatment [35].

The amplitude of $\nu_\alpha \rightarrow \nu_\beta$ transition is given by:

$$A_{\nu_\alpha \rightarrow \nu_\beta}(t) = \langle \nu_\beta | \nu_\alpha(t) \rangle = \sum_{i=1}^3 U_{\alpha i}^* U_{\beta i} e^{-iE_i t}. \quad (1.7)$$

Then the flavor transformation probability (or the oscillation probability), is given by:

$$P_{\nu_\alpha \rightarrow \nu_\beta}(t) = |A_{\nu_\alpha \rightarrow \nu_\beta}(t)|^2 = \sum_{i=1}^3 \sum_{j=1}^3 U_{\alpha i}^* U_{\beta i} U_{\alpha j} U_{\beta j}^* e^{-i(E_i - E_j)t}. \quad (1.8)$$

As neutrinos travel at the speed close to the light, at the ultrarelativistic limit (i.e. $E \sim p \gg m_i$), the neutrino energy in Eq.(1.3) is approximated by:

$$E_i \simeq p + \frac{m_i^2}{2p} \simeq E + \frac{m_i^2}{2E}, \quad (1.9)$$

where $E \approx |\vec{p}|$ is the neutrino energy neglecting the mass contribution. So,

$$E_i - E_j \simeq \frac{\Delta m_{ij}^2}{2E}, \quad (1.10)$$

where Δm_{ij}^2 is the squared mass difference with

$$\Delta m_{ij}^2 = m_i^2 - m_j^2. \quad (1.11)$$

Experimentally the distance between the neutrino source and the detector (L) can be known, instead of the traveling time. Since ultrarelativistic neutrinos propagate almost at the speed of light, the approximation $t = L$ can be applied, with the natural unit $c=1$. Therefore the oscillation probability can be approximated by,

$$P_{\nu_\alpha \rightarrow \nu_\beta}(L, E) = \sum_{i=1}^3 \sum_{j=1}^3 U_{\alpha i}^* U_{\beta i} U_{\alpha j} U_{\beta j}^* \exp(-i \frac{\Delta m_{ij}^2 L}{2E}). \quad (1.12)$$

In order to be easier to understand the different factors in the oscillation probability formula, it is convenient to write the oscillation probability as:

$$\begin{aligned} P_{\nu_\alpha \rightarrow \nu_\beta}(L, E) &= \delta_{\alpha\beta} - 4 \sum_{i>j} \Re[U_{\alpha i}^* U_{\beta i} U_{\alpha j} U_{\beta j}^*] \sin^2 \left(\frac{\Delta m_{ij}^2 L}{4E} \right) \\ &\quad + 2 \sum_{i>j} \Im[U_{\alpha i}^* U_{\beta i} U_{\alpha j} U_{\beta j}^*] \sin \left(\frac{\Delta m_{ij}^2 L}{2E} \right). \end{aligned} \quad (1.13)$$

From Eq.(1.13), it is clear that if the neutrinos have degenerate masses, i.e. $\Delta m_{ij}^2 = 0$, neutrinos will not oscillate. The observed neutrino oscillations indicate that neutrinos should be massive in a non-degenerate way, and at least two of them are massive for the oscillations to manifest. However, the oscillation characterization does not provide direct access to the absolute mass of the neutrinos. The oscillation is only sensitive to the squared mass difference Δm_{ij}^2 which is proportional to the oscillation frequency. In the three neutrino framework, there are three squared mass differences and their relation is given by:

$$\Delta m_{21}^2 + \Delta m_{32}^2 + \Delta m_{13}^2 = 0. \quad (1.14)$$

The oscillation amplitude is proportional to the PMNS matrix elements. The PMNS matrix is a 3 by 3 unitary matrix¹ and can be described by four free parameters. Most commonly it is parameterized by three mixing angles (θ_{12} , θ_{23} and θ_{13}) and one phase related to the charge conjugation-parity violation (δ_{CP}), as shown in Eq.(1.16).

$$U = \begin{pmatrix} U_{e1} & U_{e2} & U_{e3} \\ U_{\mu1} & U_{\mu2} & U_{\mu3} \\ U_{\tau1} & U_{\tau2} & U_{\tau3} \end{pmatrix} = \begin{pmatrix} 1 & 0 & 0 \\ 0 & c_{23} & s_{23} \\ 0 & -s_{23} & c_{23} \end{pmatrix} \begin{pmatrix} c_{13} & 0 & s_{13}e^{-i\delta_{CP}} \\ 0 & 1 & 0 \\ -s_{13}e^{i\delta_{CP}} & 0 & c_{13} \end{pmatrix} \begin{pmatrix} c_{12} & s_{12} & 0 \\ -s_{12} & c_{12} & 0 \\ 0 & 0 & 1 \end{pmatrix} \quad (1.15)$$

$$= \begin{pmatrix} c_{12}c_{13} & s_{12}c_{13} & s_{13}e^{-i\delta_{CP}} \\ -s_{12}c_{23} - c_{12}s_{23}s_{13}e^{i\delta_{CP}} & c_{12}c_{23} - s_{12}s_{23}s_{13}e^{i\delta_{CP}} & s_{23}c_{13} \\ s_{12}s_{23} - c_{12}c_{23}s_{13}e^{i\delta_{CP}} & -c_{12}s_{23} - s_{12}c_{23}s_{13}e^{i\delta_{CP}} & c_{23}c_{13} \end{pmatrix}, \quad (1.16)$$

where s_{ij} and c_{ij} represent $\sin \theta_{ij}$ and $\cos \theta_{ij}$ respectively.

The PMNS matrix can also be shown as the product of 3 sub-matrix as given by Eq.(1.15). Historically, the one containing θ_{23} is called atmospheric sector; the one containing θ_{12} is called solar sector; the one containing θ_{13} is called reactor sector.

In the case of Majorana neutrinos, two extra complex phases need to be added into the PMNS matrix, appearing as an additional sub matrix with the form of Eq.(1.17). Since the Majorana phases does not participate in neutrino oscillations, it will be ignored in the following discussion about neutrino oscillations.

$$\begin{pmatrix} e^{i\alpha_1/2} & 0 & 0 \\ 0 & e^{i\alpha_2/2} & 0 \\ 0 & 0 & 1 \end{pmatrix}. \quad (1.17)$$

1.3.2 Matter Effects

Even though neutrinos interact weakly with matter, when they go through a large amount of matter like the earth or the sun, their interactions with matter can become a sizable effect compared to neutrino oscillations. This effect was pointed out by Lincoln Wolfenstein, Stanislav Mikheyev and Alexei Smirnov, called matter effects or MSW effects [36, 37].

When neutrinos propagate in matter, they can experience the coherent forward elastic scattering with the particles in the medium. All three flavor neutrinos experience the neutral current (NC) weak interaction with electrons and nucleons. Electron neutrinos also experience the charged current (CC) weak interaction with electrons.

For the NC weak interaction, by assuming an electrical neutral environment (i.e. the number densities of protons and electrons are equal), the weak potential can be written as:

$$V_{NC} = \mp \frac{\sqrt{2}}{2} G_F N_n, \quad (1.18)$$

where G_F is the Fermi constant, N_n is the neutron number density of the medium, and the "-" and "+" signs correspond to neutrinos and antineutrinos respectively. The V_{NC}

1. The unitary condition is critical here and it implies the conservation of probability. As of now, the unitarity is assumed to be conserved, but it needs to be experimentally corroborated.

depends only on the neutron number density, because the electron potential and proton potential cancel out each other.

As for the CC interaction, the weak potential for electron-type neutrinos can be written as:

$$V_{CC} = \pm\sqrt{2}G_F N_e, \quad (1.19)$$

where N_e is the electron number density of the medium, and the "+" and "-" signs correspond to neutrinos and antineutrinos respectively.

The V_{NC} is the same for all three flavor neutrinos, so it has no net effect on the neutrino oscillations. However, the V_{CC} only affects the electron (anti)neutrinos, thus resulting in an impact on the oscillation patterns. For simplicity, considering the two neutrino framework with the vacuum oscillation parameters of θ and Δm^2 , the mixing angle in matter can be written as:

$$\sin^2 2\theta_m = \frac{\sin^2 2\theta}{(\cos 2\theta - \frac{2EV_{CC}}{\Delta m^2})^2 + \sin^2 2\theta}. \quad (1.20)$$

The squared mass difference in matter can be written as:

$$\Delta m_m^2 = \Delta m^2 \cdot \sqrt{(\cos 2\theta - \frac{2EV_{CC}}{\Delta m^2})^2 + \sin^2 2\theta}. \quad (1.21)$$

According to the two flavors transition, $\cos 2\theta$ has the same sign as Δm^2 [38]¹. For neutrinos, V_{CC} is positive, thus the flavor transition in matter can be enhanced to the maximum i.e. $\sin^2 2\theta_m = 1$ even for small vacuum mixing angles when the following condition is achieved:

$$\cos 2\theta = \frac{2EV_{CC}}{\Delta m^2}. \quad (1.22)$$

It is called the resonance condition leading to the possibility of the total transition between the two flavors. This mechanism explains the large solar neutrino deficit caused by the small vacuum mixing angle [39]. For the antineutrino, it leads to the deterioration of the flavor transition because of the opposite sign of the V_{CC} .

The matter effects can be used to determine the neutrino mass ordering, as it has already been used to measure $m_1 < m_2$ from solar neutrinos. Being different for neutrinos and antineutrinos, the matter effects can introduce a spurious CP violation, thus it needs to be well understood for the measurement of the CP-violation phase term in the PMNS matrix.

1.4 Neutrino Oscillation Measurements

Since the neutrino oscillation discovery through the atmospheric and solar neutrino experiments, the main objective of neutrino oscillation experiments has been gradually transitioned from the observation of neutrino oscillation to the precise measurement of oscillation parameters. In the three neutrino framework, neutrino oscillations depend on six independent parameters:

- three mixing angles θ_{12} , θ_{23} and θ_{13} ,
- two squared mass differences Δm_{21}^2 and Δm_{32}^2 ($\Delta m_{31}^2 = \Delta m_{21}^2 + \Delta m_{32}^2$),
- and one CP violation phase δ_{CP} .

1. For three flavor case, this relation is not necessarily true.

These parameters can not be predicted theoretically and need to be measured experimentally. This section aims to review the measurement of these oscillation parameters with the past and present experimental effort which are usually categorized as solar, atmospheric, accelerator and reactor neutrino experiments.

1.4.1 Solar Neutrino Oscillation

The sun is a powerful source of neutrinos. There are series of nuclear fusion reactions in the sun producing electron neutrinos. The two main reaction chains are the proton-proton (pp) chain ($> 98\%$) and the CNO (Carbon-Nitrogen-Oxygen) cycle. The overall neutrino production in pp chain can be summarized as:



The solar neutrino spectrum can be predicted by the Standard Solar Model (SSM) [40, 41, 42]. Fig.1.2 shows the prediction in the SSM based on the calculation in Ref.[41].

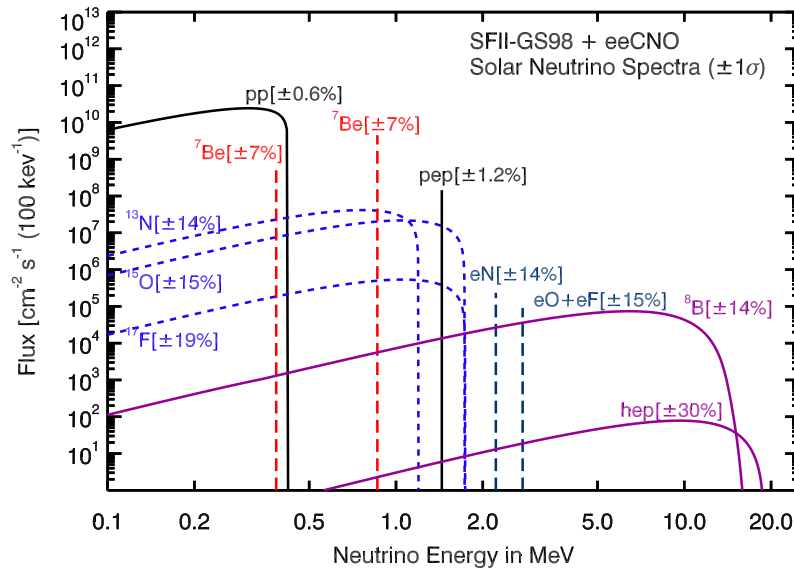


Figure 1.2 – Solar neutrino spectra predicted by the SSM in Ref.[41] (SFII-GS98 model). The proton-proton chain includes the continuous spectra of pp , hep and ${}^8\text{B}$, and also the line spectra of ${}^7\text{Be}$ and pep . The CNO cycle contains the continuous spectra shown as the dashed blue curves. The electron capture on ${}^{13}\text{N}$, ${}^{15}\text{O}$, and ${}^{17}\text{F}$ produces $ee\text{CNO}$ neutrinos as line spectra in dashed dark blue [43]. Taken from [44].

Solar Neutrino Anomaly

The first solar neutrino detection was carried out by Raymond Davis Jr. at Homestake mine by using a ${}^{37}\text{Cl}$ based detector [45]. The solar neutrinos were detected via ${}^{37}\text{Cl} + \nu_e \rightarrow {}^{37}\text{Ar} + e^-$ reaction with an energy threshold at 814 keV. The measured solar neutrino flux was dominated by the contribution of the ${}^8\text{B}$ process and was about one third of the predicted value in the SSM.

Later on, three ${}^{71}\text{Ga}$ based experiments, i.e. GALLEX [46], GNO [47] and SAGE [48], detected solar neutrinos with a lower threshold (233 keV), via ${}^{71}\text{Ga} + \nu_e \rightarrow {}^{71}\text{Ge} + e^-$. The low threshold enabled the detection of the neutrinos from the pp process. These three experiments also observed a large deficit ($\sim 50\%$) of the solar neutrino flux predicted by the SSM.

The Kamiokande and Super-Kamiokande (Super-K) experiments used the water Cherenkov technique to detect the solar neutrino through the ν - e^- elastic scattering: $\nu + e^- \rightarrow \nu + e^-$ with an energy threshold of ≥ 5 MeV. A deficit of the solar neutrino flux in ^8B process was also observed [49, 50].

All these results indicated a discrepancy between the solar neutrino observation and the SSM prediction, which was known as the *solar neutrino anomaly*. The neutrino oscillation was one of the possible reasons responsible for this anomaly, including the critical role of the matter effects to explain the variation of the disappearance at different energies.

SNO Experiment

The solar neutrino anomaly was not understood until the SNO (Sudbury Neutrino Observatory) experiment with the evidence of solar neutrino flavor transformation [27]. The SNO experiment was based on a Cherenkov detector with 1,000 tons of heavy water (D_2O), allowing the neutrino detection through the neutral current (NC), charge current (CC) and elastic scattering (ES) interactions. Therefore the total neutrino flux could be measured through the NC interaction, $\nu + \text{D} \rightarrow \nu + p + n$, and the pure electron neutrino flux could be measured through the CC interaction, $\nu_e + \text{D} \rightarrow e^- + p + p$.

The results obtained by SNO collaboration in 2002 [27] showed that the total neutrino flux is consistent with the SSM prediction, while the electron neutrino flux is about one third of the total neutrino flux. Since the sun only produces electron neutrinos, these results indicate that the electron neutrinos are transformed to other types of neutrinos. Together with other solar neutrino experiments and the KamLAND reactor neutrino observations [28], the answer to the solar neutrino anomaly was found to be the neutrino oscillation within the sun.

Later on, from the salt phase of the SNO experiment [51] in which NaCl was dissolved in the D_2O target, the NC, CC, EC fluxes were measured consistently with the previous phase as follows:

$$\begin{aligned}\Phi_{SNO}^{CC} &= 1.69_{-0.06}^{+0.06}(\text{stat.})_{-0.09}^{+0.08}(\text{syst.}) \times 10^6 \text{cm}^{-2} \text{s}^{-1} \\ \Phi_{SNO}^{NC} &= 4.94_{-0.21}^{+0.21}(\text{stat.}) + 0.38_{-0.34}(\text{syst.}) \times 10^6 \text{cm}^{-2} \text{s}^{-1}, \\ \Phi_{SNO}^{ES} &= 2.35_{-0.22}^{+0.22}(\text{stat.}) + 0.15_{-0.15}(\text{syst.}) \times 10^6 \text{cm}^{-2} \text{s}^{-1},\end{aligned}$$

which are shown in Fig.1.3. Finally the SNO collaboration obtain a total ^8B neutrino flux of $\Phi = 5.25 \pm 0.16(\text{stat.})_{-0.13}^{+0.11}(\text{syst.}) \times 10^6 \text{cm}^{-2} \text{s}^{-1}$ [52].

Borexino Experiment

Starting from 2008, the Borexino experiment uses the ultra low background liquid scintillator (~ 300 tons) to detect the ^7Be and *pep* solar neutrinos. It measured the solar neutrino deficit at 862 keV (^7Be) and 1.4 MeV (*pep*) energies [53, 54] as shown in Fig.1.4. In 2020, the Borexino collaboration reported the first experimental evidence of neutrinos from the CNO fusion cycle [55].

θ_{12} and Δm_{21}^2

Through the solar neutrino oscillation observations, the oscillation parameters of θ_{12} and Δm_{21}^2 can be extracted. By combining the results of all the solar neutrino experiments, the two parameters are given approximately in NuFit 5.0 global fit [56]

as: $\sin^2 \theta_{12} \sim 0.31$ ($\sim 7\%$ precision), $\Delta m_{21}^2 \sim 6 \times 10^{-5} eV^2$ ($\sim 30\%$ precision). The mass ordering of m_1 and m_2 has been determined to be $m_1 < m_2$ by making use of the matter effects of the solar neutrinos.

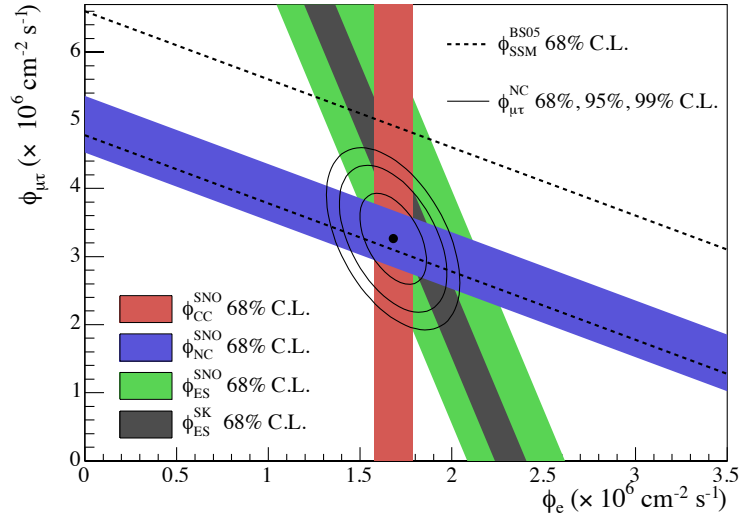


Figure 1.3 – Fluxes of ^8B solar neutrinos measured by SNO (salt phase). $\nu_\mu + \nu_\tau$ flux versus ν_e flux is deduced from the CC (red), NC (blue) and ES (green) neutrino detection channels of SNO. The total ^8B solar neutrino flux predicted by the SSM [40] is shown as dashed lines. The narrow band (grey) corresponds to the Super-Kamiokande ES measurement [57]. The bands represent the $\pm 1\sigma$ uncertainties. The point represents the ϕ_{ν_e} from the CC measurement and the deduced $\phi_{\mu\tau}$ from the NC and CC measurements. The contours represent 68%, 95%, and 99% probabilities. Taken from [51]

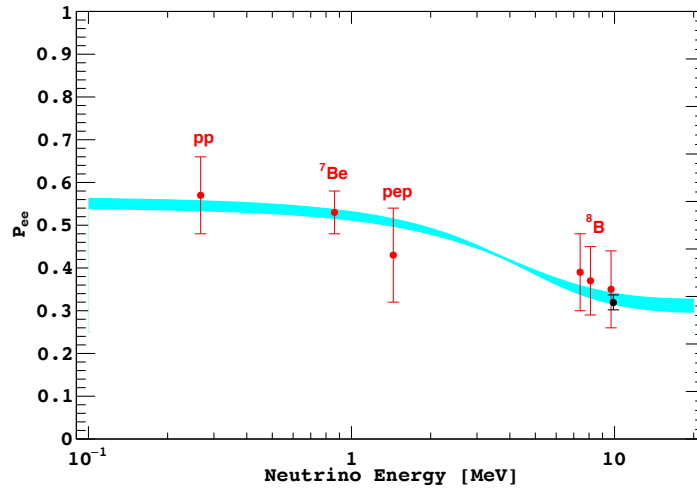


Figure 1.4 – Solar (ν_e) neutrino survival probability with respect to the neutrino energy. The Borexino solar neutrino measurements of pp , ^7Be , pep and ^8B as shown in red points. The SNO+SK ^8B data corresponds to the black point. The band is the MSW-LMA (large mixing angle) 1σ prediction. Taken from [58].

1.4.2 Atmospheric Neutrino Oscillations

Atmospheric neutrinos are created by cosmic rays (mostly protons) interacting with nuclei in the earth's atmosphere then the secondary particles (charged pions and kaons) decaying in flight. The chain decay of charged pions is the main channel for the atmospheric neutrino production, expressed as:

$$\begin{aligned}\pi^\pm &\rightarrow \mu^\pm + \nu_\mu/\bar{\nu}_\mu \\ \mu^\pm &\rightarrow e^\pm + \nu_e/\bar{\nu}_e + \nu_\mu/\bar{\nu}_\mu.\end{aligned}\tag{1.24}$$

Atmospheric Neutrino Anomaly

According to the atmospheric neutrino production processes, the muon-type neutrinos (ν_μ and $\bar{\nu}_\mu$) were expected roughly to be twice more than the electron-type neutrinos (ν_e and $\bar{\nu}_e$). However the Kamiokande [59] and IMB (Irvine-Michigan-Brookhaven) [60] water Cherenkov experiments observed a large deficit (about 40% in average) of muon neutrinos, as the following ratio:

$$R_{prediction}^{data} = \frac{[(\nu_\mu + \bar{\nu}_\mu)/(\nu_e + \bar{\nu}_e)]^{data}}{[(\nu_\mu + \bar{\nu}_\mu)/(\nu_e + \bar{\nu}_e)]^{prediction}} \sim 0.6.\tag{1.25}$$

where the prediction means the expected muon-type neutrinos and electron-type neutrinos in the absence of neutrino oscillations. This was known as the *atmospheric neutrino anomaly*.

Super-Kamiokande Experiment

The atmospheric neutrino anomaly was not solved until the Super-Kamiokande (Super-K) water Cherenkov experiment. In 1998, the Super-K collaboration gave the first compelling evidence of neutrino oscillation in atmospheric neutrinos [26].

The Super-K experiment measured the zenith angle dependence of the atmospheric neutrino deficit as shown in Fig.1.5. The zenith angle, corresponding to the direction of the incoming neutrino, contains the information of the flight distance (baseline) from the neutrino creation place to the detector. The baseline (L) dependence (i.e. zenith angle dependence), as well as the energy (E) dependence are the characteristics allowing an unambiguous identification of the neutrino oscillations.

Super-K concluded that the atmospheric neutrino anomaly is due to the neutrino oscillation, as all other alternative models were ruled out with higher precision data. The other two atmospheric neutrino experiments, MACRO [61] and Soudan-2 [62] confirmed Super-K's results with consistent observations.

Due to the fact that no deficit of electron-type neutrinos was observed, the muon-type neutrino deficit indicates the oscillation is mainly the $\nu_\mu \rightarrow \nu_\tau$. Later on, the Super-K collaboration carried out a dedicated L/E analysis, as shown in Fig.1.6. The observed dip in the L/E analysis favored strongly the $\nu_\mu \rightarrow \nu_\tau$ oscillation compared to the neutrino decay and neutrino decoherence [63]. Furthermore, the Super-K has measured the statistical appearance of ν_τ in the atmospheric neutrino data with 4.6σ significance [64].

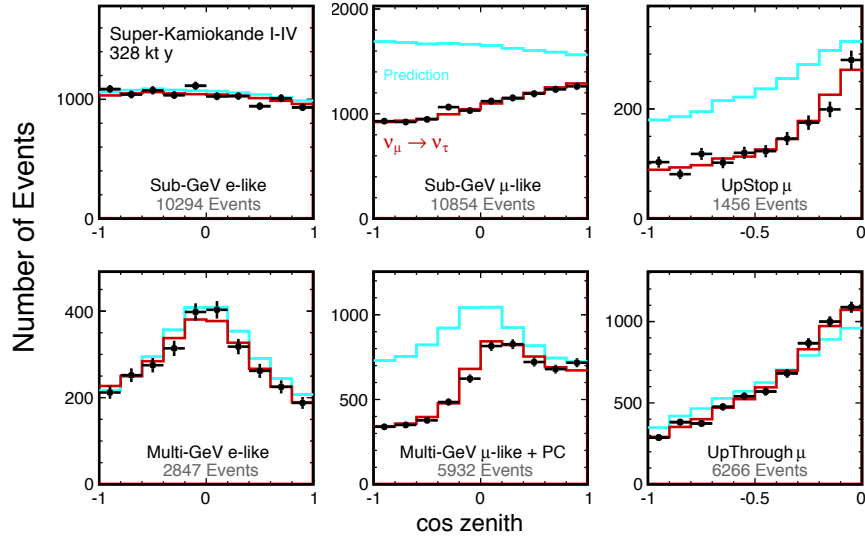


Figure 1.5 – The zenith angle distributions of atmospheric neutrino events in the Super-Kamiokande observation. Fully contained 1-ring e -like (electron-type neutrino) and μ -like (muon-type neutrino) events for sub-GeV (<1.33 GeV) and multi-GeV (>1.33 GeV) energies are shown. The upward stopping and upward through μ samples are also presented. Partially contained events are combined with multi-GeV μ -like events. The blue histograms show the non-oscillated expectation, and the red histograms show the best fit for $\nu_\mu - \nu_\tau$ oscillation. Taken from [58].

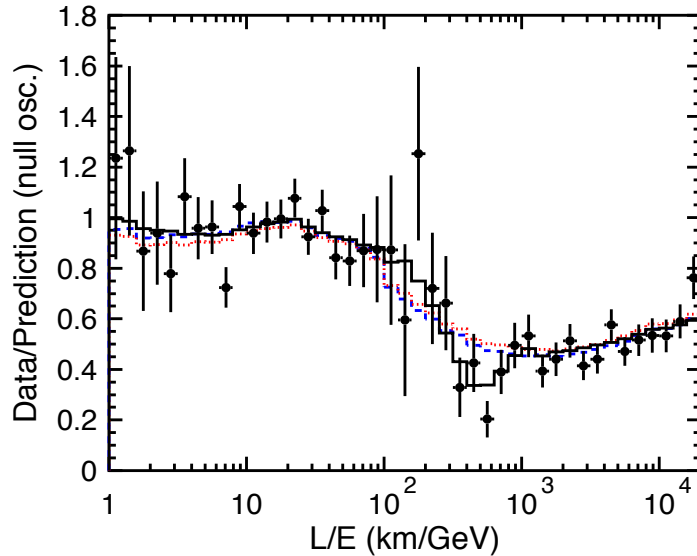


Figure 1.6 – Super-Kamiokande atmospheric neutrino L/E analysis. The ratio of the data to the no-oscillated prediction is shown as a function of the L/E . The best fit for two flavor $\nu_\mu - \nu_\tau$ oscillation is shown in solid black line. The dashed blue and dotted red lines represent the best fit for neutrino decay and neutrino decoherence respectively, which were ruled out as the main cause of today's neutrino disappearance. However, such phenomena may still manifest in a sub-dominant amplitude, for which no experimental evidence stands yet. Taken from [63].

θ_{23} and $|\Delta m_{32}^2|$

Through the atmospheric neutrino observations, the oscillation parameters of θ_{23} and Δm_{32}^2 can be extracted. For example, the Super-K reported their latest results at Neutrino 2020 as $|\Delta m_{32}^2| = 2.40_{-0.12}^{+0.11}$ and $\sin^2 \theta_{23} = 0.44_{-0.02}^{+0.05}$, if $\Delta m_{32}^2 > 0$ [65], as shown in Fig.1.7. The neutrino telescopes such as ANTARES [66] and IceCube [67] can also observe the atmospheric neutrino oscillation, and the IceCube-DeepCore measured the θ_{23} and $|\Delta m_{32}^2|$ [68] with a similar precision compared to Super-K, also as shown in Fig.1.7.

However, the sensitivity of the current experiments can not determine the sign of Δm_{32}^2 , remaining as the unknown neutrino mass ordering (MO), and also leave two octant possibilities for θ_{23} , i.e. $\theta_{23} < \pi/4$ or $\theta_{23} > \pi/4$, to be resolved.

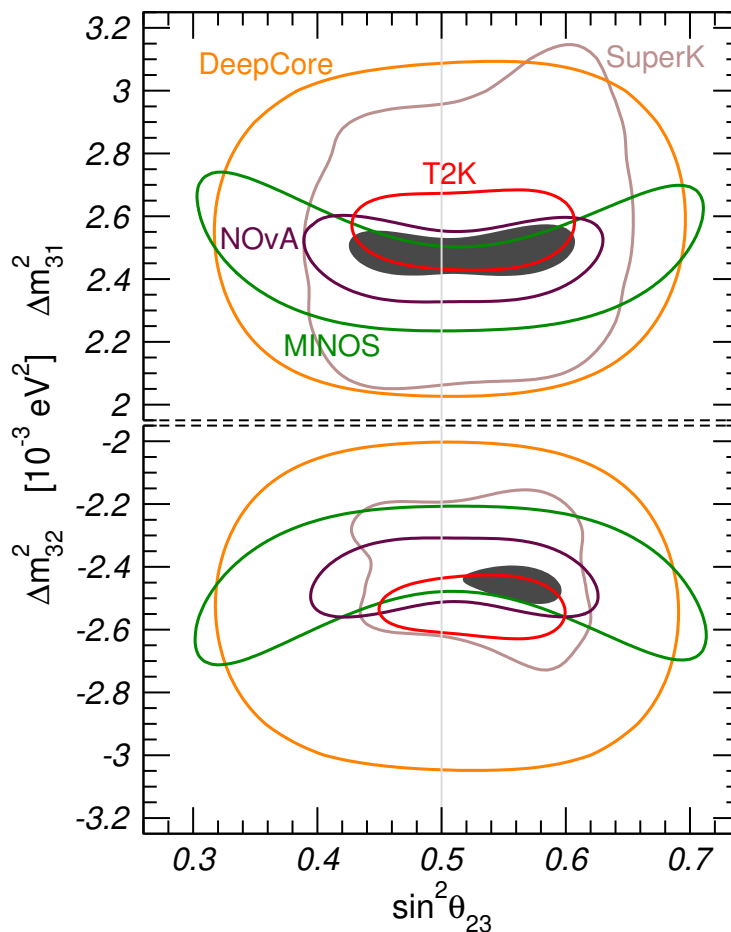


Figure 1.7 – 2σ confidence level region of θ_{23} and $\Delta m_{31(2)}^2$ for NMO (upper panel) and IMO (lower panel) with the latest results by 2020. Both appearance and disappearance data are used for the LB ν B experiments: MINOS (green), NOvA (dark redwood) and T2K (red). The atmospheric neutrino results are also shown for DeepCore (orange) and Super-Kamiokande (light brown). The combination of all of the results above is shown as the dark grey region with the NuFit 5.0 global analysis. Taken from [69].

1.4.3 Long Baseline Neutrino Beam Experiments

The accelerator neutrino beam is dominantly produced via the pion decay where the pions are the product of the protons colliding with a target:

$$\begin{aligned} p + A &\rightarrow \pi^\pm + X \\ \pi^\pm &\rightarrow \mu^\pm + \nu_\mu/\bar{\nu}_\mu. \end{aligned} \quad (1.26)$$

The neutrino beam contains mainly ν_μ and $\bar{\nu}_\mu$ with a typical energy at GeV level. It is appropriate to use this kind of neutrino beam for the study of muon-type neutrino oscillations, such as $\nu_\mu \rightarrow \nu_\mu$ disappearance, $\nu_\mu \rightarrow \nu_e$ appearance and $\nu_\mu \rightarrow \nu_\tau$ appearance, with a baseline of several hundred kilometers, namely long baseline neutrino beam (LB ν B) experiments.

For the purpose of reducing the systematic uncertainties originating from the neutrino beam flux and neutrino-nucleus interactions, a lot of LB ν B experiments use near and far two (or two sets of) detectors. The near detector is used to obtain the information about the neutrino beam flux, the energy spectrum and the interaction cross sections which are the input for predicting the observation at the far detector. The near detector techniques helps mainly the disappearance channel¹.

The LB ν B experiments can be categorized into three generations according to the running status: LB ν B-I (past), LB ν B-II (running) and LB ν B-III (future). Only LB ν B-I and LB ν B-II experiments are discussed in this section, the future LB ν B-III experiments will be discussed in Sec.1.5.

LB ν B-I

The main goal of LB ν B-I experiments was to confirm the existence of neutrino oscillation via both disappearance and also appearance channels.

The K2K (KEK to Kamioka) was the first LB ν B experiment [70]. The ν_μ beam with an average energy of 1.3 GeV was produced at KEK proton synchrotron and was directed towards the Super-K detector with a baseline of ~ 250 km. The near detector was located about 300 m downstream of the beam source. It measured the $\nu_\mu \rightarrow \nu_\mu$ disappearance with the consistent results compared to the atmospheric neutrino measurement [71].

The MINOS (Main Injector Neutrino Oscillation Search) experiment measured the $\nu_\mu \rightarrow \nu_\mu$ and $\bar{\nu}_\mu \rightarrow \bar{\nu}_\mu$ disappearances separately [72] and also $\nu_\mu \rightarrow \nu_e$ appearance [73]. Its far detector is located in Soudan mine with 735 km baseline and the near detector is about 1 km from the source. The neutrino beam came from NuMI at Fermilab with the peak energy around 3 GeV. Then it was upgraded to MINOS+ with the peak energy around 7 GeV. The oscillation parameters, θ_{23} and $|\Delta m_{32}^2|$ measured by MINOS and MINOS+ are consistent with the results of the atmospheric neutrino experiments as shown in Fig.1.7, and the final results reported at Neutrino 2020 can be found in Ref.[74, 75]. Since the $\nu_\mu \rightarrow \nu_\mu$ and $\bar{\nu}_\mu \rightarrow \bar{\nu}_\mu$ are CPT inverted processes each other, the MINOS has tested and ensured the CPT invariance with a few percent precision [76, 77].

The OPERA experiment measured the $\nu_\mu \rightarrow \nu_\tau$ appearance by sending the beam with the mean energy of 17 GeV from CERN to the Gran Sasso laboratory with 732 km baseline [78]. The beam energy was chosen such that $\nu_\mu \rightarrow \nu_\tau$ appearance could happen. It confirmed $\nu_\mu \rightarrow \nu_\tau$ oscillation with 6.1σ significance [79].

1. The appearance channels demand other additional consideration for the better control of systematics.

LB ν B-II

The LB ν B-II experiments are built to extract more precise neutrino oscillation information, including θ_{23} , $|\Delta m_{32}^2|$, and also to investigate θ_{13} , the sign of Δm_{32}^2 and δ_{CP} .

The T2K experiment, as the successor of K2K, started operation in 2010 [80]. The beam produced by J-PARK proton synchrotron is sent to the Super-K water Cherenkov detector with a baseline of 295 km, and the near detectors are located about 280 m from the beam source. It employs, for the first time, the off-axis neutrino beam in order to obtain a narrow energy range. The off-axis angle is about 2.5° obtaining the peak neutrino energy at 0.6 GeV.

The T2K experiment has measured θ_{23} and $|\Delta m_{32}^2|$ with a few percent precision dominantly through the muon neutrino disappearance channel¹, as shown with latest results [81] in Fig.1.7. Through the $\nu_\mu \rightarrow \nu_e$ appearance channel, T2K first reported an indication of non-zero θ_{13} [29], then confirmed the non-zero θ_{13} observation [82] which was first established by reactor neutrino experiments as will be discussed in the next section. By combining the neutrino and antineutrino observation, T2K has reported a first indication of CP violation close to 3σ level to rule out CP-conserving solution [81, 83]. The T2K favored region of δ_{CP} is shown in Fig.1.8, made by the NuFit group by making use the latest data in 2020.

The NO ν A experiment [84] starting from 2014 uses also an off-axis configuration (about 14.6 mrad off-axis) with the NuMI neutrino beam at Fermilab. The far detector is a 14 kt segmented liquid scintillator detector located in Minnesota, about 810 km away from the source, and the near detector is located around 1 km from the source. The neutrino energy spectrum is peaked around 2 GeV at the far detector

Similar to T2K, NO ν A has measured θ_{23} and $|\Delta m_{32}^2|$ with a few percent precision, as shown with the latest results in Fig.1.7 and it favors the NMO by close to 2σ significance [85], NO ν A also reported its favored δ_{CP} region for both orderings, and the latest results from Neutrino 2020 can be found in Ref.[86]. Fig.1.8 shows the NO ν A favored δ_{CP} in comparison with the T2K result.

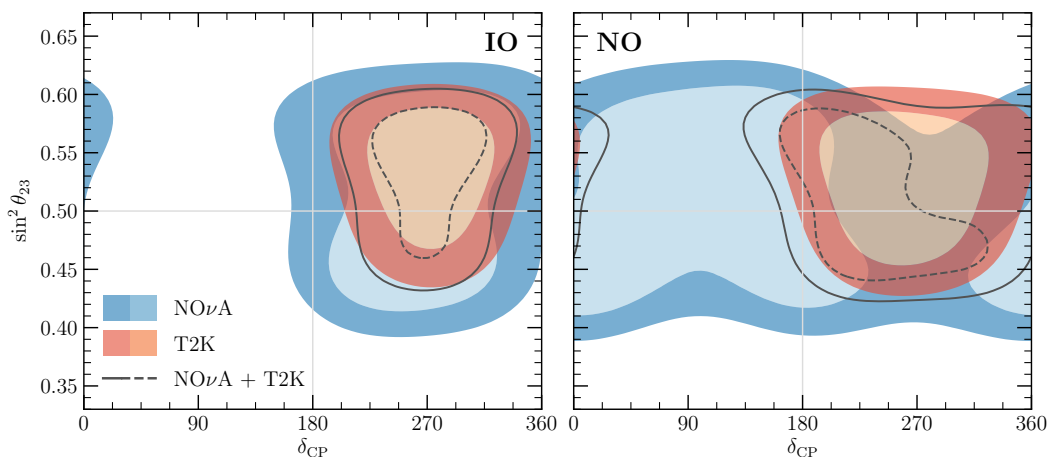


Figure 1.8 – 1σ and 2σ allowed regions of δ_{CP} and $\sin^2\theta_{23}$ for T2K (red shading) and NO ν A (blue shading). The combination between T2K and NO ν A is shown as the black curves. Taken from NuFit 5.0 [56].

1. T2K and NO ν A now respectively use the combined analysis of disappearance and appearance channels as well as the combined neutrino and antineutrinos observations.

1.4.4 Reactor Neutrino Oscillation

Nuclear reactors are powerful sources of electron anti-neutrinos ($\bar{\nu}_e$). The unstable fragments of nuclear fission go through a cascade of beta decays, emitting $\bar{\nu}_e$ with typically a few MeV energy. Generically the beta decay can be expressed as:

$${}^A_Z X \rightarrow {}^A_{Z+1} Y + e^- + \bar{\nu}_e, \quad (1.27)$$

where A and Z are the mass number and atomic number of the decaying nucleus, and X and Y are the initial and final elements.

The study of reactor neutrino oscillation is performed via the $\bar{\nu}_e \rightarrow \bar{\nu}_e$ disappearance channel. The liquid scintillator (LS) is commonly used for the reactor $\bar{\nu}_e$ detection via the inverse beta decay (IBD) reaction. The reactor neutrino experiments have contributed to the discoveries of both the $(\theta_{12}, \Delta m_{21}^2)$ driven oscillation and $(\theta_{13}, \Delta m_{32}^2)$ driven oscillation, as well as the neutrino discovery dating back to the 1950's.

KamLAND

The KamLAND (Kamioka Liquid Scintillator Antineutrino Detector) experiment is based on 1,000 tons LS to detect reactor $\bar{\nu}_e$ with an average baseline of 180 km. In 2002, KamLAND reported its first results with the evidence for reactor $\bar{\nu}_e$ disappearance at the 99.95% confidence level and confirmed the Large Mixing Angle (LMA) solution to the solar neutrino anomaly [28]. KamLAND observed a clear oscillatory feature in the ratio of the observed reactor $\bar{\nu}_e$ L/E spectrum to the no-oscillation expectation [87], which allows the most precise measurement of Δm_{21}^2 to date, as shown in Fig.1.9.

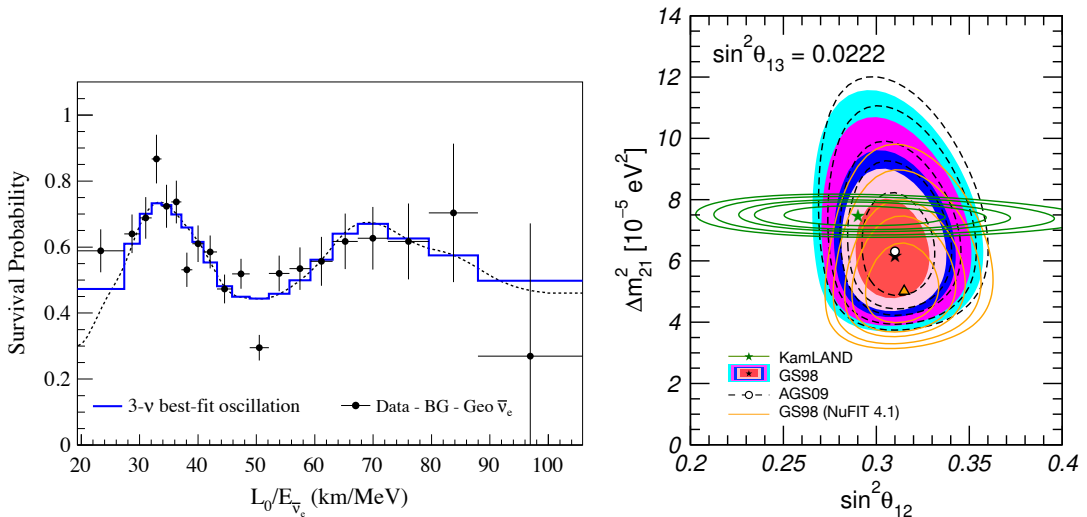


Figure 1.9 – Left: The ratio of the observed reactor $\bar{\nu}_e$ L/E spectrum to the expectation in absence of neutrino oscillation at KamLAND. A clear oscillation pattern can be seen. Taken from [87]. Right: Allowed θ_{12} and Δm_{21}^2 regions (at 1σ , 90%, 2σ , 99%, and 3σ C.L.) for KamLAND data (Green) and solar neutrino data. The solar neutrino data is shown as the results of the NuFit 5.0 combined analysis for the GS98 model (full color regions with best fit as a black star) and the AGSS09 model (dashed black contours with best fit as a white dot). The results from NuFit 4.1 [88] for the GS98 model are shown as the orange contours. Taken from [56].

The combination of the SNO solar neutrino fluxes and the KamLAND oscillatory signature implies the unambiguous demonstration that only neutrino oscillation can explain the solar anomaly.

In the three neutrino analysis, the KamLAND data indicates the oscillation parameters as [87]: $\tan^2 \theta_{12} = 0.481_{-0.080}^{+0.092}$, $\Delta m_{21}^2 = 7.54_{-0.18}^{+0.19} \times 10^{-5} eV^2$, which are shown in Fig.1.9 in comparison with the results of the solar neutrino experiments.

Reactor θ_{13} Experiments

In 1990's, the CHOOZ [89, 90] and Palo Verde [91] experiments¹, searched for reactor neutrino oscillations in the range of $10^{-3} < \Delta m^2 < 10^{-2} eV^2$ with a baseline about ~ 1 km. They could not find an evidence for reactor neutrino oscillation and set a limit on the relevant mixing angle about $\sin^2 2\theta < 0.1$ at 90% confidence level.

After the discovery and confirmation of neutrino oscillations by various experiments including atmospheric, solar, accelerator, and reactor neutrino (KamLAND) experiments, the measurement of the unknown θ_{13} became the next target. The Daya Bay, Double Chooz and RENO are the three reactor neutrino experiments being able to measure θ_{13} with the sensitivity better than the limit set by CHOOZ and Palo Verde. These three experiments are all based on the gadolinium-loaded liquid scintillator, and they all have one or several near (0.3~0.6 km baseline) and far (1~1.7 km) detectors. In 2012, Double Chooz reported an indication of reactor $\bar{\nu}_e$ disappearance excluding the no θ_{13} oscillation at 94.6% C.L. [31]; Daya Bay reported a non-zero θ_{13} with 5.2 σ significance [30]; RENO reported a non-zero θ_{13} with 4.9 σ significance [32]. Thus the non-zero θ_{13} was established.

While measuring θ_{13} , all these three experiments observed an excess in the reactor $\bar{\nu}_e$ spectrum at ~ 5 MeV region, and its origin is still unknown [92, 93, 94]. Nevertheless, these three experiments all employed the comparison of the measured spectra between the near and far detectors through which the "5 MeV excess" could be canceled out, thus the θ_{13} measurement was protected.

The latest θ_{13} measurements from these three experiments by Neutrino 2020 conference are shown in Fig.1.10. Besides the θ_{13} , Daya Bay and RENO also provided a precise measurement of $|\Delta m_{32}^2|$, and the precision of Daya Bay is around 3% [95] being competitive to the precision of the present LB ν B experiments. Double Chooz is less sensitive to Δm_{32}^2 due to its shorter baseline configuration. The measurement of θ_{13} is considered beyond today's ability to improve and it is therefore a key input to all present and future experiments.

1.4.5 Present Knowledge of Neutrino Oscillations

As just briefly reviewed in this section, since the neutrino oscillation discovery, an enormous knowledge of the neutrino oscillations has been accumulated. The neutrino oscillations based on the three neutrino framework has been well established. The state of the art knowledge of the oscillation parameters is summarized in Tab.1.1, according to the NuFit 5.0 global analysis².

1. Actually, these experiments were mainly designed to validate the finding of the Kamioka experiments by discarding the complementary oscillation mode.

2. Other global analysis exist in Ref.[96, 97] providing generally consistent results.

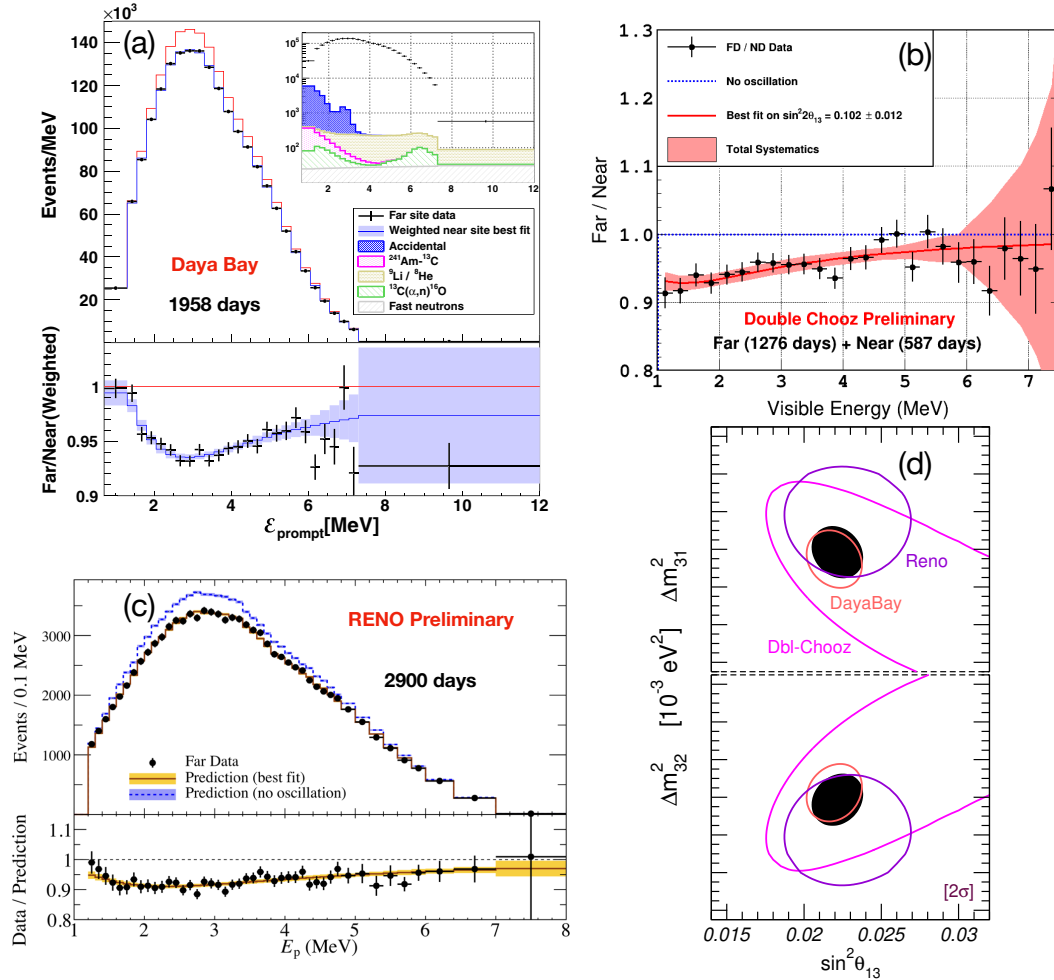


Figure 1.10 – The θ_{13} measurements from Daya Bay (a), Double Chooz (b) and RENO (c). The three experiments all observed respectively a deficit in the energy spectrum at their far detectors compared to the non-oscillation expectation. Their near to far ratios all have a clear distortion revealing the θ_{13} driven neutrino oscillation. The latest results by Neutrino 2020 for Daya Bay [95], Double Chooz [98] and RENO [99] are shown. (d): 2σ confidence level region of θ_{13} and Δm_{31}^2 for Daya Bay (pink), Double Chooz (magenta), RENO (violet), and their combination (black regions). The upper panel is for the NMO and lower panel is for the IMO. (d) is taken from NuFit 5.0 [69].

NuFIT 5.0 (2020)

	Normal Ordering (best fit)		Inverted Ordering ($\Delta\chi^2 = 2.7$)		
	bf $\pm 1\sigma$	3σ range	bf $\pm 1\sigma$	3σ range	
without SK atmospheric data	$\sin^2 \theta_{12}$	$0.304^{+0.013}_{-0.012}$	$0.269 \rightarrow 0.343$	$0.304^{+0.013}_{-0.012}$	$0.269 \rightarrow 0.343$
	$\theta_{12}/^\circ$	$33.44^{+0.78}_{-0.75}$	$31.27 \rightarrow 35.86$	$33.45^{+0.78}_{-0.75}$	$31.27 \rightarrow 35.87$
	$\sin^2 \theta_{23}$	$0.570^{+0.018}_{-0.024}$	$0.407 \rightarrow 0.618$	$0.575^{+0.017}_{-0.021}$	$0.411 \rightarrow 0.621$
	$\theta_{23}/^\circ$	$49.0^{+1.1}_{-1.4}$	$39.6 \rightarrow 51.8$	$49.3^{+1.0}_{-1.2}$	$39.9 \rightarrow 52.0$
	$\sin^2 \theta_{13}$	$0.02221^{+0.00068}_{-0.00062}$	$0.02034 \rightarrow 0.02430$	$0.02240^{+0.00062}_{-0.00062}$	$0.02053 \rightarrow 0.02436$
	$\theta_{13}/^\circ$	$8.57^{+0.13}_{-0.12}$	$8.20 \rightarrow 8.97$	$8.61^{+0.12}_{-0.12}$	$8.24 \rightarrow 8.98$
	$\delta_{CP}/^\circ$	195^{+51}_{-25}	$107 \rightarrow 403$	286^{+27}_{-32}	$192 \rightarrow 360$
	$\frac{\Delta m_{21}^2}{10^{-5} \text{ eV}^2}$	$7.42^{+0.21}_{-0.20}$	$6.82 \rightarrow 8.04$	$7.42^{+0.21}_{-0.20}$	$6.82 \rightarrow 8.04$
	$\frac{\Delta m_{3\ell}^2}{10^{-3} \text{ eV}^2}$	$+2.514^{+0.028}_{-0.027}$	$+2.431 \rightarrow +2.598$	$-2.497^{+0.028}_{-0.028}$	$-2.583 \rightarrow -2.412$
	with SK atmospheric data	$\sin^2 \theta_{12}$	$0.304^{+0.012}_{-0.012}$	$0.269 \rightarrow 0.343$	$0.304^{+0.013}_{-0.012}$
$\theta_{12}/^\circ$		$33.44^{+0.77}_{-0.74}$	$31.27 \rightarrow 35.86$	$33.45^{+0.78}_{-0.75}$	$31.27 \rightarrow 35.87$
$\sin^2 \theta_{23}$		$0.573^{+0.016}_{-0.020}$	$0.415 \rightarrow 0.616$	$0.575^{+0.016}_{-0.019}$	$0.419 \rightarrow 0.617$
$\theta_{23}/^\circ$		$49.2^{+0.9}_{-1.2}$	$40.1 \rightarrow 51.7$	$49.3^{+0.9}_{-1.1}$	$40.3 \rightarrow 51.8$
$\sin^2 \theta_{13}$		$0.02219^{+0.00062}_{-0.00063}$	$0.02032 \rightarrow 0.02410$	$0.02238^{+0.00063}_{-0.00062}$	$0.02052 \rightarrow 0.02428$
$\theta_{13}/^\circ$		$8.57^{+0.12}_{-0.12}$	$8.20 \rightarrow 8.93$	$8.60^{+0.12}_{-0.12}$	$8.24 \rightarrow 8.96$
$\delta_{CP}/^\circ$		197^{+27}_{-24}	$120 \rightarrow 369$	282^{+26}_{-30}	$193 \rightarrow 352$
$\frac{\Delta m_{21}^2}{10^{-5} \text{ eV}^2}$		$7.42^{+0.21}_{-0.20}$	$6.82 \rightarrow 8.04$	$7.42^{+0.21}_{-0.20}$	$6.82 \rightarrow 8.04$
$\frac{\Delta m_{3\ell}^2}{10^{-3} \text{ eV}^2}$		$+2.517^{+0.026}_{-0.028}$	$+2.435 \rightarrow +2.598$	$-2.498^{+0.028}_{-0.028}$	$-2.581 \rightarrow -2.414$

Table 1.1 – NuFit 5.0 global analysis of the neutrino oscillation parameters in the three neutrino framework. The upper (lower) section corresponds to the results obtained without (with) the inclusion of the Super-Kamiokande atmospheric data. The oscillation parameters are obtained by assuming the NMO or the IMO. Δm_{3l}^2 represents Δm_{31}^2 for the NMO and Δm_{32}^2 for the IMO. Taken from [56].

1.5 Outlook

Despite the tremendous progress made in neutrino physics, particularly in neutrino oscillations, in recent decades, neutrinos still leave some open questions about their fundamental properties. This section will briefly review some critical open questions and future experimental effort.

Neutrino Mass Ordering

As mentioned previously, the mass ordering of m_1 and m_2 has been established as $m_1 < m_2$ thanks to the solar neutrino observations. However, whether m_3 is the heaviest or lightest one among three neutrinos remains unknown as the unsolved neutrino mass ordering (MO) illustrated in Fig.1.11. It leaves two possibilities, namely *normal MO*: $m_1 < m_2 < m_3$ (NMO) and *inverted MO*: $m_3 < m_1 < m_2$ (IMO). The MO determination is important for some physics topics such as the absolute neutrino mass scale, the neutrinoless double beta decay and the CP violation, which will be discussed in Sec.2.1.1.

There are various future efforts towards the MO determination including mainly three approaches 1.) medium baseline reactor neutrino experiment, i.e. JUNO [100], 2.) long baseline neutrino beam experiments, e.g. NOvA with increased statistics and DUNE [101], 3) atmospheric neutrino based experiments, e.g. ORCA [102], PINGU [103], Hyper-Kamiokande [104] and INO [105]. In addition, the complementarity among different approaches provides synergic effects to enhance the MO resolution as it will be discussed in Chapter 8.

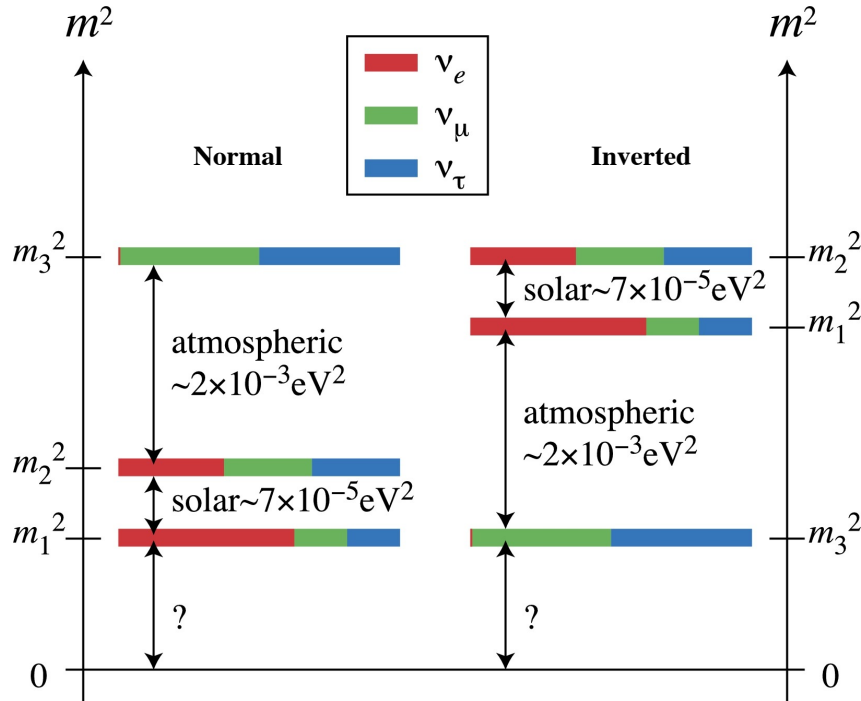


Figure 1.11 – Illustration of the neutrino MO and unknown absolute mass scale. The squared neutrino masses are shown for both the NMO (left) and IMO (right). The flavor compositions of the mass eigenstates are represented in color. The absolute neutrino mass scale is unknown. Taken from [106]

CP Violation

The charge-conjugation and parity (CP) is the symmetry between the particle and the antiparticle with mirror spatial coordinates. This implies whether particle and antiparticles behave identically or not. The CP violation was observed in the baryon sector [107]. However, in the lepton sector, whether CP symmetry is conserved or violated is not yet fully resolved. Under the assumption of CPT conservation, generally a building block for theory construction, CP violation can also be explored by the complementary channel of T symmetry violation. However, this channel is currently not competitive in precision.

The long baseline neutrino beam (LB ν B) experiments are suitable to investigate the lepton CP violation through the measurement of δ_{CP} phase via the muon neutrino to electron neutrino appearance. Although the present T2K data indicates a non-zero δ_{CP} close to 3σ significance, a resolved lepton CP violation is still requisite. If CP symmetry violates, a precise measurement of δ_{CP} is needed.

T2K and NO ν A will continue increasing their statistics, thus contributing to the δ_{CP} measurement. The future LB ν B-III, i.e. DUNE [101] and Hyper-K [104], with higher δ_{CP} resolution will likely resolve the lepton CP violation.

Beyond Neutrino Oscillations

Apart from the unresolved MO and CP violation, there are several other open questions regarding the fundamental properties of neutrinos. Some critical questions are listed as follows:

- **Dirac or Majorana neutrino.** The Dirac particle means the particle is different from its antiparticle, while the Majorana particle means the particle is its own antiparticle. Even though all the fermions except neutrinos in the SM are known to be Dirac particles, whether neutrinos are Dirac or Majorana particles has not yet been determined. The neutrinoless double beta decay ($0\nu\beta\beta$) can be used to test if neutrinos are Majorana particles or not, because this process can only occur in case of Majorana neutrinos [108], expressed as:

$$(A, Z) \rightarrow (A, Z + 2) + 2e^{-}. \quad (1.28)$$

The experimental observable of the $0\nu\beta\beta$ is its half-life $T_{1/2}^{0\nu}$. There are 35 isotopes for double beta decay, and the commonly used ones are ^{48}Ga , ^{76}Ge , ^{82}Se , ^{100}Mo , ^{130}Te , ^{136}Xe , ^{150}Nd , etc. [109]. The current best limit of the $0\nu\beta\beta$ half-life comes from KamLAND-Zen liquid scintillator experiment with ^{136}Xe isotope, and it set a bound of $T_{1/2}^{0\nu} > 1.07 \times 10^{26}$ year (90% C.L.) [110]. Various current and future experiments using different isotopes and different experimental techniques continue studying this challenging topic, a review article can be found in Ref.[109].

- **Absolute Neutrino Mass Scale.** Even though neutrino oscillation has proved that neutrinos are massive, this phenomenon is not sensitive to the absolute neutrino mass. One of the best way to search for neutrino mass is through the kinematics of tritium β decay:

$${}^3\text{H} \rightarrow {}^3\text{He} + e^{-} + \bar{\nu}_e. \quad (1.29)$$

The neutrino mass can be investigated through the end point of the e^{-} spectrum. The current best limit of the neutrino mass is set by KATRIN experiment [111] as: $m_{\nu_e}^{eff} < 1.1$ eV. The future sensitivity of KATRIN is estimated to be ~ 0.2 eV. There are also several experiments using ^{163}Ho decay kinematics to probe the neutrino mass, such as: ECHo [112], HOLMES [113], and NuMECS [114].

Another possible way to search for neutrino mass is via the $0\nu\beta\beta$. The previously mentioned $0\nu\beta\beta$ observable $T_{1/2}^{0\nu}$ can be interpreted as an effective Majorana neutrino mass $\langle m_{\beta\beta} \rangle$. The current best limits from KamLAND-Zen is $\langle m_{\beta\beta} \rangle < 61 \sim 165 \text{meV}$ [110].

- **Sterile Neutrinos.** There are several anomalies observed by the LSND experiment [115], MiniBooNE experiment [116], Gallium solar neutrino experiments [117] and reactor neutrino experiments [118]. These anomalies can not be explained in the three neutrino framework, but may be explained if additional neutrinos (*sterile neutrinos*) at eV scale exist. However, to probe whether sterile neutrinos exist or not needs more effort, some comprehensive reviews of this field are in Ref.[119, 120]. The possibility that some of those anomalies are caused by other unknown effects, such as a new background and lack of knowledge of the source, has not been full tested neither.

Chapter 2

Neutrino Physics with JUNO

The Jiangmen Underground Neutrino Observatory (JUNO) is a new generation neutrino experiment with rich scientific prospects. The primary physics topics of JUNO are the determination of the neutrino mass ordering (MO) and the precise measurement of neutrino oscillation parameters θ_{12} , Δm_{21}^2 and Δm_{32}^2 through reactor neutrino disappearance (i.e. $\bar{\nu}_e \rightarrow \bar{\nu}_e$). Beyond reactor neutrinos, JUNO is an excellent detector for geo-neutrino detection; it has the potential to observe supernova neutrinos, solar neutrinos and atmospheric neutrinos; it is also sensitive to some beyond SM physics such as the search for proton decay. The rich physics potentials make JUNO to be one of the most important future neutrino experiments.

The neutrino MO determination leads largely the experimental design. The experimental site is located in Jiangmen city, Guangdong province, southern China, which is about 53 km from both the Yangjiang and Taishan nuclear power plants (NPPs), as shown in Fig.2.1. The reactor neutrinos with a typical energy of ~ 4 MeV at ~ 53 km baseline correspond to the first maximal oscillation region driven by the solar parameters (θ_{12} , Δm_{21}^2), as shown in Fig.2.1. The JUNO central detector is based on a 20,000 tons liquid scintillator (LS) detector, located ~ 700 meters underground. For achieving the high precision reactor neutrino energy spectrum measurement, the JUNO detector is designed to have an unprecedented 3% energy resolution at 1MeV and an excellent systematics control aimed for better than 1%.

This chapter is devoted to review the relevant physics topics of JUNO, particularly focusing on the reactor neutrino oscillation topics. The neutrino MO determination mechanism at JUNO is elaborated in Sec.2.1. The precision measurement of neutrino oscillation parameters is addressed in Sec.2.2. Other JUNO physics potentials beyond reactor neutrinos are briefly reviewed in Sec.2.3, including supernova neutrinos, solar neutrinos, geo-neutrinos, proton decay, etc.

2.1 Neutrino MO Determination at JUNO

2.1.1 Motivation

The unsolved neutrino MO, as explained in Sec.1.5 with Fig.1.11, leaves two possibilities, i.e. whether *normal MO* (NMO, $m_3 > m_2 > m_1$) or *inverted MO* (noted as IMO, $m_2 > m_1 > m_3$).

The MO determination is an important step in neutrino physics for various scientific purposes. For example:

- The MO helps to understand the lower limit of the absolute neutrino mass scale. Based on present knowledge, if the IMO (NMO) is true, m_{ν_e} can be deduced to be larger than ~ 48 (8.5) meV at 95% C.L. [58].

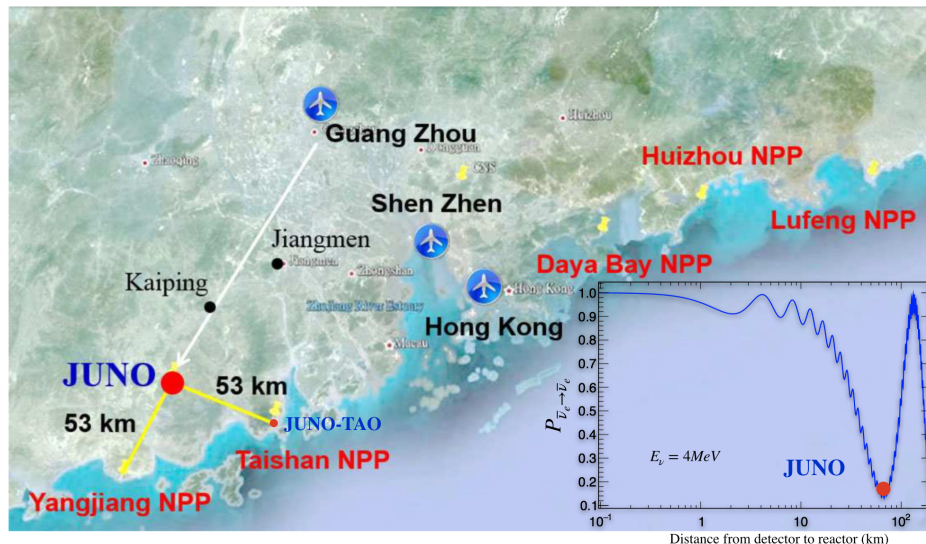


Figure 2.1 – The JUNO experimental site. The JUNO detector is located at the first maximal oscillation region driven by solar parameters (θ_{12} , Δm_{21}^2).

- The MO aids to define the target sensitivity of the neutrinoless double beta decay ($0\nu\beta\beta$) experiments, which aim to determine whether neutrinos are Dirac or Majorana particles. If the IMO is true, a lower bound on the effective Majorana mass can be set at ~ 16 meV at 95%CL, which is within the target sensitivity of the next generation $0\nu\beta\beta$ experiments [58].
- The MO can be helpful for the CP violation measurement in long baseline neutrino beam experiments, such as NOvA [85].
- The MO is also a key parameter for understanding the neutrino mass generation and also for the neutrino astronomy and neutrino cosmology [121, 122, 123].

There are three practical approaches to address the neutrino MO, namely a.) medium baseline reactor neutrino experiment i.e. JUNO, b.) long baseline neutrino beam experiments and c.) atmospheric neutrino based experiments, as reviewed in Ref.[124].

The MO determination at long baseline neutrino beam (LB ν B) experiments such as the present NOvA [85] and future DUNE [101] rely on the matter effects and they are affected by the δ_{CP} . As for the atmospheric neutrino experiments including the running Super-K [125] and IceCube [126], and future ORCA [102], PINGU [103], Hyper-K [104] and INO [105], their MO determination also rely on the matter effects and they are affected by the θ_{23} octant ambiguity. By combining current data, the NuFit 5.0 global analysis favored the NMO up to 2.7σ [56], however, this preference remains fragile.

Comparing to all the other experiments mentioned above, JUNO is the only experiment based on the vacuum oscillation to determine the MO, because of its relative short baseline inducing tiny matter effects [100, 127]. Moreover, by adding the external Δm_{32}^2 information from the LB ν B disappearance channel, the MO sensitivity of JUNO can be boosted while keeping its vacuum oscillation feature. This synergy is due to the complementarity between JUNO and LB ν B [128, 129], and was studied at JUNO [130]. This thesis addresses this boosting effect according to the updated neutrino oscillation knowledge for investigating the earliest possible resolved MO solution in Chapter 8.

Given the unique feature of the binary outcome of the neutrino MO, i.e. whether NMO or IMO, the MO determination will benefit from JUNO's vacuum oscillation measurement. The redundant information of MO from different experiments (*matter effects driven vs vacuum oscillation driven*) can serve as cross-checks, thus helping to establish

the resolved MO or to discover unexpected discrepancies. This will also be developed in Chapter 8.

2.1.2 Reactor $\bar{\nu}_e$ Disappearance in Vacuum

The MO determination at JUNO is based on the reactor $\bar{\nu}_e$ disappearance in vacuum. In the three neutrino framework, the $\bar{\nu}_e$ disappearance (or survival) probability can be derived from Eq.(1.13), written as:

$$P_{\bar{\nu}_e \rightarrow \bar{\nu}_e} = 1 - \cos^4 \theta_{13} \sin^2 2\theta_{12} \sin^2 \Delta_{21} - \sin^2 2\theta_{13} \cos^2 \theta_{12} \sin^2 \Delta_{31} - \sin^2 2\theta_{13} \sin^2 \theta_{12} \sin^2 \Delta_{32}. \quad (2.1)$$

The Δ_{ij} is defined as:

$$\Delta_{ij} = \Delta m_{ij}^2 L / 4E, \quad (2.2)$$

where $\Delta m_{ij}^2 = m_i^2 - m_j^2$ is the squared mass difference, L is the baseline and E is the neutrino energy. In order to clearly reveal the MO manifestation through the oscillation probability, by using the constrain $\Delta m_{32}^2 = \Delta m_{31}^2 - \Delta m_{21}^2$, Eq.(2.1) can be rewritten as:

$$P_{\bar{\nu}_e \rightarrow \bar{\nu}_e} = 1 - \cos^4 \theta_{13} \sin^2 2\theta_{12} \sin^2 \Delta_{21} - \sin^2 2\theta_{13} \sin^2 (|\Delta_{32}|) - \cos^2 \theta_{12} \sin^2 2\theta_{13} \sin^2 (\Delta_{21}) \cos (|2\Delta_{32}|) - [\pm \frac{1}{2} \cos^2 \theta_{12} \sin^2 2\theta_{13} \sin (2\Delta_{21}) \sin (|2\Delta_{32}|)], \quad (2.3)$$

where the sign before the last term is "+" for the NMO and "-" for the IMO. The oscillation patterns for the NMO and IMO are different, as shown in Fig.2.2. There is a "slow&big" oscillation dominated by $(\Delta m_{21}^2, \theta_{12})$ and a "fast&small" oscillation dominated by $(\Delta m_{32}^2, \theta_{13})$.

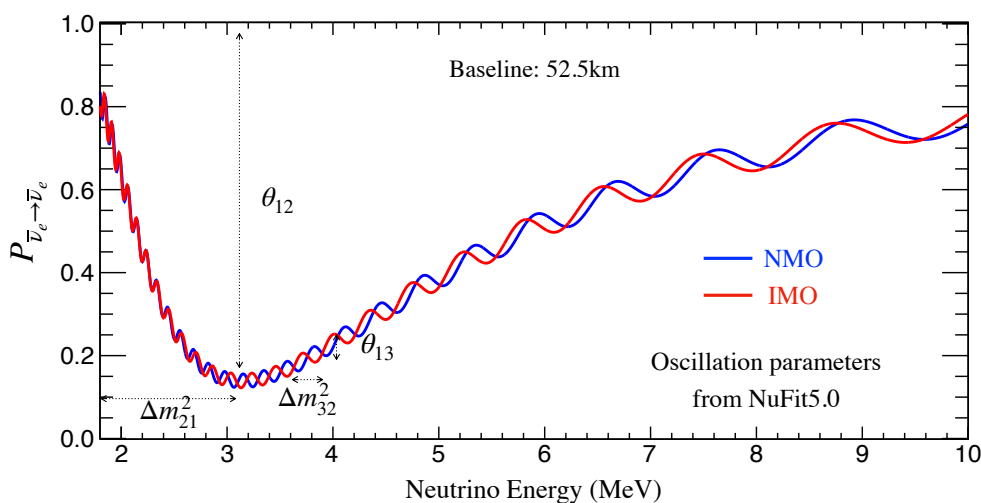


Figure 2.2 – The reactor $\bar{\nu}_e$ disappearance (or survival) probability as a function of the neutrino energy. The baseline is ~ 52.5 km. The neutrino energy is set from ~ 1.8 MeV which is the inverse beta decay (IBD) interaction threshold.

2.1.3 Reactor Neutrino Signal

Reactor Neutrino Flux

As mentioned in Sec.1.4.4, nuclear reactors produce $\bar{\nu}_e$ via the beta decays of the fission fragments. In typical commercial reactors as those used at JUNO [100], there are mainly four fuel isotopes, ^{235}U , ^{238}U , ^{239}Pu , and ^{241}Pu , contributing to more than 99.7% of the reactor $\bar{\nu}_e$. The $\bar{\nu}_e$ flux from such a reactor can be calculated according to

$$\Phi(E_\nu) = \frac{W_{th}}{\sum_i f_i e_i} \cdot \sum_i f_i \cdot S_i(E_\nu), \quad (2.4)$$

where W_{th} is the thermal power of the reactor, f_i is the fission fraction [131], e_i is the thermal energy released in each fission [90], and $S_i(E_\nu)$ is the neutrino flux per fission for the i -th isotope [132]

Assuming that a reactor core has ~ 3 GW thermal power, the thermal energy released in each fission is about 200 MeV, and 6 $\bar{\nu}_e$ are released per fission, there will be about 6×10^{20} $\bar{\nu}_e$ emitted per second. The total thermal power of the JUNO 10 reactor cores from Yangjiang and Taishan NPPs will be about 36 GW. When JUNO starts running, 8 cores from Yangjiang and Taishan NPPs will be in operation with about 27 GW thermal power.

The state of the art predictions of the reactor neutrino flux are based on the ILL data [133, 134], and these predictions claim an uncertainty of $\leq 3\%$. However, strong indications have been found by reactor- θ_{13} experiments (and others) that both the measured rate and shape deviate from the predictions [92, 135, 136, 137], which remain as open issues under investigation.

Inverse Beta Decay

The reactor $\bar{\nu}_e$ is measured via the inverse beta decay (IBD) reaction at the liquid scintillator (LS) detector:

$$\bar{\nu}_e + p \rightarrow n + e^+, \quad (2.5)$$

where the proton target is provided by the LS.

The cross section of IBD reaction can be written as [138]:

$$\sigma = 9.52 \times \left(\frac{E_{e^+} p_{e^+}}{1 \text{ MeV}^2} \times 10^{-44} \text{ cm}^2 \right), \quad (2.6)$$

where E_{e^+} and p_{e^+} are the energy and momentum of the positron respectively. The cross section error is $\leq 0.2\%$ obtained from the neutron lifetime measurement.

The neutrino energy is given by:

$$E_{\bar{\nu}_e} = E_{e^+} + 1.293 \text{ MeV}, \quad (2.7)$$

where 1.293 MeV is the difference of the proton and neutron mass. The neutrino energy threshold of the IBD reaction is ~ 1.804 MeV.

The positron carries most of the neutrino energy. It deposits quickly its kinetic energy in the LS, and then most likely annihilates with an electron emitting gammas with total energy of 1.022 MeV. It also has the chance to form a positronium, and then the positronium annihilates emitting gammas [139]. In general, the energy deposition of the positron is quick, thus forming a prompt signal with the energy E_{prompt} as:

$$E_{prompt} = E_{e^+}^{kinetic} + 1.022 \text{ MeV}, \quad (2.8)$$

where $E_{e^+}^{kinetic}$ is the positron kinetic energy and 1.022 MeV corresponds to the annihilation gamma energy.

The recoiled neutron from the IBD reaction carries small kinetic energy (typically ~ 10 keV), which is negligible in most cases. The neutron scatters in the LS until being thermalized, and then it is captured by a proton about $200 \mu s$ later (after the IBD reaction) and releases a 2.2 MeV gamma, forming a delayed signal.

Therefore, the neutrino energy can be deduced from the prompt signal, as

$$E_{\bar{\nu}_e} = E_{prompt} + 0.782 \text{ MeV}, \quad (2.9)$$

and the prompt-delayed coincidence is used to discriminate the reactor neutrino signals from the backgrounds.

Reactor Neutrino Energy Spectrum at JUNO

Given the reactor neutrino disappearance probability, the reactor neutrino flux and the IBD cross-section, the reactor neutrino energy spectrum at JUNO is illustrated in Fig.2.3, where the no oscillation, NMO oscillation and IMO oscillation cases are shown. The NMO and IMO manifest as different oscillation patterns in the energy spectrum. Experimentally, the MO and oscillation parameters information can be extracted through a precise measurement of the oscillated energy spectrum in which the energy resolution and energy scale control are critical.

It needs to be mentioned that Fig.2.3 is only used to illustrate the oscillation information embedded in the spectrum, and it does not represent the MO resolution at JUNO because neither the energy resolution nor the minimization for the wrong MO is considered. The more appropriate spectrum to illustrate the MO resolution is shown in Fig.2.5, as explained next.

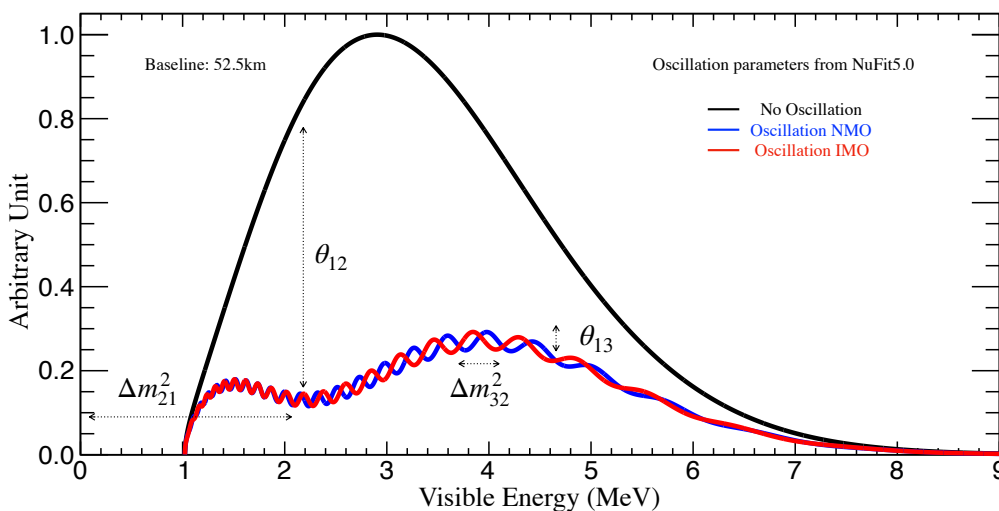


Figure 2.3 – The reactor $\bar{\nu}_e$ energy spectrum at JUNO for no oscillation (black), oscillation NMO (blue) and IMO (red) cases respectively. The visible energy corresponds to the detectable energy of the prompt signals. Here the detector response effects are not included, thus the visible energy can also be understood as the deposited positron energy. JUNO is designed to observe both the "slow&big" ($\Delta m_{21}^2, \theta_{12}$) and "fast&small" ($\Delta m_{32}^2, \theta_{13}$) oscillation patterns in which the MO and oscillation parameters information is embraced and can be extracted. The energy resolution is infinite and the minimization for the wrong mass ordering is not considered.

2.1.4 Backgrounds

The major backgrounds with respect to the reactor $\bar{\nu}_e$ IBD signals are the accidental background, ${}^8\text{He}/{}^9\text{Li}$, fast neutron and (α, n) [140, 141]. The estimated spectra of the backgrounds at JUNO are shown in Fig.2.4. Much of the design of the JUNO experimental setup is based on reducing backgrounds including the overburden, internal radiopurity control, veto system, etc. which will be addressed in the next chapter.

Accidental Background

The prompt-delayed coincidence is a signature to identify the IBD signals. However, some random single energy depositions, originating from the natural radioactivity, cosmogenic isotopes, spallation neutrons, etc. can mimic a prompt-delayed coincidence of the IBD. These are called accidental background.

A fiducial volume cut can significantly reduce the accidental background since the radioactivity mainly comes from the surrounding rock and the glass bulbs of the PMTs. The rate of the accidental background can be estimated through $R_{acc} = R_{p-like} \cdot R_{d-like} \cdot \Delta T$, where R_{p-like} and R_{d-like} are the rate of prompt-like and delayed-like signals from the random single energy depositions, respectively, and ΔT is the coincidence time window.

${}^8\text{He}/{}^9\text{Li}$

The cosmogenic ${}^8\text{He}/{}^9\text{Li}$ can also mimic IBD signals through the $\beta - n$ decays. The decay products are electrons creating prompt signals and neutrons creating correlated delayed signals. As the ${}^8\text{He}/{}^9\text{Li}$ isotopes are induced by cosmic muons, this background can be largely rejected by vetoing a sufficient detector volume along the tracks of their parent muons for a sufficient time (longer than the lifetime of these isotopes).

Fast Neutron

When the cosmic muons pass only the rock or the water pool and miss the LS, the energetic neutrons produced by these muons, i.e. fast neutrons, can enter the LS. The fast neutron can scatter off a proton, forming a prompt signal, and then it can be captured, forming a delayed signal. The prompt-delayed signals caused by the fast neutrons are also the background with respect to the reactor $\bar{\nu}_e$ IBD. The overburden of JUNO is large (~ 700 m underground), so the expected rate of fast-n is very small as listed in Tab.2.1. Similarly to the techniques developed by the reactor- θ_{13} experiments, the Top Tracker detector located on top of the JUNO central detector can help to tag these missing (by LS) muons, thus helping to reject the fast neutron background.

${}^{13}\text{C}(\alpha, n){}^{16}\text{O}$

The ${}^{13}\text{C}(\alpha, n){}^{16}\text{O}$ background derives from the alpha particles interacting with ${}^{13}\text{C}$. The alpha particles are produced from the Th and U radioactivities and the ${}^{13}\text{C}$ is in the LS. The interaction products are the neutrons and ${}^{16}\text{O}$ nuclei. The neutron can scatter on proton or ${}^{12}\text{C}$ forming a prompt signal, and then it can be captured forming a delayed signal. If the ${}^{16}\text{O}$ nucleus is in the excited state, its de-excitation can emit a gamma which also contributes to the prompt signal. This background can be estimated based on the measured rate of alpha particles. In addition, alpha particles are heavily quenched in the liquid scintillator.

Geo-neutrino

Geo-neutrinos are $\bar{\nu}_e$ produced from radioactive decays of Th and U inside the earth. They experience the same IBD reaction as reactor neutrinos, thus being irreducible from the reactor neutrinos. The geo-neutrino energy is below ~ 3 MeV, hence it does not contribute to the background for the higher energy ($3\sim 10$ MeV) reactor neutrinos. JUNO can measure the rate of geo-neutrinos with the unprecedented precision by itself, thus it can remove the geo-neutrinos according to its own measurement and at the same time provide one of the most important measurement of geo-neutrino in the world [100].

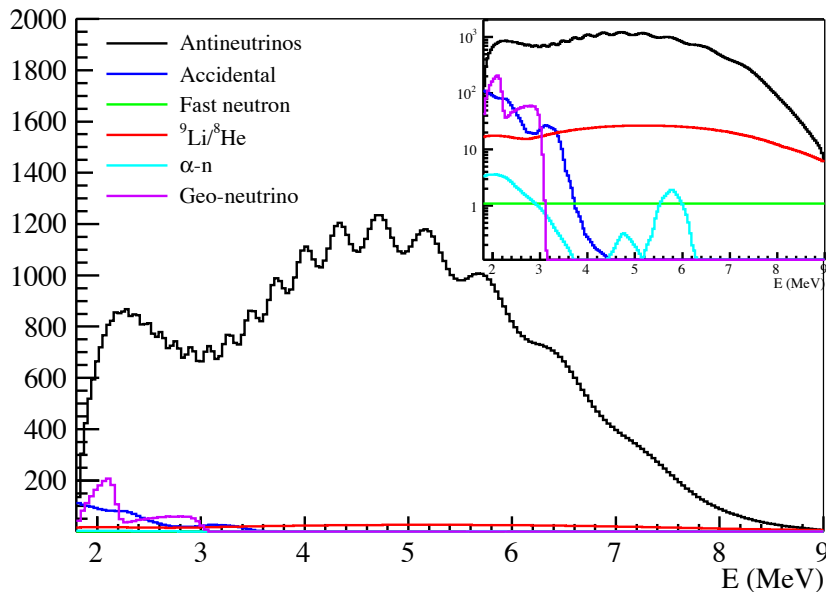


Figure 2.4 – Spectra of the accidental, ${}^8\text{He}/{}^9\text{Li}$, fast neutron and ${}^{13}\text{C}(\alpha, n){}^{16}\text{O}$ backgrounds. The antineutrino signal spectrum is also shown. $3\%/\sqrt{E(\text{MeV})}$ energy resolution is assumed in these spectra. Taken from [100].

2.1.5 Event Selection

Based on the background estimation, a set of preliminary reactor $\bar{\nu}_e$ selection criteria are listed below [100]:

- Fiducial volume cut: $radius < 17$ m.
- Prompt energy cut: $0.7 \text{ MeV} < E_{prompt} < 12 \text{ MeV}$.
- Delayed energy cut: $1.9 \text{ MeV} < E_{delayed} < 2.5 \text{ MeV}$;
- Time interval cut between the prompt and delayed signal: $\Delta T < 1.0$ ms;
- Prompt-delayed distance cut: $R_{prompt-delayed} < 1.5$ m;
- Muon veto criteria:
 - For muons tagged by the water Cherenkov detector, veto the whole LS volume for 1.5 ms.
 - For good tracked muons in the central detector and the water Cherenkov detector, veto the detector volume within 3 meters distance to the muon track for 1.2 s.

- For the tagged, non-trackable muons in the central detector, veto the whole LS volume for 1.2 s

Based on the selection criteria above, the reactor $\bar{\nu}_e$ IBD selection efficiencies, the signal rate and background rate are listed in Tab.2.1. JUNO is estimated to observe 60 reactor $\bar{\nu}_e$ IBD events per day, with about 3.8 ($\sim 6\%$) background events.

Table 2.1 – The efficiencies of the reactor $\bar{\nu}_e$ selection cuts, signal and background event rates per day at JUNO. The considered backgrounds are discussed in Sec.2.1.4. The selection cuts are described in Sec.2.1.5. By considering all backgrounds and all selection cuts mentioned above, the reactor neutrino IBD event rate is estimated to be 60 events per day, and the background rate is about 3.8 events per day.

Selection	IBD efficiency	IBD	Geo- ν s	Accidental	${}^8\text{He}/{}^9\text{Li}$	Fast n	α, n
-	-	83	1.5	$\sim 5.7 \times 10^4$	84	-	-
Fiducial volume	91.8%	76	1.4	410	77	0.1	0.05
Energy cut	97.8%	73	1.3		71		
Time cut	99.1%			1.1			
Vertex cut	98.7%	60	1.1	0.9	1.6		
Muon veto	83%	60	1.1	0.9	1.6		
Combined	73%	60	3.8				

2.1.6 MO Sensitivity from Spectral Analysis at JUNO

The MO sensitivity embedded in the reactor $\bar{\nu}_e$ energy spectrum at JUNO is illustrated in Fig.2.5 by assuming $3\%/\sqrt{E(\text{MeV})}$ energy resolution and the NMO. Since the NMO is assumed to be true but a prior unknown for the data, both NMO and IMO assumptions should be tested with the data through the minimization approach, e.g. χ^2 based minimization as explained next. The MO sensitivity relies on the rejection power for the wrong MO test. Qualitatively, the sensitivity can be illustrated as the relative spectral ratio between the true mass ordering (NMO assumed here) spectrum and the wrong mass ordering (IMO here) after the minimization, as shown in Fig.2.5. The quantification of the sensitivity is explained next.

Basic Experimental Configuration

In order to illustrate quantitatively the neutrino MO sensitivity at JUNO, first, the basic experimental configuration is defined as: 1.) 20 kt LS as the target medium, 2.) 52.5 km baseline, 3.) 36 GW_{th} total thermal power (10 cores), 4.) reactor $\bar{\nu}_e$ flux model from ILL and Vogel et al.[142, 143, 144, 145]¹, 5.) $3\%/\sqrt{E(\text{MeV})}$ energy resolution and 6.) six years (2000 effective days) statistics with 73% IBD detection efficiency.

1. The Huber [133] and Mueller [134] models are also evaluated, giving consistent MO estimation results.

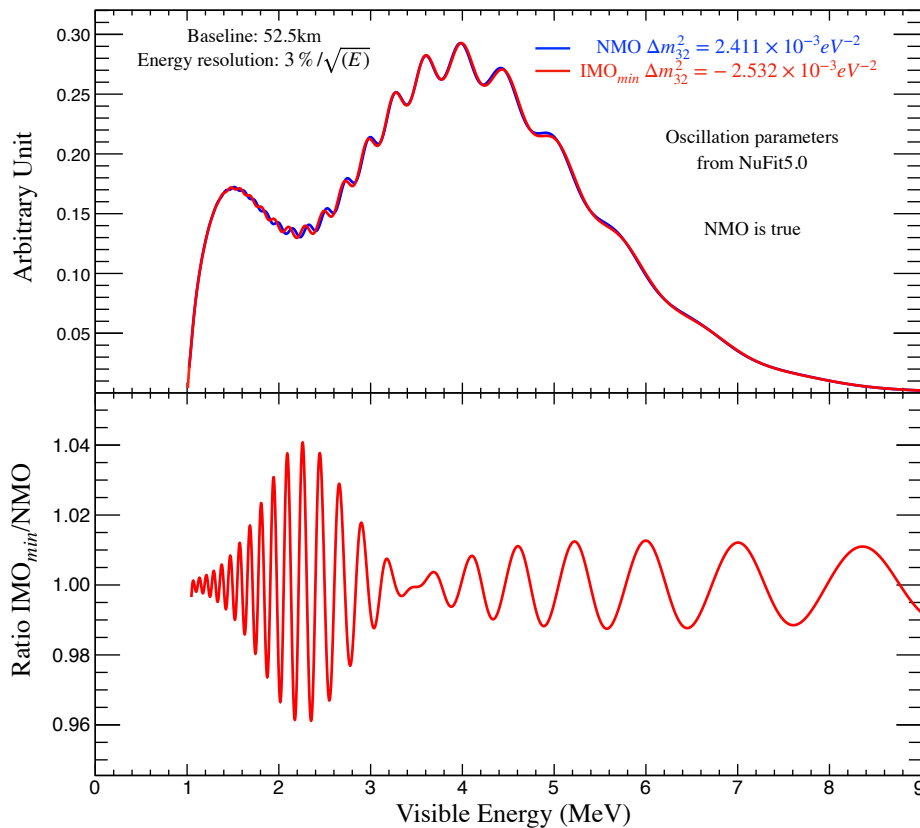


Figure 2.5 – Illustration of the MO sensitivity in the reactor $\bar{\nu}_e$ energy spectrum at JUNO (upper panel). The NMO (blue) is assumed to be true. The IMO_{min} (red) spectrum is made by setting the $|\Delta m_{32}^2|_{IMO} \approx |\Delta m_{32}^2|_{NMO} + 0.12 \times 10^{-3} eV^{-2}$. The approximate value of $0.12 \times 10^{-3} eV^{-2}$ is obtained through the χ^2 based minimization as Eq.(2.10). The lower panel shows the ratio between the NMO spectrum and the IMO_{min} spectrum illustrating the MO sensitivity as a function of the visible energy. The visible energy corresponds to the detectable energy of the prompt signal. Here the detector response effects are not included, thus the visible energy can also be understood as the deposited positron energy.

MO Discriminator

The least squares minimization method is used to quantify the MO sensitivity by defining the following χ^2 function:

$$\chi^2 = \sum_{i=1}^{N_{bin}} \frac{[M_i - T_i(1 + \sum_k \alpha_{ik} \epsilon_k)]^2}{M_i} + \sum_k \frac{\epsilon_k^2}{\sigma_k^2}, \quad (2.10)$$

where M_i and T_i are the measured and predicted events in the i -th energy bin respectively, σ_k is the systematic uncertainty to the corresponding pull parameter ϵ_k , and α_{ik} is the fraction of the event contribution of the k -th pull parameter to the i -th bin. 200 equal-size bins are used for the neutrino energy between 1.8 MeV and 8 MeV (equivalent to the visible energy between 1 MeV and 7.2 MeV). The considered systematic uncertainties (σ_k) are motivated by the state of the art knowledge from reactor- θ_{13} experiments. Those are 2% correlated reactor uncertainty, 0.8% uncorrelated reactor uncertainty, 1% spectrum shape uncertainty and 1% detector-related uncertainty.

By assuming a true mass ordering, both NMO and IMO fits can be performed by

minimizing all the relevant oscillation parameters including Δm_{21}^2 , θ_{12} and Δm_{32}^2 . The JUNO's sensitivity on θ_{13} is not better than the current reactor- θ_{13} experiments, thus, θ_{13} is an external input for JUNO. The best fit gives a χ^2 minimum for the NMO ($\chi_{min}^2(NMO)$), as well as for the IMO ($\chi_{min}^2(IMO)$). The MO discriminator can be defined as the difference between the two minima:

$$\Delta\chi_{MO}^2 = |\chi_{min}^2(NMO) - \chi_{min}^2(IMO)|. \quad (2.11)$$

Generally, the MO sensitivity can be statistically interpreted in terms of the significance as $\sqrt{\Delta\chi_{MO}^2}$ in units of σ 's.

Sensitivity

By considering the basic experimental configurations defined previously and the oscillation parameters in [146, 147], the MO sensitivities are listed in Tab.2.2 by accumulating the following experimental systematics:

- By considering only the statistical effect with the equal baseline (10 reactor cores) of 52.5 km, the MO sensitivity in terms of $\Delta\chi_{MO}^2$ is about 16 units.
- By considering the actual reactor cores distribution about ± 0.5 km with respect to 52.5 km, the spectrum will be slightly smeared, resulting in the sensitivity decreases about 3 units.
- The neutrinos from Daya Bay (215km, 17.4 GW) and Huizhou (265km, 17.4 GW) NPPs will also be detected by the JUNO detector, these neutrinos from longer baseline will also generate a spectrum smearing effect, thus reducing the sensitivity about 1.7 units.
- The assumed 1% reactor shape uncertainty will degrade the sensitivity by 1 unit.
- The background uncertainties lead to further sensitivity decrease about 0.7 unit, including the (6.3%) statistical uncertainty contribution to -0.6 unit and the (0.4%) shape uncertainty contribution to -0.1 unit.

Table 2.2 – Different contributions to the MO sensitivity.

	Stat.	Core dist.	DYB &HZ	Shape	B/S(stat.)	B/S(shape.)
Size	52.5 km	$\sim \pm 0.5$ km	~ 200 km	1%	6.3%	0.4%
$\Delta\chi_{MO}^2$	+16	-3	-1.7	-1	-0.6	-0.1

From the spectral analysis, JUNO can reach $\sim 3\sigma$ median MO sensitivity with six years statistics under the reasonable systematics assumptions. The sensitivity as the function of the energy resolution and statistics is shown in Fig.2.6.

The non-linearity in the energy measurement is another critical factor that has a significant impact on the spectral analysis for the the MO determination. If the energy non-linearity calibration is imperfect, there will be a residual non-linearity embedded in the energy spectrum. This non-linearity limitation that goes beyond the calibration capability, will lead to a misinterpretation of the MO measurement results. For example, if there is no residual energy non-linearity in the spectral analysis, the MO sensitivity in terms of $\Delta\chi_{MO}^2$ is assumed to be ~ 11 units; if the residual energy non-linearity is assume to have the following form which is inspired by Daya Bay [130]:

$$\frac{E_{rec}}{E_{true}} = \frac{1 + p_0}{1 + p_1 \exp(-0.2E_{true})}, \quad (2.12)$$

by including the energy non-linearity above into the measured spectrum M_i of Eq.(2.10), while keeping the predicted spectrum T_i unaffected, the MO sensitivity can be falsely degraded or enhanced according to the value of p_0 and p_1 , as illustrated in Fig.2.7.

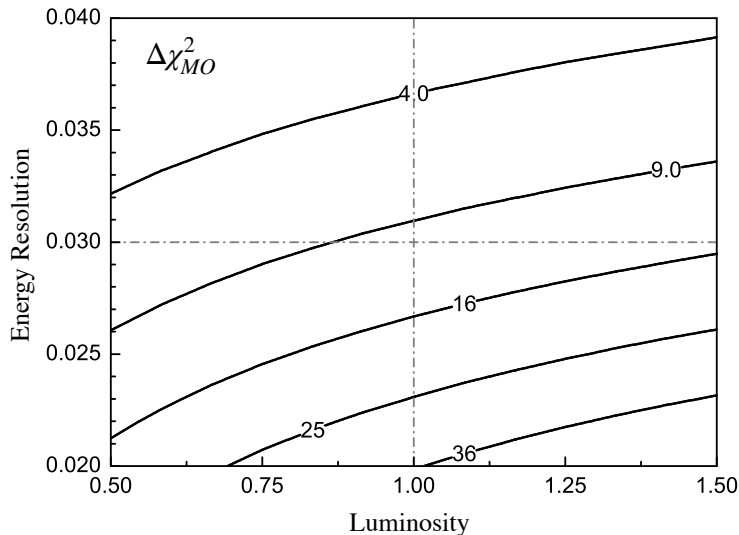


Figure 2.6 – The JUNO MO sensitivity ($\Delta\chi_{MO}^2$) contour as the function of the event statistics (luminosity) and the energy resolution, where the vertical dash-dotted line (i.e. luminosity=1) stands for the running of six years with 80% signal efficiency (10 reactor cores). Taken from Ref.[100].

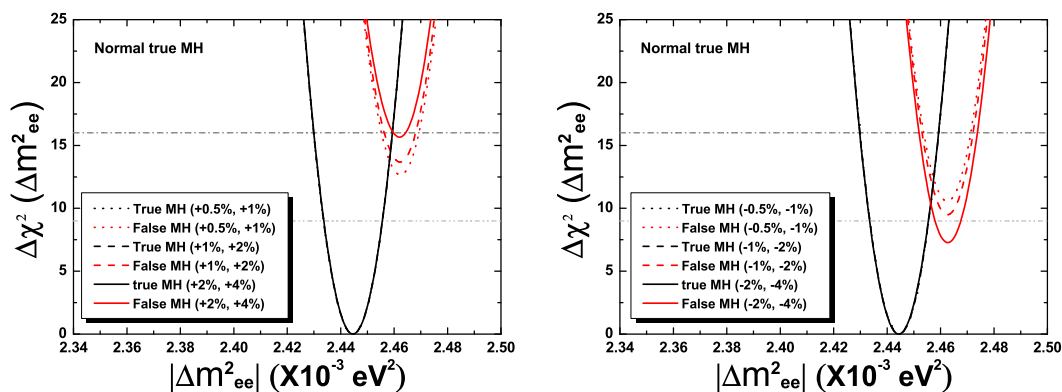


Figure 2.7 – Energy non-linearity effect in the MO sensitivity. The $\Delta\chi_{MO}^2$ is shown as a function of Δm_{ee}^2 . Δm_{ee}^2 is a combination between Δm_{31}^2 and Δm_{32}^2 as: $\Delta m_{ee}^2 = \cos^2 \theta_{12} \Delta m_{31}^2 + \sin^2 \theta_{12} \Delta m_{32}^2$. The NMO is assumed to be true. If no residual energy non-linearity, the MO sensitivity is ~ 11 units. By including the energy non-linearity of Eq.(2.12) with different (p_0, p_1) values (indicated in the legend), the MO sensitivity can be falsely either enhanced (left) or degraded (right). It turns out a misinterpretation for the MO sensitivity, hence the measurement results. Taken from Ref.[130].

In the energy spectral analysis, it needs to be emphasized that the energy controls including both the energy resolution ($\sim 3\%$ at 1 MeV as the goal) and the energy detection systematics with the energy non-linearity in particular ($< 1\%$) are of great importance for the MO determination. As anticipated, most of this thesis work will deal with those energy related topics in great depth. Hence the results in this thesis are expected to have a direct impact to one of the most important systematics and/or limitation to JUNO's MO and oscillation parameters measurements, as will be elaborated in Chapter 4, 5 and 6.

The JUNO intrinsic MO measurement is driven by the vacuum oscillation as discussed in this section. The matter effects for the MO is tiny as evaluated in Ref.[127] where a reduction of $\sim 0.6 \Delta\chi_{MO}^2$ unit is estimated. The matter effects will not change the vacuum oscillation nature in JUNO's MO determination. Moreover, by adding external information of Δm_{32}^2 from the disappearance channel of the LB ν B experiments, the JUNO MO sensitivity can be enhanced, while still keeping the vacuum oscillation nature, as will be discussed in Chapter 8.

At last, the fine structure in the reactor neutrino spectrum potentially has an impact on the MO sensitivity, as reported in Ref.[148, 149]. JUNO-TAO [150], the satellite experiment of JUNO, will study the fine structure of the reactor neutrino spectrum in order to provide a reference spectrum for JUNO and eliminate the potential impact.

2.2 High Precision θ_{12} , Δm_{21}^2 and Δm_{32}^2 Measurements

The precision measurement of the oscillation parameters is important to test the three neutrino model and to probe new physics beyond the SM. For example the precise measurement of the mixing angles contributes to the unitarity test of the PMNS matrix [151, 152]; the precise measurement of the squared mass differences will test the sum rule of " $\Delta m_{31}^2 + \Delta m_{31}^2 + \Delta m_{32}^2 = 0$ " [100]. The current precision of the oscillation parameters is shown in Tab.2.3, most of them are known with a few percent precision.

As illustrated in Fig.2.3, the JUNO spectrum contains the θ_{12} , Δm_{21}^2 , θ_{13} and Δm_{32}^2 information. With the designed excellent performance of the JUNO detector, i.e. $\sim 3\%$ energy resolution at 1 MeV and less than 1% energy detection systematics control, JUNO aims to measure θ_{12} , Δm_{21}^2 and Δm_{32}^2 with sub-percent precision. JUNO precision on θ_{13} is not better than current constraints from reactor- θ_{13} experiments, so θ_{13} can be considered as input for JUNO.

The JUNO expected precision of θ_{12} , Δm_{21}^2 and Δm_{32}^2 with six years statistics is shown in Tab.2.4 by accumulating the relevant systematics as explained in the table. JUNO alone will contribute to the measurement of half of total oscillation parameters (3 of 6 in total) with unprecedented precision for neutrino oscillation physics. To reach sub-percent precision measurements of the oscillation parameters, an extremely careful control of systematics including the energy scale and energy resolution is critical, which is the main topic of this thesis.

It has to be pointed out that the matter effects have a non-negligible impact on the measurement of the solar parameters θ_{12} and Δm_{21}^2 . The impact manifests as a shift of the best-fit values by 1σ to 2σ [127, 153]. So it has to be carefully considered for the real data analysis, however the matter effects do not affect the sensitivity studies presented above.

Table 2.3 – Current precision of neutrino oscillation parameters based on the state of the art knowledge by 2020. The individual 1σ precision corresponds to the individual dominant experiments only. The global 1σ precision is taken from NuFit 5.0. The JUNO expected precision is also listed.

	$\sin^2 \theta_{12}$	Δm_{21}^2	$\sin^2 \theta_{13}$	$ \Delta m_{32}^2 $	$\sin^2 \theta_{23}$	δ_{CP}
Dominant Exps.	SNO	KamLAND	DayaBay	T2K	NOvA	T2K
Individual 1σ	8% [52]	2.5%[87]	3.4%[95]	2.9% [81]	7%[85]	40%[81]
Global 1σ [56]	4.2%	2.8%	2.8%	1.1%	3.5%	14%
JUNO Expected 1σ	$\sim 0.7\%$	$\sim 0.6\%$	10% level	$\sim 0.4\%$	null	null

Table 2.4 – Expected precision of $\sin^2 \theta_{12}$, Δm_{21}^2 and $|\Delta m_{32}^2|$ at JUNO. The nominal case corresponds to six years statistics with $3\%/\sqrt{E(\text{MeV})}$ energy resolution. The considered systematics are the 1% bin-to-bin energy uncorrelated uncertainty (B2B), 1% energy linear scale uncertainty (EL), 1% energy non-linear uncertainty (NL) and the background related uncertainties (BG) including 6.3% statistical uncertainty and 0.4% shape uncertainty. These uncertainties are accumulated from left to right.

	Nominal(Stats.)	+B2B (1%)	+BG	+EL(1%)	+NL(1%)
$\sin^2 \theta_{12}$	0.54%	0.60%	0.62%	0.64%	0.67%
Δm_{21}^2	0.24%	0.27%	0.29%	0.44%	0.59%
$ \Delta m_{32}^2 $	0.27%	0.31%	0.31%	0.35%	0.44%

2.3 Beyond Reactor Neutrino Oscillation

JUNO, as a multipurpose neutrino observatory, has broad physics prospects beyond its primary reactor neutrino oscillation study. Its physics potentials include the detection of supernova neutrinos, geo-neutrinos, solar neutrinos, proton decay, etc. This section aims to review briefly some of those physics topics. A comprehensive overview can be found in [100].

2.3.1 Supernova Neutrinos

During a Supernova (SN) burst, $\sim 99\%$ of the energy will be released through neutrinos and antineutrinos of all flavors in a few seconds. The SN neutrinos carries precious information about the SN explosion mechanism and the neutrino intrinsic properties. JUNO is capable to detect SN neutrinos with high statistics through various detection channels.

Considering a galactic SN at a typical 10 kpc distance as an example, JUNO can register about 5000 events from the dominating IBD channel, ~ 2000 events from all flavor neutrino-proton scattering, ~ 300 events from neutrino-electron scattering and also some events from neutral current and charge current interactions on ^{12}C . The neutrino event spectra for these detection channels are estimated in Fig.2.8.

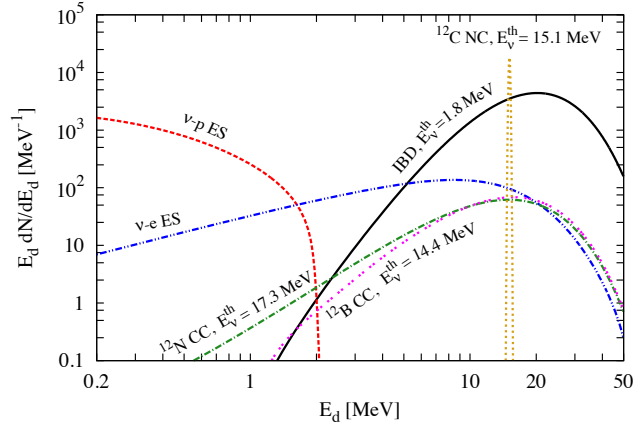


Figure 2.8 – The estimated supernova neutrino event spectra with respect to the visible energy E_d at JUNO for a SN explosion at 10 kpc. The neutrino oscillations are not considered for simplifying the illustration. These spectra corresponds to the main detection channels: IBD (black), elastic $\nu - p$ scattering (red), elastic $\nu - e$ scattering (blue) and the $(\nu, {}^{12}\text{C})$ interactions (orange, green and magenta). Taken from [100].

2.3.2 Solar Neutrinos

The solar neutrinos have played an important role in the study of neutrino oscillations as reviewed in Sec.1.4.1. and will continue contributing in neutrino physics and astrophysics.

The contributions of JUNO will come from the ${}^8\text{B}$ solar neutrino detection, and also possibly from low energy (~ 1 MeV) ${}^7\text{Be}$ solar neutrino detection. The solar neutrino detection is via the elastic $\nu - e$ scattering with the estimated spectra shown in Fig.2.9.

It is worth to highlight that the radiopurity control and the cosmogenic backgrounds control are critical for the solar neutrino detection. JUNO is designed primarily for reactor neutrino detection where the radiopurity (${}^{238}\text{U}$ and ${}^{232}\text{Th}$ in particular) is required to be $< 10^{-15} g/g$; however, the desired radiopurity for solar neutrino detection, particular for the low energy solar neutrinos, is $< 10^{-17} g/g$. The reduction of the cosmogenic backgrounds, including mainly ${}^{12}\text{B}$, ${}^8\text{Li}$, ${}^6\text{He}$, ${}^{10}\text{C}$ and ${}^{11}\text{Be}$, relies on the veto strategy, as discussed in Ref.[154]. Dedicated effort to achieve the high radiopurity control for solar neutrino detection is indispensable and under active discussion within JUNO.

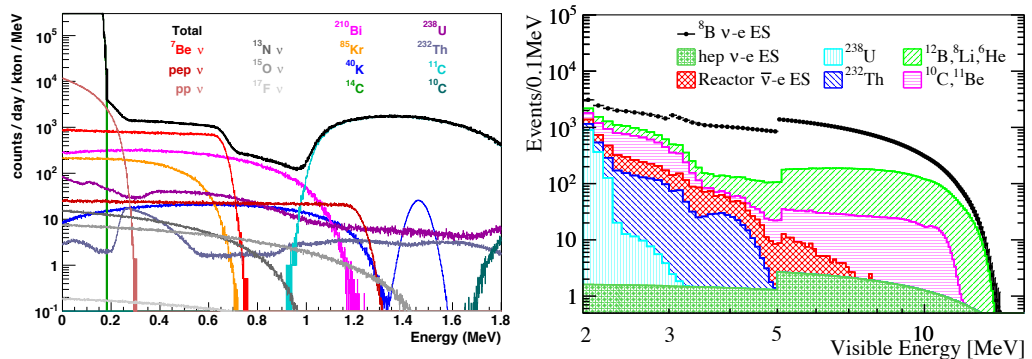


Figure 2.9 – The estimated solar neutrino spectra at JUNO. The radiopurity (${}^{238}\text{U}$ and ${}^{232}\text{Th}$ in particular) is assumed to be $< 10^{-17} g/g$. Left [100]: low energy ${}^7\text{Be}$, pp and pep and CNO solar neutrino spectra with the background spectra. Right [154]: ${}^8\text{B}$ and hep solar neutrino spectra with the background spectra in ten years of data taking.

2.3.3 Proton Decay

The proton decay is forbidden in the SM, but is predicted in some Grand Unified Theories [155]. JUNO is capable to investigate the SUSY-favored proton decay channel: $p \rightarrow K^+ + \bar{\nu}$ with a competitive and complementary sensitivity compared to other experiments such as Super-K, Hyper-K and DUNE. The signatures of $p \rightarrow K^+ + \bar{\nu}$ at JUNO can be summarized as:

- A prompt signal from K^+ .
- A delayed signal from the decay daughters of K^+ , i.e. mainly μ^+ through decay channel: $K^+ \rightarrow \mu^+ + \nu_\mu$, with a time coincidence of 12 ns.
- A further delayed signal of e^+ from $\mu^+ \rightarrow e^+ + \bar{\nu}_\mu + \nu_e$ with 2.2 μ s time coincidence.

These signatures are illustrated in Fig.2.10, by considering $K^+ \rightarrow \mu^+ + \nu_\mu$ decay channel. The time coincidence and well-defined energies provide a powerful tool to reject the background, which is crucial for the search of proton decays. The JUNO sensitivity for the proton decay search in this channel is shown in Fig.2.10, in comparison with Super-K, Hyper-K and DUNE.

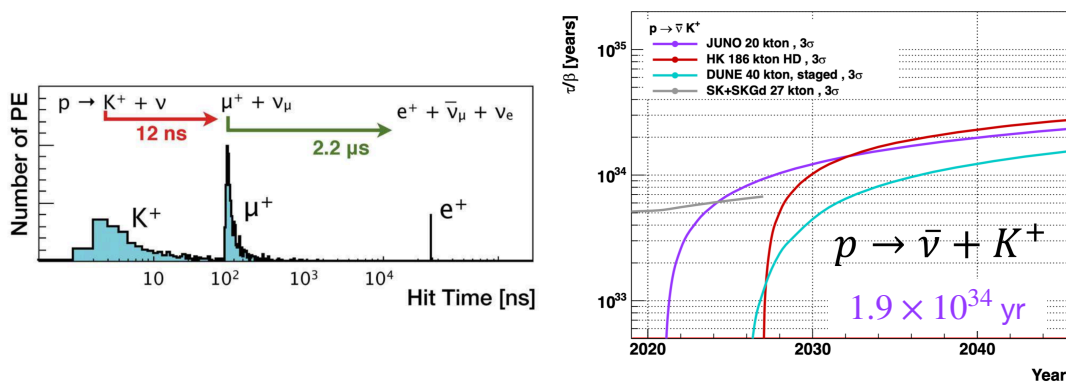


Figure 2.10 – Left: proton decay signatures at JUNO for $p \rightarrow K^+ + \bar{\nu}$ channel. Right: 3σ sensitivity to the proton lifetime for $p \rightarrow K^+ + \bar{\nu}$ channel. The sensitivity of JUNO (purple) is about 1.9×10^{34} years of the proton lifetime. The sensitivity of Super-K (grey), Hyper-K (red) and DUNE (blue) are also shown regarding the same decay channel. Taken from [156].

2.3.4 Geo-neutrinos

Geo-neutrinos are $\bar{\nu}_e$ produced from the natural radioactivity of thorium (Th), uranium (U) and potassium (K) in the earth. Geo-neutrinos from Th and U are considered as an irreducible background in the reactor $\bar{\nu}_e$ study. However, for geoscientists the situation is opposite, i.e. reactor $\bar{\nu}_e$ signals are the background. The detection of geo-neutrinos can help geoscientists to investigate the the composition and evolution of the earth, where many unknowns still remain and are, as of now, inaccessible via other means but the neutrino detection. So, the completeness of the understanding of our planet, and hence the solar system, depends strongly on geo-neutrino detection.

The liquid scintillator neutrino detector is the best known probe to detect geo-neutrinos. The main challenge is the low flux. Two LS experiments have measured geo-neutrinos, i.e. KamLAND [157] and Borexino [158]. JUNO, as the world's largest LS detector (20 kt), has the potential to measure the geo-neutrinos with the largest

statistics. About 300~500 geo-neutrino events per year can be recorded at JUNO which will surpass the total recorded events from all the current experiments.

2.3.5 Other Topics

In addition to the physics topics mentioned above, the JUNO experiment can also contribute to the diffuse supernova neutrino background detection, the atmospheric neutrinos study, the sterile neutrinos search, the dark matter search, etc. As these topics are largely irrelevant from the main topic of this thesis (reactor neutrino detection related), they are not reviewed here, the detailed discussion about these topics can be found in [100].

Chapter 3

JUNO Detector

The MO determination dominantly drives the design of the JUNO detector, imposing the requirements on statistics, energy resolution, systematics, backgrounds, etc.

To detect the reactor $\bar{\nu}_e$ efficiently, the JUNO detector is based on the liquid scintillator (LS) technology. The requirement on statistics impels the design of the world's largest LS volume, i.e. 20 kt, contained in the central detector (CD) which is an acrylic sphere of ~ 35 m diameter supported by a stainless-steel structure. Two independent readout systems are installed viewing the common LS. The two readout systems are a.) the 20-inch photomultiplier tubes and corresponding electronics (LPMT system) as the dominant contributor to the stochastic energy resolution, b.) the 3-inch photomultiplier tubes and corresponding electronics (SPMT system) contributing to the systematics control through the Dual Calorimetry as will be discussed in the next chapter. A redundant calibration system is designed to be deployed in the CD for the detector response calibration. The veto system for the muon induced background reduction consists of 1.) a water Cherenkov detector made of a cylindrical water pool where the CD is placed, 2.) a Top Tracker detector made of plastic scintillator covering the top of the CD. The overview of the JUNO detector design is shown in Fig.3.1.

This chapter aims to present the conceptual design of the JUNO detector together with the public or published testing results. The aforementioned LS, readout, calibration and veto systems are addressed in this chapter. The other systems including the data acquisition system, software, etc. are briefly introduced in this chapter, as well as the satellite experiment JUNO-TAO.

3.1 Liquid Scintillator

The liquid scintillator (LS), serving as the target medium for the detection of neutrinos, transfers the energy of neutrinos to the visible energy in terms of photons through scintillation processes. Typically the LS is composed of the solvent forming the bulk of the target medium and the solute for increasing the scintillation light yield and shifting the wavelength of photons to the photosensor sensitive region. The JUNO LS uses 1.) the linear alkyl benzene (LAB) as the solvent, 2.) the PPO as the primary fluor and 3.) the bis-MSB as the wavelength-shifter.

Scintillation Processes

The major LS scintillation processes can be understood in the following simplified ways at JUNO. First, the neutrino interactions in the LS produce ionizing particles, e.g. the reactor $\bar{\nu}_e$ IBD reactions produce positrons and neutrons. Second, the ionizing particles normally excite the molecules featuring benzene rings in the solvent (LAB), because

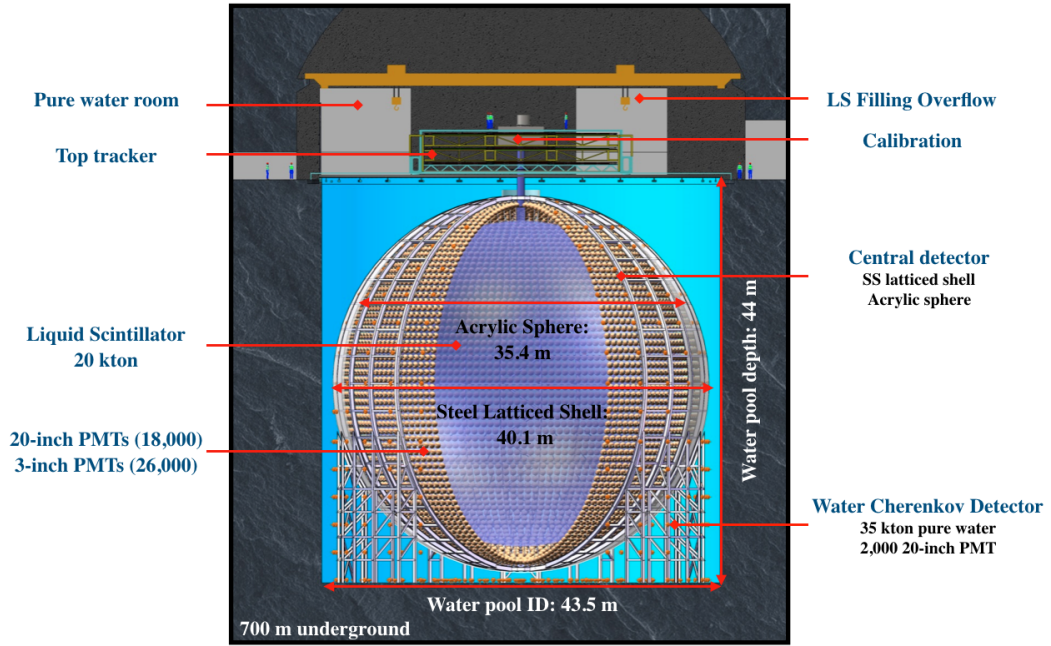


Figure 3.1 – Schematic view of the JUNO detector.

of the large proportion of the solvent. Third, the excited molecules in the solvent typically transfer the energy to the fluor (PPO) through mainly the non-radiative processes. Then the fluor deexcites mainly via the radiative processes by emitting photons. At last, the photons propagate through the medium and can be absorbed by the waveform shifter (bis-MSB), and then photons with higher wavelength (~ 430 nm) are re-emitted. These photons propagate in the LS and can be effectively detected by the PMTs as their wavelengths are located in the PMT sensitive region.

The aforementioned points are the dominant LS scintillation processes as illustrated with Fig.3.2, more complete description of the scintillation processes can be found in Ref.[159].

Specifications and Properties

The specifications and properties of the LS that matter the JUNO physics are the total mass, composition, light yield, transparency and radiopurity, detailed as follows:

- Total mass: 20,000 tons. Large LS mass ensures high statistics, e.g. in 6 years running, JUNO will collect $\sim 100,000$ reactor $\bar{\nu}_e$ IBD events.
- Composition: The LS recipe is optimized as the purified solvent LAB with 2.5 g/L PPO and 1 to 4 mg/L bis-MSB to yield highest possible light according to the joint testing results of JUNO and Daya Bay [160].
- Light yield: About 10^4 photons per MeV are emitted, leading to >1200 PE yield per MeV together with the photon detection (i.e. PMT) systems. This high light yield dominates the stochastic component of the energy resolution to an unprecedented level of $3\%/\sqrt{E}$.
- Transparency: The optical attenuation length for scintillation photons is designed to be larger than 20 m and the laboratory testing results support this point [161,

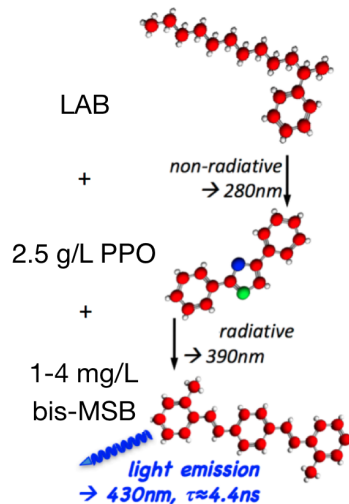


Figure 3.2 – Illustration of the JUNO LS composition and the scintillation processes.

162]. This high transparency will help to reduce the light loss during photon propagation.

- Radiopurity: The uranium (U), thorium (Th), and potassium (K) are the main sources of the LS radioactivity. These isotopes can decay, thus causing a background. The JUNO reactor neutrino physics requires the LS radiopurity with $^{238}\text{U}/^{232}\text{Th} < 10^{-15} \text{g/g}$ and $^{40}\text{K} < 10^{-16} \text{g/g}$. The radiopurity requirement from the solar neutrino measurement is more stringent as $^{238}\text{U}/^{232}\text{Th} < 10^{-17} \text{g/g}$. An online detector, called OSIRIS, will be built to monitor the LS radiopurity [163, 164].
- Purification: Several purification systems with different techniques are designed for both the optical and radioactive purification, such as the Al_2O_3 column plant, distillation plant, water extraction and gas stripping plant [165, 166].

3.2 Readout System

The readout system consists of the photosensors and readout electronics. The photosensors are responsible for the scintillation photons to charge current conversion, and the electronics is used to digitize the analog charge signals and then send them to the data acquisition system.

The JUNO central detector has two independent readout systems. 1.) The large photomultiplier tube (LPMT) system consists of 20-inch PMTs with the FADC (flash analog-to-digital converter) based electronics. 2.) The small photomultiplier tube (SPMT) system consists of 3-inch PMTs with the digital photoelectron counting based electronics. The dual readout is a unique feature of the JUNO detector, constituting the Dual Calorimetry design which is the main topic of this thesis. In this section, the focus is the general description of the two readout systems, while the interplay between the two systems (i.e. Dual Calorimetry) will be addressed in Chapter 4, 5 and 6.



Figure 3.3 – Photos of the JUNO LPMTs and SPMT. Left: NNVT 20-inch MCP-PMT. Middle: Hamamatsu 20-inch Dynode-PMT. Right: HZC 3-inch PMT.

3.2.1 LPMT Readout System

PMT Instrumentation

As the main photon detection system, the LPMT system employs $\sim 18,000$ high detection efficiency ($\sim 27\%$) 20-inch PMTs. The photosensor coverage is about 75% of the LS surface aiming for >1200 photoelectrons (PE) yield per MeV which is the key to achieve better than 3% stochastic energy resolution at 1 MeV.

Two types of 20-inch PMTs are used for JUNO, 1.) 15,000 MCP (Micro Channel Plate) PMTs provided by the NNVT (North Night Vision of Technology) company in cooperation with IHEP (Beijing), 2.) 5000 dynode PMTs provided by the Hamamatsu company, as shown in Fig.3.3. About $\sim 18,000$ LPMTs will be installed in the central detector viewing the LS, and the rest will be used for the water Cherenkov detector. The specifications of these two types LPMT are listed in Tab.3.1.

Readout Electronics

The readout electronics of the LPMT are based on the FADC technology. They are designed to provide high resolution charge sampling, large dynamic range, precise time measurement and the capability of handling high event rate for fulfilling the requirements of not only reactor neutrinos but also moons, supernova neutrinos, atmospheric neutrinos, etc.

The schematic of the LPMT electronics is shown in Fig.3.4. The main components and specifications can be listed as follows [168]:

- High Voltage Unit (HVU). It generates the high voltage and power the PMT through the voltage divider and splitter.
- Global Control Unit (GCU). It is the core of the electronics. The key elements of GCU are the analog to digital unit (FADC) and the FPGA. The FADC digitizes the analog PMT waveform at 1 Gsample/s speed with a 12~14 bit resolution, and the dynamic range is from 1 PE to about 1000 PE. Then the data is transferred to the FPGA for the packaging, processing and buffering. The digitized waveform is stored in the local memory provisionally. When the trigger condition is fulfilled, the data is transferred to the data acquisition system (DAQ) through ethernet.

Table 3.1 – LPMT (20-inch) specifications for MCP-PMT and Dynode PMT [167]. The detection efficiency corresponds to 420 nm photons. The dark noise rate is measured at 0.25 PE. The transit time spread is measured at the top point of the PMT. The rising and falling times corresponds to the single PE waveform.

Characteristics	Unit	MCP-PMT (NNVT)	Dynode PMT (R12860, Hamamatsu)
Detection Efficiency (QE×CE)@420nm	%	27, >24	27, >24
Peak-to-Valley Ratio		3.5, >2.8	3, >2.5
Transit Time Spread (FWHM)	ns	12, <15	2.7, <3.5
Dark noise rate @0.25 PE	Hz	20k, <30k	10k, <50k
Rising Time/Falling Time	ns	1.7/12	5/9
Pre-pulsing/After-pulsing	%	0.5/1.0 (count)	1.5/15(charge)
High Voltage@ 10^7 Gain	V	2500, <2800	2000, <2500
Non-linearity(0~1000PE)	%	10	10
Radioactivity of Glass	ppb	^{238}U :50 ^{232}Th :50 ^{40}K :20	^{238}U :400 ^{232}Th :400 ^{40}K :40

There is also a 2 GB DDR3 memory in the GCU enabling to handle high trigger rate events, e.g. supernova neutrinos events.

- Back End Card (BEC). It is used to link the GCU to the DAQ and trigger systems. Its main task is to transfer the data, handle the synchronous signals and distribute the power.

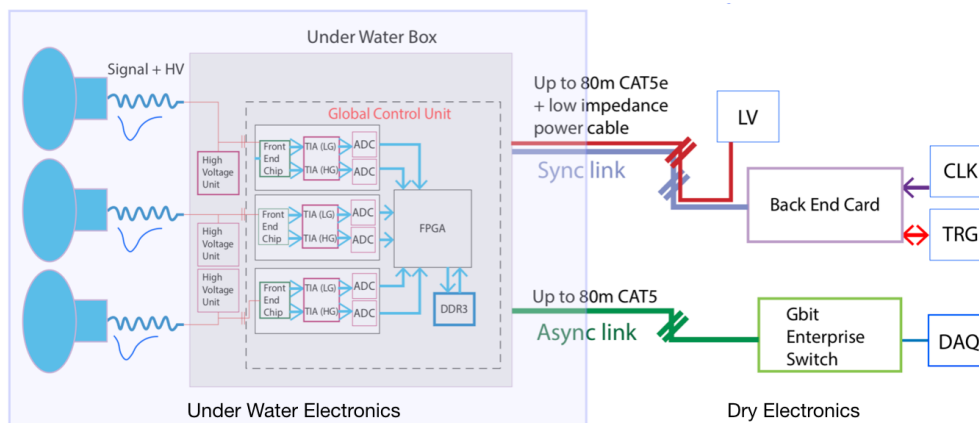


Figure 3.4 – The LPMT system readout scheme. The wet (underwater) electronics, including the HVU and GCU etc., are contained in the underwater box. The FADC unit embedded in the GCU consists of a Front-End Chip (FEC), two Trans-Impedance Amplifiers (TIA), two drivers, and two ASIC ADCs. Each box hosts the electronics for three LPMTs. For the dry (on the surface) electronics, one BEC serves for 48 channels. Taken from [169].

3.2.2 SPMT Readout System

PMT Instrumentation

The SPMT readout system is introduced as an auxiliary readout system for JUNO providing an independent energy estimator. It is designed to use 3-inch PMTs, and because of the small size, the single photoelectron (PE) detection is dominant for the reactor neutrino signals. Compared to the LPMT energy estimator with the waveform reconstruction, the SPMT energy estimator, based on the digital PE counting, is much simple.

The $\sim 26,000$ SPMTs are provided by the HZC (Hainan Zhanchuang Photonics Technology) company, as shown in Fig.3.3. The specifications of the SPMT are listed in Tab.3.2.

Table 3.2 – JUNO SPMT (3-inch) specifications [170]. The detection efficiency corresponds to 420 nm photons. The dark noise rate is measured at 0.25 PE.

Characteristics	Unit	3-inch PMT (HZC)
Detection Efficiency (QE \times CE)@420nm	%	~ 25 , >22
Peak-to-Valley Ratio		~ 3.2
Transit Time Spread (FWHM)	ns	~ 5
Single PE width	%	~ 33
Dark noise rate@0.25 PE	Hz	~ 500
Pre-pulsing/After-pulsing	%	0.4/4.8
High Voltage@ 3×10^6 Gain	V	~ 1100
Radioactivity of Glass	ppb	$^{238}\text{U} < 400$ $^{232}\text{Th} < 400$ $^{40}\text{K} < 200$

Readout Electronics

The SPMT electronics is designed primarily to operate in the digital single PE counting mode. Conceptually, the electronics is trigger-less and a threshold can be set between the pedestal and the single PE; once the signal pulse passes the threshold, it will be counted digitally. The discrimination between the pedestal and the single PE (i.e. threshold effect) is critical and it requires a low electronics noise level. In addition, the SPMT electronics can also record the charge information of a signal pulse about its amplitude and the time over threshold, thus helping for the multi-PE detection.

The schematic of the SPMT electronics is shown in Fig.3.5. The main components and specifications are listed as follows [171]:

- High voltage splitter (HVS). Two HVS boards serve for 128 SPMTs, each board holds 8 HV units and these units are grouped by two; for each pair, one unit powers 16 SPMTs and the other serves as a backup.
- ASIC Battery Card (ABC). It consists of two key elements, i.e. the CATIROC (Charge And Time Integrated Read Out Chip) chips and the FPGA (Field Programmable Gate Array). Each ABC board serves for 128 SPMTs. Each CATIROC provides an adjustable threshold common for 16 channels. It can perform the charge and time measurement by channel. The FPGA is responsible for the data capture, processing and packaging. The FPGA can receive the sampled data with charge and time information from the CATIROC, forming the charge data stream.

It can also register directly and digitally the signal passing the threshold (like a discriminator), forming a digital PE counting output, i.e. the discriminator data stream. Moreover, the FPGA can perform the time measurement with high precision (1 ns), thus being able to record the time over threshold information of the signal pulse. The two data streams provide an almost deadtime-less readout. More detailed description of the ABC board will be in Chapter 7 together with some testing results.

- Global control unit. It is almost common to the LPMT and responsible for the data transfer from the FPGA to the DAQ, the absolute time synchronization etc.

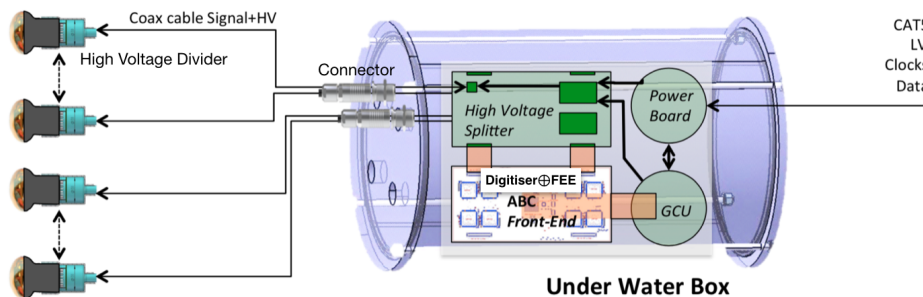


Figure 3.5 – The SPMT system readout scheme. One underwater box hosts the electronics for 128 SPMTs. Two HV splitter boards are placed above and below the ABC board. The GCU, power board and other components are also shown. The wet (underwater) electronics is connected to the surface with the common design as the LPMT.

3.3 Calibration

The detector response calibration is critical for the energy detection systematics control, hence the energy scale and energy resolution control. The energy scale represents the conversion relationship from the observable charge to the true deposited energy with the non-linearity of great importance. There are two major contributions in the energy scale non-linearity: 1.) the non-linearity effect during the energy deposition in the LS (LSNL) caused primarily by the ionization quenching and Cherenkov radiation; 2.) the non-linearity effect during the charge measurement (QNL) originating from the PMT and electronics. The energy resolution represents the measurement precision of which the non-stochastic component is largely affected by the position non-uniformity. More detailed discussions about the energy scale and energy resolution are in Chapter 6.

The energy scale non-linearity and the position non-uniformity calibrations are the major tasks and drive the design of the multi-source and multi-position calibration system, as well as the design of the Dual Calorimetry. This section focuses on the hardware design of the multi-source and multi-position calibration system, while the Dual Calorimetry is addressed in Chapter 4, 5 and 6.

3.3.1 Calibration Sources

In order to cover the energy range of the reactor neutrinos, multiple radioactive sources, mainly gamma sources, are designed, as listed in Tab.3.3. The LS non-linearity of the positrons (IBD prompt signals) can be deduced from the gamma calibration data.

A UV laser source centered at ~ 260 nm is also designed with a tunable intensity from a few hundreds keV to TeV level [172], as shown in Fig.3.6. The combination of the UV laser source and the Dual Calorimetry is powerful for the charge non-linearity calibration, as it will be detailed in Chapter 5.

Apart from the artificial calibration sources, the cosmogenic signals can also be useful for the calibration, and an example of using ^{12}B spectrum for calibration at Daya Bay can be found in Ref.[173].

Table 3.3 – The designed radioactive calibration sources for JUNO with the radiation type and emitted energy. Taken from [174].

Source	Type	Radiation
^{137}Cs	γ	0.662 MeV
^{54}Mn	γ	0.835 MeV
^{60}Co	γ	1.173+1.333 MeV
^{40}K	γ	1.461 MeV
^{68}Ge	e^+	annil 0.511+0.511 MeV
$^{241}\text{Am-Be}$	n, γ	neutron +4.43 MeV ($^{12}\text{C}^*$)
$^{241}\text{Am-}^{13}\text{C}$	n, γ	neutron +6.13 MeV ($^{16}\text{O}^*$)
(n, γ)p	γ	2.22 MeV
(n, γ) ^{12}C	γ	4.94 MeV or 3.68+1.26 MeV

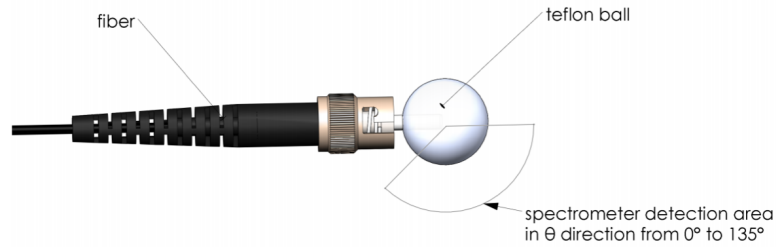


Figure 3.6 – Design of the UV laser source. The wavelength of the UV laser is centered at ~ 260 nm. The laser intensity can be tuned from hundreds of keV to a few TeV. The UV photons will be transmitted through the optical fiber, be directed to a diffuser ball made of teflon and then enter into the LS. Taken from [172].

3.3.2 Calibration System

For achieving the multiple position accessibility, the hardware of the calibration system consists of four subsystems [174], as shown is Fig.3.7.

Automatic Calibration Unit (ACU)

The ACU can deploy the calibration sources along the vertical axis (1D) of the CD with the control of the cable length by spools. The positioning precision is at centimeter level. Not only the radioactive sources can be used in the ACU, and the UV laser source can also be attached to the ACU.

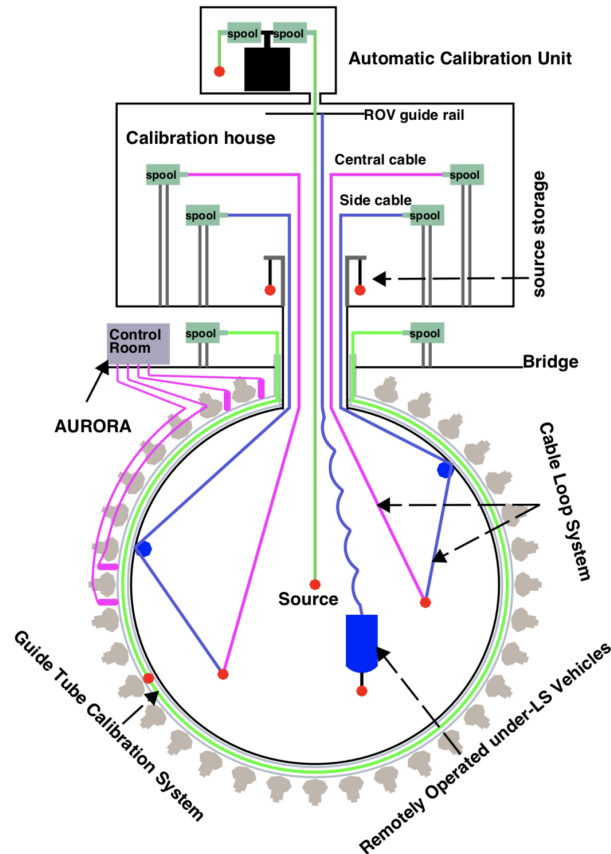


Figure 3.7 – Schematic of the calibration system. Four sub-systems are ACU, CLS, GT and ROV.

Cable Coop System (CLS)

The CLS [175] can scan the source positions in a 2D half plane by controlling two cables. Two CLSs are designed for JUNO in two opposite half planes. An independent ultrasonic positioning system is developed and can be used for CLS to obtain the precise (centimeter level) source position information [176].

Guide Tube System (GT)

The GT [177] is designed to deploy the radioactive source along a longitudinal circle outside the acrylic sphere. The cables are attached to the radioactive sources for positioning with also centimeter level precision. Even though the GT is outside the LS, the gammas can easily penetrate the acrylic boundary and deposit their energy in the LS. Thus the GT can be used to calibrate the boundary position non-uniformity.

Remotely Operated under-LS Vehicles (ROV)

The ROV [178] is designed as a supplementary system of ACU, CLS and GT. The ROV is designed to be capable to deploy the radioactive source in any place of the LS volume. The independent ultrasonic positioning system can be used for the ROV to obtain the precise source position information. If needed, the ROV can be used to calibrate the positions that are not reachable by the other three subsystems.

3.4 Veto Detectors

The cosmic muon induced backgrounds, such as ${}^9\text{Li}/{}^8\text{He}$ and fast neutrons, are ones of the main backgrounds to reactor neutrino signals, as discussed in Sec.2.1.4. For reducing the cosmic muon rate, the experimental hall is located ~ 700 m underground, lowering the muon rate to ~ 0.003 Hz/m². The average muon energy is about 200 GeV. For tagging the muons and rejecting muon induced backgrounds, two veto detectors, i.e. a water Cherenkov detector and a Top Tracker detector, will be built. Certainly, the central detector with the LPMT and SPMT systems will also contribute to the muon induced background veto, as studied in Ref.[179, 180]. The earth magnetic field will affect the PMT properties, so a shielding system based on compensation coils, generating a magnetic field opposite to earth magnetic field, will be included in the veto system [181].

3.4.1 Water Cherenkov (WC) Detector

The WC detector is composed of 35 kton ultra pure water in the water pool and ~ 2000 20-inch PMTs, as illustrated in Fig.3.1. The Tyvek films are coated on the water pool and the CD surfaces to increase the light detection. A water circulation system will be built to keep the water quality with the radon removal [182]. The detection efficiency for cosmic muons is estimated to be larger than 95% [183].

3.4.2 Top Tracker

The Top Tracker (TT) is a 3-layer muon tracker on top of the water pool with the capability of precise muon tracking. The TT consists of 62 walls made of plastic scintillator strips inheriting from the OPERA experiment [184], covering about 60% of the top surface. The dimension of each TT wall is 6.8m \times 6.8m. Each TT wall is composed of eight modules, and each module has 64 scintillator strips read out by the wave length shifting (WLS) fibres coupled to two 64-channel multianode PMTs. The schematic view of Top Tracker is shown in Fig.3.8.

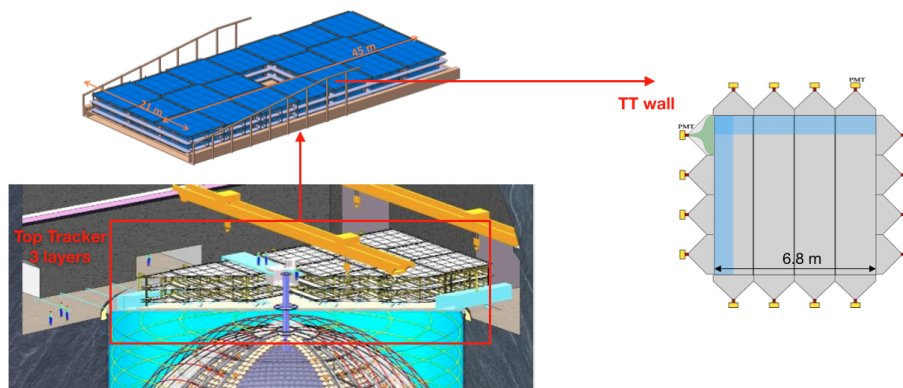


Figure 3.8 – Schematic view of the Top Tracker (left) and a TT wall (right).

3.5 Other Detector Related Systems

The JUNO experiment has also other important systems as detailed in Ref.[165], they are briefly listed as follows:

Data Acquisition System (DAQ)

The DAQ is responsible for the data acquisition of the different subsystems including the LPMT readout, SPMT readout, the Top Tracker and the water Cherenkov detector.

Detector Control System (DCS)

The DCS is responsible for monitoring the running status of the experiment equipment including the high voltage, electronics, calibration system, water system, gas system, power supply, environment of experimental hall, etc.

Software

The JUNO offline simulation software is based on the SNI_{PER} (Software for Non-collider Physics ExpeRiment) framework with dependencies on external packages including ROOT, Geant4, Python, CLHEP and Boost. The software includes the detector geometry description, the physics generator, the detector simulation and electronics simulation, etc. It is widely used for the Monte Carlo (MC) simulation studies in JUNO collaboration in order to optimize the detector parameters and the reconstruction methods, and also to study the physics sensitivity. A large amount simulation work in this thesis is based on the JUNO offline simulation software.

JUNO-TAO

The Taishan Antineutrino Observatory (TAO or JUNO-TAO) is the satellite experiment of JUNO [150]. The TAO detector is located at ~ 30 m from the Taishan NPP. The major tasks of the TAO experiment are 1) to provide a reference reactor $\bar{\nu}_e$ spectrum for JUNO, in order to eliminate the model dependence of the unknown fine structure in the spectrum [185], 2) to provide a benchmark measurement to test the nuclear databases.

The TAO detector is based on a 2.8 ton gadolinium-doped LS with 10 m² silicon photomultipliers. The photoelectron yield is expected to be unprecedentedly about 4500 PE per MeV corresponding to $\sim 1.5\%$ energy resolution at 1 MeV. The detector is designed to operate at -50 °C in order to reduce the dark noise of the SiPMs.

Chapter 4

Dual Calorimetry Concept

The JUNO central detector has two readout systems surrounding the common liquid scintillator (LS) as detailed in Sec.3.2. As the initial readout design of JUNO, the LPMT system is based on the 20-inch PMTs and the FADC (flash analog-to-digital converter) electronics [165]. Its charge measurement is realized through the reconstruction of the PMT pulse waveform. The LPMT readout system pursues maximal photo-coverage while balancing the economic cost on the PMTs and electronics. The second readout system, i.e. the SPMT system, was first proposed in 2014, and fully approved in 2016. It is designed to utilize small size (3-inch) PMTs and the digital photoelectron (PE) counting based electronics in order to perform the charge measurement in a robust and independent way compared to the LPMT. The two independent readout systems are linked through the common exposure to the same energy deposition inside the LS, constituting the Dual Calorimetry design. This design allows the direct readout response comparison between the two systems. It provides some unique insights for the calorimetry systematics control, which will be addressed in this chapter.

In this chapter, the motivation of bringing the second calorimetry, i.e. the SPMT system, hence the Dual Calorimetry design, is presented in Sec.4.1. Then the principle of Dual Calorimetry is explained in Sec.4.2. At last, several possible Dual Calorimetry implementations are briefly discussed in Sec.4.3, and the most important implementation, namely channel-wise implementation, will be explained in detail in Chapter 5.

4.1 JUNO Challenge and Motivation of Dual Calorimetry

As presented in Sec.2.1 and 2.2, the neutrino MO determination and oscillation parameters measurement, as the primary physics goals of JUNO, rely on the high precision measurement of the reactor $\bar{\nu}_e$ energy spectrum [100, 130, 186, 131]. This high precision measurement imposes several unprecedented experimental requirements listed as follows.

(1.) The world's largest ($\sim 20,000$ tons) LS is designed as target medium in order to obtain high statistics ($\sim 100,000$ reactor $\bar{\nu}_e$ IBD events) within a reasonable period of time (~ 6 years). The detector size predominantly specifies the single channel optical acceptance range. This range corresponds primarily to the solid angle variation between the single PMT and the event vertex, as the event could happen anywhere in the detector volume. At JUNO, this single channel optical acceptance range is more than 2 orders of magnitude due to the large detector size. In addition, the reactor neutrino energy range (roughly $1\sim 10$ MeV) gives 1 order of magnitude variation. So the detector size together with the reactor neutrino energy range defines a 3 orders of magnitude dynamic range in terms of the single channel mean illumination. Here, the single channel mean illumination represents the average charge detection at one channel for a certain energy

deposition occurring at a certain position in the detector volume. Emphatically, this dynamic range is at least 1 order of magnitude larger than that of the previous reactor neutrino LS experiments, such as Daya Bay, Double Chooz, Kamland and RENO.

(2.) The energy resolution is desired to be better than 3% at 1MeV, given the following model:

$$\frac{\sigma_E}{E} = \sqrt{\frac{\sigma_{stochastic}^2}{E} + \sigma_{non-stochastic}^2(E)}. \quad (4.1)$$

The stochastic term of the energy resolution drives the design of the light production and light collection both to be as high as possible. For achieving the high light production, the JUNO LS is designed to have the highest possible light yield ($\sim 10^4$ photons per MeV) and high transparency (attenuation length larger than 20 meters) that reduces the light loss during propagation. For achieving the high light collection, around 18,000 high detection efficiency ($\sim 27\%$) 20-inch PMTs will be installed, covering $\sim 75\%$ of the LS surface. The detected light (or PE) yield is expected to be larger than 1200 PEs per MeV, which is more than 2 times higher compared to the current highest PE yield LS detector, i.e. ~ 500 PE/MeV in Borexino [53].

(3.) The non-stochastic term of the energy resolution is aimed to be controlled better than 1% assuming the energy resolution model of Eq.(4.1). The current best control of the non-stochastic term in reactor neutrino LS experiments is about 2% [30, 93, 187], if fitting to the energy resolution model of Eq.(4.1).

The energy scale, i.e. the conversion relationship from the direct observable to the true energy, should be accurate and its uncertainty is aimed to be controlled at sub-percent level. The energy scale including the non-linearity, non-uniformity and non-stability will be defined and discussed in Chapter 6. The control of energy scale and energy resolution non-stochastic term imply the calorimetry systematics control, which is realized mainly through the dedicated calibration of detector responses, including non-linearity, non-uniformity and non-stability.

The points (1.) and (2.) make JUNO be the largest and highest PE yield LS detector ever built. Meanwhile, these two points result in the main challenge for JUNO, i.e. calorimetry systematics control, especially for the non-linearity control during the charge measurement, referred to as charge non-linearity and noted as QNL.

Specifically, for each single LPMT, the aforementioned vast mean illumination dynamic range (3 orders of magnitude) and high PE yield (~ 1200 PEs per MeV) lead to a 2 orders of magnitude charge detection variation, i.e. $1 \sim 10^2$ PE. The current best QNL control is about 1% in $1 \sim 10$ PE range through the waveform reconstruction. For example, Fig.4.1 shows the Daya Bay single channel residual QNL from the PMT pulse waveform reconstruction in the FADC based electronics system, and $\sim 1\%$ residual QNL is achieved with a data tuned electronics simulation [173].

However, as for the $1 \sim 10^2$ PE charge detection range, no LS detector has ever experienced such a vast dynamic range along with sub-percent precision requirement. A lot of effects during the charge measurement can introduce non-linearity, such as the electronics noise, the overshoot, the integration time window and even the waveform reconstruction algorithm.

The unnoticed QNL beyond the traditional calibration capability can directly enlarge the energy scale uncertainty or even bias the energy scale. Thus it can affect detector ability to realize the physics measurements. Some studies show that a small uncalibrated

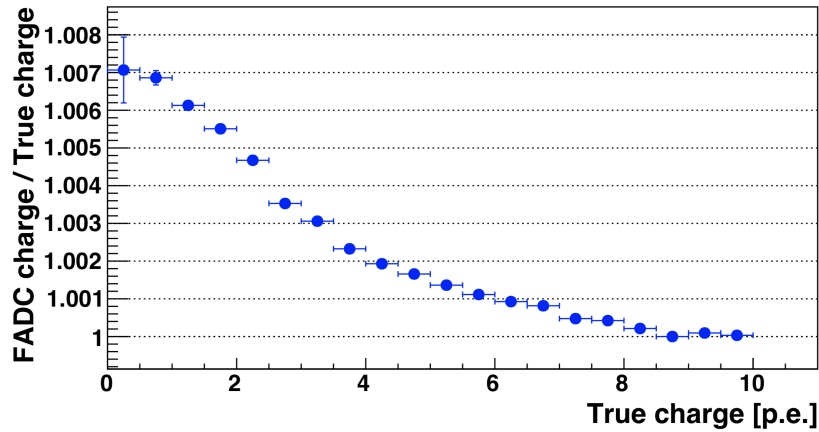


Figure 4.1 – Residual QNL of the waveform reconstruction for a single channel in the FADC based electronics system of the Daya Bay experiment. The QNL control is estimated with an electronics simulation tuned to data. Taken from Ref.[173]

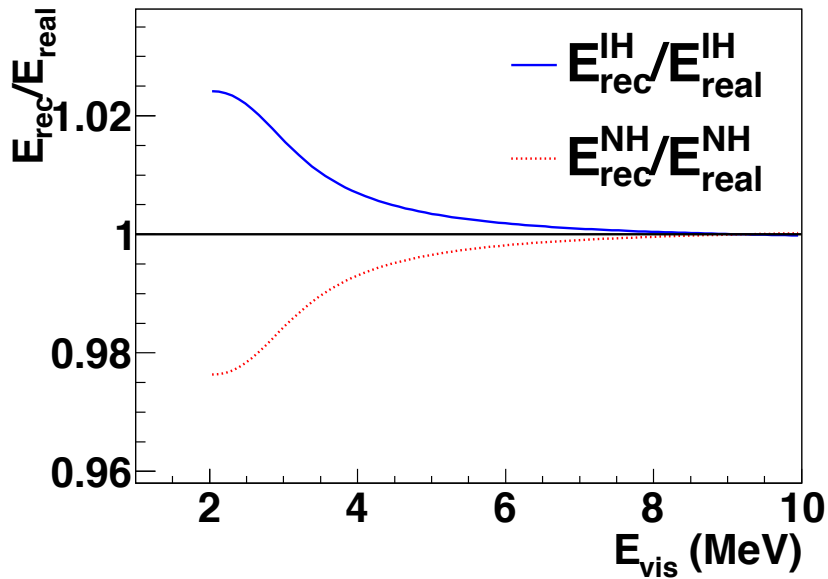


Figure 4.2 – The non-linearity defined in Ref.[188] to illustrate the importance of energy scale non-linearity control for the MO determination. The energy non-linearity is defined as the ratio of reconstructed energy E_{rec} to real energy E_{real} as a function of the visible energy. If the energy scale has an unnoticed non-linearity as the red dashed (blue solid) curve for the NMO (IMO), and this non-linearity is not included during the energy reconstruction from data, then the analysis of the energy spectrum would lead to a wrong MO result. Because in the scenario of the NMO (IMO) and the red dashed (solid blue) non-linearity, the pattern of the reactor neutrino disappearance probability of Eq.(2.1) regarding the atmospheric term will be exactly the same as in the IMO (NMO) case. Taken from Ref.[188].

non-linearity in energy scale could lead to a substantial misinterpretation of the MO discovery significance [130, 188, 189], as illustrated in Sec.2.1.6. The study in Ref.[188] even pointed out that the unnoticed non-linearity in the energy scale with the form displayed in Fig.4.2 would lead to a wrong neutrino MO result.

Another essential fact is that the QNL effects occur at the readout level, i.e. PMT, electronics and DAQ including the interface in between. Other detector response effects, such as the non-linearity during energy deposition in LS (LSNL) and the non-uniformity during light collection (NU), all need to be read out. It turns out that the QNL at readout level is normally degenerated with other effects, thus causing the ambiguity between non-linearity and non-uniformity. For instance, the QNL can mimic some detector nonuniform response as illustrated in Fig.4.3. Once the QNL becomes a main constraint for understanding the whole detector response, on the one hand, it is not trivial or even impossible to perform an independent calibration of the QNL because of the degeneracy. On the other hand, it can affect the modelings of the LSNL and NU. In a word, the proper handle of the potential LPMT nonlinear charge response has great importance for the calorimetry systematics control, hence the neutrino oscillation physics measurements foreseen by JUNO.

The challenges of the systematics control in the LPMT calorimetry can be summarized as the diagnosis and calibration of the QNL and the disentanglement of the degeneracy between the non-linearity and non-uniformity. Given these challenges, the second readout system, i.e. the SPMT system, is conceived for JUNO, constituting the Dual Calorimetry design, for providing some insights for the calorimetry systematics control. The Dual Calorimetry is designed to perform the direct response comparison between the LPMT calorimetry and the SPMT calorimetry. Through this comparison, the degeneracy between the charge response effect and other response effects can be broken down. Thus it provides a unique way to isolate the charge response effect which has been most challenging in past experiments, as will be explained in detail in the next section.

Because of the small size of 3-inch PMT, i.e. roughly 50 times smaller than the 20-inch PMT for the photo-cathode surface, the charge detection of SPMT is dominated by the single PE. Therefore, the charge estimation of the SPMT can be realized through the PE counting technique while bypassing the complexity of charge integration (such as waveform reconstruction). The robustness of PE counting (upon possible correction) ensures the charge linearity of the SPMT by design, which will be demonstrated in the Sec.5.4 with the Dual Calorimetry implementation. Thus, in short, the Dual Calorimetry is designed to utilize the SPMT as the linear in-detector reference to the LPMT aiming for the LPMT QNL calibration.

In brief, the Dual Calorimetry design is motivated by the high precision neutrino oscillation measurement at JUNO. It aims to contribute to the calorimetry systematics control including both energy scale and energy resolution through the direct QNL calibration and possibly other scrutiny approaches, as will be illustrated and demonstrated later.

4.2 The Principle of Dual Calorimetry

The Dual Calorimetry always implies the response comparison between the LPMT and SPMT calorimetries to the common energy deposition. This statement involves three concepts that matter the Dual Calorimetry. In order to facilitate the explanation of the Dual Calorimetry principle, these concepts, i.e. the energy deposition, the calorimetry response and the response comparison, are introduced as follows.

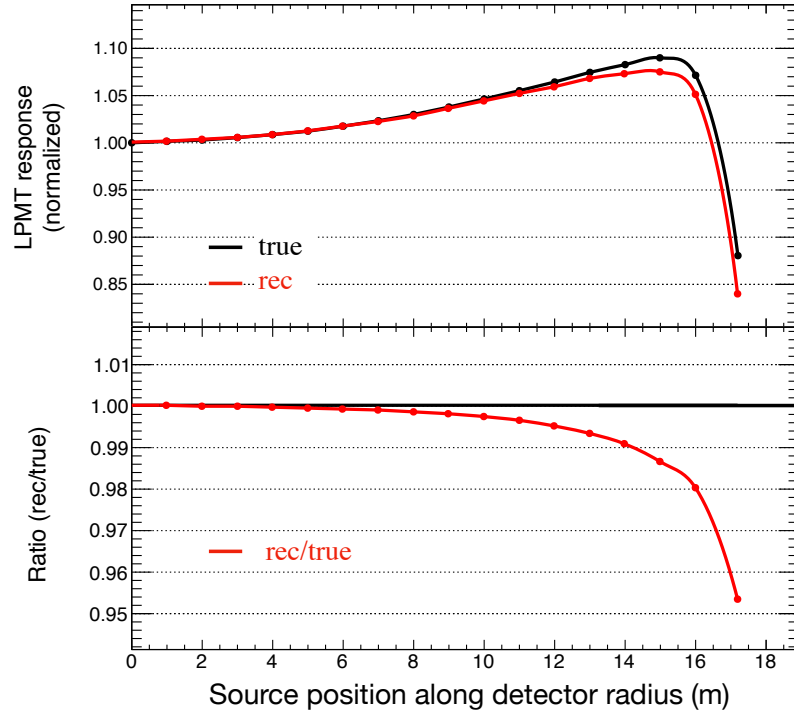


Figure 4.3 – The non-uniformity (NU) bias induced by the charge non-linearity (QNL). The upper figure is the nonuniform response of the LPMT system simulated by using the electrons sources with fixed energy (8 MeV kinetic energy) as a function of the source position along detector radius. (z-axis, 0 m means the detector center and 17.7 m means the detector top). The black curve corresponds to the true nonuniform response, meaning a perfect linear charge response. The red curve corresponds to the reconstructed nonuniform response by assuming a large QNL (about 50% over 1~100 PE, defined in Eq.(4.5)). The response is normalized to the detector center. The lower figure represents the ratio of the reconstructed NU to the true one. This ratio is also normalized to the detector center, and it should be 1 if there is no QNL effect and it biases from 1 due to the QNL.

First, for the energy deposition, it can correspond to neutrinos, radioactive sources, light sources, cosmogenic signals or other signals.

Second, for the calorimetry response, it contains typically the energy deposition response, the detector nonuniform response, the readout charge response and the detector non-stability response. Since the non-stability effects mainly make sense when the detector is running, and this thesis focuses on the simulation study, the detector non-stability response is not discussed but should be contemplated in the future.

Last, as for the Dual Calorimetry response comparison, it can be done at different levels, e.g. the two systems comparison, the single LPMT to the SPMT system comparison, the single LPMT to the single SPMT comparison and other comparisons in the intermediate cases. Some of the comparisons can be meaningful for implementation, while others are challenging. The possible Dual Calorimetry implementations will be discussed in Sec.4.3. In this section, the main purpose is to illustrate the principle of Dual Calorimetry while avoiding the implementation details. In order not to lose the generality, the LPMT and SPMT response comparison has general meaning in this section, unless it is specified for a given level comparison. Since the Dual Calorimetry always means the response comparison, the wording "*response relation*" between the two

systems is used to represent this comparison.

After clarifying these concepts, the explanation of the Dual Calorimetry working principle can be started from classifying the types of response relations. In this thesis, the response relations will be classified into three categories, according to whether there exist the common effects or not. These three categories are:

- a.) the fully correlated response relation indicating the energy and particle dependent LS non-linearity (LSNL).
- b.) the partially correlated response relation indicating the position dependent non-uniformity (NU).
- c.) the uncorrelated response relation indicating the energy, position and also particle dependent charge non-linearity (QNL).

4.2.1 Fully Correlated Response Relation

As mentioned in Sec.3.1, the photon production in the LS is not linear with respect to the deposited energy, primarily owing to the ionization quenching and the Cherenkov radiation. This nonlinear response, i.e. LS non-linearity (LSNL), is typically particle and energy dependent. Due to the fact that the LPMT and SPMT are both installed in the central detector viewing the common LS, they are always exposed to the same energy deposition inside the detector. Therefore, the LS nonlinear response, noted as \mathcal{R}_{LSNL} , is common hence fully correlated to the LPMT and the SPMT. So, the LS response ratio between the LPMT and the SPMT is constant as illustrated in Fig.4.4.

$$\frac{\mathcal{R}_{LSNL}^{LPMT}}{\mathcal{R}_{LSNL}^{SPMT}} = \text{constant} (= 1 \text{ after normalization}). \quad (4.2)$$

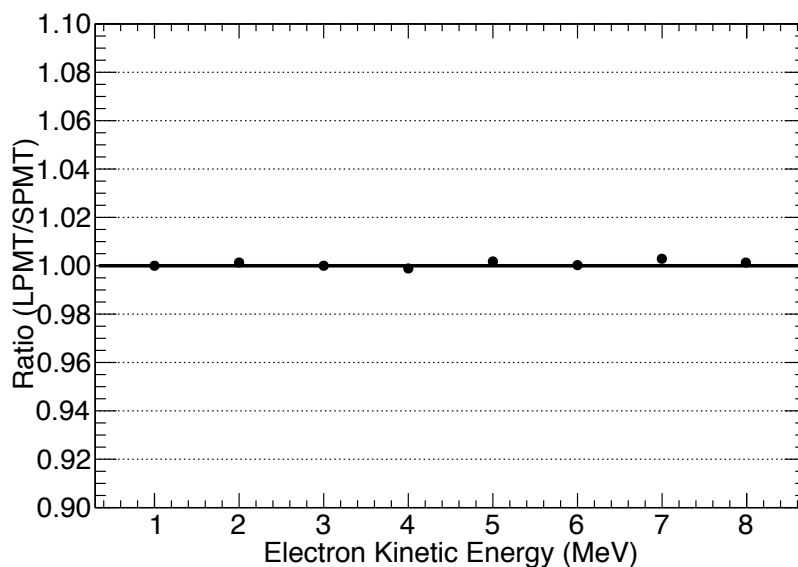


Figure 4.4 – The LS response ratio between the LPMT and SPMT systems. The LS response is simulated with energy deposition of electrons. The response ratio is shown as a function of the electron kinetic energy, while the electron source is kept at the center of the detector. Since only the absolute source energy is variable in this case and the Dual Calorimetry is immune to this absolute source energy changing, this response ratio is constant and becomes 1 after normalizing it to 1MeV.

The \mathcal{R}_{LSNL} is always canceled upon the LPMT and SPMT calorimetry response comparison. This implies the Dual Calorimetry is immune to any absolute source changing and bias in itself.

4.2.2 Partially Correlated Response Relation

The photon collection by the PMTs is, in general, position dependent. The position here can be understood as the relative position between the event vertex and PMT. When comparing the photon collections between the LPMT and the SPMT, there are some common effects and also some independent effects. The event vertex position where the energy deposition actually happens, as well as the photon propagation in the LS, are common for the LPMT and the SPMT. These common effects do not yet involve the PMT information, neither the PMT position nor PMT optical properties, so they are fully correlated. However, once the PMT itself is considered as the active object for the photon collection, this fully correlated relation is broken to some extent. Specifically, each PMT position and arrangement (i.e. the solid angle between event vertex and PMT) are different, and each PMT could have different optical properties such as quantum efficiency and collection efficiency. The PMT-to-PMT difference exists between the LPMT and the SPMT and also among the LPMTs (or SPMTs).

When focusing on a single PMT, these PMT-to-PMT differences will induce significant photon collection difference. For example, Fig.4.5 illustrates several possible cases regarding the single channel photon collection difference in terms of the response ratio between a single LPMT and the SPMT system.

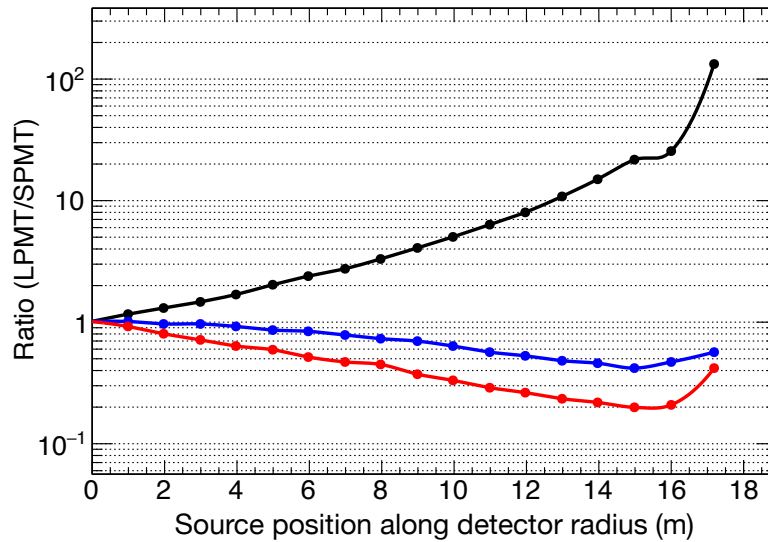


Figure 4.5 – The response ratio between a single LPMT and the SPMT system as the function of the source position along the detector radius. For the x-axis, from 0 m to 17.7 m, the source position is moved from the detector center to the detector top. The electron source kinetic energy is fixed. This ratio is normalized to detector center. The black, blue and red curves correspond to a single LPMT at the top, equator and bottom of the detector respectively. The three LPMTs all have the total SPMT system for comparison respectively. For this kind of comparison, the PMT-to-PMT differences induce significant photon collection difference.

When focusing on the whole LPMT and SPMT systems comparison, the total PMT-to-PMT differences of all channels will be compromised at detector level by arranging the PMTs as uniformly as possible. But they can not be totally eliminated and still exist as the NU difference between the two systems. Especially for the events happening at the detector edge, the NU difference is significant between the two systems. As illustrated in Fig.4.6, while changing the source position (or event vertex position), the response ratio between the LPMT system and the SPMT system is not constant and varying a lot when the source is placed towards the detector edge.

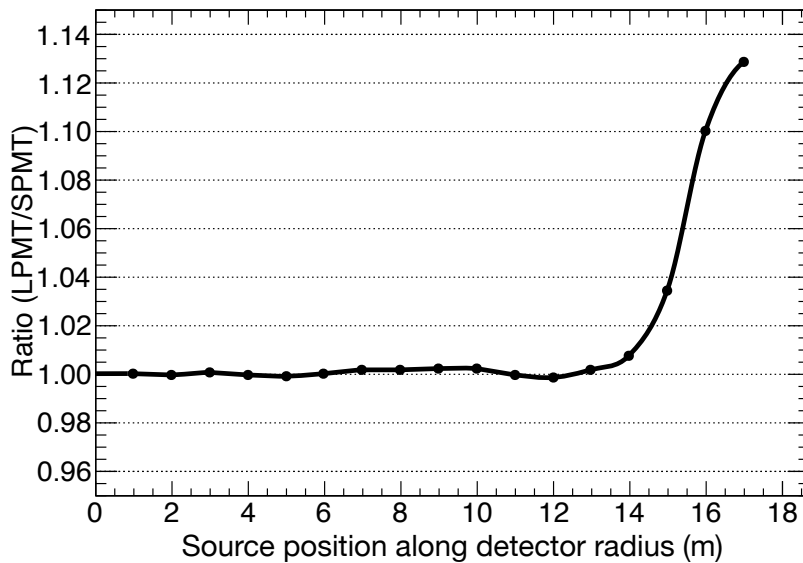


Figure 4.6 – The response ratio between the LPMT and SPMT systems with respect to the electron source position along the detector radius. The electron source kinetic energy is fixed. This ratio is normalized to the detector center. The nonuniform responses of LPMT and SPMT are partially correlated. When the source is placed within a certain region (i.e. radius smaller than 13 meters), this correlation is strong as this ratio is approximately constant. When the source is placed towards the detector edge, the NU difference between the two systems is significant as this ratio varies a lot.

All these common effects and independent effects during photon collection contribute to the nonuniform response, noted as \mathcal{R}_{NU} . The nonuniform responses of the LPMT and the SPMT are considered as partially correlated, meaning:

$$\frac{\mathcal{R}_{NU}^{LPMT}}{\mathcal{R}_{NU}^{SPMT}} \neq constant. \quad (4.3)$$

The proper treatment of the partially correlated nonuniform responses is critical for the Dual Calorimetry implementations, of which the goal is to cancel the partially correlated responses between the two systems. The details will be discussed in Sec.4.3 and also in Chapter 5.

4.2.3 Uncorrelated Response Relation

The photoelectrons collected at first dynode¹, as primary electrons, are multiplied by the first dynode until the last dynode, and are then sent to the anode. The anode collects the secondary electrons produced in the dynodes cascade process and outputs the electron current to the external electronics. The electronics reads the PMT signals, digitizes and processes the signals, and then transfers the data to the data acquisition system. The raw charge information is then recorded and used for reconstruction. All the processes described above are, in short, considered as the charge measurement implemented at single channel level. The charge reconstruction being the first stage has direct impact on the subsequent event reconstruction processes. The charge measurements of the LPMT and SPMT are designed to be independent and different (i.e. charge integration *vs* PE counting), hence are considered as uncorrelated.

The channel-wise charge response depends on, in general, the number of PEs collected by the single PMT (i.e. charge dependent) and the time profile of these PEs. It can also be channel dependent due to the channel-to channel difference.

Charge Dependence

The number of PEs collected by the single PMT depends directly on the deposited energy and the solid angle (or relative position) between the event vertex and the PMT. In other words, the channel-wise charge dependence is effectively contained in (not equivalent to) the event-wise energy dependence and position dependence.

The LPMT has a 20-inch diameter, resulting in a large charge detection range. For the reactor $\bar{\nu}_e$ IBD events, the charge fraction of the LPMT, in terms of the number of PE collected at the single PMT, is shown in Tab.4.1. This table indicates that, for the LPMT, a non-negligible fraction of charge is measured at high PE region, up to 10^2 .

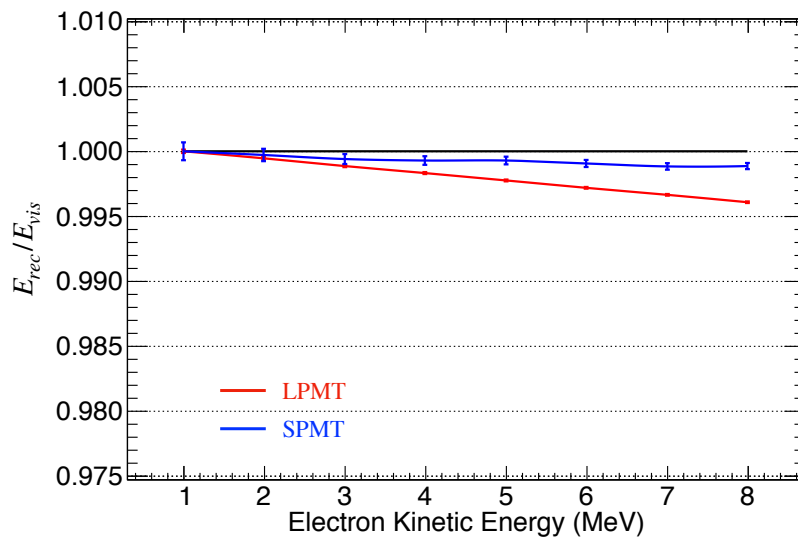
Table 4.1 – The charge fraction in terms of the number of PE collected at the single PMT for the reactor $\bar{\nu}_e$ IBD events. 100,000 reactor $\bar{\nu}_e$ IBD events uniformly distributed in detector volume are simulated for this calculation. The charge fraction for the LPMT and the SPMT are both shown.

	1PE	2~5PE	5~10PE	10~20PE	20~50PE	50~100PE	>100PE
LPMT	42.56%	40.54%	8.74%	5.12%	2.80%	0.24%	0.003%
SPMT	95.19%	4.80%	0.01%	0%	0%	0%	0%

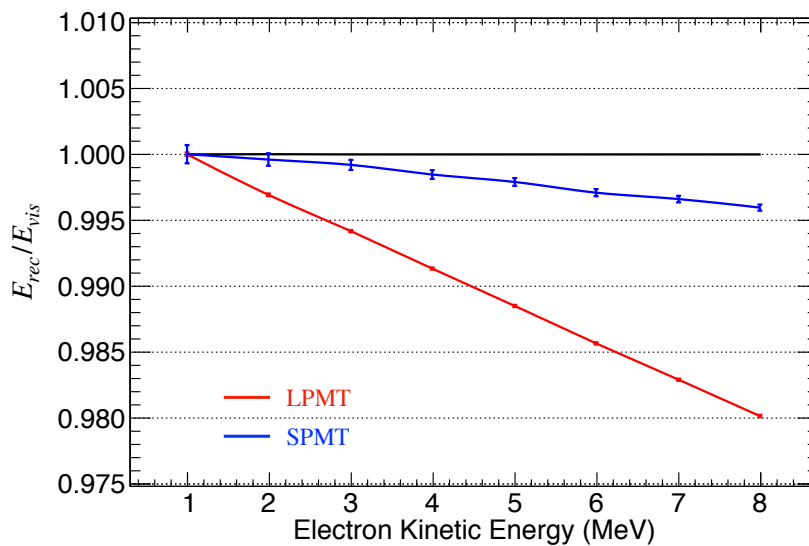
Given the vast charge detection range of the LPMT, the FADC based electronics are designed to record the PMT pulse waveform. The accuracy of PMT waveform reconstruction is critical for the direct charge measurement. A lot of effort has been done and is still ongoing in order to improve the accuracy of PMT waveform reconstruction, such as deconvolution method, waveform fitting and machine learning [190, 191, 192, 193]. A $\sim 1\%$ residual QNL control has been reached in $1\sim 10$ PE range, as illustrated in Fig.4.1. But the precise QNL control with respect to the range of $1\sim 10^2$ PE remains challenging.

Based on the current best channel-wise QNL control, i.e. $\sim 1\%$ in $1\sim 10$ PE, an extrapolated simple channel-wise QNL model in $1\sim 100$ PE range is used to conjecture the possible QNL effect at detector level for the LPMT system, as shown in Fig.4.7.a.

1. The dynode PMT is used for illustration here.



(a)



(b)

Figure 4.7 – Detector level (or event-wise) QNL manifestation at JUNO in simulation. The detector level QNL is defined as the ratio between the reconstructed energy and the visible energy. For the upper figure (a.), the channel-wise QNL is assumed to be $\sim 10\%$ over $1\sim 100$ PE range, following the toy model of Eq.(4.4) both for the LPMT and the SPMT, and the charge of each single channel is used to reconstruct the energy of the event. The channel-wise QNL could induce a $\sim 0.4\%$ non-linearity for the LPMT (red curve) at detector level, while only a $\sim 0.1\%$ non-linearity for the SPMT (blue curve). For the lower figure (b.), the channel-wise QNL is assumed to be $\sim 50\%$ over $1\sim 100$ PE range, following the toy model in Eq.(4.5) both for the LPMT and the SPMT. The channel-wise QNL could induce a $\sim 2\%$ energy non-linearity for the LPMT (red curve) event-wise, while only a $\sim 0.4\%$ non-linearity for the SPMT (blue curve). The simulation is based on the mono-energy electrons uniformly distributed in detector volume at each kinetic energy from 1 MeV to 8 MeV with $\sim 50,000$ statistics.

This simple channel-wise QNL model is at 10% level in 1~100 PE range and defined as:

$$\frac{Q_{rec}}{Q_{true}} = \frac{-0.01}{9}Q_{true} + \frac{9.01}{9}, \quad (4.4)$$

where the Q_{true} is the true charge and Q_{rec} is the reconstructed charge. Given this ~10% channel-wise QNL, a ~0.4% non-linearity in the energy scale is estimated, as shown in Fig.4.7.a. By assuming 5 times worse channel-wise QNL control (i.e. ~50% QNL in 1~100 PE range), as the following model:

$$\frac{Q_{rec}}{Q_{true}} = \frac{-0.05}{9}Q_{true} + \frac{9.05}{9}, \quad (4.5)$$

the QNL effect in the energy scale can be up to 2%, as shown in Fig.4.7.b.

The SPMT has a much smaller (3-inch) diameter, hence a much smaller charge detection range. As shown in Table 4.1, more than 95% of the charge is detected in single PE regime for the reactor $\bar{\nu}_e$ IBD events. Based on this fact, the SPMT electronics is designed to yield the digital PE counting. Specifically, the SPMT is designed to be triggerless, it can count digitally the signal pulse passing the threshold. Since most (>95%) of these countings are, in essence, single PEs for the reactor $\bar{\nu}_e$ IBD events, the precision of the charge estimation through PE counting is expected to be largely guaranteed. Detailed SPMT electronics response characterization will be discussed in Chapter 7. Further corrections for the PE counting can be done in order to accommodate to specific Dual Calorimetry implementations, which will be introduced in Sec.5.4.

In addition, the SPMT electronics could provide analog charge information about the signal pulse amplitude and the time over threshold. When several PEs hit a single SPMT for one event, these analog charge information will be useful for measuring the charge, thus helping the multi-PE charge measurement.

In brief, the SPMT charge detection is robust and redundant by design, hence it can be considered as the charge linear reference to the LPMT. Even though by assuming that the SPMT suffers the same level channel-wise QNL as the LPMT (i.e. same QNL model), due to its small charge detection range, the QNL effect at detector level (event-wise) is much less significant than that of LPMT, as shown in Fig.4.7.a and Fig.4.7.b. And the SPMT is still a relative linear reference to the LPMT in these cases. The limiting (or worst) QNL of the SPMT such that the SPMT is no longer a linear charge reference for the LPMT will be investigated in Sec.5.5.4.

Time Profile Dependence

The channel-wise charge response depends also on the time profile of the PEs collected at the PMT. This time profile corresponds to, in essence, the decay time profile of the LS, i.e. de-excitation of the molecules in the LS. There are two main contributions to the time profile dependence as explained next.

The first contribution is the particle dependent time profile effect during the energy deposition [159]. This is a well-known effect, for instance the optical photons, positrons/electrons/gammas, protons and alpha particles exhibit different time profiles, and some testing results can be found in Ref.[194, 195, 196]. To illustrate this point, the simulated results of the time profiles with the JUNO LS are shown in Fig.4.8 where the UV laser photon and the positron (or gamma) have different time profiles.

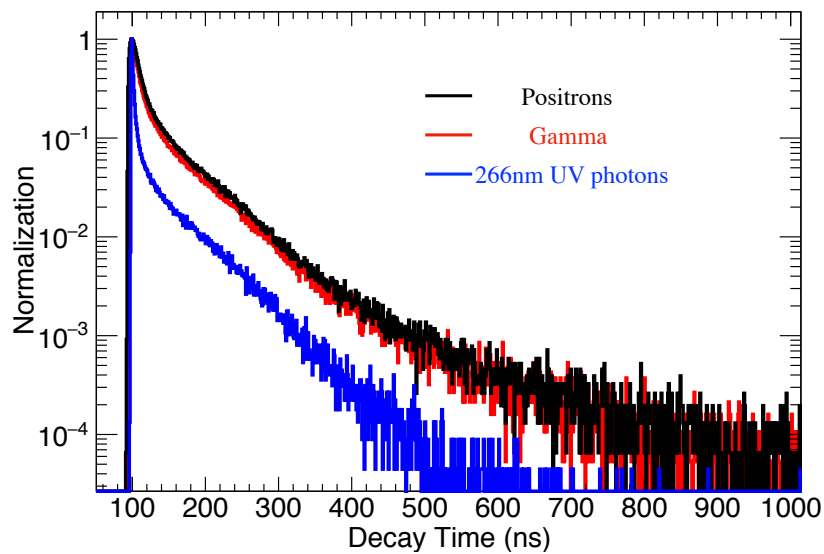


Figure 4.8 – Particle dependent time profile. The simulated LS decay time profile at JUNO for positrons (black), gammas (red) and 266 nm UV laser photons (blue). The positron source, gamma source and UV laser source are all simulated at the detector center. The x-axis corresponds to the time when the photons are converted to PEs and collected by PMTs. In order to do the comparison, the three time profiles are aligned at the maximal point of the normalization.

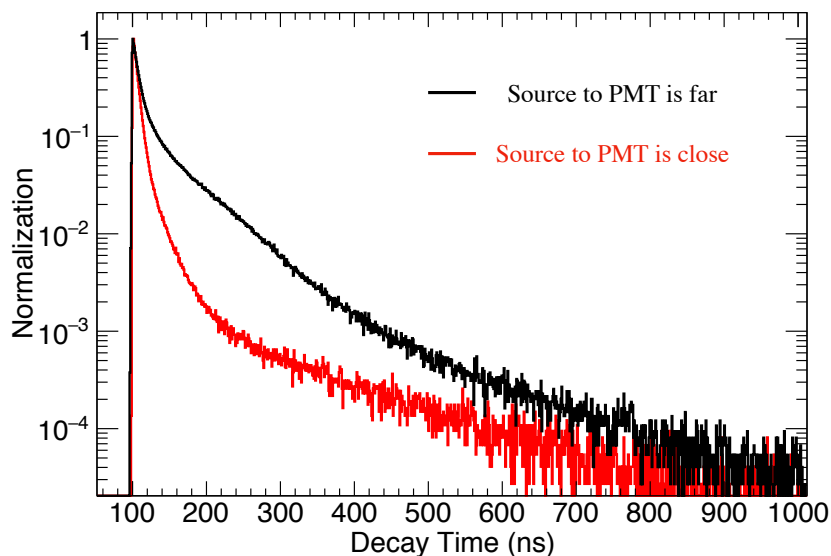


Figure 4.9 – Position dependent time profile. The simulated LS decay time profile at JUNO for two different cases. (1.) The electron source is simulated at the top of detector volume (17 meters to detector center). The time profile of the PEs collected by the closest PMT to source position is shown as the red curve. (2.) The electron source is simulated at detector center. The time profile of the PEs collected by the same PMT used in (1.) is shown as the black curve. The distance between the source and the PMT of case (1.) is closer than that of case (2.). So the time profile for case (1.) is faster than case (2.). The x-axis corresponds to the time at which the photons are converted to PEs and collected by PMTs. In order to do the comparison, the two time profiles are aligned at the maximal point of the normalization.

The second contribution is the position dependent time profile effect which is affected by the Rayleigh scattering (dominant) as well as the absorption and re-emission processes during the photon propagation. The probability for the photons got scattered or absorbed and then re-emitted is proportional to the distance between the PMT and the event vertex. This can be understood as the Rayleigh scattering length and absorption length of the LS component in Fig.4.10 [197, 198, 199]. Once photons are got scattered or absorbed and then re-emitted, these processes cause some time delay.

Fig.4.9 shows the simulated time profile for the events occurring close to the PMT and the events occurring far to the PMT respectively. When the distance between the event vertex and the PMT is closer, the scintillation photons will travel, in average, less distance; therefore, the probability that the scintillation photons got scattered is lower; it results in a smaller time delay hence a faster time profile.

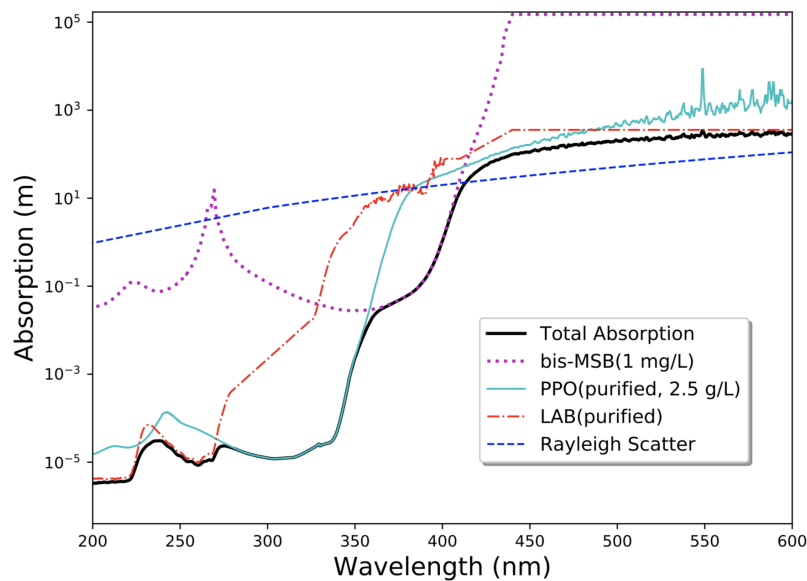


Figure 4.10 – Measured absorption length of each LS component and total absorption, superimposed with Rayleigh scattering length. LS mixture is composed of LAB, PPO (2.5 g/L) and bis-MSB (1 mg/L). These lengths represent the scattering or absorption probabilities of the photons in LS. When the length is small, it indicates higher scattering or absorption probability. Taken from Ref.[197].

The particle and position dependent time profile can affect the multi-PE detection, since when the time profile is faster, the pile-up effect will be more significant for multi-PE. Seeing that the multi-PE hitting one PMT is frequent for the LPMT, the time profile effect could affect the LPMT charge measurement. However, the SPMT is mainly in the single PE detection mode, and the multi-PE detection is rare. Consequently the SPMT charge measurement is robust and largely immune to the time profile effect.

Channel Dependence

Since the charge measurement is performed channel-wise and each single channel could not be exactly identical, the channel-to-channel difference leads to potential channel dependent charge response effect. This is particularly important for JUNO, since two types of 20-inch PMT, i.e. MCP-PMT and dynode PMT, are used. The implication is that any channel-wise treatment should take the channel dependence into account.

Summary of the Uncorrelated Responses

The LPMT and SPMT charge measurements are designed to be different both from the charge detection range point of view and from the charge detection mechanism point of view, thus they are fully uncorrelated. The charge responses of the LPMT and the SPMT are noted respectively as:

$$\mathcal{R}_{QNL}^{LPMT} \text{ and } \mathcal{R}_{QNL}^{SPMT}. \quad (4.6)$$

4.2.4 Response Comparison

As mentioned above, the Dual Calorimetry always means the response comparison between the LPMT and the SPMT. To summarize all the aforementioned response features in a simple manner, the full calorimetry responses of the LPMT and SPMT are written respectively as,

$$\mathcal{R}^{LPMT} = \mathcal{R}_{LSNL} \cdot \mathcal{R}_{NU}^{LPMT} \cdot \mathcal{R}_{QNL}^{LPMT}, \quad (4.7)$$

$$\mathcal{R}^{SPMT} = \mathcal{R}_{LSNL} \cdot \mathcal{R}_{NU}^{SPMT} \cdot \mathcal{R}_{QNL}^{SPMT}. \quad (4.8)$$

The reason to write \mathcal{R}_{LSNL} , \mathcal{R}_{NU} and \mathcal{R}_{QNL} in multiplication is that these different terms are conceptually independent. Even though this independence could be not totally valid due to the actual experimental complexity, it is still meaningful to separate these terms conceptually.

The basic principle of the Dual Calorimetry can be understood through the full calorimetry response comparison between the LPMT and the SPMT, i.e. Eq.(4.7) and Eq.(4.8). The fully correlated \mathcal{R}_{LSNL} terms are canceled. The partially correlated terms \mathcal{R}_{NU}^{LPMT} and \mathcal{R}_{NU}^{SPMT} can be canceled with careful treatment according to the actual implementation as will be explained in the next section. Then only the uncorrelated charge response terms \mathcal{R}_{QNL}^{LPMT} and \mathcal{R}_{QNL}^{SPMT} are left. Thus the comparison of the full calorimetry responses becomes the direct readout charge response comparison, expressed as the following ratio:

$$\frac{\mathcal{R}^{LPMT}}{\mathcal{R}^{SPMT}} = \frac{\mathcal{R}_{QNL}^{LPMT}}{\mathcal{R}_{QNL}^{SPMT}}. \quad (4.9)$$

Since the SPMT charge measurement is robust and linear by design, the potential non-linear charge response of the LPMT can be diagnosed and possibly be calibrated through the Dual Calorimetry approach. Moreover, once the QNL can be calibrated independently, the LSNL and the NU control can eliminate the QNL ambiguity, hence the overall calorimetry systematics control can be improved.

4.3 Dual Calorimetry Possible Implementations

As mentioned in Sec.4.2, the response comparison between the LPMT and the SPMT can be done at different levels (e.g. the two systems comparison and the single channel to the system comparison) with different signals (e.g. neutrinos, radioactive sources, optical photon sources and cosmogenic sources). This section will discuss the basic ideas of several possible Dual Calorimetry implementations.

4.3.1 Dual Calorimetry Calibration Channel-wise

Since the QNL takes root at single channel level, it leads naturally to explore the channel-wise Dual Calorimetry for possible direct QNL calibration. The potential goal of this implementation is defined to control directly the charge response for each LPMT. As for the SPMT serving as the linear reference, from reducing the statistical fluctuation point of view, the usage of the full SPMT system would be preferable. However, other options of the using of SPMT could also be possible.

When focusing on the single LPMT, the photon collection is strongly position dependent and not fully correlated between the LPMT and the SPMT, as explained in Sec.4.2.2 with Fig.4.5. But there are several ways to overcome this challenge. For example by fixing the source position, the nonuniform response difference is then fixed. If the source energy can be tuned to cover the LPMT charge detection range at one fixed position, this nonuniform response difference remains constant, thus it can be factored out. Then this channel-wise approach can isolate the QNL and provide possible calibration for each LPMT. The technical details and performance of this approach will be explained in the next chapter, together with another channel-wise approach which can deal with a scanning source position.

In brief, the channel-wise Dual Calorimetry is supposed to provide the direct, data-driven and powerful handle for the potential QNL of the LPMT, thus contributing to the high precision energy measurement for the neutrino oscillation physics.

4.3.2 Dual Calorimetry with Neutrino Oscillation

Even though the energy resolution of the SPMT system is relative poor ($\sim 18\%$ at 1 MeV), it can still measure the "slow&big" oscillation parameters (Δm_{21}^2 and $\sin^2 \theta_{12}$) with a similar precision compared to that of the LPMT system, as illustrated in Fig.4.11 or Tab.4.2.

Since the neutrino events are common for the two systems, the LS responses are fully correlated. The partially correlated nonuniform responses are factorized out when extracting the neutrino oscillation parameters from the spectral analysis in the two systems respectively. Thus the measured values of these two parameters from the two systems are sensitive to the charge responses and could shed light on the potential charge response issues.

Table 4.2 – $\sin^2 \theta_{12}$ and Δm_{21}^2 sensitivity with LPMT system and SPMT system. Results taken from [200]

	$\sin^2 \theta_{12}$	Δm_{21}^2
LPMT	0.59%	0.34%
SPMT	0.63%	0.39%

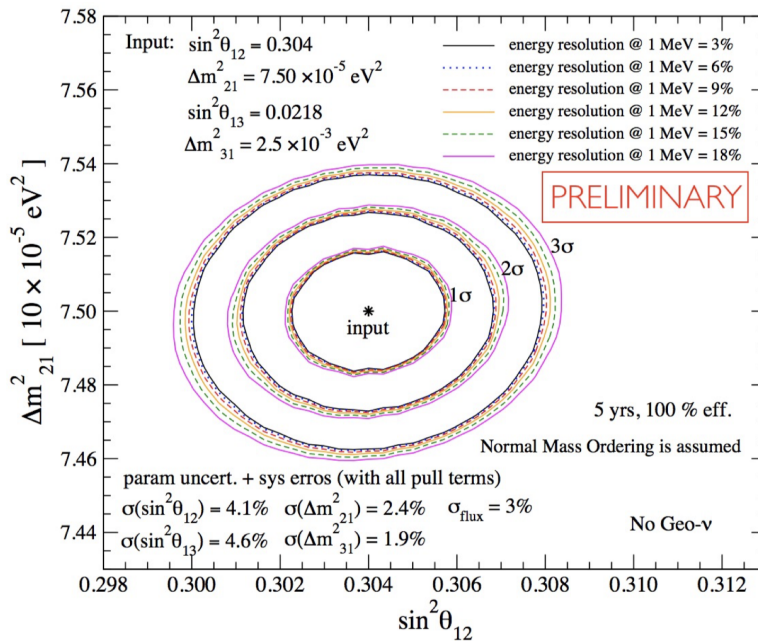


Figure 4.11 – LPMT and SPMT sensitivities on the "solar" oscillation parameters $\sin^2 \theta_{12}$ and Δm_{21}^2 . The LPMT has $\sim 3\%$ energy resolution at 1MeV. The SPMT has $\sim 18\%$ energy resolution at 1MeV. The two systems have similar sensitivity on these two parameters. Taken from [201].

4.3.3 Other Possible Implementations

— Dual Calorimetry event-wise

The event-wise implementation was one of the original ideas of the Dual Calorimetry. It aims to help understanding the charge response of the entire LPMT system by exploiting the calibration sources with the SPMT system as a reference. From the whole PMT system point of view, it is critical to deal with the NU difference between the two readout systems, as illustrated in Fig.4.5.

The idea to use a double ratio was proposed for the event-wise Dual Calorimetry. The double ratio could be defined as,

$$Double\ Ratio = \frac{\frac{\mathcal{R}_{data}^{LPMT}}{\mathcal{R}_{MC}^{LPMT}}}{\frac{\mathcal{R}_{data}^{SPMT}}{\mathcal{R}_{MC}^{SPMT}}} = \frac{\mathcal{R}_{data}^{LPMT}}{\mathcal{R}_{data}^{SPMT}} \cdot \frac{\mathcal{R}_{MC}^{SPMT}}{\mathcal{R}_{MC}^{LPMT}}, \quad (4.10)$$

where the $\mathcal{R}_{data}^{LPMT}$ and $\mathcal{R}_{data}^{SPMT}$ are the full responses of the LPMT and SPMT systems based on data, and the \mathcal{R}_{MC}^{LPMT} and \mathcal{R}_{MC}^{SPMT} are the full responses based on the Monte Carlo (MC) simulation. This double ratio approach relies on a reference which needs to be built heavily through the MC simulation. This MC reference needs to be further explored in order to properly deal with the NU difference between the two systems. And the MC accuracy would be critical and challenging. Nevertheless, since the channel-wise implementation by construction can provide a direct and data-driven QNL control, there is a priori less urgency to explore the challenging event-wise implementation.

— Dual Calorimetry with cosmogenic signals

The Dual Calorimetry could be possibly implemented through utilizing some cosmogenic signals, such as the ^{12}B β spectrum (up to ~ 13 MeV) and the Michel electron spectrum (up to ~ 50 MeV) induced by stopping muons. These cosmogenic signals provide high energy depositions across the full detector volume. The two readout systems can provide the independent measurements of the same cosmogenic signals. Therefore, the comparison of the measured spectra from the two systems could provide some diagnosis information on the charge response systematics as the LSNL and NU are canceled (or extracted).

Under the basic principle of the Dual Calorimetry, there could be other possible implementations. The key point among all these implementations can be summarized as the isolation of the charge response while performing the full response comparison between the LPMT calorimetry and the SPMT calorimetry. At the same time, the actual SPMT system performance must meet the designed goal, i.e. negligible or very small but for sure extremely well controlled QNL. Last, even though the Dual Calorimetry is born within the JUNO experiment, it could be also meaningful for other experiments in the sense of calorimetry systematics control, being worth for further exploration.

Chapter 5

Dual Calorimetry Calibration

As elaborated conceptually in the previous chapter, the Dual Calorimetry design is a unique handle for the potential QNL effects of JUNO. As discussed previously, the QNL effects take root channel-wise through PMT, electronics, DAQ, and even the charge reconstruction algorithm. Conceptually, the channel-wise QNL control should be the most direct approach, as it addresses the problem at its root. This chapter aims to introduce the channel-wise implementation, named as the Dual Calorimetry calibration (DCC), for the direct QNL control.

The DCC focuses on the calibration of the potential QNL of the LPMT at single channel level using the SPMT as the linear reference. Before explaining the DCC methodology, the general requirements and prospects of DCC can be beforehand listed as follows.

(1.) Charge Response Isolation

The DCC specifies the comparison between the single LPMT response ($r^{i,LPMT}$ with i as the channel label) and the SPMT system response (\mathcal{R}^{SPMT}), expressed as the following ratio:

$$\begin{aligned} \frac{r^{i,LPMT}}{\mathcal{R}^{SPMT}} &= \frac{\mathcal{R}_{LSNL} \cdot r_{NU}^{i,LPMT} \cdot r_{QNL}^{i,LPMT}}{\mathcal{R}_{LSNL} \cdot \mathcal{R}_{NU}^{SPMT} \cdot \mathcal{R}_{QNL}^{SPMT}} \\ &= \frac{r_{NU}^{i,LPMT}}{\mathcal{R}_{NU}^{SPMT}} \cdot \frac{r_{QNL}^{i,LPMT}}{\mathcal{R}_{QNL}^{SPMT}}, \end{aligned} \tag{5.1}$$

where the subscript of LSNL, NU and QNL represents the liquid scintillator nonlinear response, the nonuniform response, and the charge nonlinear response respectively. As explained in Sec.4.2.1, the Dual Calorimetry regardless of the implementation is immune to the LS response, thus the \mathcal{R}_{LSNL} is canceled in Eq.(5.1) by definition. For DCC, in order to isolate the charge response, it is vital to deal with the nonuniform response difference between the single LPMT and the SPMT system, i.e. $r_{NU}^{i,LPMT}$ and \mathcal{R}_{NU}^{SPMT} , such that this difference can be eliminated or corrected.

(2.) Charge Non-linearity of Physics Signals

As elaborated in Sec.4.2.3, the channel-wise QNL has a charge dependence and also a time profile dependence. It is equivalent to the event-wise energy, position and particle dependence. The QNL of the physics signals should always be targeted while defining the calibration strategy and deploying the calibration operation. For the JUNO primary

physics, these signals are mainly the reactor $\bar{\nu}_e$ prompt signal of the inverse beta decay (IBD) reactions. These physics signals correspond to the positrons uniformly distributed in the detector volume with the deposited energy roughly from 1 to 10 MeV. For simplicity, the wording of reactor neutrino signal will be used in the following text, and the IBD reaction and prompt signal are implicit in this expression.

(3.) Channel Dependence

The charge response can be channel dependent because of the potential channel-to-channel differences in the PMTs and electronics. So it is desired that the DCC should be designed to calibrate every channel of the LPMT system.

(4.) SPMT Reference

For the SPMT, as the charge linear reference, the usage of the SPMT system, i.e. $\sim 26,000$ SPMTs, is preferred for two reasons. The first one is to reduce the statistical uncertainty for the DCC from the SPMT contribution. The second one is to provide exactly the same reference for each channel of LPMT in order to have the maximal sensitivity to channel-to-channel charge response differences.

In order to meet the aforementioned (1.) \sim (4.) requirements of DCC, two methodologies are developed, i.e. DCC with UV laser source and DCC with radioactive sources, which will be explained in detail in Sec.5.1 and 5.2. These two methods have complementary advantages, and can form a comprehensive QNL calibration strategy for JUNO, as detailed in Sec.5.3. As it will be demonstrated, the DCC strategy has the capability to calibrate effectively the potential QNL of every channel of LPMT for the reactor neutrino signals. The performance of DCC is presented along with the methodology introduction in this chapter. The particular role of the SPMT in DCC, especially the PE counting based linear charge estimation, is discussed in Sec.5.4. Last, in Sec.5.5, the major systematic effects of DCC are explained, and the outlook for possible higher order DCC calibration is briefly discussed in Sec.5.6.

5.1 Dual Calorimetry Calibration with UV Laser Source

5.1.1 UV Laser Advantages in DCC

The combination of the Dual Calorimetry and the UV laser source, noted as DCC-laser, is particularly powerful, because of the unique features of the UV laser source highlighted as follows:

- The wide range of the laser intensity makes possible to use one source position to cover the reactor neutrino related charge detection range (i.e. $1 \sim 10^2$ PE) for every channel of LPMT.

The benefit brought by using one source position is that the charge response is isolated by construction while doing the response comparison implied by the Dual Calorimetry. Since the source position (or event vertex position) is fixed, the nonuniform response difference between the single LPMT and the SPMT system, i.e. $r_{NU}^{i,LPMT}$ and \mathcal{R}_{NU}^{SPMT} in Eq.(5.1), is then constant by definition, thus it is factorized out. Therefore, the charge response is fully isolated, and the ambiguity between the QNL and the NU is eliminated by construction.

The benefit brought by the wide range of the laser intensity is that the tunable laser intensity can reach the $1 \sim 10^2$ PE charge detection range for every LPMT while the source is always kept at one position. It implies that the isolation of the

charge response can always be achieved. The intensity of the laser source designed in JUNO can be tuned from a few hundreds of keV to TeV equivalent energy [172], covering the desired charge detection range. For example, one LPMT is illuminated in average at ~ 60 PE when a ~ 8 MeV calibration source is located ~ 2.5 meters away from that LPMT (i.e. the source close to the edge of the detector); the same illumination level can be mimicked by placing the laser source at the detector center with ~ 1 GeV intensity. The geometrical center of the detector is the ideal position to deploy the laser source, because it can lighten equivalently every channel of LPMT simultaneously.

- The UV photon will excite the LS and produce the similar emission spectrum as the ionizing particles [202]. Therefore it does not make any difference for the PMT photon detection about whether the LS photons are produced through the UV photons or through the ionizing particles. The designed UV laser source at JUNO has 266 nm wavelength, and its spectrum is shown in Fig. 5.1. The LS emission spectrum induced by the UV laser is centered around 420 nm as shown also in Fig. 5.1.

Another benefit from the LS excitation and emission is that these processes will make the emitted LS photons further isotropic in all directions. So it can evenly illuminate different channels of LPMT when the laser source is placed at the detector center, particularly for the channels which potentially suffer from some shadowing effects caused by the laser system [172].

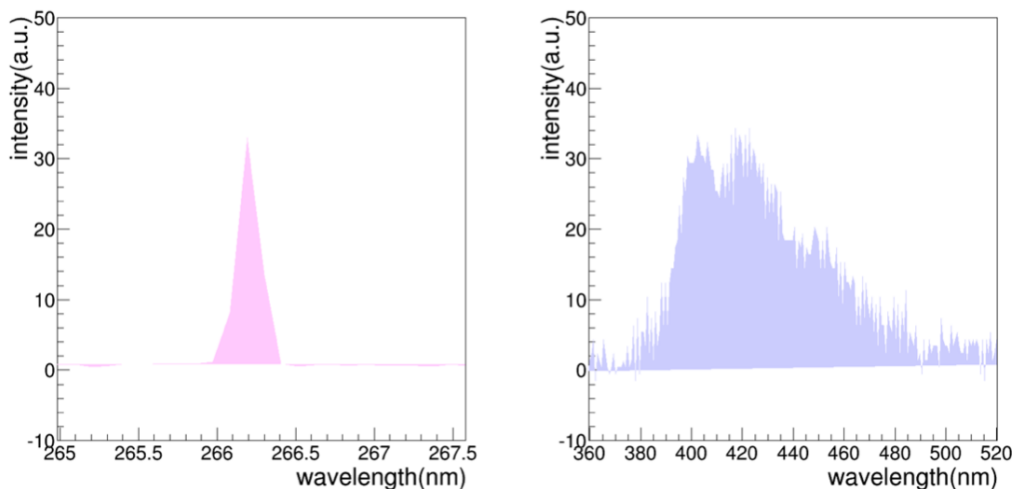


Figure 5.1 – Left figure: UV laser wavelength spectrum in the JUNO laser system. Right figure: LS emission spectrum when the LS is excited by the UV laser. Taken from Ref.[172]

5.1.2 Methodology

Taking the unique advantages of the UV laser source, DCC-laser aims to yield the QNL calibration for every channel of LPMT independently covering the $1 \sim 100$ PE (or even beyond) charge range. The methodology can be understood in the following three steps.

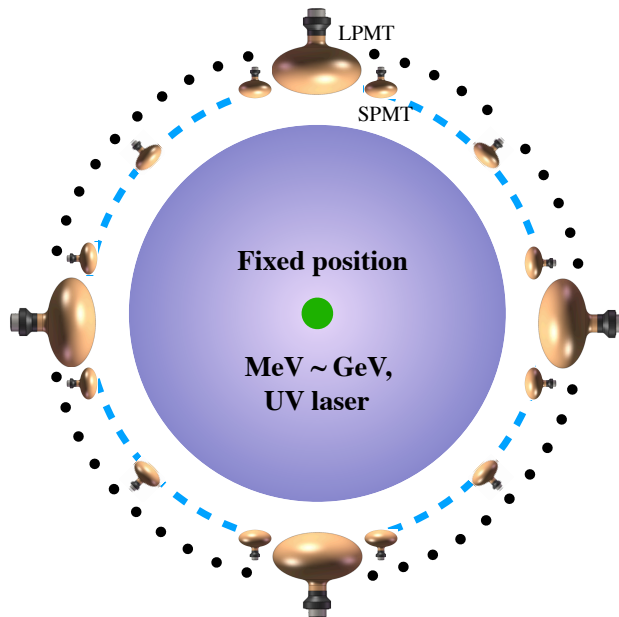


Figure 5.2 – Illustration of the DCC-laser. The UV laser source can be attached to the ACU (automatic calibration unit) system and placed at the detector center. The laser intensity can be tuned from MeV to GeV level.

Step 1. LPMT and SPMT Response Comparison

By placing the UV laser¹ source at the detector center, for a certain laser intensity, the single LPMT response and the SPMT system response can be characterized by their corresponding mean illumination respectively. For instance, when the laser source is placed at the detector center with 1 MeV intensity, a single LPMT will detect in average ~ 0.07 PE, and the total SPMT system will detect in average ~ 40 PE. While changing only the laser intensity, the response relation changes correspondingly. When the laser intensity changes from 1 MeV to 1.5 GeV at the detector center, every single LPMT will be illuminated equivalently from ~ 0.07 PE to ~ 100 PE, thus covering the charge detection range of the reactor neutrino signal. By assuming a linear charge response of the LPMT, together with the designed SPMT linear charge response, the response relation between these two is then linear as illustrated with the dashed black curve in Fig.5.3. However if the LPMT suffers some QNL, e.g. $\sim 10\%$ over 100 PE as described in Eq.(4.4), the response relation is then biased compared to the linear case, shown as the solid red curve in Fig.5.3.

However, the perfect linear charge response of the LPMT is not observable if it suffers some QNL. Thus it is critical to establish an experimentally feasible reference which can maximally recover the linear response relation.

1. Due to the extremely low speed of simulating high intensity UV laser events in JUNO software (Sniper based), the simulation of high laser intensity (up to 1.5 GeV) events are mimicked by using multiple low energy (≤ 10 MeV) electrons and generalizing the UV laser time profile obtained with low intensity to the high intensity events. Thus, the relevant features (i.e. intensity and time profile) of the UV laser energy deposition can be simulated.

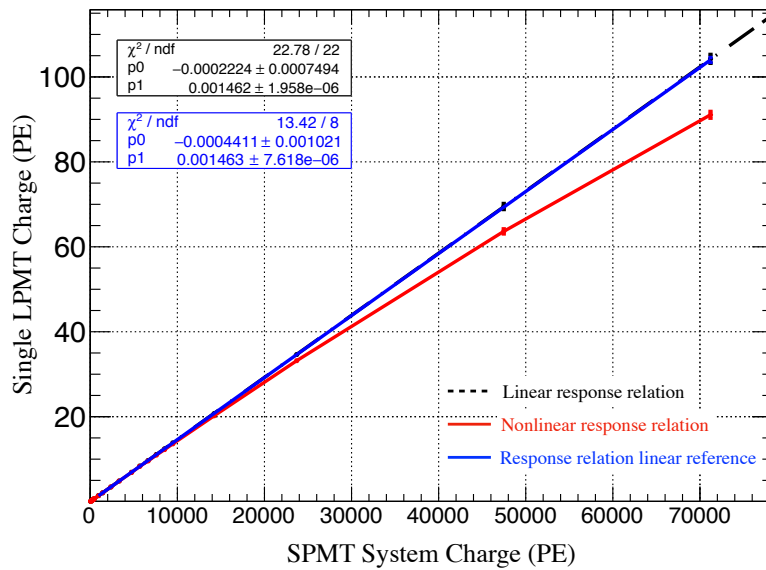


Figure 5.3 – Response comparison between the single LPMT and the SPMT system. The UV laser source is kept at the detector center and the laser intensity is varied from 1 MeV to 1.5 GeV. In this case the response relation is only sensitive to the QNL. As the SPMT is always charge linear, if the LPMT charge response is also linear, the response relation between these two is then linear as the dashed black curve. If the LPMT suffers a $\sim 10\%$ QNL defined with Eq.(4.4), this relation is biased as the solid red curve. The linear response relation can be reconstructed from the extrapolation of the linear region in the actual nonlinear response relation, shown as the blue curve.

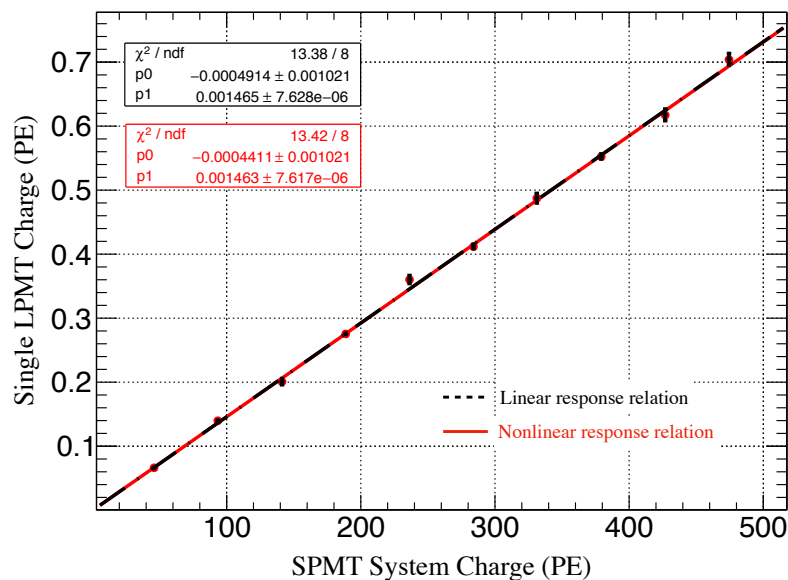


Figure 5.4 – The linear region of the response relation between the single LPMT and the SPMT system. The SPMT is always charge linear based on PE counting by design. At low laser intensity region, the LPMT is also dominated by the single PE detection, thus being charge linear. The low laser intensity (or low illumination) region can be considered as the linear region represented as the solid red curve. The dashed black curve corresponds to the perfect linear case.

Step 2. Response Relation Linear Reference

The key feature of the SPMT that can ensure the linearity is its low illumination. The low illumination makes the SPMT to be dominated by the single PE detection, and the robustness of PE counting (including corrections which will be discussed in Sec.5.4) makes the SPMT to be charge linear by design.

Following the same principle as the SPMT, there also exists a single PE dominant regime for the LPMT in its low illumination region. For example, for the laser intensity lower than 10 MeV equivalent energy when the source is placed at the detector center, the mean illumination of the single LPMT is well below 1 PE, thus enabling the PE counting (upon possible corrections). Then this region can be considered to be charge linear for the LPMT, as illustrated in Fig.5.4. For simplicity, this thesis defines preliminarily the laser intensity lower than 10 MeV as the charge linear region of the LPMT in DCC. However the exact experimental linear region should be defined according to the actual hardware performance and can be possibly extended.

Through extrapolating this linear region, the linear response relation can be approximately recovered, shown as the blue curve in Fig.5.3. This extrapolated linear response relation is experimentally feasible and matches largely the perfect linear case, thus being considered as the response relation linear reference.

To summarize, there are two references to be clarified. One is the SPMT that is always the linear reference for the LPMT, and this reference is the metric to reveal the QNL of the LPMT. The other is the response relation linear reference, and this reference is established to recover effectively the LPMT linear response. These two references are indispensable for DCC. By comparing the potential nonlinear response relation (solid red curve in Fig.5.3) with its linear reference (solid blue curve in Fig.5.3), the LPMT QNL is then diagnosed.

Step 3. Calibration and Performance

Once the QNL is diagnosed through step 1. and 2., the charge bias induced by the QNL for the LPMT can be shown as a function of the true charge, as illustrated in Fig.5.5. The diagnosed QNL can be compared with the true QNL, as shown also in Fig.5.5. It needs to point out that the diagnosed QNL does not perfectly match the true one due to the systematic effects of the method itself, such as the Poisson statistics and the PMT charge resolution effects. These effects will be discussed in detail in Sec.5.5. The diagnosed charge bias (or QNL) is then the correction that can be used to calibrate the reconstructed charge.

For the moment, the QNL is considered to be only charge dependent. If the LPMT suffers a $\sim 10\%$ true channel-wise QNL over 1~100 PE range, the residual QNL after the DCC-laser calibration can be controlled at $\sim 2\%$ level, as shown in Fig.5.5. Even though by assuming the true QNL of the LPMT as large as $\sim 50\%$ over 1~100 PE range, it can be largely calibrated to $\sim 5\%$ level, as shown in Fig.5.6.

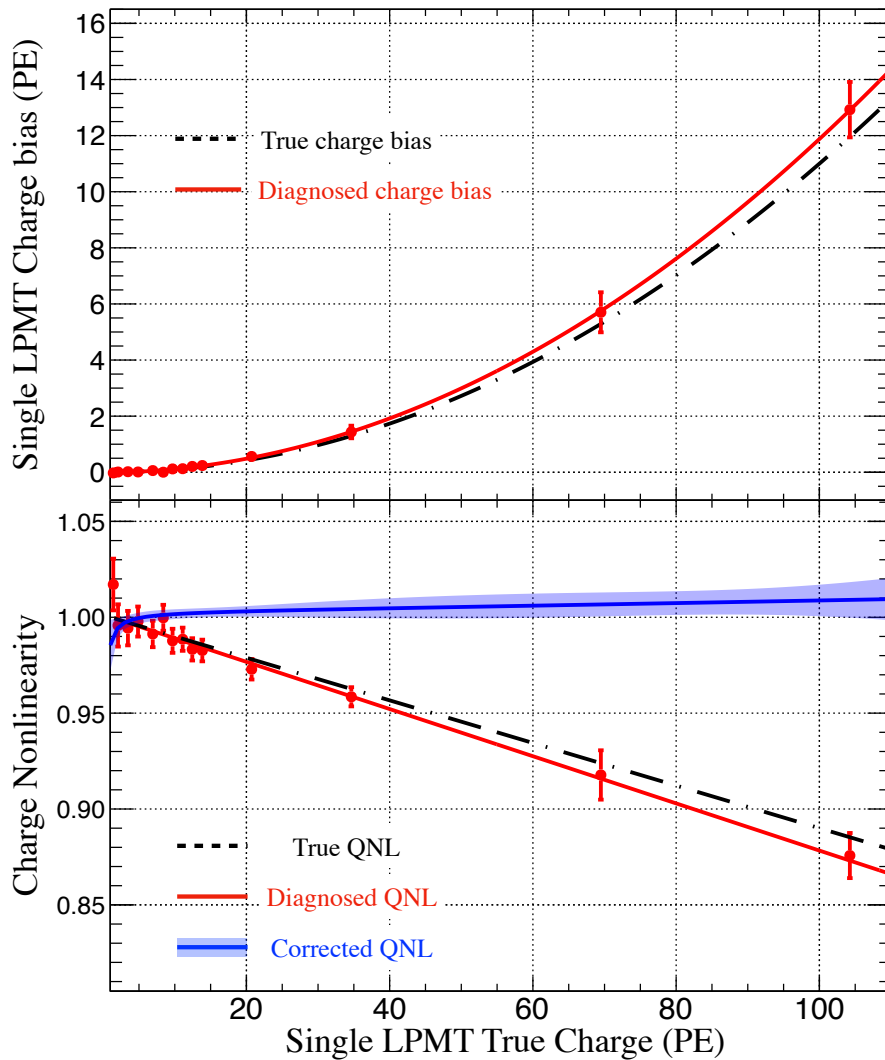


Figure 5.5 – DCC-laser performance under the assumption of $\sim 10\%$ channel-wise QNL over $1\sim 100$ PE. The upper figure is the LPMT charge bias caused by the QNL as a function of the true charge. The dashed black curve corresponds to the true charge bias, and the solid red curve corresponds to the diagnosed charge bias. The lower figure is the channel-wise QNL. The y-axis is the reconstructed charge (calibrated or uncalibrated) over the true charge. The dashed black curve corresponds to the true QNL of Eq.(4.4) ($\sim 10\%$ level), which is considered to be only charge dependent. The solid red curve is the diagnosed QNL through DCC-laser. The solid blue curve is the residual QNL after the calibration. A 10% QNL can be calibrated to 2% level over the $1\sim 100$ PE range.

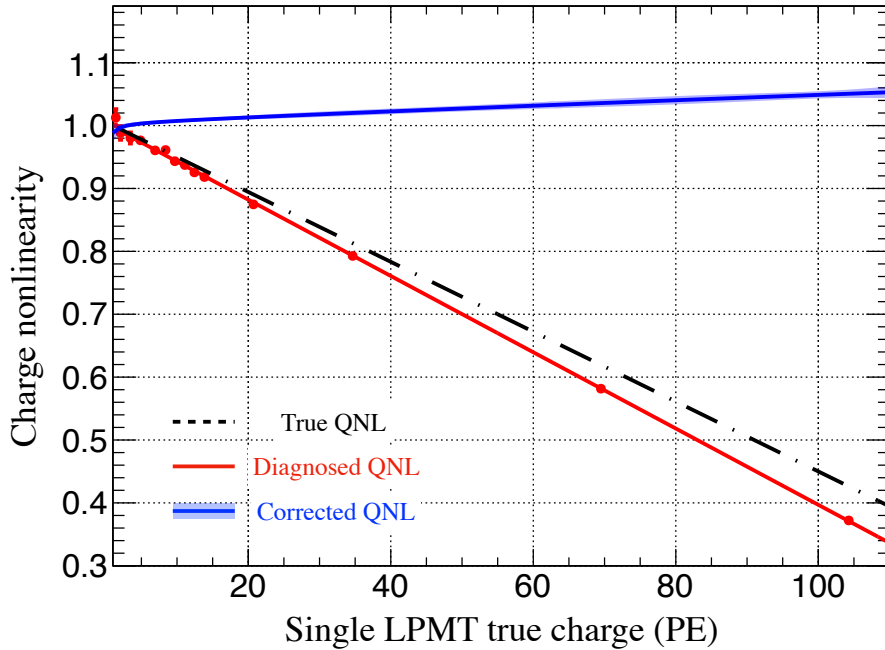


Figure 5.6 – DCC-laser performance under the assumption of $\sim 50\%$ channel-wise QNL over $1\sim 100$ PE (QNL model of Eq.(4.5)). The dashed black curve is the true QNL. The solid red curve is the diagnosed QNL through DCC-laser. The solid blue curve is the residual QNL after the calibration. A $\sim 50\%$ QNL can be calibrated to 5% level over the $1\sim 100$ PE range.

5.1.3 Advantages and Challenges

Advantages

The advantages of DCC-laser approach can be summarized in the following two aspects.

On the one hand, this approach can be done at one source position. It implies a perfect isolation of the QNL, since the LSNL and the NU are totally eliminated from the QNL by construction.

On the other hand, the DCC-laser can be implemented for each channel of LPMT respectively, while covering the full charge detection range ($1\sim 10^2$ PE) of the reactor neutrino signals, thanks to the wide range of the laser intensity. And it can even go beyond with higher laser intensity possibly for other physics topics. In conclusion, the charge dependence and channel dependence of the LPMT QNL control can be well treated by DCC-laser.

Challenges

The previous assumption of the QNL for one channel is only charge dependent, in other words, it is only laser intensity (or energy) dependent. While considering the time profile dependence of the QNL, the challenges of DCC-laser arise.

As illustrated in Sec.4.2.3, the charge response depends also on the time profile of the collected PEs at the PMT. This time profile is particle and position dependent. Regard-

ing the reactor neutrino signals, the particle dependence corresponds to the positrons, and the position dependence corresponds to the uniformly distributed signals.

As for the particle dependence, unlike positrons which excites the LS solvent (i.e. LAB), the UV photons will directly excite the LS fluor (i.e. PPO) due to its large optical absorption [197]. The energy transfer from solvent to fluor causes a certain time delay [196], but the UV laser excitation does not (or much less) experience such a time delay. Thus the UV laser has a faster time profile than positrons, as illustrated with the simulated results in Fig.4.8.

As for the position dependence, as explained in Sec.4.2.3, it is dominated by the Rayleigh scattering, and also affected by the absorption and re-emission processes during the photon propagation. All these processes are proportional to the distance between the event vertex and the PMT, resulting in some time delay.

Two cases are specified for the position dependence as follows:

- **"Full volume" case:** uniformly distributed energy deposition in the full detector volume.
- **"Center" case:** energy deposition at the detector center.

The reactor neutrino signal corresponds to the "full volume" case, while DCC-laser corresponds to the "center" case. Regarding the distance between the PMT and the event vertex, actually this distance for the "full volume" case can be larger or smaller than that for the "center" case. However, when it is larger, the single LPMT mean illumination is well below 1 PE for the reactor neutrino signals, thus being not interesting for the QNL control. Therefore, the distance between the PMT and the event vertex for the "full volume" case can be safely considered to be always smaller than that for the "center" case in the following discussion.

For example if the laser illuminates one LPMT in average at 60 PE with 1 GeV intensity at the detector center (i.e. roughly 19 meters from the PMT to the event vertex), the positrons (related to the reactor neutrinos) with 8 MeV deposited energy should be located much closer (i.e. roughly 2 meters) to that LPMT in order to get the same illumination. In this case, there will be more time delay caused by the scattering processes for the "center" case.

In conclusion, from the position dependence point of view, the time profile for the "center" case is, in general, slower than that for the "full volume" case.

If both the particle dependence and the position dependence are considered for the time profile effect, the case of UV laser at the detector center has a faster effect (i.e. particle dependence) and also a slower effect (i.e. position dependence) compared to the reactor neutrino signals (i.e. positrons uniformly distributed in the full detector volume).

Currently, it is challenging to describe the time profile impact on the QNL at JUNO, due to the lack of experimental evidence. It is assumed in this thesis that when the time profile is faster, there will be larger QNL. The basic idea behind this assumption is that when the time profile is faster, there will be more chance for the pile-up of PEs, hence, it will be more difficult to reconstruct the charge.

In order to illustrate the time profile effect on the QNL, some assumptions are made next. These assumptions are needed to provide some quantitative estimation of the effect of the different time profiles in DCC-laser. The corresponding performance of the DCC-laser is discussed under these assumptions. For simplicity, the case of UV laser placed at the detector center is noted as "laser case", and the reactor neutrino signal is noted as "reactor neutrino case".

— **Common assumption:**

For the "laser case", the LPMT suffers a $\sim 10\%$ QNL over 1~100 PE range, following the QNL model as:

$$\frac{Q_{rec}}{Q_{true}} = (1.11 \cdot 10^{-3})Q_{true} + 1.0011, \quad (5.2)$$

where Q_{true} is the true charge, and Q_{rec} is the reconstructed charge. Q_{true} and Q_{rec} are in the unit of PE, and the dimensions of the numbers in this equation are adjusted to make both sides of the equation dimensionless.

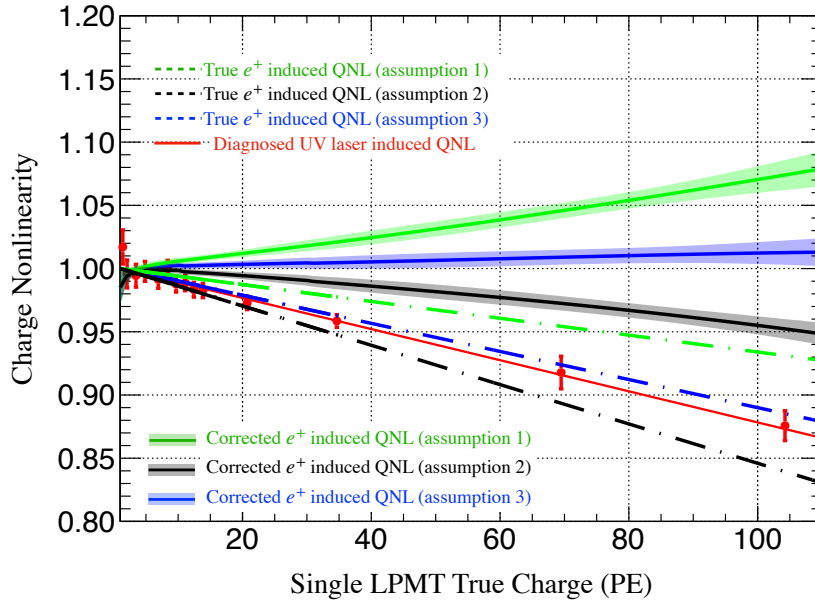


Figure 5.7 – The particle and position dependent time profile impact on the QNL and the corresponding DCC-laser performance. The diagnosed QNL through DCC-laser is shown as the solid red curve assuming it suffers a $\sim 10\%$ QNL over 1~100 PE range (Eq.(5.2)). The dashed green, black and blue curves are the true QNL for positrons uniformly distributed in the detector volume under assumption (1.), (2.) and (3.) respectively. Correspondingly, the solid green, black and blue curves are the residual QNL after DCC-laser calibration.

— **Assumption (1.):**

The particle dependence impact on the QNL is more significant, while the position dependence impact is less significant as the following QNL model at 5% level over 100 PE for the "reactor neutrino case":

$$\frac{Q_{rec}}{Q_{true}} = (6.46 \cdot 10^{-6}d - 6.81 \cdot 10^{-4})Q_{true} - 6.46 \cdot 10^{-6} \cdot d + 1.000681, \quad (5.3)$$

where d is the distance between the PMT and the event vertex with the unit of meter.

Under assumption (1.), the "laser case" in general has a faster time profile, implying a larger QNL, than the "reactor neutrino case". So the diagnosed QNL for the "laser case" through DCC-laser (shown as the solid red curve in Fig.5.7) is larger than the QNL

induced by the "reactor neutrino case" (shown as the dashed green curve in Fig.5.7). Therefore, the QNL for "reactor neutrino case" is over corrected through DCC-laser, which is shown as the solid green curve in Fig.5.7.

— **Assumption (2.):**

The particle dependence impact on the QNL is less significant while the position dependence impact is more significant as the following QNL model at 15% level over 100 PE for the "reactor neutrino case":

$$\frac{Q_{rec}}{Q_{true}} = (3.23 \cdot 10^{-5}d - 1.63 \cdot 10^{-3})Q_{true} - 3.23 \cdot 10^{-5} \cdot d + 1.00163. \quad (5.4)$$

Under assumption (2.), the "laser case" in general has a slower time profile than the "reactor neutrino case". So the diagnosed QNL for the "laser case" through DCC-laser is smaller than the QNL induced by the "reactor neutrino case" (shown as the dashed black curve in Fig.5.7). Therefore, the QNL for the "reactor neutrino case" is under corrected through DCC-laser, shown as the solid black curve in Fig.5.7.

— **Assumption (3.):**

The particle dependence and the position dependence impacts on the QNL are at the similar level as the following QNL model at 10% level over 100 PE for the "reactor neutrino case":

$$\frac{Q_{rec}}{Q_{true}} = (3.23 \cdot 10^{-5}d - 1.18 \cdot 10^{-3})Q_{true} - 3.23 \cdot 10^{-5} \cdot d + 1.00118. \quad (5.5)$$

The particle dependence and position dependence on time profile are opposite when considering the "laser case" and "reactor neutrino case". If these two effects are at the same level as the assumption (3.), they could cancel one another. Thus the diagnosed QNL for the "laser case" could be similar to the one for the "reactor neutrino case", shown as the dashed blue curve in Fig.5.7. In this scenario, the calibration bias caused by the difference between the "laser case" and the "reactor neutrino case" could be alleviated to some extent, shown as the solid blue curve in Fig.5.7. It turns out that the DCC-laser can effectively calibrate the QNL caused by the reactor neutrino signals.

In conclusion, DCC-laser potentially has some challenges to calibrate the QNL of the reactor neutrino signals because of the particle and position dependent time profile effects. This challenge could be eased due to the opposite impacts of these two dependences for the "laser case" and "reactor neutrino case". However, the UV laser source has no means to entirely overcome this challenge, despite the Dual Calorimetry methodology. As a consequence, a further stage of calibration may be needed to correct the potential bias in DCC-laser or at least a validation method is needed to demonstrate the efficiency of using DCC-laser to calibrate reactor neutrino signals. Such a method will be introduced in Sec.5.2 to complete the DCC.

Nevertheless, the unique advantages of DCC-laser, i.e. 1.) perfect isolation of QNL, 2.) all channels coverage and 3.) wide charge detection coverage, make it indispensable for the control of the potential QNL of the LPMT at JUNO.

5.2 Dual Calorimetry Calibration with Radioactive Sources

5.2.1 Radioactive Source Advantages in DCC

From the particle dependence of the time profile point of view, the radioactive sources, mainly gamma sources with roughly 0.5~8 MeV energy, have more similarity to the reactor neutrino signals i.e. positrons¹. The gammas will excite the solvent in a similar way as positrons, thus experiencing a similar time profile, as shown in Fig.4.8.

From the position dependence of the time profile point of view, in order to mimic to some extent the uniformly distributed signals with the radioactive sources, the easiest (or most time-saving) approach is to scan the source position along one diametral direction (e.g. from the detector top to the bottom). In this way, there will be several PMTs at each end in the diametral direction that experience the similar position dependence of the time profile as the reactor neutrino signals.

The energy of the designed radioactive sources in JUNO (0.5~8 MeV) can largely cover the reactor neutrino energy range [174]. Therefore, by scanning the source position and the energy of the gammas sources, the reactor neutrino signal induced QNL can be mimicked for several channels of LPMT. By deploying the Dual Calorimetry technique, it is possible to calibrate effectively the QNL for these channels. This approach is named as the Dual Calorimetry calibration with radioactive (gamma) sources, noted as DCC-gamma.

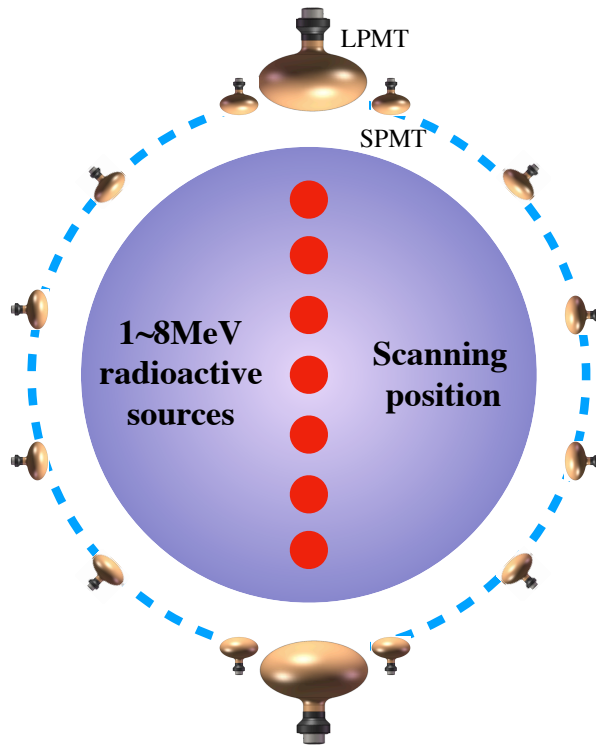


Figure 5.8 – Illustration of the DCC-gamma. The gamma calibration sources can be deployed with the ACU (automatic calibration unit) system and scanned from the detector top to the bottom. The energy of the gamma sources is roughly in the range of 1 ~ 8 MeV.

1. In practice, due to the lack of practical positron calibration sources, the detector energy response is calibrated with gamma sources, and then it is converted to positron energy response.

5.2.2 Methodology

As a channel-wise calibration, DCC-gamma also focuses on the single LPMT charge response and uses the SPMT system as the linear charge reference. Despite that the reactor neutrino induced QNL can be mimicked by scanning the radioactive sources, it is not trivial to isolate the QNL when the source position is changing. The reason is that once the source position is not fixed, the NU will fold in, and the QNL can not be isolated directly while doing the Dual Calorimetry comparison. Thus it is critical to deal with the NU difference between the LPMT and the SPMT in order to carry out the DCC-gamma. The detailed methodology for achieving this point will be explained in the following steps.

Step 1.: LPMT and SPMT Response Comparison

Similar to DCC-laser, when the radioactive source is kept at one position, the single LPMT response and the SPMT system response can be characterized by their mean illumination respectively. While deploying different radioactive sources with different energy emissions at the same position, the response relation between the LPMT and SPMT changes correspondingly. It is important to keep the same single LPMT for the response comparison while changing the source energy. If the LPMT charge response is linear, together with the designed charge linear response of the SPMT, this response relation is then linear. For instance if the source is kept at the detector center, the response relation is shown as the orange curve in Fig.5.9.

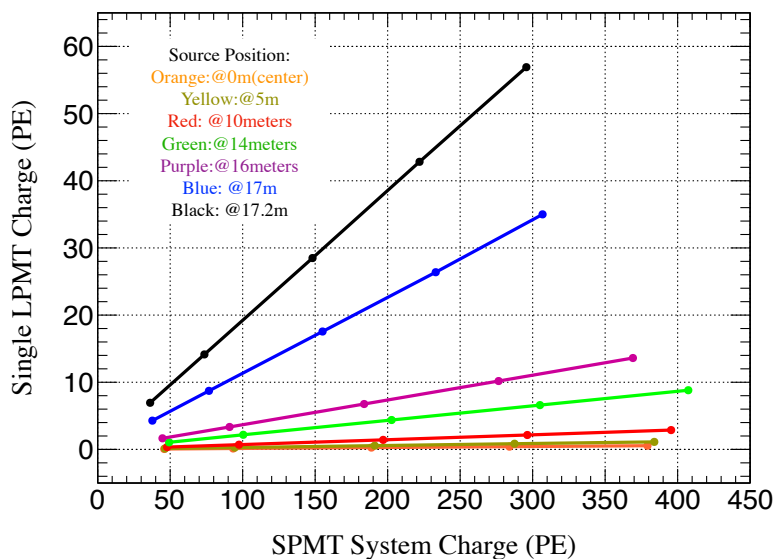


Figure 5.9 – The response relation between the single LPMT and the SPMT system while scanning the source position and scanning the radioactive source energy at each position. The LPMT is the one which is placed at the top of the detector. Since the SPMT is always charge linear, if the LPMT charge response is also linear, this response relation at one position is then linear as each curve with different color in this figure. The source position represents the distance from the calibration source to the detector center along the vertical diametral direction. For example 0 m (orange curve) represents that the source is placed at the detector center. And 17.2 m (black curve) represents that the source is placed close to the top of the detector.

When the calibration source is placed at another position, by scanning the source energy and focusing on the same LPMT as before, the response relation will be different compared to that of the former position. For instance, if the source is placed at 10 meters away from the detector center towards that LPMT, the response relation is shown as the red curve in Fig.5.9.

While scanning the source position from the detector center to the detector edge and scanning the source energy at each position, a set of independent response relations can be got as the different curves in Fig. 5.9.

At each position, the response relation is only sensitive to the QNL by construction. In principle, each response relation curve can be used to calibrate the QNL for a certain charge range, following the same methodology as DCC-laser. Such an approach can be understood as a segmented calibration. However, experimentally it is not easy to use each independent response relation to implement the segmented calibration because of the limited available radioactive sources. For example when the source is placed at ~ 2 meters to one LPMT, in order to establish a response relation linear reference (similar to the one in DCC-laser), several radioactive sources with energy below 100 KeV (or even below 10 KeV) are needed, which is not practical. So other feasible approaches are needed for using these independent response relations.

Step 2. Alignment of the Independent Response Relations

Instead of trying to use each independent response relation for a segmented QNL calibration, the alignment of all these independent response relations is another option to explore possible DCC-gamma implementation. In order to achieve such an alignment, the following two steps are indispensable.

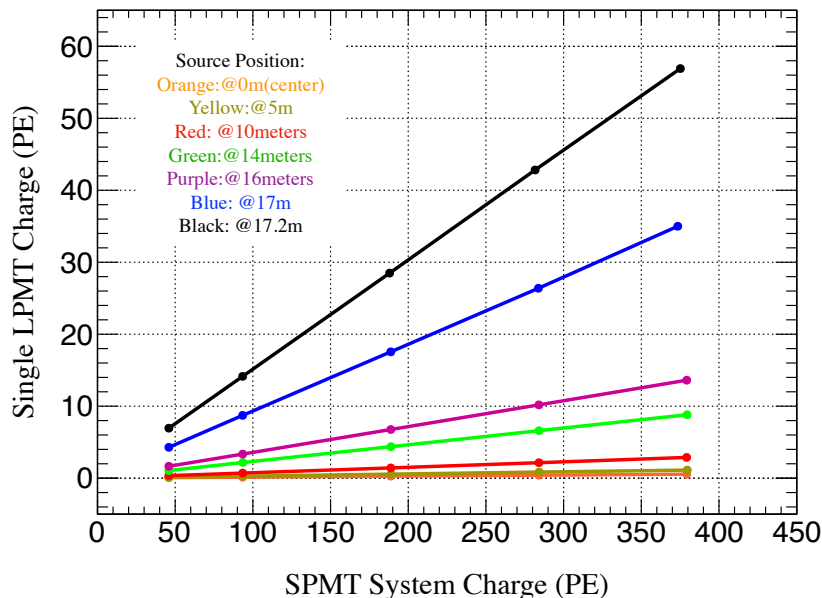


Figure 5.10 – Response relations with the aligned SPMT responses. In Fig.5.9, by applying C_1 correction (one dimension SPMT NU correction) to the SPMT responses, the SPMT responses are aligned to be identical for different source positions. It manifests like all these independent response relations (different colors in this figure) well aligned in x-axis.

— **C_1 : The corresponding SPMT system non-uniformity (NU) correction**

While scanning the source position in one dimension along the vertical diametral direction, the SPMT system response is not uniform, as the projection on x-axis of each response relation curve is not superposed one to another in Fig.5.9. The corresponding one dimension SPMT system NU map, as shown in Fig.5.11a, can be used to calibrate the nonuniform response of the SPMT system in these response relation curves, noted as C_1 correction. Therefore, the SPMT system responses are aligned, illustrated as the projection on x-axis of each response relation curve being superposed one to another in Fig.5.10. Since the SPMT is designed to be charge linear, the C_1 correction is foreseen not to bring the ambiguity between the QNL and the NU.

— **C_2 : The application of the single LPMT nonuniformity map on the SPMT system response**

After aligning the SPMT responses, for a fixed energy deposition, the SPMT will have the same response wherever the source position is. The single LPMT response is heavily position dependent, shown as the projection on y-axis of each response relation curve in Fig.5.10. The single LPMT relative optical acceptance can be defined as the ratio of the LPMT mean illumination for a given source position to that for the detector center position, as shown in Fig.5.11b, while the source energy is kept unchanged.

This relative optical acceptance represents the single LPMT NU response map, noted as C_2 correction. The way to align the segmented response relations is to apply this map (C_2) to the SPMT system response while keeping the LPMT response unmodified. Thus the aligned LPMT and SPMT response relation is shown in Fig.5.12. If the LPMT is charge linear, the aligned response relation is then linear, shown as the dashed black curve in Fig.5.12. If the LPMT suffers a QNL at 10% level with the form of Eq.(5.5), the nonlinear behavior is shown as the solid red curve in Fig.5.12.

Since the LPMT potentially suffers some QNL effects, the C_2 correction is also affected by the QNL, thus bringing the ambiguity between the QNL and the NU. It is possible to reduce this ambiguity through a careful consideration of calibration source to get the C_2 correction. If the QNL is positively correlated to the source energy, the source with lowest possible energy should be the best option to obtain C_2 for reducing this ambiguity. In addition, it is not limited to the radioactive sources, and the laser source can also be applicable to get the C_2 correction if needed. In Sec.5.5, there will be a dedicated discussion about the systematic effects of DCC including this C_2 correction.

Step 3. Response Relation Linear Reference

Similar to the DCC-laser, a linear region in the actual nonlinear response relation (red curve in Fig.5.12) can be defined for DCC-gamma. In this linear region (i.e. low illumination region), the LPMT charge linearity can be ensured through the PE counting. Through the extrapolation of the linear region, an experimentally feasible response relation linear reference can be built, shown as the solid blue curve in Fig.5.12. Thus the potential QNL of the LPMT can be diagnosed through the comparison between the linear reference and the actual nonlinear response relation.

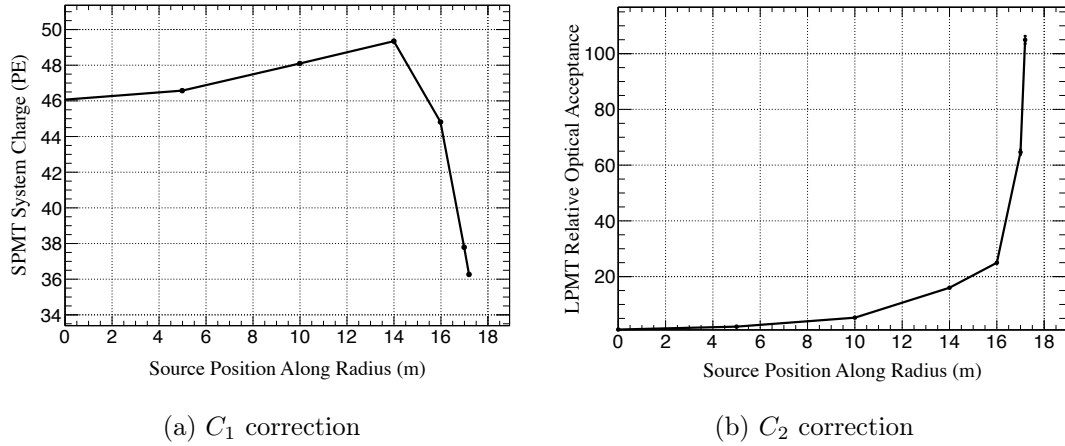


Figure 5.11 – (a): The SPMT one dimension NU map (or C_1 correction map). The x-axis is the source position along the radial direction from the detector center (0 m) to the detector top (17.2 m). The y-axis is the SPMT system response. (b): The single LPMT one dimension NU map (or the C_1 correction map). This NU is represented by the single LPMT relative optical acceptance. The x-axis is also the source position. The y-axis is defined as the single LPMT optical acceptance ratio between one source position and the detector center position. The sources used in the simulation both for (a) and (b) are 1 MeV electrons.

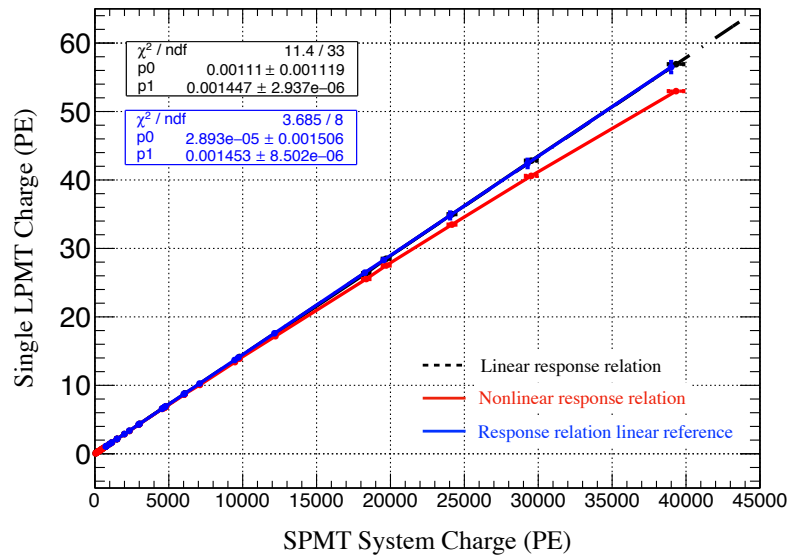


Figure 5.12 – Aligned response relation. The single LPMT non-uniformity map (C_2 correction) is applied to the C_1 corrected SPMT response in order to align the segmented response relations. If the LPMT is charge linear, the aligned response relation is shown as the dashed black curve. If the LPMT suffers a QNL at 10% level of Eq.(5.5), the aligned response relation is biased, shown as the solid red curve. A linear reference of the response relation can be established through the extrapolation of the linear region, shown as the solid blue curve.

Step 4. Calibration and Performance

Once the QNL is diagnosed through steps (1.)~(3.), the charge bias caused by the QNL can be shown as a function of the true charge in the upper panel of Fig.5.13. The diagnosed QNL can be compared with the true QNL of reactor neutrino signals, as shown in the lower panel of Fig. 5.13. As illustrated in Fig. 5.13, by assuming that the LPMT suffers a QNL at 10% level with the form of Eq.(5.5) for reactor neutrino signals, the residual QNL after DCC-gamma can be controlled $<2\%$ in the range of 1~60 PE.

For the systematic effects of DCC-gamma, there are some common effects as DCC-laser, and also some unique effects during the alignment of the independent response relations such as the C_2 correction. The systematic effects will be discussed in Sec.5.5.

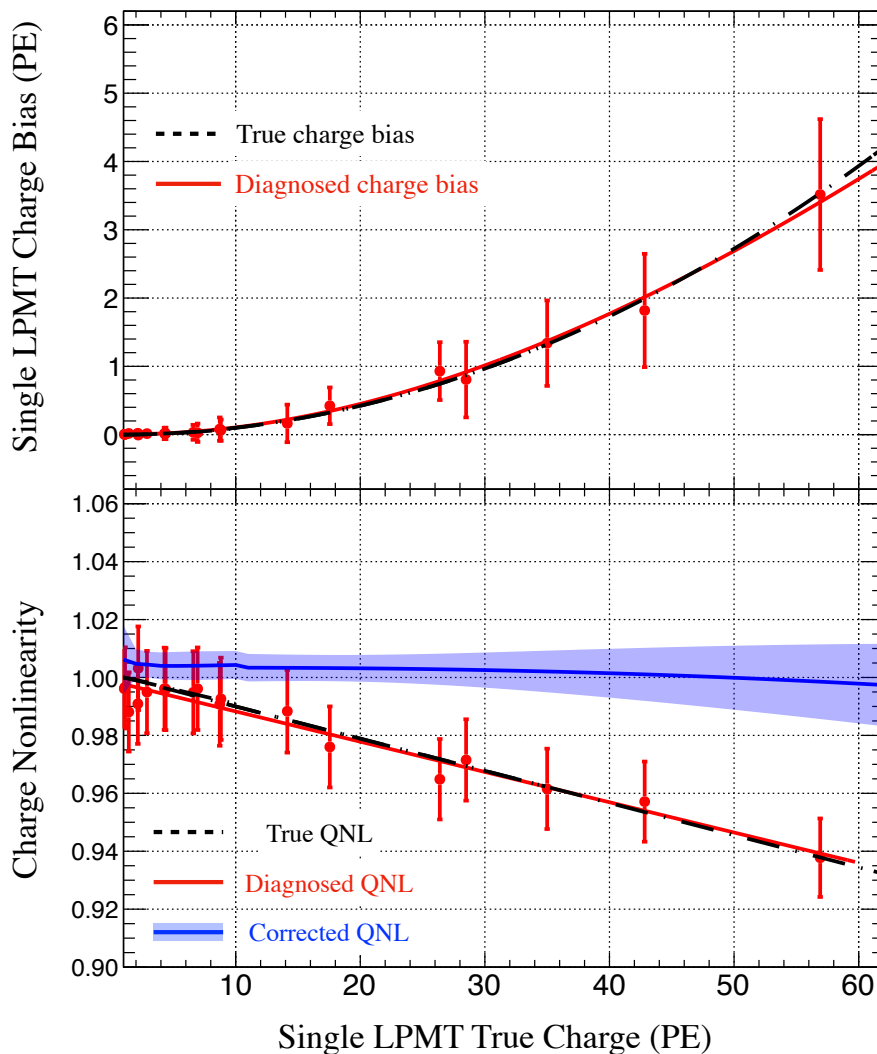


Figure 5.13 – DCC-gamma performance under the assumption of a $\sim 10\%$ QNL with the form of Eq.(5.5). The upper figure is the LPMT charge bias caused by the QNL defined as a function of the true charge. The dashed black curve corresponds to the true charge bias, and the solid red curve corresponds to the diagnosed charge bias. The lower figure is the channel-wise QNL. The y-axis is the reconstructed charge (calibrated or uncalibrated) over the true charge. The dashed black curve corresponds to the assumed $\sim 10\%$ QNL induced by reactor neutrino signals. The solid red curve corresponds to the diagnosed QNL through DCC-gamma. The solid blue curve corresponds to the residual QNL after the DCC-gamma calibration.

5.2.3 Advantages and Challenges

The advantage of DCC-gamma is that the reactor neutrino signal induced QNL can be effectively calibrated. It overcomes the time profile challenge that remains in the DCC-laser. However, the limitation of DCC-gamma makes it challenging to achieve a comprehensive calibration by itself alone. The challenges can be summarized in the following three aspects.

(1.) Unlike DCC-laser which can perform a QNL calibration for each channel of LPMT respectively, it is expected to be extremely time consuming and difficult to calibrate every channel of LPMT with DCC-gamma. Because it requires potentially thousands of times (even much beyond this number) data-taking with high statistics. If DCC-gamma can only be done for several channels of LPMT through, e.g. one dimension source position scanning, it implies that a lot of channels can not be calibrated accurately.

To illustrate the potential importance of calibrating every channel, an assumption can be made in the following way: one channel of LPMT, noted as channel 1, suffers the QNL at 10% level of Eq.(5.5) (dashed blue curve in Fig.5.14). And the channel 1 is reachable by DCC-gamma, thus the QNL can be calibrated, shown as the blue curve in Fig.5.14. However, another channel not reachable by DCC-gamma, noted as channel 2, could suffer a different QNL, e.g. 15% level shown as the dashed black curve in Fig.5.14, under the following model:

$$\frac{Q_{rec}}{Q_{true}} = (3.23 \cdot 10^{-5}d - 1.74 \cdot 10^{-3})Q_{true} - 3.23 \cdot 10^{-5} \cdot d + 1.00174. \quad (5.6)$$

If these two channels are, a priori, wrongly considered to be identical, and the obtained correction from channel 1 is applied to channel 2, then there will be a large bias for the calibration of channel 2, as illustrated by the solid black curve in Fig.5.14. As explained previously, the channel-to-channel difference may come from the PMTs, electronics, etc., and it is difficult to precisely know a priori. For channel-wise targeted calibration, it should have the capability to cover every channel. Even though the channel dependence might be eventually not significant, at least a validation is still necessary and useful.

(2.) As mentioned in Sec.5.2.2, the C_2 correction can bring the ambiguity between the NU and the QNL. This map need to be carefully considered in the experiment in order to minimize this ambiguity and maximize the isolation of the QNL.

(3.) By using the current designed radioactive sources at JUNO [174], the 1~100 PE charge detection range can not be fully covered. As illustrated in Fig.5.13, this approach can reach up to ~ 60 PE when using the radioactive source up to 8 MeV^1 . From Tab.4.1, it can be extracted that more than 99% of the charge for the reactor neutrino events will be detection in terms of less than 50 PE at single channel of LPMT, implying that the calibration capability up to 50 PE can cover more than 99% of the reactor neutrino signals. Therefore the current radioactive source design does not incur a limitation for DCC-gamma.

1. Neutron capture on iron emitting $\sim 8 \text{ MeV}$ gamma is possibly the highest energy of the artificial radioactive calibration source at JUNO

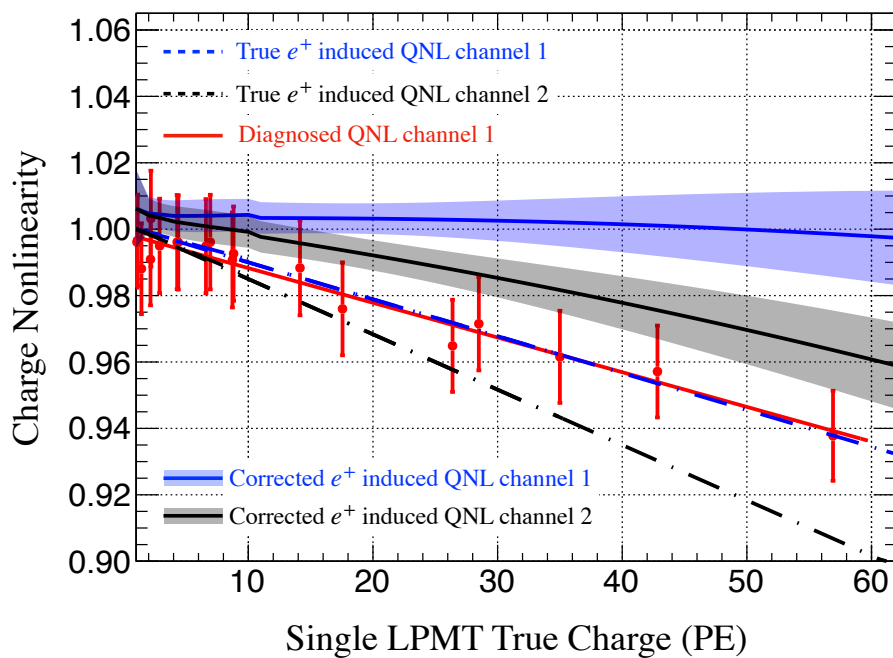


Figure 5.14 – Illustration of DCC-gamma challenge for calibrating two channels of which one is not reachable. For channel 1, the reactor neutrino signal induces a QNL at 10% level in the form of Eq.(5.5) (dashed blue curve). Channel 1 can be calibrated through DCC-gamma. The diagnosed QNL for channel 1 is shown as the solid red curve, and the corresponding corrected QNL is shown as the solid blue curve. For channel 2, the reactor neutrino prompt signal induces a QNL at 15% level in the form of Eq.(5.6) (dashed black curve). Channel 2 is not reachable by DCC-gamma if only a few source positions are scanned. By applying the DCC-gamma correction got with channel 1 to channel 2, the calibration of channel 2 is then biased, shown as the solid black curve.

5.2.4 Implications on Single Calorimetry

The success of dealing with the scanning position for the QNL calibration has not only significance on the Dual Calorimetry at JUNO, but also can be useful for the single calorimetry. If a detector is designed with a single PMT system, by moving the calibration source towards one direction inside the detector, e.g. from the detector center to the detector edge, there will be some PMTs at high illumination and also some PMTs at low illumination due to the optical acceptance. If the PMTs at low illumination enters a charge linear regime, such as the single PE counting regime, then it can be used as the linear reference for the high illumination PMTs. It is conceptionally possible to divide the single PMT system (i.e. single calorimetry) effectively to two PMT systems (i.e. mimic the dual calorimetry) according to the robustness of charge detection. However, the experimental implementation depends on the detector configuration, and this thesis will not expand the discussion.

Such an approach might be helpful to control the charge response for a single calorimetry detector, and the methodology should be similar to Sec.5.2.2 experiencing the same advantages and challenges as explained in Sec.5.2.3.

5.3 Dual Calorimetry Calibration Strategy and Performance

As mentioned previously, the QNL is typically charge (i.e. energy and position), time profile (i.e. position and particle) and channel dependent. For a comprehensive QNL calibration for JUNO reactor neutrino physics, the DCC should calibrate the potential QNL caused by the reactor neutrino signals for every channel of LPMT. As explained in Sec.5.1, DCC-laser can effectively cover the charge dependence and channel dependence, while it is expected to suffer from the time profile dependence of the UV laser. Also as explained in Sec.5.2, DCC-gamma can cover the time profile dependence, and largely cover the charge dependence, while it is expected to suffer from an incapability to calibrate every channel of LPMT.

These two methods have complementary advantages. So, by combining these two methods as one calibration with two stages, all the three aspects of dependence in the QNL can be well treated. Thus it is supposed to yield a comprehensive QNL calibration strategy for JUNO reactor neutrino signals as explained next.

5.3.1 Dual Calorimetry Calibration First Stage

The first stage (DCC-I) is considered to deploy the DCC-laser approach to characterize and calibrate the potential QNL (the "laser" related QNL) for each channel of LPMT respectively. The methodology is described in Sec.5.2.2. The UV laser source can be always kept at the detector center. The laser intensity should be tuned from ~ 1 MeV to ~ 1.5 GeV in order to cover the full charge detection range of reactor neutrinos.

5.3.2 Dual Calorimetry Calibration Second Stage

The second stage (DCC-II) is based on the DCC-gamma approach. By scanning the source position along the vertical diametral direction, the DCC-gamma can be applied to several channels of LPMT that locate at the top and the bottom of the detector. If time allowed, more channels of LPMT can be calibrated by scanning more source positions. In fact these channels that are calibrated through DCC-gamma can also be calibrated by DCC-laser. Thus the difference between the two calibrations for these channels can be considered as the second stage calibration for every channel of LPMT.

To be brief, the second stage generalizes the DCC-gamma calibration information got from several channels to every channel of LPMT. The reason for this generalization is that the difference between the two calibrations for different channels should contain a lot of common effects since it is dominated by the time profile dependent effect. And the time profile dependence is mainly related to the LS intrinsic property, which is common for every channel.

However, some subtle channel dependent effects may still exist on the difference between the two calibrations for different channels, which depends on the actual channel-wise hardware characterization and performance. These subtle effects are supposed to be compromised through the following treatment:

- 1.) The most representative channels of LPMT can be selected to be covered by the two calibrations (i.e. median performance LPMTs for both MCP-PMT and dynode-PMT). It imposes some requirements on the PMT installation, e.g. to install these most representative LPMTs at the top and the bottom of the detector.

- 2.) The differences between the DCC-laser and DCC-gamma of all the reachable channels can be taken the average, thus being further representative.

5.3.3 Performance

Under the two stages DCC strategy proposed above, the charge, time profile and channel dependences are all largely under control. Thus the potential QNL related to the reactor neutrino signals can be effectively calibrated for every channel of LPMT.

To illustrate the performance of the two stages calibration, two channels are considered: channel 1 and channel 2 suffer the reactor neutrino signal induced QNL differently at $\sim 10\%$ (Eq.(5.5)) and $\sim 15\%$ (Eq.(5.6)) respectively, shown as the dashed blue and dashed black curves in Fig.5.15. While, channel 1 is reachable by both DCC-laser and DCC-gamma, channel 2 is only reachable by DCC-laser. By applying the two stages DCC, the QNL control for these two channels can be improved significantly (better than 3 times), shown as the solid blue and black curves respectively in Fig.5.15.

The aforementioned example of two channels calibration can be generalized for every channel, so it indicates the capability of the two stages DCC strategy for the entire LPMT calorimetry QNL control. Through the direct QNL calibration, the energy control including the energy scale and the energy resolution control can be improved, which will be discussed in detail in Chapter 6.

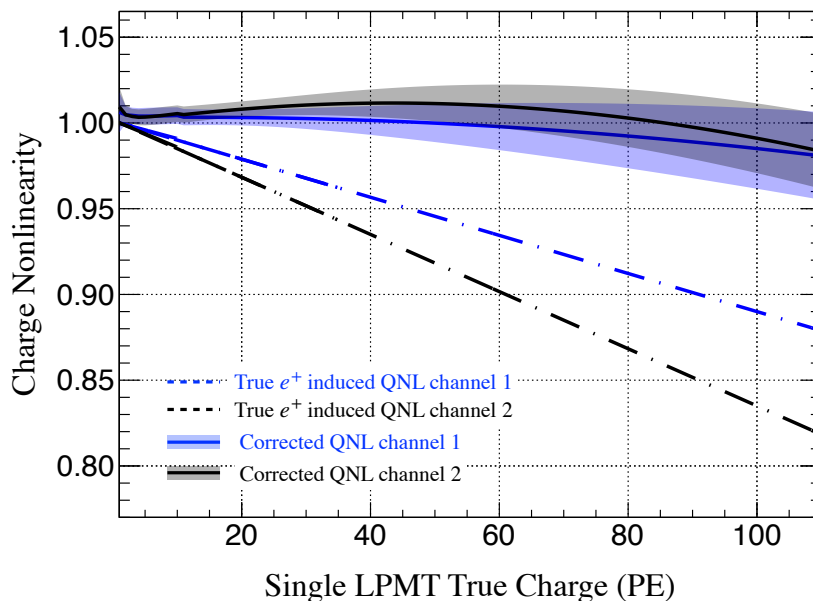


Figure 5.15 – DCC two stages strategy performance. Channel 1 and channel 2 suffer different reactor neutrino (IBD e^+) induced QNL at $\sim 10\%$ level as the dashed blue curve (Eq.(5.5)) and at $\sim 15\%$ level as the dashed black curve (Eq.(5.6)) respectively. Channel 1 is reachable both for DCC-laser and DCC-gamma. Channel 2 is only reachable for DCC-laser. The solid blue and solid black curves are the residual QNL after the application of the two stages DCC for channel 1 and channel 2 respectively. The two stages DCC can improve significantly the QNL control for the two channels, thus indicating the capability of the QNL calibration for every channel of LPMT.

5.4 SPMT in Dual Calorimetry Calibration

In the previous sections, the DCC methodology and strategy exhibits great potential for the QNL control for JUNO. From the instrumentation point of view, the most critical requirement of DCC is the charge linearity of the SPMT readout. Indeed, the initial design goal is to have a robust charge linear SPMT readout.

The key feature to ensure the linearity of the SPMT is its small size. The small size makes the SPMT illumination to be low enough such that the charge measurement can be done through PE counting. Unlike the charge integration (including waveform reconstruction) whose performance is affected by the pile-up, the electronic noise, the overshoot, the integration time window, etc., the PE counting is based on the fact that the illumination of the PMT is very low, such that the single PE hit is absolutely dominating. Therefore, by just counting how many times the PMT is got hit (or triggered in the readout), the charge is then estimated, since these hits are essentially single PEs. The PE counting can largely get rid of the effects in the charge integration by construction. Thus by introducing the SPMT, the PE counting based charge estimator is enabled for JUNO, which is independent and complementary to the LPMT charge integration based estimator.

In addition to the PE counting, the SPMT readout also records the analog charge information of the signal pulse for helping the multi-PE detection. The charge information will be independently calibrated and provide complementary redundancy for the PE counting.

The SPMT is considered to be charge linear in the DCC previously based on the PE counting concept, while illustrating the calibration methodology. This section aims to demonstrate the robustness of the charge linearity of the SPMT in DCC by using the PE counting technique, especially the Poisson-zero PE counting technique (explained next). The most important factor for PE counting is claimed to be the pedestal and single PE discrimination (i.e the threshold effect) and it is also addressed in this section.

5.4.1 Direct PE Counting in SPMT Readout

The direct PE counting can be simply defined as follows: a threshold can be set between the pedestal and the single PE; once the PMT is hit and the signal pulse passes the threshold, it will be counted digitally as a single PE regardless of the exact number of PEs in this hit.

For the SPMT (3-inch) at JUNO, more than 95% charge are detected in terms of single PE for the reactor neutrino events. So the robustness of PE counting can be largely (> 95% level) ensured for the reactor neutrino detection. The rest < 5% charge in terms of multi-PE can be measured redundantly through the analog charge response upon relevant calibrations.

However the DCC, especially the DCC-laser, goes beyond the direct PE counting regime. Because in the DCC-laser approach the laser intensity needs to be tuned up to 1.5 GeV in order to cover the reactor neutrino signal range, each SPMT mean illumination goes up to 2 PE. For DCC-gamma, the most lightened SPMT can also reach up to ~ 2 PE level. For instance, if the mean illumination is ~ 2 PE, the direct PE counting will introduce at worst $\sim 60\%$ bias for the estimated charge, as shown in Fig.5.16. Here the worst scenario is considered, i.e. one event is considered only as either one single PE or zero.

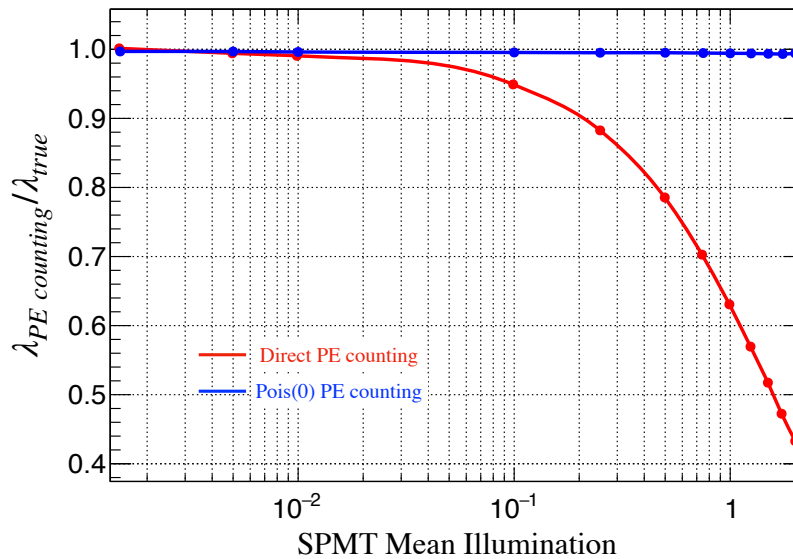


Figure 5.16 – SPMT QNL control through PE counting. The SPMT QNL is shown in terms of the mean illumination for one channel. The y-axis is the ratio between the mean illumination with PE counting and the true mean illumination. The red curve represents the direct PE counting through which a large (at worst $\sim 60\%$) bias exists. The blue curve represents the $Pois(0)$ PE counting through which the SPMT QNL can be controlled within 0.5%. The SPMT charge response is simulated with 30% PMT charge resolution, 0.05 PE pedestal width and a threshold at 0.25 PE.

5.4.2 Poisson Zero PE Counting in the SPMT Readout

The direct PE counting is challenging for the SPMT QNL control in DCC, as just explained in the previous section. In order to still preserve the PE counting estimator and meanwhile ensure the charge linearity of the SPMT in DCC, the technique known as Poisson zero ($Pois(0)$) PE counting, can be applied. This is a well known technique, and an application can be found in [203] and many other scenarios. It is based on the feature of Poisson statistics and currently can only be used for the calibration purpose (e.g. DCC).

Methodology

The methodology of the $Pois(0)$ PE counting can be understood as follows.

For a calibration data sample, i.e. the calibration source with a certain energy emission is placed at a certain position inside the detector for the data taking within a certain time period. Through the direct PE counting, the number of digital hits for one channel can be known, noted as N_{hit} . Regardless of the exact number of PEs in one hit with one event, it is always counted as one hit. The total number of events N_{total} in this calibration data sample can be obtained from the event reconstruction by using the whole detector information. Thus the number of "zero-hit" events can be calculated for this single channel as $N_{zero} = N_{total} - N_{hit}$.

For N_{total} calibration events, the number of PEs collected by one channel follows the Poisson statistics:

$$P(k) = \frac{\lambda^k e^{-\lambda}}{k!} \quad (5.7)$$

where P is the probability of one PMT to be hit by k PEs and λ represents the mean value of PE distribution (i.e. mean illumination).

The Poisson mean value can be deduced from the direct PE counting observables N_{zero} and N_{total} , given by:

$$\lambda = -\ln\left(\frac{N_{zero}}{N_{total}}\right). \quad (5.8)$$

This is the so called *Pois(0)* PE counting in the calibration scheme. Such a technique requires that the N_{zero} is not zero indicating low illumination which is exactly the SPMT working mode. The calculated Poisson mean can be used to represent the PMT mean illumination.

Performance in DCC

Based on the *Pois(0)* PE counting, the SPMT QNL can be controlled within 0.5% in the $10^{-3} \sim 2$ PE mean illumination range (equivalent to 1~10 PE channel-wise charge detection range), as shown in Fig.5.16. This shows a significant improvement compared to the direct PE counting and ensures the SPMT linearity in the DCC scheme.

In order to illustrate the performance in the context of the DCC, the LPMT QNL control through DCC is shown in Fig. 5.17 for the case of 1.) perfect charge linear response of SPMT and 2.) *Pois(0)* PE counting in SPMT. It demonstrates that the *Pois(0)* PE counting can make SPMT to be a robust charge linear reference, thus ensuring the DCC performance.

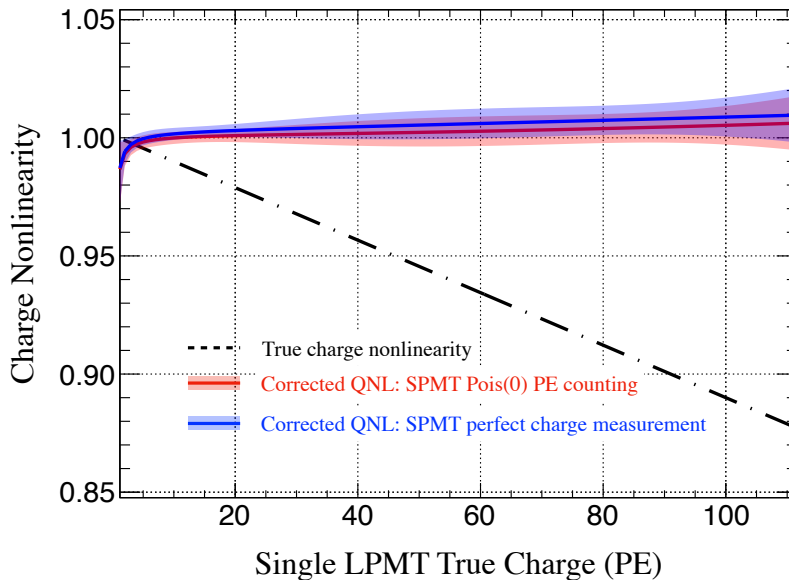


Figure 5.17 – LPMT QNL control through DCC with the *Pois(0)* PE counting. The dashed black curve corresponds to the assumed $\sim 10\%$ QNL of the LPMT. The solid blue curve corresponds to the corrected QNL through DCC, assuming a perfect charge linear response of SPMT. The solid red curve corresponds to the corrected QNL through DCC by performing the *Pois(0)* PE counting for SPMT ensuring the linearity of the SPMT.

5.4.3 Threshold Effect

The most important factor affecting the PE counting including the $Pois(0)$ PE counting is the pedestal and single PE discrimination, also known as the threshold effect. Since the PE counting works at low PMT illumination regime, the noise events (pedestal) may significantly affect the detection of signal events (mainly single PE). Therefore the threshold has direct and critical impact on the SPMT charge estimation and QNL control.

There are three major aspects regarding the pedestal and single PE discrimination, namely the pedestal width, the single PE width and the threshold optimization.

For the purpose of investigating these three aspects for the SPMT relative QNL control in the $Pois(0)$ PE counting method, the following assumptions are made.

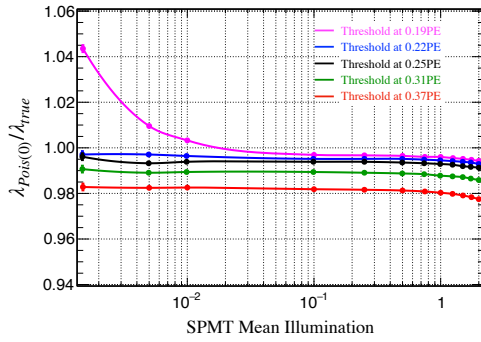
- **Assumption (1.)** : The pedestal and single PE distributions are assumed to have the width of 0.05 PE and 0.3 PE respectively.

Both the pedestal width and the single PE width are considered to be optimistic under assumption (1.), given the preliminary testing results of the SPMT instrumentation and electronics [170, 204]. By scanning the threshold position, the SPMT charge response based on the $Pois(0)$ PE counting is shown in Fig.5.18a. Under assumption (1.), a threshold around 0.22 PE gives the best SPMT QNL control ($<0.5\%$). By considering the optimized threshold to be ~ 0.22 PE, it is noticed that a higher threshold setting (relative to the optimized one) generates much less relative QNL than a lower threshold setting, as it can be seen in Fig.5.18a. For instance, when the threshold is set slightly lower, such as 0.19 PE, the SPMT QNL can be up to 5%. When the threshold is set quite high, such as 0.37 PE, the relative SPMT QNL can still be controlled within 1%. But there will be an offset ($\sim 2\%$) in terms of the absolute charge response (i.e. $\lambda_{Pois(0)}/\lambda_{true} \sim 0.98$ instead of 1 in Fig.5.18a) due to the high threshold setting. This offset is irrelevant to the DCC approach and performance, since only the relative SPMT QNL matters for DCC. However a high threshold will affect the absolute charge estimation, hence the energy estimation, which is not ideal for SPMT physics measurements (e.g. solar oscillation parameters).

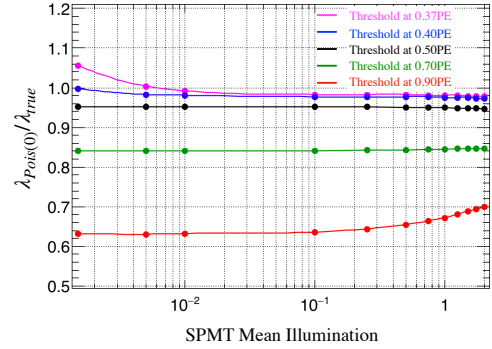
- **Assumption (2.)** : The pedestal and single PE distributions are assumed to have the width of 0.1 PE and 0.3 PE respectively.
- **Assumption (3.)** : The pedestal and single PE distributions are assumed to have the width of 0.05 PE and 0.4 PE respectively.
- **Assumption (4.)** : The pedestal and single PE distributions are assumed to have the width of 0.1 PE and 0.4 PE respectively.

Under assumption (2.), (3.) and (4.) the pedestal width and single PE width are considered more conservative compared to assumption (1.). By scanning the threshold position, the SPMT QNL control through $Pois(0)$ PE counting is shown respectively in Fig.5.18b, 5.18c, 5.18d for these three cases.

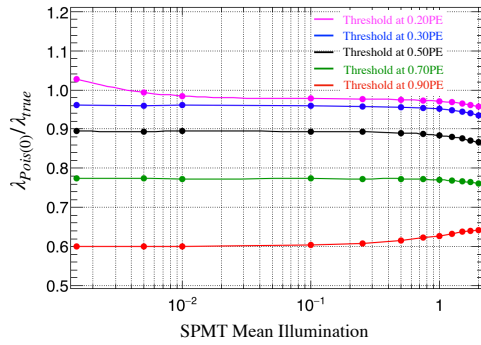
Under each of these three assumptions, it is challenging to ensure the linearity of SPMT while preserving the absolute charge response. But a relative high threshold (e.g. ~ 0.5 PE, even ~ 0.7 PE) can ensure a good relative linearity ($\sim 1\%$) for the SPMT charge response, even though there will be some light loss because of this high threshold setting. Here, the high threshold is compared to the optimized threshold (typically ~ 0.3 PE) which pursues the maximal pedestal and single PE separation. Again only the



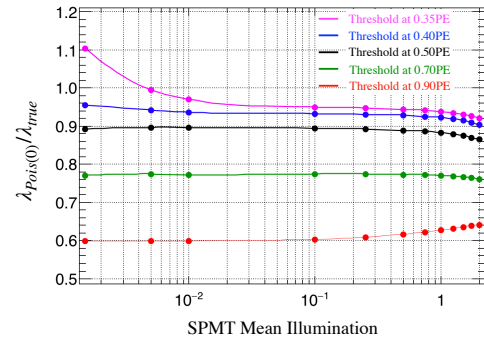
(a) Assumption (1.): the pedestal width is 0.05 PE, and the single PE width is 0.3 PE. The magenta, blue, black, green and red curves corresponds to the threshold setting at 0.19 PE, 0.22 PE, 0.25 PE, 0.31 PE and 0.37 PE respectively.



(b) Assumption (2.): the pedestal width is 0.1 PE, and the single PE width is 0.3 PE. The magenta, blue, black, green and red curves corresponds to the threshold setting at 0.37 PE, 0.4 PE, 0.5 PE, 0.7 PE and 0.9 PE respectively.



(c) Assumption (3.): the pedestal width is 0.05 PE, and the single PE width is 0.4 PE. The magenta, blue, black, green and red curves corresponds to the threshold setting at 0.2 PE, 0.3 PE, 0.5 PE, 0.7 PE and 0.9 PE respectively.



(d) Assumption (4.): the pedestal width is 0.1 PE, and the single PE width is 0.4 PE. The magenta, blue, black, green and red curves corresponds to the threshold setting at 0.35 PE, 0.4 PE, 0.5 PE, 0.7 PE and 0.9 PE respectively.

Figure 5.18 – SPMT QNL (channel-wise) control through Poisson counting under assumption (1.), (2.), (3.) and (4.) respectively. The SPMT QNL is shown in terms of the mean illumination. The y-axis is the ratio of the mean illumination based on $Pois(0)$ PE counting to the true mean illumination. λ_{true} represents the perfect absolute linear charge response of the SPMT. $\lambda_{Pois(0)}$ is the charge response based on $Pois(0)$ PE counting method. The SPMT QNL can be well controlled within 1% under all these four assumptions covering largely the potential situations.

relative QNL control of SPMT matters for the DCC, thus the high threshold setting is acceptable under these assumptions.

To summarize, the $Pois(0)$ PE counting is not going to investigate the absolute charge response if the threshold is set high (e.g. 0.5 PE). The advantage is that, consequently, a relative high threshold can ensure the relative linearity for the SPMT charge response in the $Pois(0)$ PE counting regime, thus ensuring the DCC performance.

In summary, this section demonstrates that the SPMT charge linearity can be ensured in the context of DCC by applying the $Pois(0)$ PE counting technique. The threshold effect is recognized as the most critical factor for the PE counting. However, as for the role of the SPMT in DCC, only the relative SPMT QNL control is required, and the $Pois(0)$ PE counting technique can provide a robust relative linear charge response for the SPMT, effectively regardless of the threshold effect. The statement above makes sense only for the SPMT in the DCC regime. It needs to be highlighted that the threshold effect remains critical and is worth for further investigation for other SPMT physics topics, such as the solar oscillation parameters measurement, since the $Pois(0)$ PE counting technique can not be used in these physics cases. The actual hardware performance of the SPMT readout electronics for properly performing the PE counting is vital and will be addressed in Chapter 7.

5.5 Dual Calorimetry Calibration Systematics

This section focuses on the major systematic effects of DCC. Most of them apply to both DCC-laser and DCC-gamma.

5.5.1 The Poisson Statistics Effect

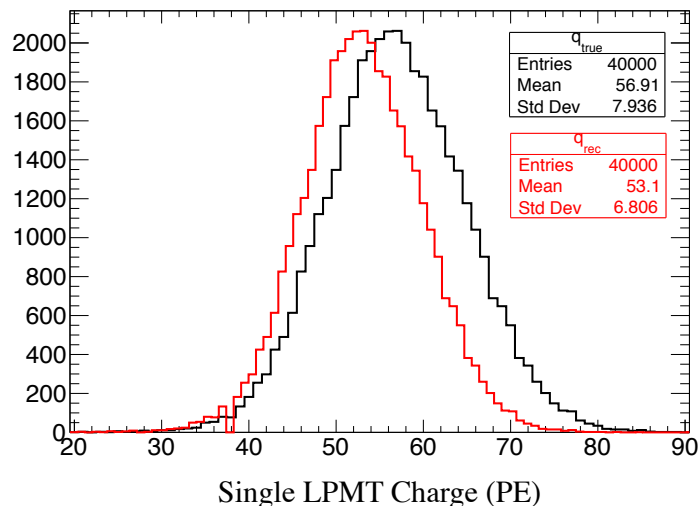


Figure 5.19 – Unbiased and biased Poisson distributions. For 40,000 calibration events of 8 MeV (electron) energy deposition at 17.2 m away from the detector center in simulation, let's focus on the photons (PEs) collected at one single LPMT (close to the calibration source). If the charge response is linear, the measured charge q_{true} follows the unbiased (by QNL) Poisson distribution shown as the black histogram with the $\lambda_{lin} \sim 57$ PE. If the charge response is not linear ($\sim 10\%$ over 100 PE), the measured charge q_{rec} follows a biased (by QNL) Poisson distribution with $\lambda_{non-lin} \sim 53$ PE.

The Poisson statistics effect here specifies that the LS photons collected at the PMT for a certain energy deposition at a certain position, in general, follows the Poisson distribution. When these photons are converted to PEs and measured as charge, by assuming that the PMT has a negligible charge resolution, the measured charges then remain a Poisson distribution.

By assuming a simple QNL model, i.e. first order polynomial, as follows:

$$\frac{Q_{rec}}{Q_{true}} = aQ_{true} + b, \quad (5.9)$$

where Q_{true} and Q_{rec} are the true charge and reconstructed charge respectively, a and b are the constant coefficients, and the dimensions of a and b are chosen to make the equation to be dimensionless in right side. The QNL model can also be given by:

$$Q_{rec} = aQ_{true}^2 + bQ_{true}. \quad (5.10)$$

The QNL calibration uses the observable Poisson mean (λ) to investigate the charge (Q). One hypothesis test can be proposed to investigate the systematic effect of the Poisson statistics:

The introduced QNL (Eq.(5.10)) in the charge measurement is exactly the observable QNL through the Poisson mean value.

Under the simple QNL model of Eq.(5.10), if the charge response is perfect linear (i.e. $a = 1, b = 0$), the measured charge for each event denoted as q_{rec} is the true charge q_{true} ($=q_{rec}$). The q_{true} follows a Poisson statistics with the mean value of λ_{lin} in the linear case as the example shown in Fig.5.19. The λ_{lin} is used to investigate the charge Q_{true} (or Q_{rec}), and in this perfect zero QNL case, these quantities are equal:

$$\lambda_{lin} = Q_{true} = Q_{rec}. \quad (5.11)$$

If the charge response is not linear and follows the model of Eq.(5.10), the measured charge for each event q_{rec} ($\neq q_{true}$) follows a biased Poisson distribution, and its mean value is noted as $\lambda_{non-lin}$ as the example shown in Fig.5.19. Each value of q_{rec} has a corresponding q_{true} value according to the model of Eq.(5.10). And the probability of measuring q_{rec} in the biased Poisson distribution is the same as the probability of measuring the corresponding q_{true} in the unbiased Poisson statistics ($Pois(\lambda_{lin})$). Thus the relation between $\lambda_{non-lin}$ and λ_{lin} can be got from the following derivation:

$$\begin{aligned} \lambda_{non-lin} &= \sum q_{rec} \times Pois(\lambda_{lin}) \\ &= \sum (aq_{true}^2 + bq_{true}) \times Pois(\lambda_{lin}) \\ &= \sum \left(\frac{\lambda_{lin}^{q_{true}} e^{-\lambda_{lin}}}{q_{true}!} \times q_{true} \times aq_{true} \right) + b\lambda_{lin} \\ &= \sum \left[\frac{\lambda_{lin}^{q_{true}-1} e^{-\lambda_{lin}}}{(q_{true}-1)!} \times a(q_{true}-1+1) \times \lambda_{lin} \right] + b\lambda_{lin} \\ &= a\lambda_{lin}^2 + a\lambda_{lin} + b\lambda_{lin} \\ &= aQ_{true}^2 + aQ_{true} + bQ_{true}, \end{aligned} \quad (5.12)$$

where the last step uses the relation in Eq.(5.11).

If the hypothesis is true, $\lambda_{non-lin}$ should obey exactly the introduced QNL model of Eq.(5.10) as:

$$\lambda_{non-lin}^{hyp} = aQ_{true}^2 + bQ_{true}. \quad (5.13)$$

However, the fact is that $\lambda_{non-lin}$ follows the Eq.(5.12) being different from Eq.(5.13), thus the hypothesis is incorrect. The difference between the fact Eq.(5.12) and the hypothesis Eq.(5.13) is the systematic effect of the Poisson statistics, given by:

$$\lambda_{non-lin} - \lambda_{non-lin}^{hyp} = aQ_{true}. \quad (5.14)$$

It means that by using the Poisson mean value (λ) of the charge distribution to investigate the charge (Q), if the charge response is nonlinear as Eq.(5.10), there will always be a bias as large as aQ_{true} for the actual measured charge.

For the measured (or diagnosed) QNL with the Poisson mean value, i.e the ratio between the measured Poisson mean λ_{rec} and the true Poisson mean λ_{true} , the bias caused by the Poisson statistics effect is:

$$\frac{\lambda_{rec}}{\lambda_{true}} - \frac{Q_{rec}}{Q_{true}} = a, \quad (5.15)$$

where $\frac{\lambda_{rec}}{\lambda_{true}} = \frac{\lambda_{non-lin}}{\lambda_{lin}}$.

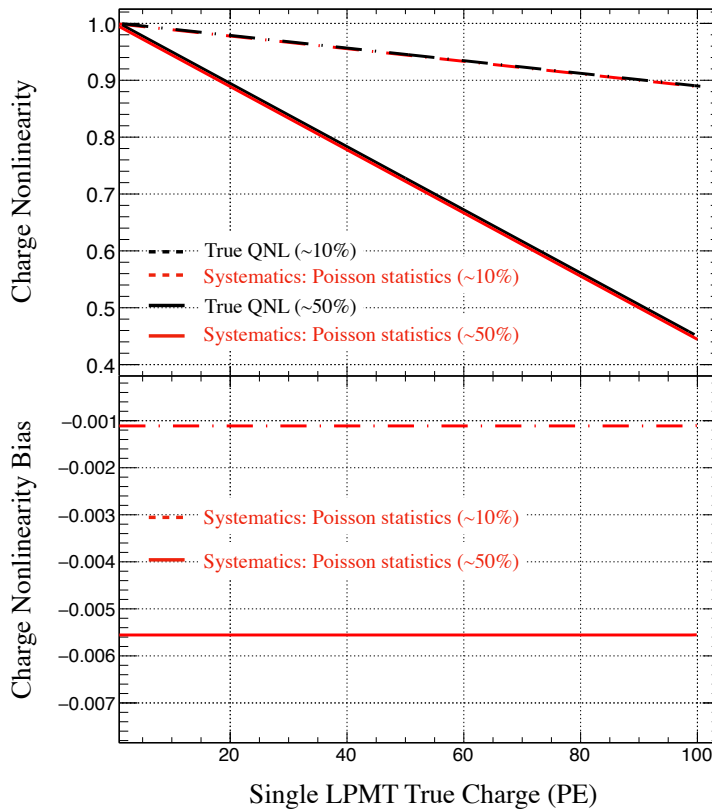


Figure 5.20 – Poisson statistics effect. The upper figure represents the QNL defined as the measured (or reconstructed) charge over the true charge. The dashed black curve corresponds to a $\sim 10\%$ true QNL over 100 PE. Because of the Poisson statistics effect, this measured QNL is biased by $\sim 0.11\%$, as the dashed red curve. By assuming a $\sim 50\%$ true QNL over 100 PE as the solid black curve, the Poisson statistics effect will bias the measured QNL by $\sim 0.56\%$, as the solid red curve. The lower figure represents the difference between the true QNL and the Poisson effect biased QNL. The dashed red line and the solid red line corresponds to $\sim 10\%$ and $\sim 50\%$ cases respectively.

If the QNL model is defined with $a = -0.01/9$ and $b = 9.01/9$, the systematical bias from the Poisson statistics effect is $\sim 0.11\%$, illustrated as the dashed red curve in both upper and lower panels of Fig.5.20. This bias is proportional to the true QNL. If the QNL model is defined with $a = -0.05/9$ and $b = 9.05/9$, the bias is $\sim 0.56\%$, illustrated as the solid red curve in both upper and lower panels of Fig.5.20.

When the QNL model is more complicated, such as a parabola model or an exponential model, the bias caused by the Poisson statistics effect will still exist and can also be estimated in a similar way. The physics reason for this bias can be understood as follows: the QNL will distort the Poisson distribution (in shape), and then bias the Poisson mean value; the Poisson mean value does not follow the true QNL model (channel-wise); when the charge is investigated with the Poisson mean value in calibration, eventually there will be a bias for the diagnosed QNL.

5.5.2 The PMT Charge Resolution Effect

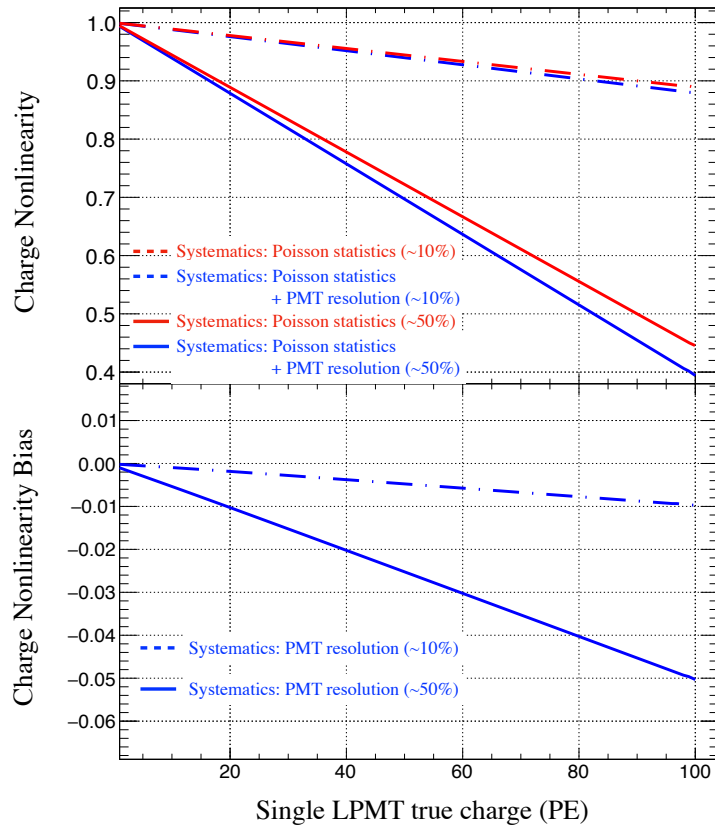


Figure 5.21 – PMT charge resolution effect. The upper figure represents the QNL defined as the measured (or reconstructed) charge over the true charge as a function of the true charge. The dashed red curve corresponds to the Poisson effect biased QNL for a $\sim 10\%$ true QNL case. Because of the PMT charge resolution effect, this QNL is further biased up to $\sim 1\%$, as the dashed blue curve. By assuming a $\sim 50\%$ true QNL, the Poisson statistics effect will bias the QNL as the solid red curve. And the PMT charge resolution effect will further bias the QNL up to $\sim 5\%$, as the solid blue curve. The lower figure represents the QNL bias caused by the pure PMT charge resolution effect. The dashed blue line and the solid blue line correspond to $\sim 10\%$ and $\sim 50\%$ cases respectively.

When the PEs hit the first dynode¹, the generated secondary electrons can be assumed to follow the Poisson statistics [205]. The amplification process through the dynodes can also be assumed to follow the Poisson statistics. For example, if all these hits are single photoelectrons at the first dynode, the collected electrons at the anode will follow several stages superimposed Poisson statistics, which is approximately a Gaussian distribution according to the *Central Limit Theorem*. The width of the Gaussian distribution represents the PMT charge resolution.

Since these are, in essence, several stages of Poisson statistics, the bias introduced by the PMT charge resolution will follow the similar mathematical derivation described in Sec.5.5.1. Due to the complexity of the analytical derivation, the numerical calculation is used for illustrating the PMT charge resolution effect. By assuming that the QNL is defined with $a = -0.01/9$ and $b = 9.01/9$ in Eq.(5.9) and the PMT charge resolution is about 30%, the bias induced by the PMT charge resolution is up to $\sim 1\%$, as shown in Fig.5.21.

This bias is also proportional to the true QNL. If the QNL is defined with $a = -0.05/9$ and $b = 9.05/9$ in Eq.(5.9), the bias caused by the PMT charge resolution is as large as $\sim 5\%$, as shown in Fig.5.21.

5.5.3 The LPMT Effective Threshold Effect

The threshold effect (i.e. the pedestal and single PE discrimination) will affect not only the SPMT as detailed in Sec.5.4.3, but also the LPMT in DCC at the low illumination region.

For the LPMT, as the signal pulse waveform will be recorded, the threshold for the LPMT can be understood as an effective threshold to separate the noise events and the signal events during the reconstruction. For instance, if the pedestal and the single PE can be totally separated for the LPMT, i.e. an ideal threshold setting, there will be no bias on the QNL, illustrated as the solid blue curves in Fig.5.22. If the threshold is set too low (compared to the ideal one) such that quite a lot of noise events are considered as single PE events, the QNL will be biased, illustrated as the dashed green curves in Fig.5.22. On the contrary, if the threshold is set too high such that quite a lot of single PE events are considered as noise events, the QNL will also be biased, illustrated as the solid green curves in Fig.5.22.

To conclude, the LPMT effective threshold effect could introduce systematic bias on the QNL at the low illumination region. This low illumination region is particularly important for establishing a response relation linear reference as detailed in Sec.5.1.2, and a careful study of the LPMT effective threshold setting is worth upon the PMT instrumentation and electronics performance. For the simulation results presented in this thesis, the LPMT effective threshold setting is always optimized in order to minimize this bias.

1. The dynode PMT is used for illustration here.

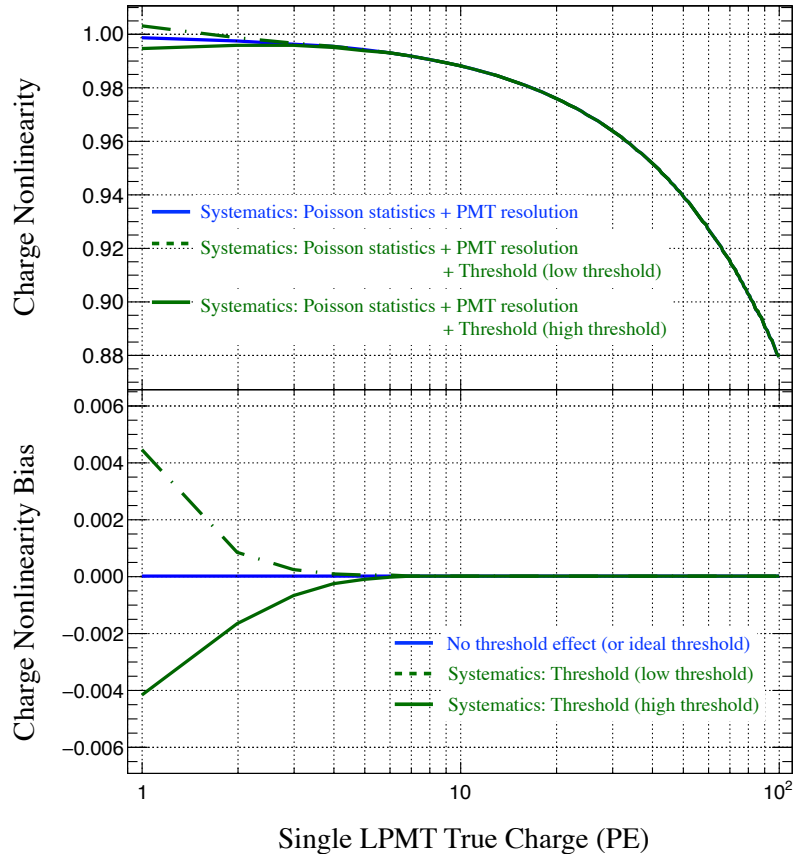


Figure 5.22 – LPMT effective threshold effect. The upper figure represents the QNL. The true QNL is assumed as $\sim 10\%$ over 100 PE. Under the following simulation condition: 30% PMT charge resolution and 0.05 PE pedestal width (the optimal threshold should be ~ 0.25 PE), if the pedestal and single PE can be perfectly discriminated (no threshold effect), there will be no bias for the QNL as the dashed blue curve. If the threshold is set too low (e.g. 0.1 PE), the bias generated by this effect is shown as the dashed green curve. If the threshold is set too high (e.g. 0.4 PE), the bias is shown as the solid green curve. The lower plot represents the pure QNL bias caused by this effect for low threshold (dashed green curve) and high threshold (solid green curve). The PMT charge resolution and pedestal width are considered optimistically, while the low threshold (0.1 PE) and high threshold (0.4 PE) are exaggerated in this figure.

5.5.4 DCC Capability with the SPMT QNL Control

The Pois(0) PE counting is demonstrated conceptually in Sec.5.4 to have the capability to ensure the relative charge linearity of the SPMT in DCC. The actual performance of the SPMT QNL control is worth for further investigation experimentally. This section aims to make some conservative assumptions to explore the limit of the SPMT QNL such that the SPMT could not provide any diagnosis information for the LPMT QNL.

Both the QNL model and the PMT mean illumination dynamic range matter for the QNL. For the overall QNL control, the SPMT gains a factor of 50 compared to the LPMT in terms of the dynamic range primarily owing to the fact that the SPMT is roughly 50 times smaller than the LPMT. Thus the other aspect, i.e. the QNL model, can be tuned in order to investigate the SPMT limit. By assuming a $\sim 10\%$ (over 100 PE) QNL model for the LPMT, four assumptions of the SPMT QNL model are made to investigate the corresponding performance of the DCC. These four assumptions are:

- (1.) The SPMT QNL model is the same as the LPMT
- (2.) The SPMT QNL model is 10 times worse the LPMT
- (3.) The SPMT QNL model is 30 times worse the LPMT
- (4.) The SPMT QNL model is 50 times worse than the LPMT

The corresponding calibration performance under these four assumptions are shown in Fig.5.23 respectively. According to these simulation results, even if the SPMT QNL model is 10 times worse than the LPMT, the LPMT QNL can still be largely corrected. If the SPMT QNL model is 50 times worse than the LPMT, then the DCC loses its capability to calibrate the LPMT QNL.

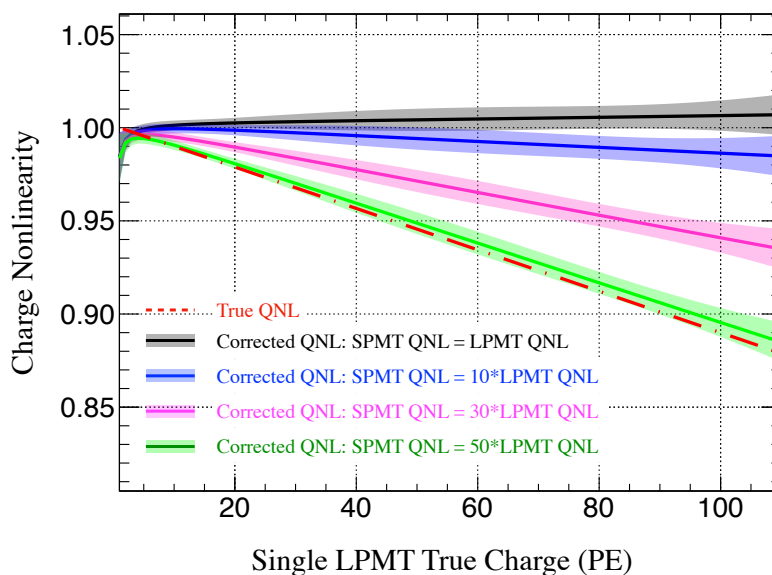


Figure 5.23 – SPMT charge QNL effect. The dashed red curve represents the assumed true LPMT QNL ($\sim 10\%$ over 100 PE). The black curve is the corrected QNL by assuming the SPMT having the same QNL model as the LPMT, i.e. assumption (1.). The blue, magenta and green curves are the corrected QNL by assuming the SPMT having respectively 10% times, 30% times and 50% times worse QNL model than the LPMT, i.e. assumption (2.), (3.) and (4.).

5.5.5 The Single LPMT NU Map Effect (C_2 Correction)

As presented in Sec.5.2.2, in order to achieve DCC-gamma, a single LPMT NU map need to be applied as a correction (C_2 correction) to the SPMT response. As the LPMT potentially suffers QNL, the single LPMT NU map could bring in, to some extent, the ambiguity between the QNL and NU, hence some systematic bias.

As illustrated in Fig.5.24, if this map can be free from the QNL, the corresponding calibration performance is shown as the blue curve; however, if this map (C_2 correction) suffers some QNL, e.g. $\sim 10\%$ over 100 PE, the calibration performance is shown as the black curve. There will be $\sim 1\%$ relative bias compared to the linear map case in this scenario.

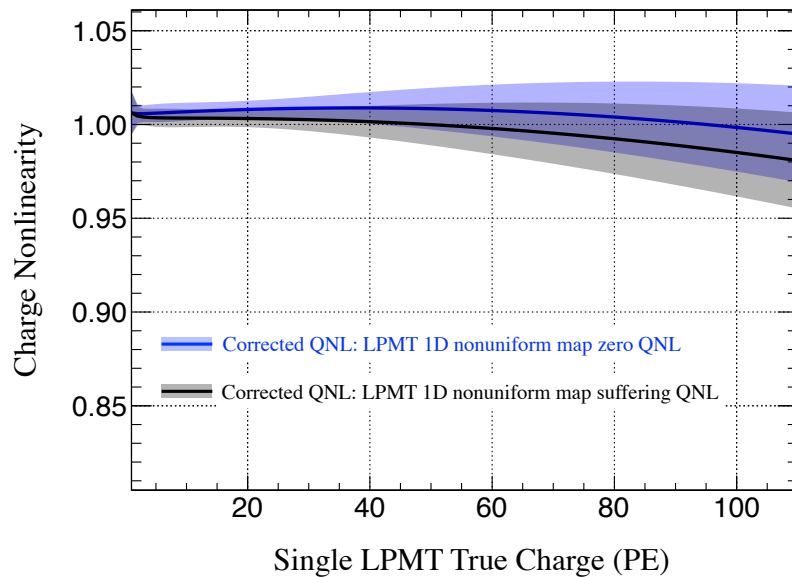


Figure 5.24 – The single LPMT NU map (C_2 correction) effect. The true QNL is assumed as $\sim 10\%$ over 100 PE. If the single LPMT NU map does not suffer QNL, the corrected QNL is shown as the blue curve. If the single LPMT NU map suffers the QNL ($\sim 10\%$), and this map is simulated with 1 MeV electrons, the corrected QNL is then biased by $\sim 1\%$, shown as the black curve.

5.5.6 Other Systematic Effects

There are also other systematic effects that could affect the DCC performance, such as the PMT dark noise and the response relation linear reference determination in Sec.5.1.2 and 5.2.2. For the dark noise, it is foreseen not to introduce systematic bias, thus being not addressed here. For the response relation linear reference determination, the key is to establish (or identify) a linear region in the actual response relation between the LPMT and the SPMT, as shown in Fig. 5.4, being the PE counting regime both for the LPMT and SPMT a possible criterion. And it is worth for a careful consideration according to the PMT characterization or the running of the detector since this linear region relies on the actual detector performance. As for the systematic effect from the calibration sources, i.e. UV laser source and radioactive sources, since the Dual Calorimetry is immune to the absolute source knowledge, these systematic effects are supposed not to fold in the DCC.

5.6 Summary and Outlook

In this chapter, two methodologies of the QNL calibration are elaborated for JUNO, i.e. DCC-laser and DCC-gamma. These two methods both are channel-wise implementations of the Dual Calorimetry and together they can form a comprehensive QNL calibration strategy for JUNO. It is demonstrated that the DCC can significantly correct the potential QNL of the LPMT. It has at least better than 3 times (up to 1 order of magnitude) improvement of the QNL control upon the assumed QNL configuration. Even though when starting with a pessimistic assumption, i.e. $\sim 50\%$ QNL in 1 \sim 100 PE range for the LPMT, the DCC is able to improve the QNL control by 1 order of magnitude.

One should notice that the DCC is a data-driven approach. In this chapter, several assumptions about the QNL are made in order to facilitate the study and illustration of the DCC methodology and performance. As a data-driven approach, the actual LPMT QNL should be diagnosed and calibrated through the DCC with the real data in the full detector configuration.

The prototype test can help to demonstrate the basic principle of DCC. But the results from prototype test could be not representative for the full detector configuration since the target QNL is about the reactor neutrino signals in the full detector configuration. Therefore it is necessary to perform the DCC on site once the detector is running.

The SPMT charge response is demonstrated to be linear through the $Pois(0)$ PE counting technique in DCC, which meets the designed goal. Therefore the SPMT can be considered as a robust charge linear reference for the LPMT in DCC.

The major systematic effects of DCC are studied and understood. These effects are illustrated in a simple manner in this chapter. If the systematics can be well controlled experimentally with data, it is conceptually possible to develop higher order calibration based on proportionality between the DCC performance and the true QNL. If the calibration precision is further required, it is worth to explore such higher order calibrations. This implies that the DCC could become a three stages calibration scheme, as compared the two stages scheme here proposed. However, data is a must to consider this necessity and evaluate the performance in realistic scenario.

This chapter presents the DCC performance at channel level in terms of the charge. As the detector energy estimator is the sum of the charge of all channels, the direct control of the channel-wise charge response will eventually reflect on the energy accuracy (energy scale) and energy precision (energy resolution) control. The impacts of the DCC on the energy control will be discussed in Chapter 6.

Chapter 6

Energy Control with Dual Calorimetry Calibration

As explained previously, the information of the neutrino MO and oscillation parameters is embedded in the reactor $\bar{\nu}_e$ energy spectrum at JUNO. The energy control, including both accuracy and precision, is vital for the high precision spectral shape measurement in order to extract the physics content including the MO, θ_{12} , Δm_{21}^2 and Δm_{31}^2 .

The energy accuracy here can be understood as the correctness of the reconstructed energy compared to the true deposited energy. The key is to define accurately the conversion relationship from the observable, i.e. the reconstructed charge, to the true deposited energy.

This conversion relationship is typically dominated by the response effects that are discussed in the previous chapters including the LS non-linearity (LSNL), the charge non-linearity (QNL), the position non-uniformity (NU) and the non-stability (NS). This conversion relationship is normally called the energy scale and can be defined as:

$$E_{dep} = Q_{PE} \times f_{PE/MeV} \times f_{QNL} \times f_{NU} \times f_{LSNL} \times f_{NS} \quad (6.1)$$

. The Q_{PE} is the direct observable charge in the unit of PE. The $f_{PE/MeV}$ is the absolute energy scale definition anchoring the charge (PE) to energy (MeV) conversion. The f_{QNL} can be understood as the convoluted channel-wise QNL effect at detector level (or event-wise). The f_{LSNL} , f_{NU} and f_{NS} correspond to the LS non-linearity, the position non-uniformity and the non-stability respectively. All f terms except the absolute energy scale definition are unit-less. It is worth pointing out that f indicates the intrinsic detector response, which also can be understood as the perfect (or ideal) response calibration. However, no calibration is perfect, and there is always some uncertainty or even bias due to the effective approximation behind each calibration step. From the observable Q_{PE} to the energy E_{dep} , it is critical to characterize and calibrate all the relevant effects with the control of the accuracy and precision as high as possible, as this will have direct impact to the final performance and quality of the calibration scheme.

The energy precision here means the closeness of the repetitive energy measurements to each other. It is typically understood as the energy resolution as illustrated in Eq.(4.1). The stochastic component of the energy resolution represents the statistical fluctuation, while the non-stochastic component reflects the imperfect detector response, including spatial, temporal variations, etc.

The QNL has impacts on both the energy scale and the energy resolution. As explicitly written in Eq.(6.1), the QNL is a part of the energy scale definition. As illustrated

in Fig.4.3, the QNL can mimic a spatial variation manifesting as the NU, thus affecting the energy resolution control. So the proper handle of the QNL is vital.

As elaborated in Chapter 4 and 5, the Dual Calorimetry calibration (DCC) is a powerful tool to calibrate the potential QNL for JUNO, and its excellent performance is demonstrated in terms of the direct channel-wise QNL control in Sec.5.3. This chapter aims to present the DCC role and performance in terms of the event-wise energy control including the energy scale and the energy resolution.

6.1 Energy Scale Control with DCC

As defined in Eq.(6.1), the non-linearity, non-uniformity and non-stability effects are all of importance for the energy scale, leading to the corresponding calibrations. All these effects except the non-stability will be addressed in this section, since the non-stability mainly makes sense when the detector is running.

In order to better illustrate the energy non-linearity and non-uniformity effects. This thesis adopts the following energy definitions:

- 1.) The particle true deposited energy in the LS is E_{dep} .
- 2.) The scintillation photons, as the outcome of the energy deposition, can be converted into photoelectrons (PEs) by the photo-cathode of the PMT. The visible energy (E_{vis}) corresponds to the total number of these PEs¹.
- 3.) These PEs are then amplified, digitized, processed and reconstructed in terms of charge. The reconstructed energy (E_{rec}) corresponds to the observable charge. With the PMT gain calibration, the charge can be expressed in the unit of the PE¹.

According to the definitions above, the LS non-linearity (LSNL) can be expressed as the E_{vis}/E_{dep} . Normally the LSNL specifies all the energy depositions occurring at one position while leaving the position dependence into the non-uniformity characterization. The event-wise charge non-linearity (QNL) can be expressed as E_{rec}/E_{vis} . The overall energy scale non-linearity (ESNL) is defined as the coupling of the LSNL and event-wise QNL, expressed as $\frac{E_{vis}}{E_{dep}} \cdot \frac{E_{rec}}{E_{vis}}$. The non-uniformity (NU) reflects the position dependence of the visible energy $E_{vis}(\vec{x})$ (or the reconstructed energy $E_{rec}(\vec{x})$). This section aims to illustrate the QNL impact on the overall ESNL and NU, and demonstrate the improvement of the corresponding control with the DCC.

In addition, there exists another conversion relationship, i.e. the true particle energy to the deposited energy conversion. For example, for the reactor $\bar{\nu}_e$ IBD event, the neutrino energy is converted dominantly to the positron kinetic energy and the annihilation gammas energy, and a tiny fraction of the neutrino energy is converted to the neutron recoiling energy ($\sim O(10keV)$), as explained in Sec.2.1.3. This energy conversion should also be included for the energy spectrum analysis. However, it is largely irrelevant for the DCC study in the energy scale control, thus this thesis does not open further discussion on this topic.

1. With the proper absolute energy definition (PE-to-MeV conversion), the E_{vis} and E_{rec} energy can be expressed in the unit of MeV

6.1.1 Energy Scale Non-linearity

LSNL

By assuming the absence of the QNL, the energy scale non-linearity (ESNL) contains only the LSNL effect. The LSNL is particle and energy dependent primarily owing to the quenching and Cherenkov effects, as illustrated in Fig.6.1. Since no position dependence exists under this assumption, the ESNL (here equivalent to LSNL) is generally universal everywhere in the detector.

For example, at any position in the detector, by changing the particle information including the type and energy, the relative nonlinear behavior of the energy deposition, i.e. Fig.6.1 should be the same. One exception is that when the calibration source is placed at the very edge (close to the boundary) of the LS, there could be some energy leakage or energy deposited in the acrylic glass that needs to be considered. But this is a corner effect and does not affect the general description of the detector response in this thesis due to the fiducialization for physics extraction, thus being ignored. The position NU will only affect the absolute light yield due to the position dependent optical effects such as the optical acceptance, attenuation and shadowing effect. Typically, the modeling of the LSNL can be done at the detector center as illustrated in Fig.6.1.

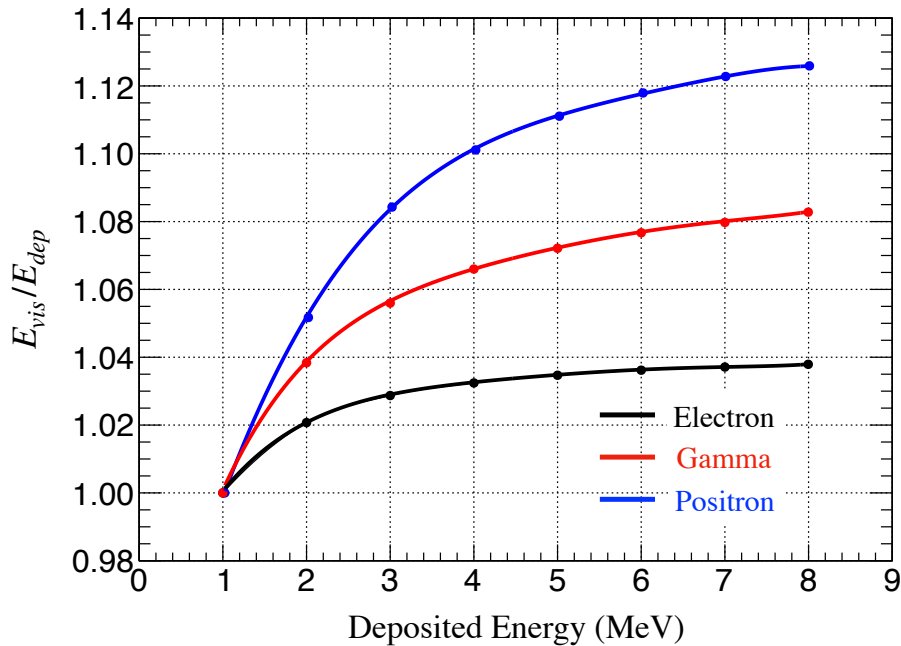


Figure 6.1 – Liquid scintillator non-linearity (LSNL) for electrons (black), gammas (red) and positrons (blue). It is equivalent to the energy scale non-linearity (ESNL) in absence of the QNL. Since no QNL is assumed, E_{rec} is scaled linearly with E_{vis} . The LSNL curves are obtained by simulating the calibration sources at the detector center. These curves are almost universal everywhere in the detector, since it is independent of the NU effect and no QNL effect is assumed. Here only the statistical uncertainty is considered, and it is too small to be visible.

Experimentally the gamma non-linearity can be obtained by deploying the radioactive calibration sources¹. The electron non-linearity can be deduced from the gamma non-linearity as widely used in the reactor neutrino LS experiments. For the reactor $\bar{\nu}_e$ induced LSNL, i.e. the positron non-linearity, the kinetic energy part is similar to that of electron, and the annihilation energy deposition corresponds to gammas.

QNL

When the QNL is considered in the energy scale, on the one hand the QNL has a direct impact on the ESNL which is the convolution of the channel-wise QNL of all channels; on the other hand the QNL brings the position dependence into the ESNL. So the ESNL at one specific position in the detector is not representative for the whole detector. In order to illustrate the ESNL in the presence of the QNL effect, the ESNL at the detector center and that at the edge are shown in Fig.6.2 by assuming a $\sim 10\%$ channel-wise QNL over 100 PE. The QNL can directly bias the ESNL, and this bias is supposed to be larger towards the detector edge where the charge detection is more dedicated.

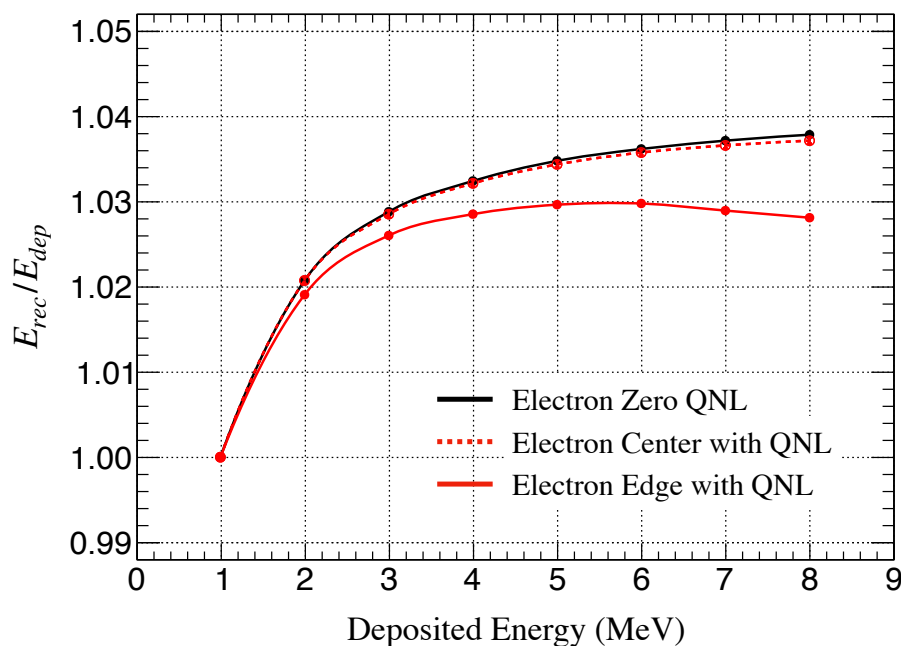


Figure 6.2 – Energy scale non-linearity (ESNL) for electrons with zero QNL (black), QNL at the detector center (dashed red) and QNL at the detector edge (solid red). A $\sim 10\%$ channel-wise QNL over 100 PE is assumed (defined in Eq.(4.4)). The QNL impact is expected to be small at the detector center as the charge detection dynamic range is small at the center. However, at the detector edge, the QNL can significantly affect the ESNL. Here only the statistical uncertainty is considered, and it is too small to be invisible.

1. Due to practical limitations, there are no easy deployable sources for unbiased electron and positron response characterization. So the calibration takes place in gamma energy equivalent as highlighted above.

Energy Scale Non-linearity Control with DCC

As the QNL will bring the position dependence into the ESNL, the uniformly distributed calibration signals are, in principle, desirable to characterize the ESNL for the whole detector volume. However, experimentally, such calibration source is not practical despite major effort to achieve so. Therefore the optimal approach is to calibrate the QNL channel-wise beforehand with DCC to eliminate the position dependence, and then perform the LSNL calibration at one fixed position (like the detector center). Thanks to the DCC approach, JUNO is the first experiment ever capable to articulate a complete calibration scheme where each response component can be fully (or almost) disentangled from first principles.

In order to illustrate the performance of DCC in the ESNL control, the uniformly distributed mono-energy electron signals are useful in simulation, even though these signals are not attainable experimentally. These uniformly distributed signals are calibrated to the detector center according the NU calibration which will be discussed in detail in the next section.

By assuming a 10% (over 100 PE) level channel-wise QNL of the LPMT, the QNL impact on the ESNL (or event-wise QNL) is at 0.4% level, as shown in Fig.6.3. By applying the DCC for every channel of LPMT, the QNL effect on the ESNL is significantly reduced to 0.1% level. When assuming an extreme case where the channel-wise QNL effect is $\sim 50\%$ over 100 PE, its impact on the ESNL can be up to 2% level, as shown in Fig.6.4. After the QNL calibration with DCC, the ESNL bias induced by the QNL is significantly reduced to $\sim 0.3\%$. This is a stunning number, which suggest the potential for an almost negligible role of QNL effects upon the DCC application and it is to be demonstrated experimentally.

There is still some residual QNL effect on the ESNL after the DCC correction, and the reason for this residual effect (or not perfect calibration) is driven by the DCC systematics as explained in detail in Sec.5.5. This residual QNL effect can possibly be further reduced, if necessary, by developing higher order DCC method, which is to use the proportionality between the residual bias and the diagnosed QNL as highlighted in Sec.5.6. However such an effort awaits for detector data since other detection effects currently not covered by the simulation accurately may be found to have an impact to the DCC implementation. Those are to be understood and tackled first upon detector commissioning.

If the residual bias can not be reduced, experimentally, it can be scrutinized for systematics quantification either through the data driven approach or the data tuned MC simulation approach. For example, two calibration sources with different energies (e.g. 1 MeV and 8 MeV) can be used to scrutinize the residual bias; by scanning the position of the two calibration sources, the detector responses corresponding to these two sources at the same position can be got respectively; if there is no residual bias, the ratio between these two responses should be constant; any bias from the constant can be used for the systematics quantification. Another possible approach is to develop Dual Calorimetry implementation with the cosmogenic signal spectra (like ^{12}B), and as mentioned in Sec.4.3.3 by comparing the measured cosmogenic signal spectra from the two readout systems, some charge response diagnosis information may be helpful for the systematics quantification. All those cross-checks will be implemented to test the DCC performance upon the first data available.

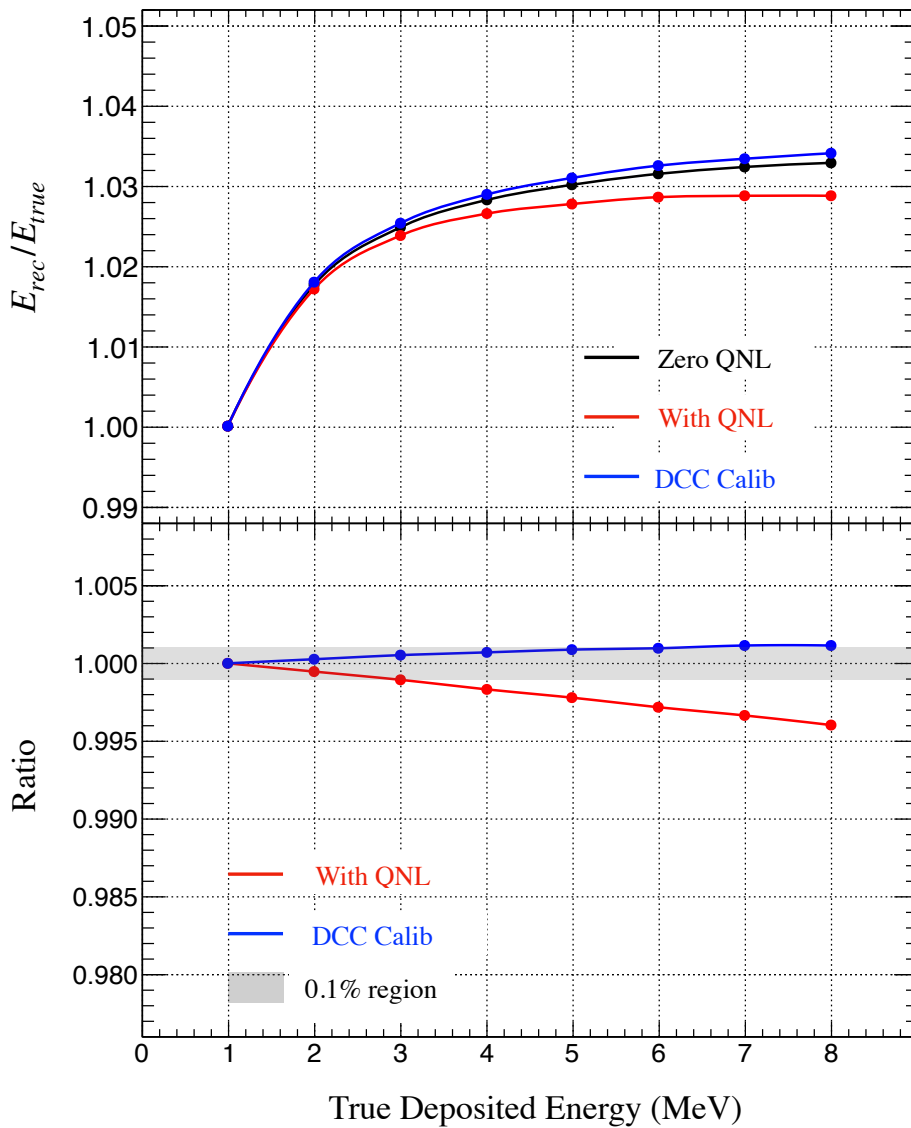


Figure 6.3 – QNL ($\sim 10\%$ channel-wise) impact on the ESNL and the control with DCC. The ESNL corresponds to the uniformly distributed electron signals in the detector volume. Upper panel: the ESNL in absence of the QNL is shown in black; by assuming a $\sim 10\%$ channel-wise QNL over 100 PE, the ESNL is then shown in red; after the DCC correction, the ESNL is shown in blue. Lower panel: the pure QNL effect on the ESNL which is defined as the ratio of the uncalibrated or calibrated ESNL to the ESNL with zero QNL; A 0.4% QNL effect on the ESNL can be reduced to 0.1% level with the DCC control. Here the statistical uncertainty and the uncertainties from the NU calibration and DCC calibration are considered, and they are too small to be invisible.

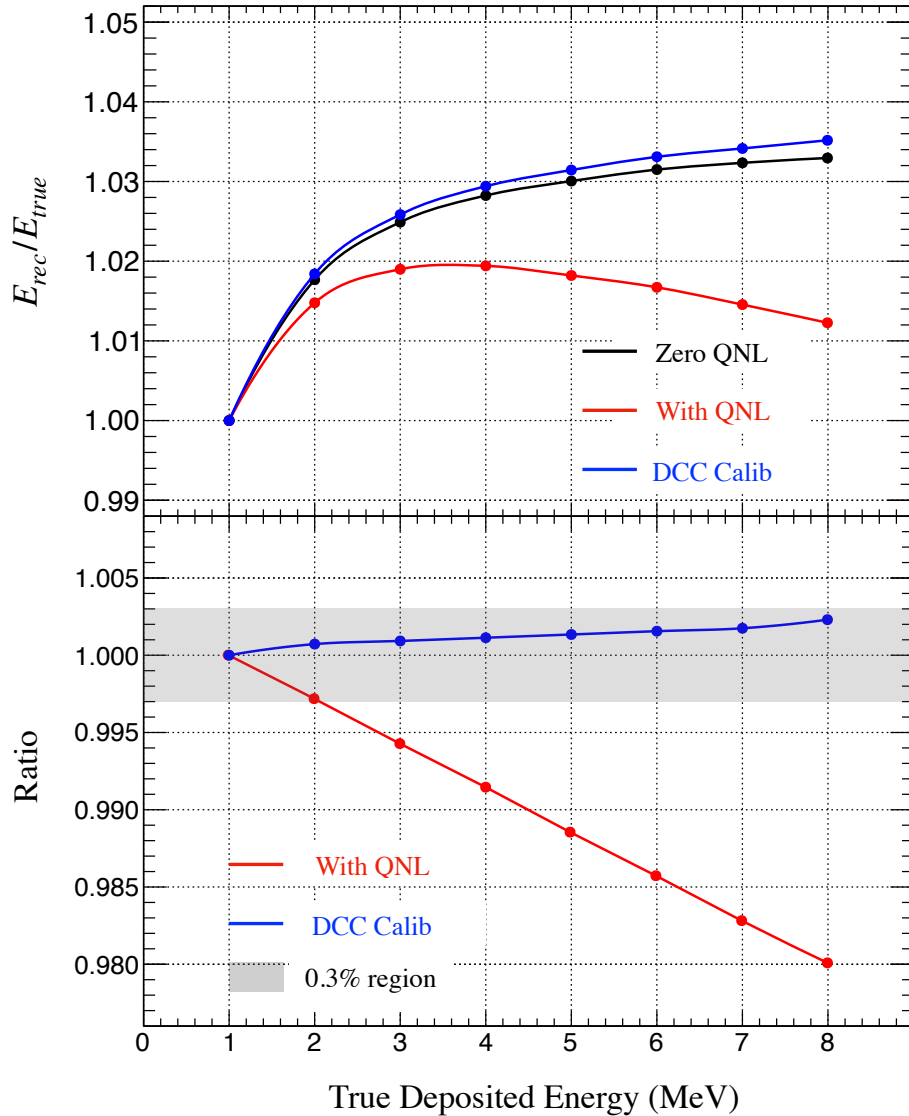


Figure 6.4 – QNL ($\sim 50\%$ channel-wise) impact on the ESNL and the control with DCC. The ESNL corresponds to the uniformly distributed electron signals in the detector volume. Upper panel: the ESNL in absence of the QNL is shown in black; by assuming a $\sim 50\%$ channel-wise QNL over 100 PE, the ESNL is then shown in red; after the DCC correction, the ESNL is shown in blue. Lower panel: the pure QNL effect on the ESNL which is defined as the ratio of the uncalibrated or calibrated ESNL to the ESNL with zero QNL; A 2% QNL effect on the ESNL can be reduced to 0.3% level with the DCC control.

6.1.2 NU in Energy Scale

Apart from the ESNL, the non-uniformity (NU) is another key aspect in the energy measurement accuracy (or energy scale). The NU is also important for the energy resolution control as will be addressed in the next section.

As mentioned previously, the nonuniform light (or photon) collection is primarily owing to the optical acceptance including the solid angle between the PMTs and the event vertex, the shadowing effect, the light attenuation, etc. Moreover the QNL effect can mimic the NU effect as illustrated with Fig.4.3. Therefore, the calibration of the NU requires not only a precise characterization of the NU map, but also an independent calibration to the QNL.

NU Response Map

The geometry of the JUNO detector is spherical, and the PMTs are designed to be distributed as symmetrically as possible. Ideally, if the spherical symmetry holds at JUNO, the NU can be represented with a one dimension (1D) response map by scanning the calibration source along any radial direction. However, due to the actual PMT distribution, the nodes for supporting the acrylic ball, the chimney for deploying the calibration system, etc., the spherical symmetry is poorly preserved at JUNO. The azimuthal symmetry is expected according to the current design and the geometry simulation at JUNO, thus being assumed for the following study.

In the spherical coordinate system, by assuming the azimuthal symmetry, the NU can be represented by the responses in a 2D r - θ plane. About 300 optimized positions are used for characterizing the NU in this thesis, as illustrated in Fig.6.5. The corresponding NU response map in this 2D r - θ plane is got by simulating 1 MeV electrons at each position with $\sim 10,000$ statistics and applying a cubic interpolation, as shown in Fig.6.6.

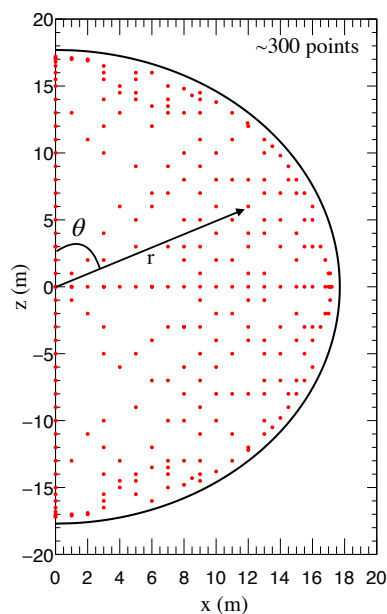


Figure 6.5 – NU calibration points at JUNO by assuming the azimuthal symmetry of the detector response. About 300 calibration positions are optimized in 2D r - θ plane within the fiducial volume ($r < 17.2$ m). The selection of these 300 positions are driven by minimizing the residual NU bias after the calibration with the NU map for the uniformly distributed signals in the full fiducial volume. The calibration systems including ACU, CLS, GT and ROV can provide the accessibility to these positions.

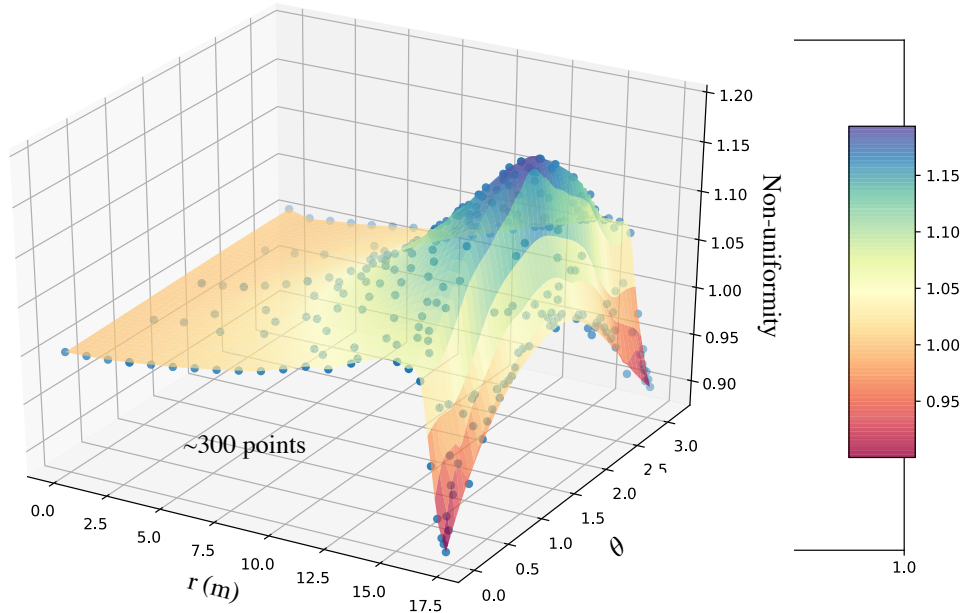


Figure 6.6 – The JUNO detector NU response in the 2D r - θ plane. The z-axis is defined as the detector response normalized to the detector center. About 300 optimized positions are used according to Fig.6.5, and for each position 1 MeV electrons are simulated with 10,000 statistics. A cubic interpolation is applied in order to interpolate the NU response in the full r - θ plane. No QNL is assumed here.

QNL Impact on NU

The QNL is position dependent because of its charge dependence relying on the optical acceptance as elaborated in Sec.4.2.3. As illustrated with a 1D NU response map in Fig.4.3, the QNL can mimic a NU behavior, thus biasing the NU response map.

The QNL induced position dependent response can be expressed as the ratio of $E_{rec}(\vec{x})_{QNL}/E_{rec}(\vec{x})_{zero\ QNL}$. By assuming an extreme case of $\sim 50\%$ channel-wise QNL, the 2D NU response map of Fig.6.6 will be biased by the QNL effect up to 1%, as illustrated in Fig.6.7. If the 2D NU response map is obtained by higher energy (>1 MeV) calibration sources, the QNL induced NU bias is foreseen to be larger.

NU Bias Control with DCC

As just illustrated, the QNL can mimic a NU behavior, hence bias the modeling of the intrinsic NU response in the energy scale. Moreover, this NU bias will also affect the energy resolution as will be explained in the next section. The DCC is capable to reduce the QNL induced NU bias by calibrating the QNL channel-by-channel. As illustrated in Fig.6.8, the DCC can control the QNL induced NU bias to 0.1% level, being one order of magnitude improvement.

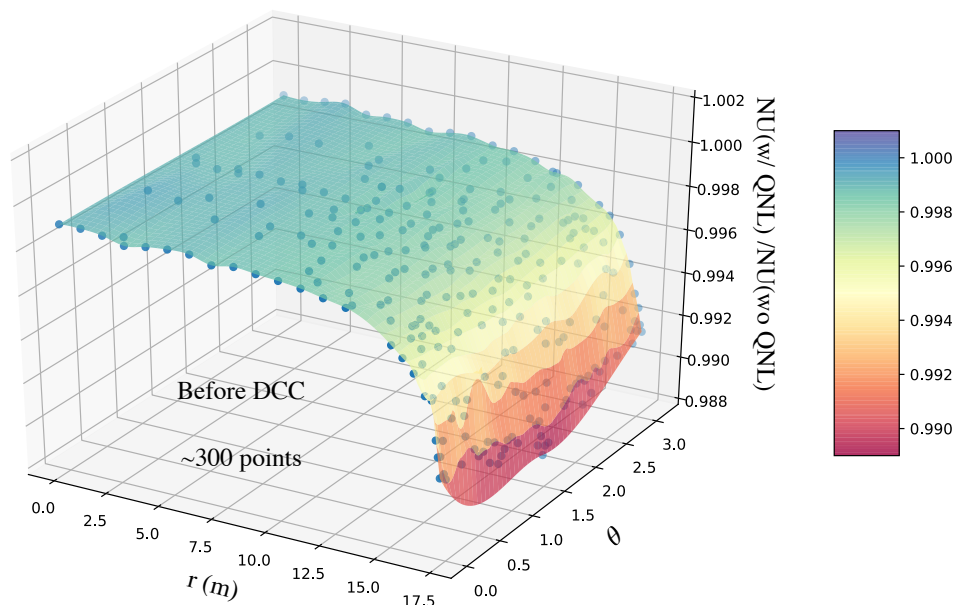


Figure 6.7 – The QNL induced NU bias by an extreme case of $\sim 50\%$ channel-wise QNL. The NU bias is expressed as the ratio of the NU response map with QNL to that without QNL. In the presence of the QNL, the 2D NU response map of Fig.6.6 will be biased up to 1%.

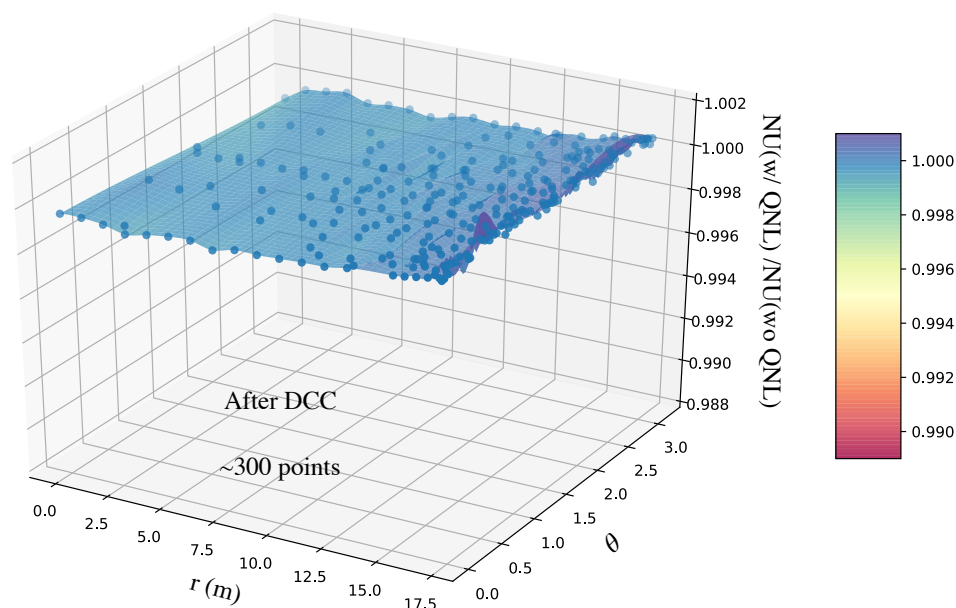


Figure 6.8 – The DCC control for the QNL induced NU bias. By applying the DCC for the QNL calibration, the QNL induced NU bias (by $\sim 50\%$ channel-wise QNL) can be controlled at 0.1% level.

6.2 Energy Resolution Control with DCC

6.2.1 Energy Resolution of JUNO

The energy resolution characterizes the precision of the energy measurement, and can be defined as the standard deviation (σ_E) over the mean value (E) of the measured energy distribution for a given energy, namely $\frac{\sigma_E}{E}$. The energy resolution typically includes the stochastic component dominated by statistical fluctuation, and the non-stochastic component affected by the detector response effects. Different types of detectors may focus on different aspects about the energy resolution due to the specific detector design. To be simple and concrete, the JUNO energy resolution simulated through the official JUNO software is used for illustrating different components of the energy resolution in this section.

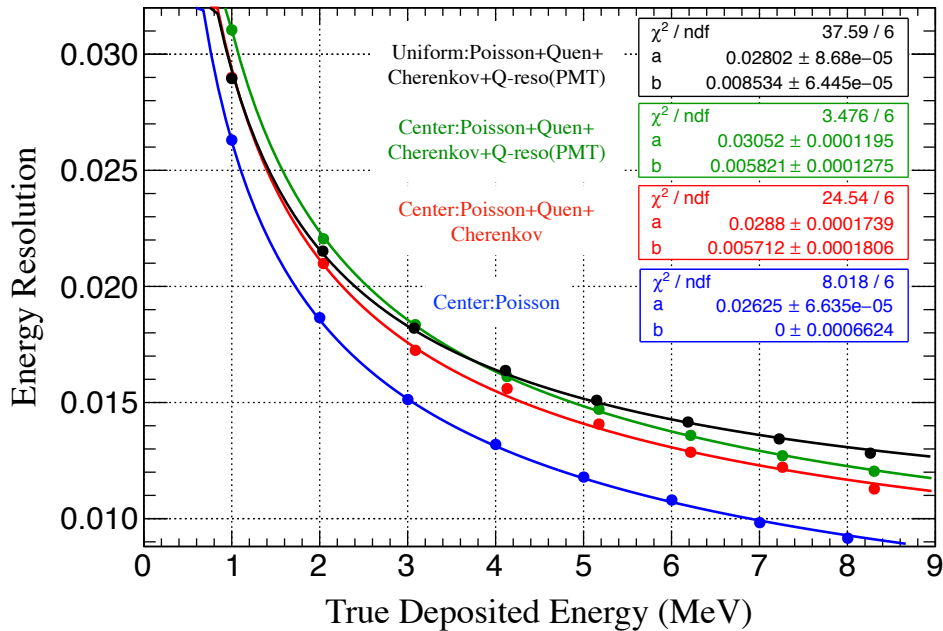


Figure 6.9 – Illustration of different contributions for the electron energy resolution at JUNO. The fitting adopts the energy resolution model of Eq.(6.2): a stochastic term "a" and a constant term "b". When considering only the photon statistics (Poisson) effect, the energy resolution at the detector center is shown in blue. By adding the quenching and Cherenkov effects, the energy resolution is in red. If the PMT charge resolution (30%) is also added, then the energy resolution is shown in green. For the uniformly distributed signals with the quenching, Cherenkov and PMT charge resolution effects, after the NU calibration (Fig.6.6), the energy resolution is shown in black.

Photon Statistics (Poisson)

The stochastic component of the energy resolution is dominated by the fluctuation of the LS photon statistics. As the scintillation photons hit stochastically the PMTs, the collected photons follow the Poisson statistics, for a Poisson distribution with the mean

value of N^1 , its standard derivation is given by \sqrt{N} . So the photon statistics component of the energy resolution follows $1/\sqrt{N}$ law (or a/\sqrt{E} law), shown as the blue curve in Fig.6.9. This component ("a" term) is the leading term for JUNO, a better than 3% energy resolution at 1 MeV requires large than 1200 PE yield per MeV.

Quenching and Cherenkov effects

The non-stochastic component of the energy resolution is affected by various response effects. Ones of the major contributions are the quenching and Cherenkov effects, and they contribute to (by increasing or decreasing) the photon statistics largely in a non-stochastic (or no $1/\sqrt{N}$) way. When the quenching and Cherenkov effects are considered, the energy resolution manifests as the red curve in Fig.6.9. For simplicity, the non-stochastic component is considered only as a constant term ("b"), and then the energy resolution model is defined as:

$$\frac{\sigma_E}{E} = \sqrt{\left(\frac{a}{\sqrt{E}}\right)^2 + b^2}. \quad (6.2)$$

By fitting the energy resolution with the model above, the quenching and Cherenkov effects contributes to the constant term of $\sim 0.57\%$.

PMT Charge Resolution

The PMT charge resolution also affects the energy resolution. Since the PMT charge resolution corresponds to mainly the electron amplification processes, following the Poisson statistics, it contributes to the energy resolution in terms of the stochastic term "a". For example, if $\sim 30\%$ charge resolution is considered, the energy resolution is shown as the green curve in Fig.6.9 where the "a" term is increased from 2.88% to 3.05%.

Imperfect NU Calibration

Another major contribution for the non-stochastic energy resolution comes from the imperfect NU calibration. The imperfect NU calibration results in a smearing effect in the measured energy distribution, thus worsening the energy resolution. In order to illustrate this point, by applying the NU calibration (imperfect 2D NU response map of Fig.6.6) to the mono-energy electron signals uniformly distributed in the detector volume, the energy resolution is then shown as the black curve in Fig.6.9.

It turns out that the non-stochastic term, here a simple constant term "b", is increased from 0.58% to 0.85% because of the smearing effect from the imperfect NU calibration. It is worth pointing out that the uniformly distributed signals in the detector volume result in a better stochastic energy resolution compared to the signals at the detector center, from 3.05% to 2.80%. The reason is that the average photon yield of the uniformly distributed signals is higher than that of the signals at the detector center, so a higher photon (or PE) yield leads to a better energy resolution following the $1/\sqrt{N}$ law.

1. Typically N is large enough such that the Poisson distribution is approximately to a Gaussian distribution

Other Effects

Another important effect that matters for the energy resolution is the QNL and it will be discussed in particular in the next section together with the corresponding DCC control.

Besides, there are other effects that will contribute to the energy resolution including the PMT dark noise, the smearing from the vertex reconstruction, etc. These effects are also important and a dedicated study at JUNO can be found in Ref.[174]. However, these effects are likely irrelevant to the QNL impact on the energy resolution. For the sake of a clear illustration of the QNL impact and DCC performance for the energy resolution, these effects are not included in the following studies.

6.2.2 QNL in Energy Resolution and DCC Control

The QNL can affect the energy resolution in the following ways. On the one hand, the QNL can directly affect (or bias) the charge measurement, thus distorting the charge distribution (i.e. the energy distribution) including both the mean value and the standard deviation. On the other hand, the QNL can bias the NU response map as explained in Sec.6.1.2, appearing like additional spatial variation, and the biased NU response map results in additional non-stochastic energy resolution.

The DCC is demonstrated in this thesis to provide the direct channel-wise QNL calibration, hence both the QNL induced bias in charge distribution and the QNL induced bias in the NU response map can be largely corrected.

For instance, if there exists $\sim 10\%$ channel-wise QNL over 100 PE (Eq.(4.4)), the non-stochastic term (here constant term "b") of energy resolution will be worsened from $\sim 0.85\%$ to $\sim 0.95\%$ if fitting to the model of Eq.(6.2). The relative deterioration of the overall energy resolution is up to $\sim 5\%$ in 1~8 MeV range as illustrated in Fig.6.10. By applying the DCC correction both for the energy measurement and the NU response map, the energy resolution deterioration can be largely corrected and be controlled at 1% level, also as illustrated in Fig.6.10.

The non-stochastic component of the energy resolution may not be able to be expressed in a simple constant term, if the QNL effect is more significant. For example, by considering an extreme case where $\sim 50\%$ channel-wise QNL over 100 PE (Eq.(4.5)) is assumed, the energy resolution is shown as the red curve in Fig.6.11. In this case only a constant term can not model the energy resolution well, and it is found that a E^2 term can be added in the energy resolution model for keeping the fitting quality, as:

$$\frac{\sigma_E}{E} = \sqrt{\left(\frac{a}{\sqrt{E}}\right)^2 + b^2 + d^2 E^2}. \quad (6.3)$$

Under this extreme QNL assumption, the relative deterioration of the energy resolution can be as large as 60%, while with the DCC correction it still can be controlled at 1% level, as illustrated in Fig.6.11.

In summary, through the two examples above, it is demonstrated that the DCC can control the energy resolution deterioration caused by the QNL effect to 1% level (relatively) and keep the non-stochastic component below 1%.

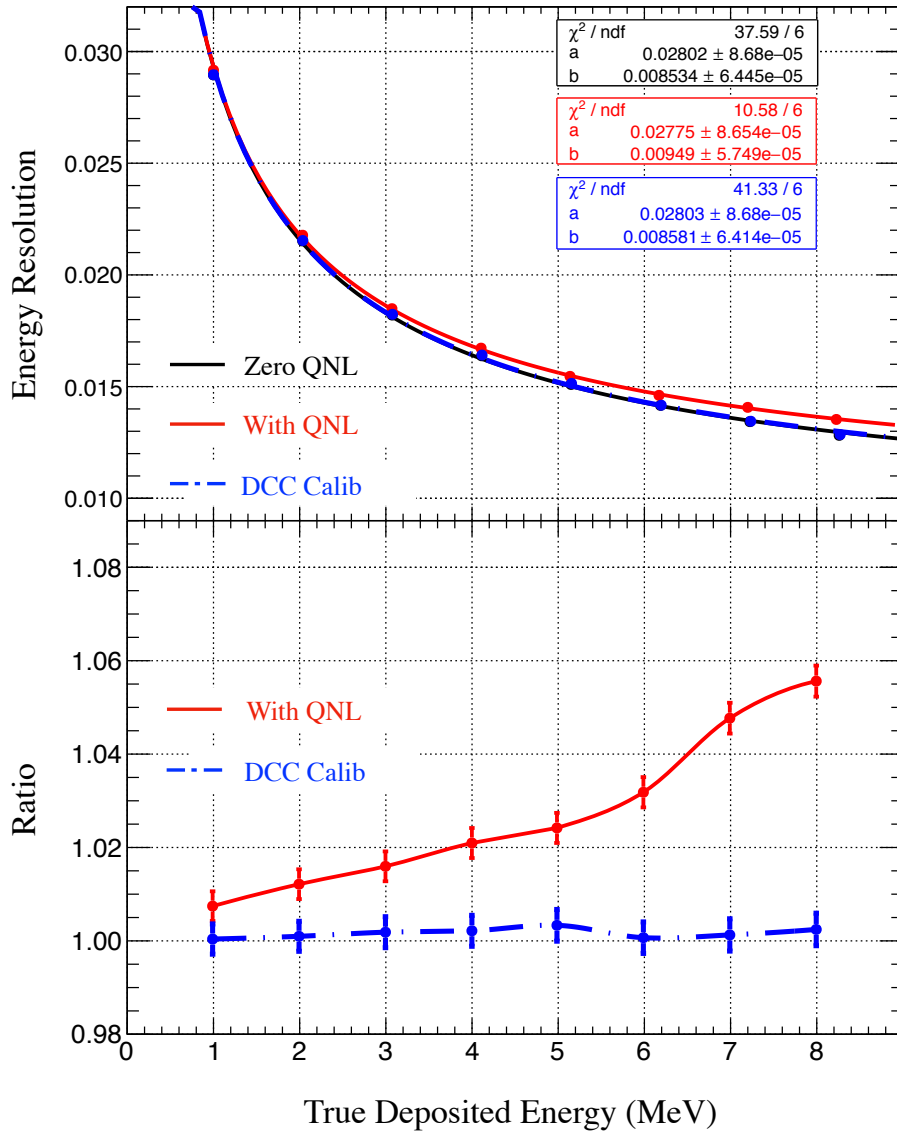


Figure 6.10 – QNL ($\sim 10\%$ channel-wise) impact on the energy resolution and the control with DCC. The energy resolution corresponds to the uniformly distributed electron signals in the detector volume with the NU response calibration. The quenching, Cherenkov and 30% PMT charge resolution effects are considered. The fitting adopts the energy resolution model of Eq.(6.2): a stochastic term "a" and a constant term "b". Upper panel: the energy resolution in absence of the QNL is shown in black; by assuming a $\sim 10\%$ channel-wise QNL over 100 PE, the energy resolution is then shown in red; after the DCC correction, the energy resolution is shown in blue. Lower panel: the pure QNL effect on the energy resolution which is defined as the ratio of the uncalibrated or calibrated energy resolution to that with zero QNL. A 5% relative energy resolution deterioration caused by the QNL can be reduced to 1% level with the DCC control.

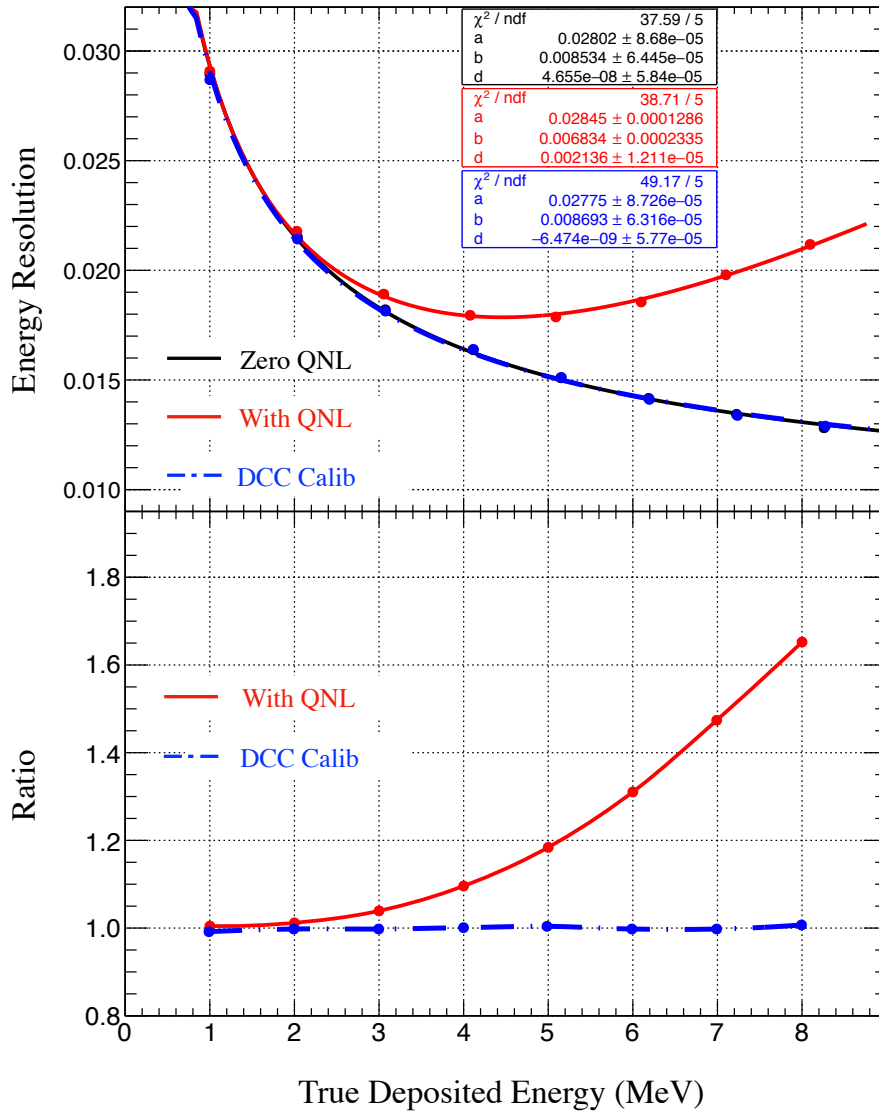


Figure 6.11 – QNL (an extreme case of $\sim 50\%$ channel-wise) impact on the energy resolution and the control with DCC. The energy resolution corresponds to the uniformly distributed electron signals in the detector volume with the NU response calibration. The quenching, Cherenkov and 30% PMT charge resolution effects are considered. The fitting adopts the energy resolution model of Eq.(6.3): a stochastic term "a", a constant term "b" and an additional term "d". Upper panel: the energy resolution in absence of the QNL is shown in black; by assuming a $\sim 50\%$ channel-wise QNL over 100 PE, the energy resolution is then shown in red; after the DCC correction, the energy resolution is shown in blue. Lower panel: the pure QNL effect on the energy resolution. A 60% relative energy resolution deterioration caused by the QNL can be reduced to 1% level with the DCC control.

6.3 Summary and Outlook

As highlighted with many examples in this chapter, the QNL is a critical factor in the detector response having significant impact on the energy scale and the energy resolution. The energy scale and energy resolution are of greatest importance for the reactor neutrino oscillation physics at JUNO. The DCC developed in this thesis exhibits great capability to control both the energy scale and the energy resolution through the direct LPMT QNL calibration.

The QNL impact on the ESNL can be controlled better than 0.3% level with the DCC, an 0.1% control seems attainable. The QNL impact on the energy resolution can also be controlled well with the non-stochastic term below 1%. In the relative sense, the energy resolution deterioration caused by QNL can be reduced from a few percent (even more than 50%) to 1% level.

Since the detector is not yet built, the instrumentation driven QNL effect can not be well predicted, several assumptions and examples are made in order to illustrate the prospect performance of the DCC in this thesis. The performance obtained even in the worst case scenario¹ (expected to be much worse than JUNO) demonstrates that the DCC can handle the situation if unexpected control of the QNL ever took place. So, this thesis has demonstrated a major redundancy system for JUNO experiment to be able to successfully achieved its energy control goals. As a data driven approach, understanding the methodology of the DCC for handling the QNL and the energy control is more important, as elaborated in the thesis.

In the future, the experimental quantification of the energy scale systematics is worth for further development, including the Dual Calorimetry based on cosmogenic signals and neutrino oscillations (distribution-wise), as well as higher order channel-wise DCC based on both data and MC. Upon the improvement of the MC configuration, the detector commissioning and running, more effort for the energy resolution parameterization, especially for the non-stochastic term breakdown, is requisite.

1. The worst scenario appears as the $\sim 50\%$ channel-wise QNL in the 1~100 PE range.

Chapter 7

SPMT Readout Electronics Performance for Dual Calorimetry

In the Dual Calorimetry, the SPMT system plays the role of the charge linear calibration reference. The key to achieve the SPMT charge linearity eventually relies on the hardware performance of the SPMT readout electronics.

As briefly presented in Sec.3.2.2, the core of the SPMT readout electronics is the ASIC Battery Card (ABC) that was conceived and designed by APC and IJClab teams.. The SPMT system has about 200 ABC boards, and each of them handles the signals of 128 SPMTs. The ABC board is designed to provide the capabilities of the digital PE counting, charge measurement, time measurement, high trigger rate handling, etc. This chapter gives more details about the ABC design and functionality together with the performance testing results contributing to the Dual Calorimetry hardware validation.

7.1 ABC Board

The ABC board features eight CATIROC chips and one FPGA, as shown in Fig.7.1. The CATIROC chip [206], as one of the key element in the ABC board, is provided by the OMEGA microelectronics laboratory. Each chip provides 16 independent channels with a common trigger threshold, and each channel can perform the charge and time measurement in the auto-trigger (or trigger-less) mode.

In fact, each channel has two effective sub-channels, working in the "ping-pong" mode, in order to reduce the effective deadtime. The ping and pong correspond to two capacitors that can store the signals. For example, two signals arrive at one channel; if the ping channel is occupied by the first signal, the second signal can be processed with the pong channel. With the "ping-pong" mechanism, the deadtime of the CATIROC can reach about 9 μs if the full chip is occupied and it can reach about 6 μs if only one channel is occupied [204].

The charge measurement records effectively the amplitude of the signal pulse with the dynamic range up to 400 PE. The time measurement records the arrival time of the signal pulse with the designed precision better than 100 ps. The data stream from the CATIROC digitization is called the charge data stream (QDS) and it is captured by the FPGA for further processing and packaging.

The Kintex-7 FPGA (Field Programmable Gate Array) is the other key element provided by Xilinx. Besides the aforementioned data handling of the QDS, the FPGA can yield a discriminator data output. Specifically, the trigger threshold (common for 16 channels) of the CATIROC is programmable and it can serve as a signal-noise discriminator; the signals passing the threshold can be counted digitally and recorded directly

by the FPGA, i.e. the discriminator data stream (DDS). Since it does not experience the digitization process of the CATIROC, the deadtime is much smaller (<100 ns). The DDS provides the essential information for the single PE counting and also for the Poisson zero PE counting correction that is introduced in Sec.5.4.2. The short deadtime of DDS extends the capability of handling high rate supernova neutrino events.

In addition, the FPGA provides an accurate time sampling for recording the time of the event and also the time over threshold information with 1 ns precision. The time over threshold information is proportional to the charge and complementary to the CATIROC charge information of the signal pulse amplitude. Thus it can help the charge measurement for multi-PE events.

The FPGA is also used for the communication with the CATIROC configurations (slow control), the local synchronisation, the data transfer to the GCU, etc.

Apart from the CATIROC and FPGA, there is also a FPGA mezzanine card (FMC) providing a fast path to the GCU and a 1 GB DDR memory providing data buffering in the ABC board.

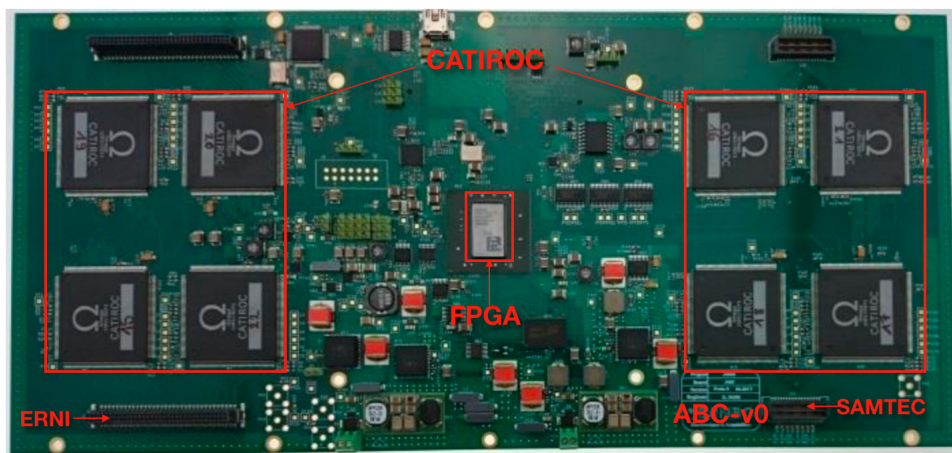


Figure 7.1 – Prototype of the ABC board version 0. The eight CATIROC chips are symmetrically distributed in the board and the FPGA is located in the center. For the version 0 prototype, two types connector (left: ERNI, right: SAMTEC) for signal injection are designed in order to test their performance respectively. The final selection is the SAMTEC (right) connector.

7.2 ABC Version 0 Performance Test

The purposes of the ABC version 0 test in this thesis are 1.) to test and validate the general performance of the two data streams (QDS and DDS) contributing to the Dual Calorimetry hardware validation, 2.) to help the electronics engineers for the firmware and software debugging, 3.) to help improving the design of the new version of ABC (version 1).

In order to simplify the explanation of the following testing results, three trigger

configurations are introduced.

- Auto-trigger mode. In this mode, a common trigger threshold can be set per CATIROC (16 channels), and once the input signal passes the threshold, it will be recorded.
- Force-trigger mode. In this mode, the FPGA generated periodic pulse can force the board to take data regardless of the input signals. It can realize the control from a single channel to the entire board (128 channels). The frequency of the periodic pulse has 16 options from ~ 1 kHz up to 30 kHz. If there is no input signal, the force-trigger will take the noise data getting the pedestal distribution.
- External-trigger mode. This mode is similar to the force-trigger mode. Instead of using the periodic pulse generated by the FPGA, an external pulse can be injected as a common trigger to force the board to take data according to the rate of the external pulse, regardless of the input signals.

The force-trigger and the external-trigger mode are largely used to take the pedestal data for the performance test in this thesis. Through the pedestal analysis, a lot of functionalities can be tested including the charge measurement, correlations among channels, discriminator output, timing, stability, etc.

7.2.1 Charge Data Stream

The essential information recorded in the QDS is the charge and time measured by the CATIROC chip. The data format of the QDS [207] is:

$$\begin{aligned}
 & \text{"00"} \text{ (2 bits)} - \text{"Channel.Nb"} \text{ (4 bits)} - \text{"Coarse Time"} \text{ (26 bits)} - \text{"Gain"} \text{ (1 bit)} \\
 & - \text{"Event Counter"} \text{ (11 bits)} - \text{"Charge"} \text{ (10 bits)} - \text{"Fine Time"} \text{ (10 bits)} \\
 & - \text{"00000 Sanity"} \text{ (5 bits)} - \text{"ASIC.Nb"} \text{ (3 bits)} - \text{"Card.Nb"} \text{ (8 bits)}, \quad (7.1)
 \end{aligned}$$

where the "00" is the identifier of the QDS and "00000 Sanity" can be used to check if data is misaligned or corrupted.

This section aims to study the correlation between different channels, the time resolution and the stability of the QDS mainly by means of the pedestal analysis.

7.2.1.1 Pedestal

Under the force-trigger (or external-trigger) mode, when there is no signal injection to any channel, only the electronics noise will be sampled by the CATIROC, forming pedestal distributions. A typical pedestal distribution for one channel is shown in Fig.7.2. The pedestal distributions for all 128 channels are shown in Fig.7.3. The pedestal mean values indicating the electronics noise level have a dependence on the CATIROC with about 30% difference by CATIROC, but within one CATIROC the pedestal mean values differ less (about 10%) by channel. The pedestal width is typically from 1.1 to 1.5 ADC unit.

These results indicate that the channel by channel pedestal calibration is necessary. As explained previously, the pedestal control is critical for the SPMT response control, a preliminary study of the pedestal width with the single PE injection was done by the collaborators [204] and a typical 0.05 PE pedestal width was observed in the early stage. The pedestal should be in high priority in future ABC test, combined test and commissioning.

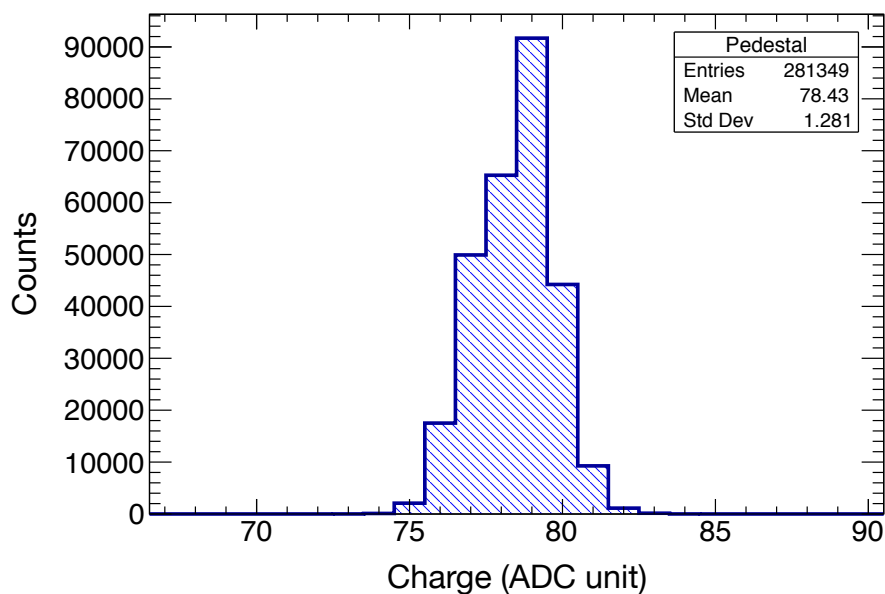


Figure 7.2 – The typical pedestal distribution of one channel in the ping mode of the ABC board under ~ 1 kHz force-trigger.

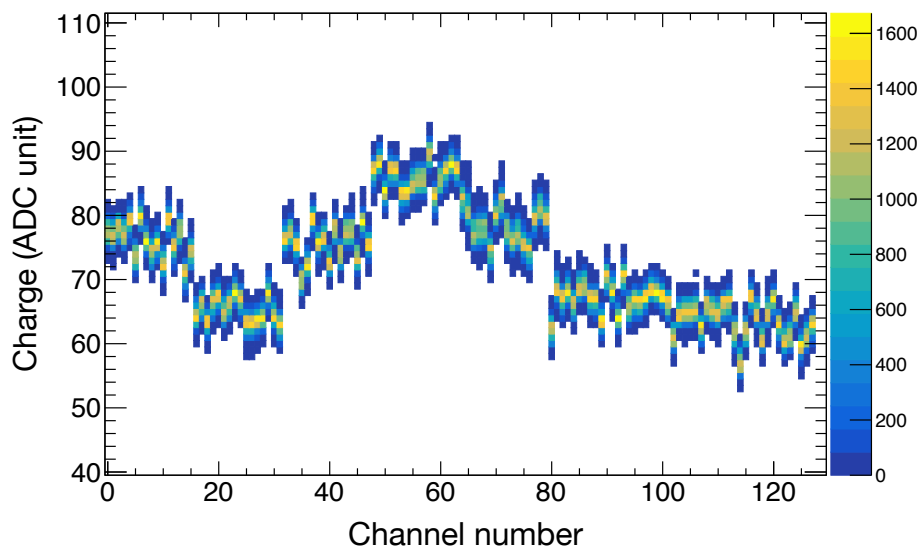


Figure 7.3 – Pedestal distributions for 128 channels (ping mode) of the ABC board under ~ 1 kHz force-trigger. From channel 0 to 127, every 16 channels in sequence correspond to one CATIROC. For the 128 channels in the pong mode, the results are the same.

7.2.1.2 Correlation

Under the force-trigger (or external-trigger) mode, the data samplings for all the channels occur almost simultaneously. If there are some correlations (or cross-talks) between different channels, the correlation level can be estimated by the correlation coefficient, given by:

$$\rho_{a,b} = \frac{\text{cov}(a, b)}{\sigma_a \sigma_b}, \quad (7.2)$$

where σ_a and σ_b are the standard derivations of the pedestal distributions for channel a and channel b respectively, and $\text{cov}(a, b)$ is the covariance between pedestal distributions of channel a and b.

Fig.7.4 shows an example of the correlation between two channels, where the correlation coefficient is about 0.4. The correlation relations among all the channels are shown as a matrix in Fig.7.5 together with the correlation coefficient distribution. The correlation between two different channels can be up to $\rho = 0.5$, and the correlation within the same CATIROC is typically stronger than that in different CATIROCs, as expected. The measured correlation coefficients indicate a certain level cross-talk among channels.

Another cross-talk study was performed by collaborators through injecting a large charge signal into one channel and observing the pedestal variation in the other channels [208]. The preliminary results indicated that the cross-talk was less than 0.1%, namely if the injected signal is 100 PE in one channel, the mean value of the pedestal distribution of other channels will be increased by 0.1 PE at most.

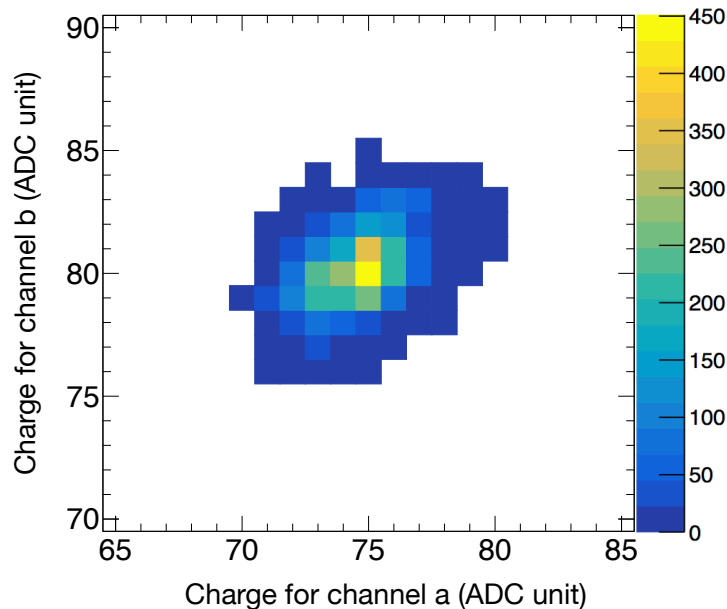


Figure 7.4 – An example of the correlation between two different channels (ping mode). Channel a and b are forced to sample the noise data almost simultaneously. The measured charges for channel a and b under the same trigger is plotted. The correlation coefficient between these two channels is about 0.4.

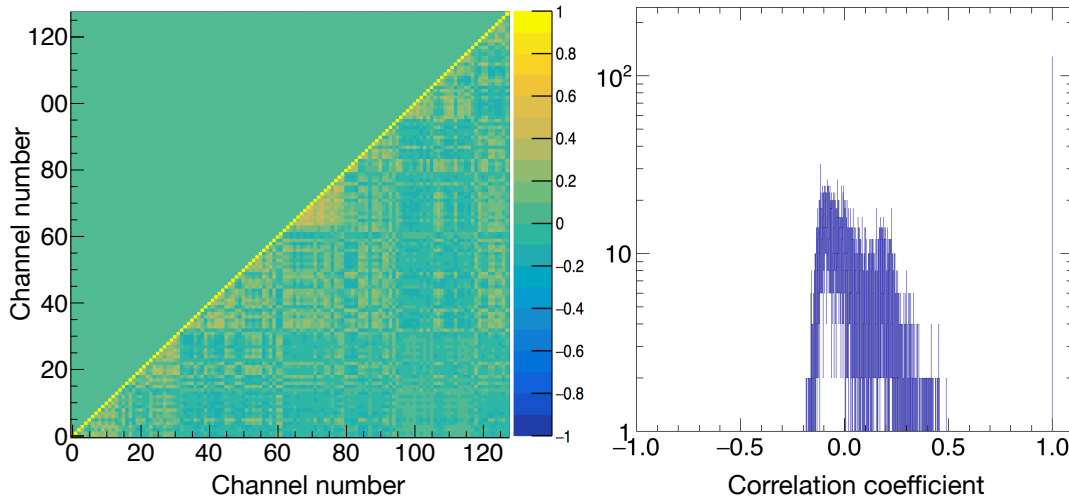


Figure 7.5 – Left: correlation matrix for all the 128 channels (ping mode). The color corresponds to the correlation coefficient value. Right: the correlation coefficient distribution for all the 128 channels (ping mode). Each channel is fully correlated with itself as $\rho_{i,i} = 1$. The results in pong mode are similar.

7.2.1.3 Timing

In the QDS, the time of one event is recorded with two variables, i.e. the coarse time with 25 ns precision and the fine time with roughly 25 ps precision in 0~25 ns range. The time recorded for an event can be calculated as the sum of the coarse time and the fine time.

The fine time needs to be calibrated. The maximal fine time variation is 0~1023 TDC unit. However, the actual fine time variation is not exact 0~1023 and it is different by channel. In order to perform the fine time calibration, a large amount of statistics (> 10,000) need to be collected for each channel to get the fine time distribution; then the minimal (t_{min}) and maximal (t_{max}) fine time values in terms of the TDC unit can be identified; the calibration corresponds to computing the exact fine time precision as $25 \text{ ns}/(t_{max} - t_{min})$, as illustrated in Fig.7.6.

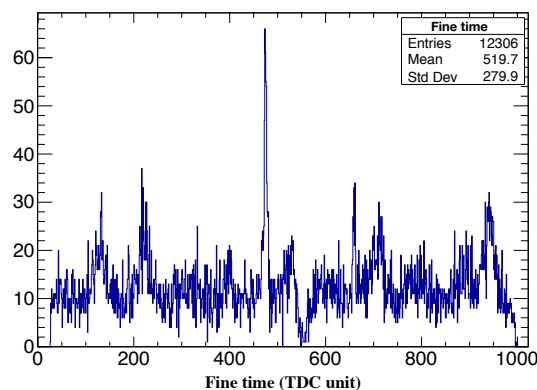


Figure 7.6 – A typical fine time distribution for one channel (ping mode). The maximal variation range of the fine time is 0~1023 (TDC unit). For the channel presented in this figure, the actual fine time variation is identified to be 26~997 (TDC unit), so the fine time precision is calibrated to be $25 \text{ ns}/971 \approx 25.75 \text{ ps}$ for this channel.

7.2.1.4 Time Resolution

If two channels are triggered at the same time, the difference of the recorded time between the two channels can be used to represent the time resolution of the QDS. The time difference can be defined as:

$$\Delta t_{ij} = t(k_{trigger}, i_{channel}) - t(k_{trigger}, j_{channel}), \quad (7.3)$$

where $k_{trigger}$ is the label of the trigger number, i and j are the labels of channels.

The advantage of using this time difference to represent the time resolution is that the time measurement uncertainty caused by the jitter in the pulse generator can be eliminated. The disadvantage is that it is sensitive to the channel-to-channel systematics such that if this systematics has a non-negligible impact, this time difference does not represent the intrinsic time resolution of the QDS.

Under the force-trigger (or external-trigger) mode to all channels, by considering channel 0 as the reference channel, the computed Δt_{i0} distributions with $i = 1, \dots, 127$ are shown in Fig.7.7. It is interesting to notice that under the force-trigger (or external-trigger) mode, even though the force-trigger is common to all the channels, it does not trigger all the channels exactly at the same time because of the trigger distribution.

When Δt_{ij} is negative (positive), it means that the force trigger arrives early (later) at channel i than channel j . The value of Δt_{ij} is proportional to the travel distance of the force trigger signal. In the ABC layout, the FPGA is in the middle of the board, and there are four CATIROCs in each side; the FPGA distributes the force-trigger first to one half board (channel 64~127), then to the other half board (channel 0~63); within one CATIROC, the force-triggers arrive at each channel chronologically according to the channel number, as illustrated in Fig.7.7. The clear chronological order (a few hundreds ps) of the trigger distribution indirectly reflects the good time resolution of the QDS.

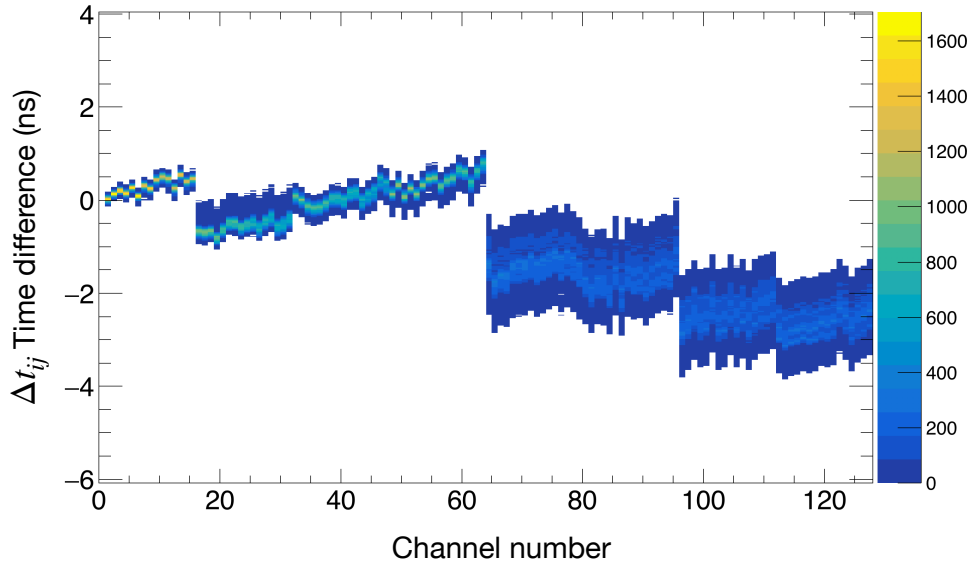


Figure 7.7 – Time difference Δt_{ij} with channel 0 as the reference channel ($j=0$) under the force trigger mode for 128 channels in the QDS. The x-axis is the channel i number from 1 to 127. The mean value the Δt_{ij} represents the chronological order of the force-trigger distribution. The standard derivation of Δt_{ij} represents the CATIROC time resolution with the existence of the channel-to-channel systematics. The fine time calibration is applied channel by channel for calculating Δt_{ij} .

The time resolution can be represented by the standard derivation of the Δt_{ij} distribution, i.e. $\sigma_{\Delta t_{ij}}$. Fig.7.8 shows three examples of the Δt_{ij} distribution. If the two channels are within the same CATIROC, the $\sigma_{\Delta t_{ij}}$ is about 50 ps; if two channels are within the same half board, but different CATIROC, $\sigma_{\Delta t_{ij}}$ is about 100 ps; as for two channels in the two different half boards, the $\sigma_{\Delta t_{ij}}$ is about 300 ps and there are several peaks in the Δt_{ij} distribution dominated by the channel-to-channel systematics in this case. The exact reason for this multiple peaks structure remains unknown. One possible reason could be related to the force trigger distribution. Since the force trigger goes across from one half board to the other, one reasonable guess is that some systematic effects exist in the across region between the two half boards and cause some uncertainties in the time measurement. If the reason is exactly only related to the force trigger distribution, the multiple peaks structure will unlikely affect the time resolution in the auto-trigger mode used in the physics case, because it does not experience such a force trigger distribution. Otherwise, this multiple peaks structure should be seriously investigated.

Nevertheless, the time resolution represented by the $\sigma_{\Delta t_{ij}}$ is within 300 ps which is much smaller than the PMT transit time spread (~ 5 ns).

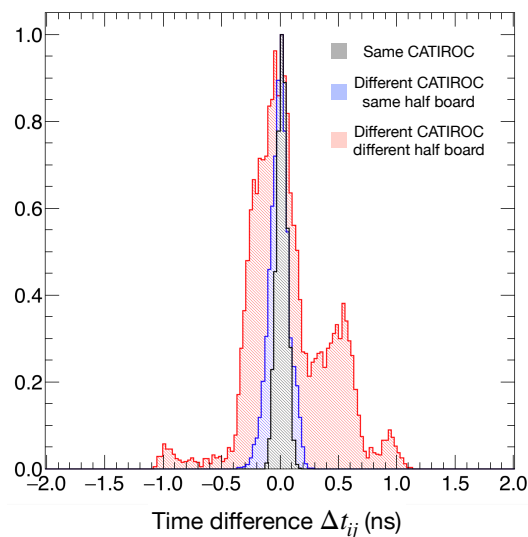


Figure 7.8 – Three examples of the Δt_{ij} for 1.) two channels within the same CATIROC (black), 2.) two channels within the same half board but different CATIROCs (blue) and 3.) two channels at different half boards (red). The multiple peaks structure in case 3.) shows some unknown systematic effects possibly due to the force-trigger distribution when the trigger goes across the two half boards.

There is another way to investigate the time resolution of the QDS, and that is to compute the time difference between two successive events within one channel under a fixed trigger rate, defined as:

$$\delta t_{k+1,k} = t((k_{trigger} + 1), i_{channel}) - t(k_{trigger}, i_{channel}). \quad (7.4)$$

Being opposite to the Δt_{ij} , the $\delta t_{k+1,k}$ is insensitive to the channel-to-channel systematics but sensitive to the jitter in the pulse generator. Due to the existence of a large jitter (~ 500 ps) in the pulse generator for this test, the time resolution was not able to be investigated with $\delta t_{k+1,k}$. However, a similar study was performed by the collaborators and less than 150 ps time resolution was observed [204].

7.2.1.5 Stability

The stability of the ABC board can be monitored through the pedestal. Under the force trigger mode, the stability of the pedestal mean value and the width were monitored for 16 days with in-continuous data taking but same configurations including the trigger configuration, ABC configuration, environment of experiment, etc.

During the 16 days monitoring, the pedestal mean values for different channels within one CATIROC move with approximately the same pattern (common move) corresponding to each restarting of the ABC board as illustrated in Fig.7.9. The common move exists differently in each CATIROC. Despite that, the pedestal mean value variation is small and at 0.3% level for all channels. The pedestal width variation is within 5% during the 16 days observation. This information aids both to characterize the intrinsic stability of the electronics and to define the possible pedestal calibration frequency of the experiment.

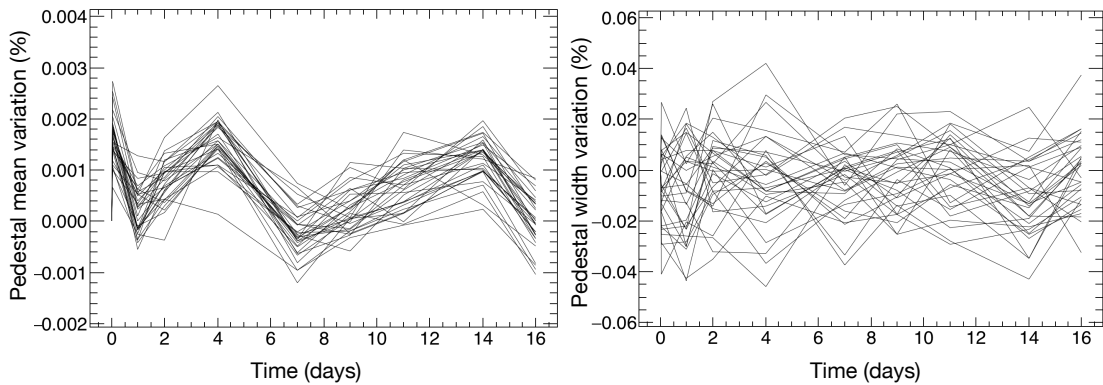


Figure 7.9 – Pedestal stability during 16 days observation. Left: pedestal mean value variation. The variation is at 0.3% level and the variation is largely common for all the channels within the same CATIROC. The common move corresponds to each restarting of the ABC board. Right: pedestal width variation; the pedestal width variation is within 5%. Both 16 ping and 16 pong channels of one CATIROC are shown. The similar behavior was observed in all the other CATIROCs of the ABC board even though the common move patterns for different CATIROC are different.

7.2.1.6 Unexpected Feature with High Loading

During the ABC test, an unexpected feature in the QDS was observed as illustrated in Fig.7.10. This feature can be described as the “quasi periodic fake charge” appearing in the full charge range (0~1023 ADC unit), while there should be only the charge distribution within an expected charge range.

Since the reason causing this feature remains unknown but under investigation, here the observations related to this unexpected feature are listed as follows:

- 1.) The same unexpected feature of Fig.7.10 appears under different trigger configurations including the auto-trigger with high rate, the external-trigger with high rate, the combination of external-trigger and force-trigger, etc.

- 2.) This unexpected feature seems related to the loading of the CATIROC. The loading is defined as the multiplication between the trigger rate and the number of enabled

channels. The trigger rate can be understood as $1/\delta t$, where δt is the time difference between two successive triggers. When the loading is high, e.g. 200 kHz trigger rate with 16 enabled channels or random trigger rate with the chance of $\delta t \rightarrow 0$ (i.e. effectively high rate), the unexpected feature of Fig.7.10 will appear.

3.) Even though the unexpected feature appears, the sanity words "00000" are correct in QDS. This implies that the data in the QDS is not misaligned. There are two places where this can take place, i.e. the actual CATIROC data encoder (i.e. a hardware problem) and/or the CATIROC-to-FPGA data conversion by the firmware. These two scenarios are under investigation.

4.) With the existence of this unexpected feature, the discriminator data stream works correctly, or at least nothing beyond the expectation was observed. This suggests that the hardware discriminator and the firmware again works as expected.

These observations imply that potentially there may be some issues of handling high loading configuration is the QDS. The origin of the unexpected feature was not fully understood and the solution to handle this issue is under investigation but beyond the scope of this thesis work. However, as will be demonstrated next, the DDS complete functionality of the ABC works as expected. So, this issue affects only a fraction of the readout.

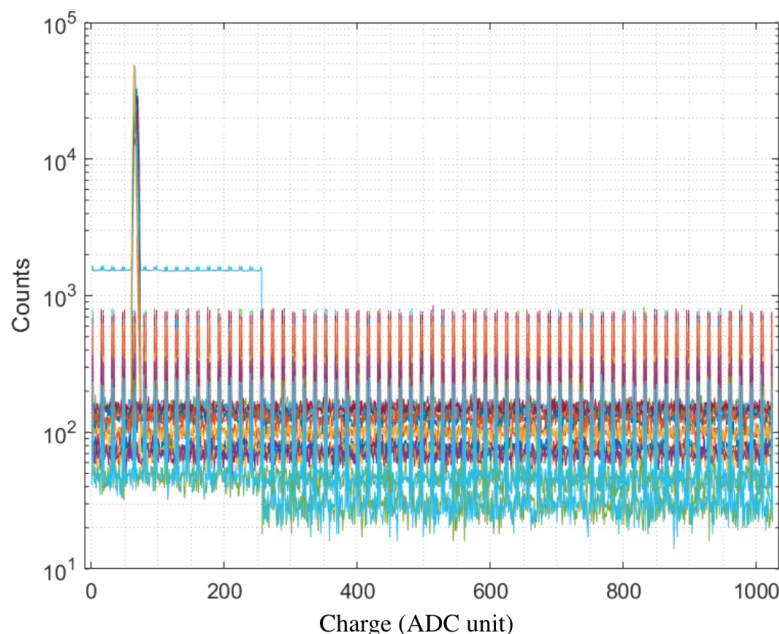


Figure 7.10 – Unexpected feature with high loading in QDS. With the high loading in the CATIROC, the unexpected “fake charge” appears quasi periodically in the full charge range (0~1023 ADC unit). The expected charge distribution is the high statistics peak in the range from ~ 50 to ~ 100 ADC unit. Different color corresponds to different channels.

7.2.2 Discriminator Data Stream

The DDS is not an intrinsic feature of the CATIROC standard readout strategy, but an innovation designed by the APC/IJCLab teams for the ABC board specific for JUNO SPMT system. The DDS contains the digital PE counting information, the time of each signal and the time over threshold of the signal pulse. As the deadtime of the DDS (<100 ns) is much smaller than that of the QDS (i.e. ~ 6 μ s for a single channel, ~ 9 μ s for the full CATIROC), the DDS is capable to handle higher event rate. The data format of the DDS [207] is:

$$\begin{aligned}
 & \text{"10"} \text{ (2 bits)} - \text{"Edge"} \text{ (1 bits)} - \text{"Channel.Nb"} \text{ (4 bits)} - \text{"Event Counter"} \text{ (25 bits)} \\
 & - \text{"Time stamp"} \text{ (26 bits)} - \text{"Fine Time"} \text{ (6 bits)} - \text{"00000 Sanity"} \text{ (5 bits)} \\
 & - \text{"ASIC.Nb"} \text{ (3 bits)} - \text{"Card.Nb"} \text{ (8 bits)}, \tag{7.5}
 \end{aligned}$$

where the "10" is the identifier of the DDS and "00000 Sanity" can be used to check if data is misaligned.

7.2.2.1 Digital PE Counting

When the DDS is enabled, under the external trigger mode, the noise is sampled and recorded digitally in the DDS, as illustrated in Fig.7.11. In comparison with the recorded events in the QDS, the DDS is able to count digitally all the events without failure.

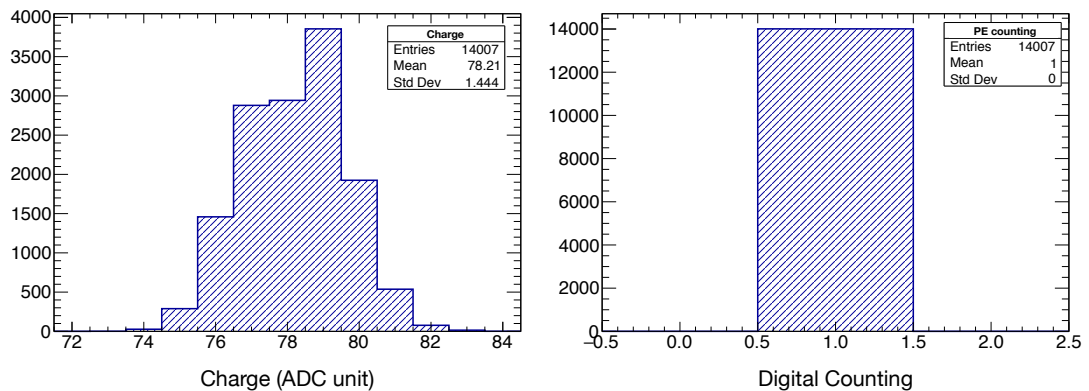


Figure 7.11 – The digital counting in the DDS (right) in comparison with the charge measurement in the QDS (left). 1 kHz external trigger is applied. All the events are successfully recorded by both the QDS in terms of charge and DDS in terms of digital counting. The histograms correspond to only one channel. But the results for all the other channels are the same.

7.2.2.2 Timing

The embedded time to digital converters (TDC) in the FPGA allows the time sampling with 1 ns precision. The time of a signal pulse is sampled two times, i.e. at the falling and rising detected edges of the pulse respectively. It means that not only the

arrival time of the signal pulse but also the time over threshold information (i.e. pulse width) can be recorded.

In practice, the timing information can be recorded either 1.) in the format of the two edges (160 bits) where the difference between the two edges corresponds to the time over threshold, or 2.) in the format of the falling edge with the interval between the two edges (80 bits) which is computed in the FPGA.

The time over threshold (or the pulse width) can be used to estimate the charge of the input signal pulse, which is complementary to the QDS measurement of the pulse amplitude.

For testing the timing properties of the DDS, under the auto-trigger mode, an input signal with 6 ns falling time, 6 ns rising time and 12 ns width is injected into one channel, and the measured time over threshold is about 17 ns within the expected range (12~24 ns), as illustrated in Fig.7.12. For testing the whole board, the force-trigger is used to sample the noise, the results indicate that each sampling by the force-trigger is about 20 ns as illustrated in Fig.7.13.

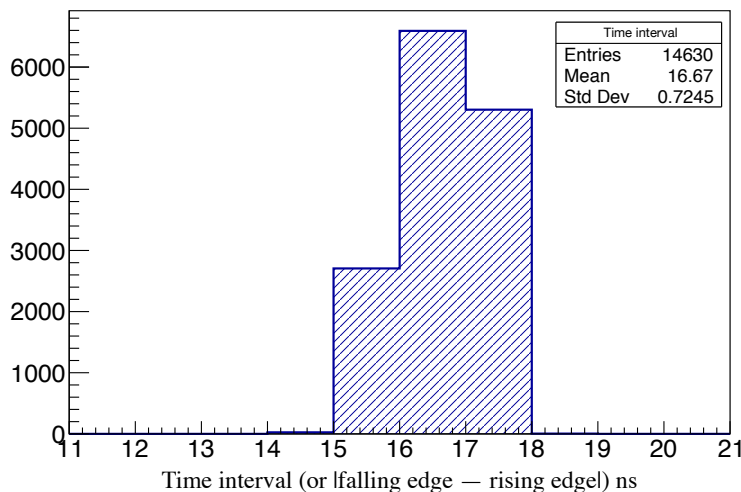


Figure 7.12 – Time over threshold measurement in DDS for one channel. The auto-trigger mode is enabled. The injected signal has 6 ns falling time, 6 ns rising time and 12 ns width. The expected time over threshold is in the range of 12~24 ns. The measured time over threshold is about 17 ns within the expectation.

Similar to the QDS, the time resolution of the DDS can be estimated with the Δt_{ij} under the force-trigger mode as illustrated in Fig.7.14. It is worth to point out that the value of Δt_{ij} in the DDS also indicates a chronological order of the trigger distribution, i.e. the force trigger is first distributed to one half board (channel 64~127) then to the other half board(channel 0~63). The chronological order in the DDS is consistent with that in the the QDS as illustrated in Sec.7.2.1.4. However, due to the relative poor time precision (1 ns), the chronological orders by CATIROC and by channel observed in QDS are not observed in DDS. The typical standard derivation of the Δt_{ij} ($\sigma_{\Delta t_{ij}}$) distribution in the DDS is about 500 ps.

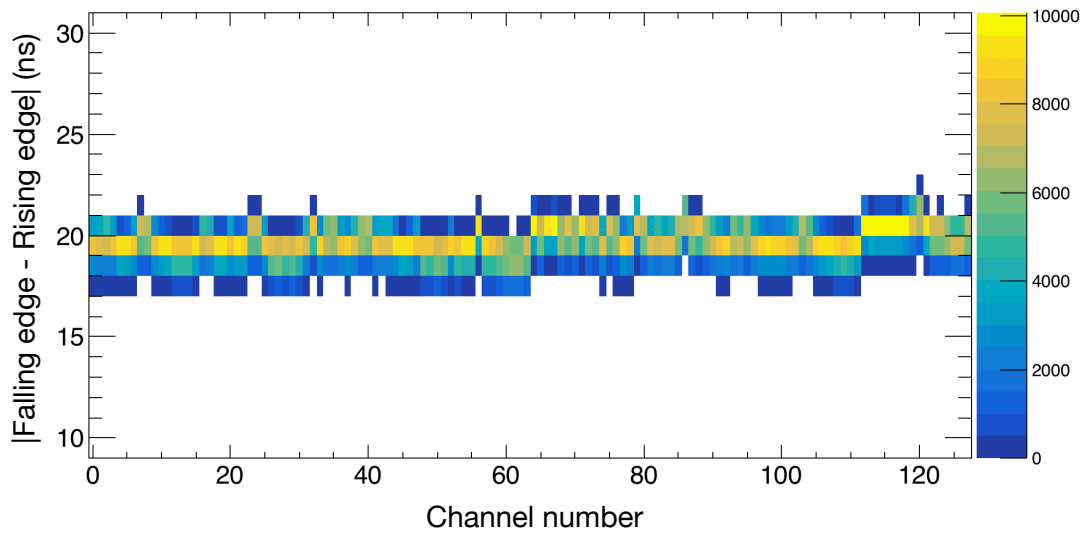


Figure 7.13 – Time difference between the falling edge and the rising edge under the force-trigger mode in the DDS. The force-trigger sampling time is about 20 ns.

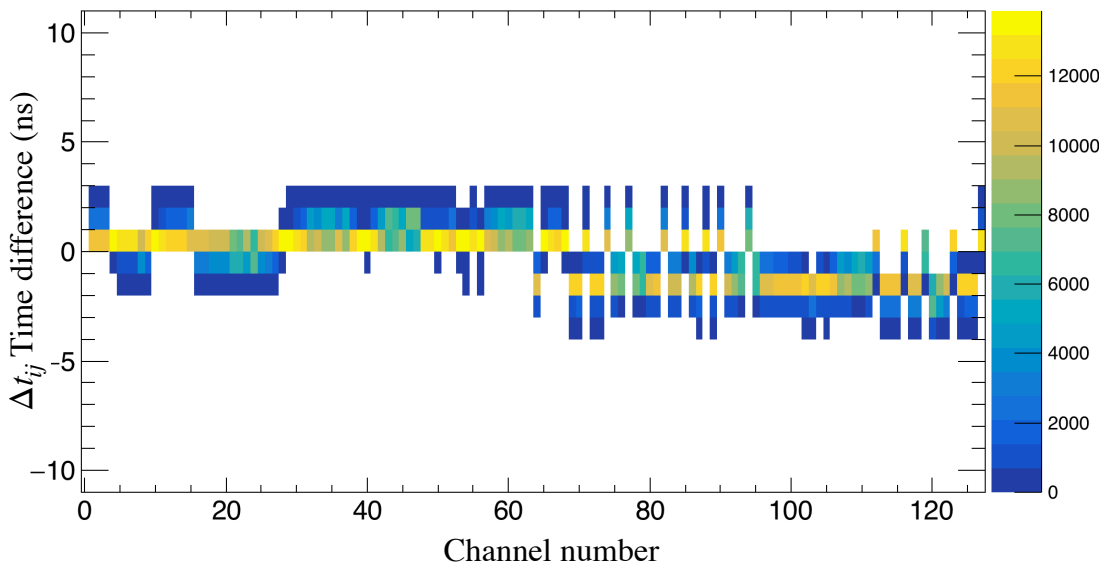


Figure 7.14 – Time difference Δt_{ij} with channel 0 as the reference channel ($j=0$) under the force trigger mode for 128 channels in the DDS. The x-axis is the channel i number from 1 to 127. A chronological order is observed, i.e. the force trigger is first distributed to one half board (channel 64~127), then to the other half board (channel 0~63). The standard derivation of Δt_{ij} is typically 500 ps.

7.2.2.3 High Trigger Rate Handling

Under the auto-trigger mode, a periodic signal with high rate is injected into one channel. If the injected signal rate surpasses the deadtime of the QDS ($6\mu\text{s}$ for one channel occupation), some events can not be recorded by the QDS, but they can still be counted by the DDS. As illustrated in Fig.7.15, when the signal rate is beyond ~ 200 kHz, some events are lost in the QDS, but these events are well registered in the DDS; however, limited by the bandwidth of the data transferring in ABC version 0 (USB 2), the testing rate can only reach 500 kHz. With the new version of the ABC board (version 1) having higher bandwidth for data transfer, a complete DDS high trigger rate handling test with the signal rate upto 10 MHz should be planned.

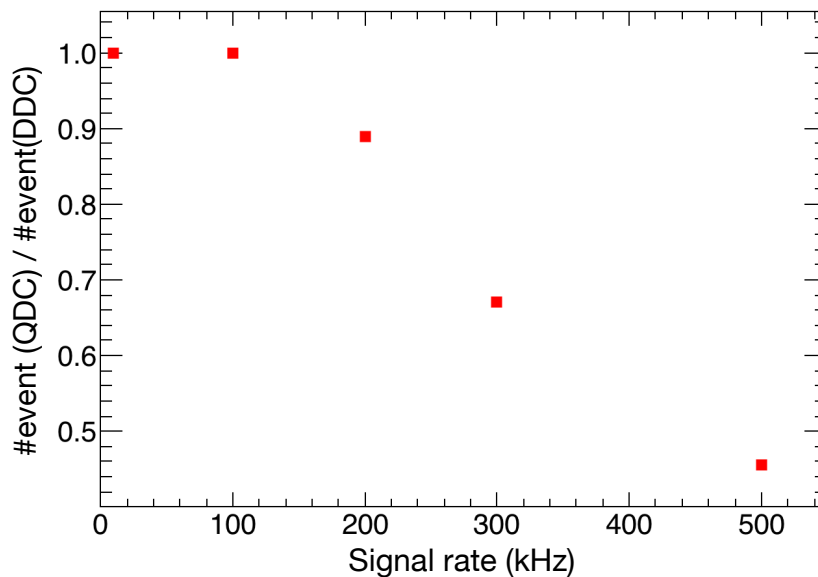


Figure 7.15 – The high trigger rate handling with the DDS for one channel. A periodic signal generated by a signal generator is injected into one channel. The x-axis is the injected signal rate. The y-axis is the ratio between the number of events recorded in the QDS and that in the DDS. Starting from ~ 200 kHz some events are lost in the QDS due to its deadtime. Up to 500 kHz, there is no signal loss in the DDS.

7.3 Summary

The electronics tests done in this thesis preliminarily validated the functionalities of the PE counting, time, charge measurements, etc. in the QDS and DDS of the ABC version 0. The DDS works smoothly and provide the necessary information for PE counting providing the essential information for the Dual Calorimetry calibration. The charge information about the pulse amplitude in the QDS and the time over threshold information provided by DDS are both reachable, thus helping the charge measurement for multi-PE events. The time resolution of the QDS is measured preliminarily less than 300 ps despite some features potentially related to the trigger distribution to be understood. The time resolution of the DDS is measured preliminarily at 500 ps level. These testing results indicate that the performance of the ABC version 0 can fulfill the requirement for the Dual Calorimetry and also physics measurement.

However, several questions need to be further investigated, including the unexpected feature with the high loading in the QDS (standard readout of the CATIROC chip) and the multiple peaks structure while investigating the time resolution of the QDS. Another important feature is the grouping of every 16 SPMTs. Since each CATIROC has only one common trigger threshold for 16 SPMTs, the grouping of 16 SPMTs with similar parameters such as high voltage and charge resolution needs to be investigated according to the PMT testing results. The pre-amplifier gain of each channel can be adjusted individually in the CATIROC, thus it can be used to compensate the different responses of different PMTs operated with the similar high voltage.

These electronics testing results in this thesis are also used to help the electronics engineers to improve the ABC firmware and software development, as well as the design of the ABC version 1. More electronics tests in combination with the SPMTs, high voltage splitter board and other electronics components are ongoing with the collaboration effort towards the SPMT system pre-commissioning¹, installation and on-site commissioning.

1. There is a prototype detector, called *JINO*, under construction at IJCLab. It will be used for the pre-commissioning of the SPMT readout and the proof-of-principle demonstration of the Dual Calorimetry.

Chapter 8

Neutrino Mass Ordering Synergy between JUNO and LB ν B

8.1 Motivation

The JUNO intrinsic neutrino mass ordering (MO) resolution is at 3σ level from the spectral analysis where the energy control has greatest importance as elaborated in Sec.2.1.6. The Dual Calorimetry, as demonstrated in Chapter 6, can contribute the energy control, hence the intrinsic MO measurement at JUNO. Besides, JUNO is the unique experiment investigating the MO through the reactor neutrinos in vacuum driven oscillation. It is complementary to the matter effects driven MO experiments including the long baseline neutrino beam (LB ν B) experiments and atmospheric neutrino experiments. There exist synergies between JUNO and other MO experiments and these are also addressed in this thesis in addition to the Dual Calorimetry study.

Several studies have investigated the MO synergy between JUNO and other MO experiments. For instance, a JUNO MO sensitivity study with external $\Delta m_{\mu\mu}^2$ information coming from the disappearance channel of LB ν B can be found in Ref.[130], and the combined MO sensitivity study between JUNO and IceCube-Upgrade/PINGU can be found in Ref.[209].

For the purpose of investigating a possible strategy of the earliest MO resolution $\geq 5\sigma$ according to the time scale of JUNO, a dedicated study of combining the JUNO and LB ν B experiments was performed during the thesis. This study exploits the MO synergy between JUNO and the current generation LB ν B experiments (i.e. T2K and NOvA). It also explores the prospect of a fully resolved MO only based on vacuum driven oscillations. In addition, this study has considered possible data fluctuation and key ambiguity in order to obtain a realistic estimation of the MO resolution.

The MO study during the thesis was initiated for understanding different MO determination mechanisms, the complementarity and synergy among different approaches. Then it was developed to investigate a possible strategy for the resolved MO solution $\geq 5\sigma$ by combining JUNO and the potentially available LB ν B data according to JUNO timeline. In cooperation with several collaborators from JUNO, NOvA, DUNE and HyperK, this study finally became a dedicated paper submitted to arXiv [210] in the end of August, 2020, and it is planned to be submitted for publication later. This chapter presents this MO synergy study directly in the format of the paper.

8.2 Publication: Earliest Resolution to the Neutrino Mass Ordering?

Earliest Resolution to the Neutrino Mass Ordering?

Anatael Cabrera^{*1,2,4}, Yang Han^{†1,2}, Michel Obolensky¹, Fabien Cavalier², João Coelho², Diana Navas-Nicolás², Hiroshi Nunokawa^{‡2,7}, Laurent Simard², Jianming Bian³, Nitish Nayak³, Juan Pedro Ochoa-Ricoux³, Bedřich Roskovec³, Pietro Chimenti⁵, Stefano Dusini^{6a}, Marco Grassi^{6b}, Mathieu Bongrand^{8,2}, Rebin Karaparambil⁸, Victor Lebrin⁸, Benoit Viaud⁸, Frederic Yermia⁸, Lily Asquith⁹, Thiago J. C. Bezerra⁹, Jeff Hartnell⁹, Pierre Lasorak⁹, Jiajie Ling¹⁰, Jiajun Liao¹⁰, and Hongzhao Yu¹⁰

¹APC, CNRS/IN2P3, CEA/IRFU, Observatoire de Paris, Sorbonne Paris Cité University, 75205 Paris Cedex 13, France

²IJCLab., Université Paris-Saclay, CNRS/IN2P3, 91405 Orsay, France

³Department of Physics and Astronomy, University of California at Irvine, Irvine, California 92697, USA

⁴LNCA Underground Laboratory, CNRS/IN2P3 - CEA, Chooz, France

⁵Departamento de Física, Universidade Estadual de Londrina, 86051-990, Londrina - PR, Brazil

^{6a}INFN, Sezione di Padova, via Marzolo 8, I-35131 Padova, Italy

^{6b}Dipartimento di Fisica e Astronomia, Università di Padova, via Marzolo 8, I-35131 Padova, Italy

⁷Department of Physics, Pontifícia Universidade Católica do Rio de Janeiro, Rio de Janeiro, RJ, 22451-900, Brazil

⁸SUBATECH, CNRS/IN2P3, Université de Nantes, IMT-Atlantique, 44307 Nantes, France

⁹Department of Physics and Astronomy, University of Sussex, Falmer, Brighton BN1 9QH, United Kingdom

¹⁰Sun Yat-sen University, NO. 135 Xingang Xi Road, Guangzhou, China, 510275

August 27, 2020 – v3.5

We hereby illustrate and numerically demonstrate via a simplified *proof of concept* calculation tuned to the latest average neutrino global data that the combined sensitivity of JUNO with NOvA and T2K experiments has the potential to be the first fully resolved ($\geq 5\sigma$) measurement of neutrino Mass Ordering (MO) around 2028; tightly linked to the JUNO schedule. Our predictions account for the key ambiguities and the most relevant $\pm 1\sigma$ data fluctuations. In the absence of any concrete MO theoretical prediction and given its intrinsic binary outcome, we highlight the benefits of having such a resolved measurement in the light of the remarkable MO resolution ability of the next generation of long baseline neutrino beams experiments. We motivate the opportunity of exploiting the MO experimental framework to scrutinise the standard oscillation model, thus, opening for unique discovery potential, should unexpected discrepancies manifest. Phenomenologically, the deepest insight relies on the articulation of MO resolved measurements via at least the two possible methodologies *matter effects* and purely *vacuum* oscillations. Thus, we argue that the JUNO vacuum MO measurement may feasibly yield full resolution in combination to the next generation of long baseline neutrino beams experiments.

The discovery of *neutrino* (ν) *oscillations* phenomenon have completed a remarkable scientific endeavour lasting several decades that has changed forever our understanding of the phenomenology of the leptonic sector of the *standard model of elementary particles* (SM). A few modifications were accommodated to account for the new phenomenon [1]. This means the manifestation of massive neutrinos and leptonic mixing along with an embedded mechanism for the intrinsic difference between ν and $\bar{\nu}$ due to the violation of charge conjugation parity symmetry, or CP-violation (CPV); e.g. review [2].

Neutrino oscillations imply that the neutrino mass eigenstates (ν_1, ν_2, ν_3) spectrum is non-zero and non-degenerate, so at least two neutrinos are massive. Each mass eigenstate (ν_i ; with $i=1,2,3$) can be regarded as a

non-trivial mixture of the known neutrino flavour eigenstates (ν_e, ν_μ, ν_τ) linked to the three (e, μ, τ) respective charged leptons. Since no significant experimental evidence beyond three families exists so far, the mixing is characterised by the 3×3 so called *Pontecorvo-Maki-Nakagawa-Sakata* (PMNS) [3, 4] matrix, assumed unitary, thus parametrised by three independent mixing angles ($\theta_{12}, \theta_{23}, \theta_{13}$) and one CP phase (δ_{CP}). The neutrino mass spectra are indirectly known via the two measured *mass squared differences* indicated as $\delta m_{21}^2 (\equiv m_2^2 - m_1^2)$ and $\Delta m_{32}^2 (\equiv m_3^2 - m_2^2)$, respectively, related to the ν_2/ν_1 and ν_3/ν_2 pairs. The neutrino absolute mass is not directly accessible via neutrino oscillations and remains unknown, despite major active research [5].

As of today, the field is well established both exper-

* Contact: anatael@in2p3.fr

† Contact: yang.han@apc.in2p3.fr

‡ Contact: nunokawa@puc-rio.br

imentally and phenomenologically. All key parameters (θ_{12} , θ_{23} , θ_{13} and δm_{21}^2 , Δm_{32}^2) are known to the few percent precision. The δ_{CP} phase and the sign of Δm_{32}^2 , the so called Mass Ordering (MO), remain unknown despite existing hints (i.e. $<3\sigma$ effects). CPV arises if δ_{CP} is different from 0 or $\pm\pi$; i.e. CP-conserving solutions. The unique binary MO measurement outcome means the resolution between the *normal* (NMO) and *inverted* (IMO) mass ordering, respectively implying positive (or $\Delta m_{32}^2 > 0$) or negative (or $\Delta m_{32}^2 < 0$) signs. NMO implies ν_3 is heavier than ν_2 , while IMO is the opposite. The resolution of the positive sign of δm_{21}^2 is known from solar neutrino data [6, 7, 8, 9, 10] combined with KamLAND [11], thus establishing the solar large mixing angle MSW [12, 13] solution.

Mass Ordering Knowledge

This publication focuses on the global strategy to achieve the earliest and most robust MO determination scenario. MO has rich implications not only for the terrestrial oscillation experiments, to be discussed in this paper, but also from a fundamental theoretical, e.g. see review [14], an astrophysical, e.g. see review [15], and a cosmological, e.g. see review [16], points of view. Preliminary knowledge from global data [5, 17, 18, 19] implies a few σ hints on both MO and δ_{CP} , where the latest results were reported at *Neutrino 2020 Conference* [20]. According to latest NuFit5.0 [21] global data analysis, NMO is favoured up to 2.7σ . However, this preference remains fragile, as it will be explained later on.

Experimentally, MO can be addressed via three very different techniques (see e.g. [22] for earlier work): a) medium baseline reactor experiment (i.e. JUNO) b) long baseline neutrino beams (labelled here LBνB) and c) atmospheric neutrino based experiments. LBνB and atmospheric rely heavily on *matter effects* [12, 13] as neutrinos traverse the Earth over long enough baselines. Anti-neutrinos exhibit the opposite effect since the planet is made of matter (not anti-matter). Instead, JUNO is the only experiment able to resolve MO via *vacuum* dominant¹ oscillations, thus holding a unique insight and role in the MO world strategy. This implies complementarity and possible synergies among the different techniques. The scenario for possible discrepancies is not negligible since the experimental setups and observables are not fully redundant. Indeed, new physics may manifest as differences in the binary outcome of, at least, two well resolved MO measurements.

The relevant LBνB experiments are the running

LBνB-II², both NOvA [27] and T2K [28] experiments. These are to be followed up by the next generation LBνB-III with DUNE [29] and the Hyper-Kamiokande (HK) [30] experiments, which are expected to start taking data around 2027. The possibility of the second HK detector, in Korea, would enhance its MO determination sensitivity [31]. We will here focus mainly on the immediate impact of the LBνB-II. Nonetheless, we shall highlight the prospect contributions by LBνB-III, due to their leading order implications to the MO resolution. The relevant atmospheric neutrino experiments are Super-Kamiokande [32] (SK) and IceCube [33] (both running) as well as future specialised facilities such as INO [34], ORCA [35] and PINGU [36]. Compared to LBνB, one advantage is that of probing many baselines simultaneously but one disadvantage is the larger uncertainties in both baseline and energy reconstruction. The HK experiment may also offer key MO insight via atmospheric neutrinos. Contrary to all those experiments, JUNO [37] relies on high precision spectral analysis with reactor neutrinos for the extraction of MO sensitivity.

Despite their different MO sensitivity potential and time schedules (discussed in the end), it is worth highlighting the complementarity of each techniques as a function of the most important neutrino oscillation unknowns today. In terms of θ_{23} , the dependence is limited by the so called *octant ambiguity*³ [38]. The MO sensitivity of atmospheric experiments is heavily dependent on this ambiguity solution while LBνB exhibit a smaller dependence. JUNO is totally independent; a unique asset. In terms of the unknown δ_{CP} , its role in atmospheric and LBνB's inverts, while JUNO remains again uniquely independent. This way, the MO sensitivity dependence on δ_{CP} is less important for atmospheric (i.e. washed out) but LBνB are largely handicapped by the degenerate phase-space competition to resolve simultaneously both δ_{CP} and MO. In brief, while the MO sensitivity of ORCA/PINGU swings from 3σ to about 5σ based on the value of θ_{23} , LBνB-II sensitivities are effectively blinded to MO for more than half of the δ_{CP} phase-space. DUNE though has the unique ability to resolved MO, also via matter effects only, regardless of δ_{CP} . Although not playing an explicit role, the constraint on θ_{13} , from reactor experiments (Daya Bay [39], Double Chooz [40] and RENO [41]), is critical for the MO (and δ_{CP}) quest for both JUNO and LBνB experiments.

This publication aims to illustrate, and numerically demonstrate, via a simplified proof-of-concept estimation, the most important ingredients to reach a fully

¹JUNO has a minor matter effect impact, mainly on the δm_{21}^2 oscillation while tiny on MO sensitive Δm_{32}^2 oscillation [23].

²The first generation LBνB-I are here considered to be K2K [24], MINOS [25] and OPERA [26] experiments.

³This implies the approximate degeneracy of oscillation probabilities for the cases between θ_{23} and $(\pi/4 - \theta_{23})$.

resolved (i.e. $\geq 5\sigma$) MO measurement strategy relying, whenever possible, only on existing (or imminently so) experiments to yield the fastest timeline⁴. Our approach relies on the latest 3ν global data information [21], summarised in Table 1, to tune our analysis to the most probable and up to date measurements on θ_{23} , δ_{CP} and Δm_{32}^2 , using only the LB ν B inputs, as motivated later.

NuFit5.0	δm_{21}^2	$\sin^2 \theta_{12}$	$\sin^2 \theta_{13}$
Both MO	$7.42 \times 10^{-5} \text{ eV}^2$	0.304	0.0224
LB ν B	Δm_{32}^2	$\sin^2 \theta_{23}$	δ_{CP}
NMO	$2.411 \times 10^{-3} \text{ eV}^2$	0.565	-0.91π
IMO	$-2.455 \times 10^{-3} \text{ eV}^2$	0.568	-0.46π

Table 1: In this work, the neutrino oscillation parameters are reduced to the latest values obtained in the NuFit5.0 [21], where Δm_{32}^2 , $\sin^2 \theta_{23}$ and δ_{CP} were obtained by using only LB ν B experiments by fixing δm_{21}^2 , $\sin^2 \theta_{12}$ and $\sin^2 \theta_{13}$ to the values shown in this table.

We also aim to highlight some important redundancies across experiments that could aid not only the robustness of the MO resolution but also to exploit – likely for the first time – the MO measurements for high precision scrutiny of the standard 3ν flavour scheme. This way, MO exploration might open the potential for manifestations of beyond the standard model (BSM) physics; e.g. see reviews [42, 37]. Our simplified approach is expected to be improvable by more complete developments to yield further accuracy, once data is available. Such developments though are considered beyond our scope. We think those are unlikely to significantly change our findings and conclusions, given the level of precision available today. In order to better accommodate the known limitations of our approach, we have intentionally err to a conservative rationale, so that our conclusions are more likely to be only reinforced by future studies and additional information. We shall elaborate these points further during the final results discussion.

Mass Ordering Resolution Analysis

Our analysis relies on a simplified combination of experiments able to yield MO sensitivity intrinsically (i.e. standalone) and via an inter-experiment synergies, where the gain may be direct or indirect. The indirect gain implies that the sensitivity improvement occurs due to the combination itself; i.e. hence not accessible to neither experiment alone but caused by the complementary nature of the observables provided by the different experiments. These effects will be carefully studied as a function of the delicate dependences to ensure the most

accurate prediction. The existing synergies embody a framework for powerful sensitivity boosting to yield MO resolution upon combination. To this end, we shall combine the running LB ν B-II experiments together with the shortly forthcoming JUNO. The valuable additional information from atmospheric experiments will be considered qualitatively, for simplicity, only at the end during the discussion of results. Unless otherwise stated explicitly, throughout this work, we shall use only the NuFit5.0 best fit values summarised in Table 1, to guide our estimations and predictions by today’s data.

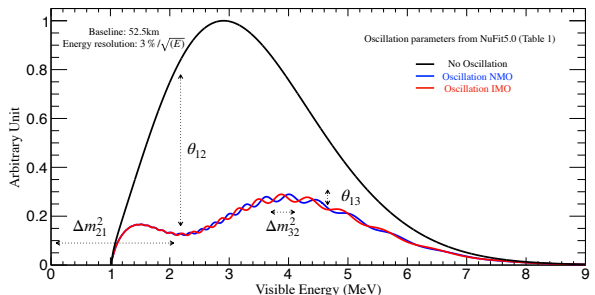


Figure 1: **JUNO Neutrino Bi-Oscillation Spectral Distortion.** JUNO was designed to exploit the spectral distortions from two oscillations simultaneously manifesting via reactor neutrinos in a baseline of ~ 52 km. The slow and large amplitude ($\sin^2 2\theta_{12}/2 \approx 42\%$) disappearance oscillation is driven by θ_{12} and δm_{21}^2 with a minimum at ~ 2 MeV. The fast and smaller amplitude ($\sin^2 2\theta_{13}/2 \approx 5\%$) disappearance oscillation is driven by θ_{13} and Δm_{32}^2 instead. The frequency pattern of the θ_{13} oscillation depends on the sign of Δm_{32}^2 , thus directly sensitive to mass ordering (MO) via only *vacuum* oscillations. This is a unique and complementary feature to all other MO experiments, regardless of their final sensitivity. JUNO’s high statistics allows shape-driven neutrino oscillation parameter extraction, with minimal impact from rate-only systematics. Hence, high precision is possible without the need of permanent reactor flux monitoring; often referred as *near detector*(s). JUNO’s shape analysis relies on the excellent control of reactor reference spectrum, implying high resolution, energy scale control and a robust data-driven reference spectrum obtained with the TAO detector.

Mass Ordering Resolution Power in JUNO

JUNO experiment [37] is one of the most powerful neutrino oscillation high precision machines as well as the first experiment able to exhibit the spectral distortion due to two simultaneous oscillations; i.e. a *bi-oscillation* pattern, driven by “solar” δm_{21}^2 and “atmospheric” Δm_{32}^2 . The JUNO spectral distortion effects are described in Figure 1 and its data-taking is to start by late 2022 [43]. Complementary 3ν interference ef-

⁴The timelines of experiments is a complex subject, as the construction schedules may delay beyond the control of the scientific teams. Our approach aims to provide a minimally timing information to contextualise the experiments but variations may be expected.

fects, such as those enabling the δ_{CP} manifestation, are exploited by the LBνB experiments. JUNO alone can yield the most precise measurements of θ_{12} , δm_{21}^2 and $|\Delta m_{32}^2|$, at the level of $\leq 1\%$ precision for the first time. This implies JUNO is to lead the measurements of about half (i.e. three out of six) of the parameters in the field.

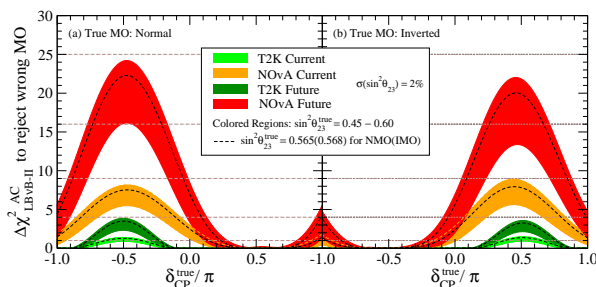


Figure 2: **LBνB-II Mass Ordering Sensitivity.** The Mass Ordering (MO) sensitivity of LBνB-II experiments via the appearance channel (AC), constrained to a range of θ_{23} , is shown as a function of the true value of δ_{CP} . The bands represent the cases where the true value of $\sin^2 \theta_{23}$ lies within the interval $[0.45, 0.60]$ with a relative experimental uncertainty of 2%. The $\sin^2 \theta_{23} = 0.60$ (0.45) gives the maximum (minimum) sensitivity for a given value of δ_{CP} . The NuFit5.0 best fitted $\sin^2 \theta_{23}$ value is indicated by the black dashed curves. The NMO and IMO sensitivities are illustrated respectively in the (a) and (b) panels. The sensitivity arises from the fake CPV effect due to matter effects, which are proportional to the baseline (L). The strong dependence on δ_{CP} is due to the unavoidable degeneracy between NMO and IMO, thus causing the sensitivity to swigs by 100%. T2K, now (light green) and future (dark green), exhibits very small intrinsic sensitivity due to its shorter baseline ($L_{\text{T2K}} = 295$ km). Instead, NOvA, now (orange) and future (red), hold leading order MO information due to its larger baseline ($L_{\text{NOvA}} = 810$ km). The future full exposure for T2K and NOvA imply a $\sim 3\times$ more statistics relative to today's. NOvA is unfortunately not expected to resolve (i.e. reach $\Delta\chi^2 \geq 25$) alone. These curves are referred as $\Delta\chi^2_{\text{LB}\nu\text{B}}^{\text{AC}}$ and were derived from data as detailed in Appendix A.

JUNO has been however designed to yield a unique MO sensitivity via vacuum oscillation upon the spectral distortion 3ν analysis formulated in terms of δm_{21}^2 and Δm_{32}^2 (or Δm_{31}^2). JUNO's MO sensitivity relies on a challenging experimental articulation for the accurate control of the spectral shape related systematics arising from energy resolution, energy scale control (nonlinearities being the most important) and even the reactor reference spectra to be measured independently by the TAO project [44]. The nominal intrinsic MO sensitivity is $\sim 3\sigma$ ($\Delta\chi^2 \approx 9$) upon 6 years of data taking. All JUNO inputs follow the collaboration prescription [37]. Hence, JUNO is unable to resolve ($\Delta\chi^2 \geq 25$) MO alone. In our

simplified approach, we shall characterise JUNO by a simple $\Delta\chi^2 = 9 \pm 1$. The uncertainty aims to illustrate possible minor variations in the final sensitivity due to the experimental challenges behind.

Mass Ordering Resolution Power in LBνB-II

In all LBνB experiments, the intrinsic MO sensitivity arises via the *appearance channel* (AC), from the transitions $\nu_\mu \rightarrow \nu_e$ and $\bar{\nu}_\mu \rightarrow \bar{\nu}_e$; also sensitive to δ_{CP} . MO manifests as an effective *faked* CPV bias. This effect causes the oscillation probabilities to be different for neutrino and anti-neutrinos even under CP-conserving solutions. Disentangling the genuine (δ_{CP}) and the faked CPV terms is not trivial. Two main strategies exist based on the fake component, which is to be either a) minimised (i.e. shorter baseline, like T2K) enabling to measure only δ_{CP} or b) maximised (i.e. longer baseline) so that matter effects are strong enough to disentangle them from the δ_{CP} , and both can be measured simultaneously. The latter implies baselines >1000 km, best represented by DUNE (1300 km). NOvA's baseline (810 km) remains a little too short for a full disentangling ability. Still, NOvA remains the most important LBνB to date with sizeable intrinsic MO sensitivity due to its relatively large matter effects, as compared to T2K.

The current and future intrinsic MO sensitivities of LBνB-II experiments are shown in Figure 2, including their explicit θ_{23} and δ_{CP} dependences. The obtained MO sensitivities were computed using a simplified strategy where the AC was treated as *rate-only* (i.e. one-bin counting) analysis, thus neglecting any shape-driven sensitivity gain. This approximation is particularly accurate for off-axis beams (narrow spectrum) specially in the low statistics limit where the impact of systematics remains small (here neglected). The background subtraction was accounted and tuned to the latest experiments' data. To corroborate the accuracy of our estimate, we reproduced the LBνB-II latest results [20]; as detailed in **Appendix A**.

While NOvA AC holds major intrinsic MO information, it is unlikely to resolved ($\Delta\chi^2 \geq 25$) alone. This outcome is similar to that of JUNO. Of course, the natural question may be whether their combination could yield the full resolution. Unfortunately, as it will be shown, this is unlikely but not far. Therefore, in the following, we shall consider their combined potential, along with T2K, to provide the extra missing push. This may be somewhat counter-intuitive, since T2K has just been shown to hold very small intrinsic MO sensitivity; i.e. ≤ 4 units of $\Delta\chi^2$. Indeed, the role of T2K, along with NOvA, has an alternative path to enhance the overall sensitivity, which is to be described next.

Synergetic Mass Ordering Resolution Power

A remarkable synergy exist between JUNO and $\text{LB}\nu\text{B}$ experiments thanks to their complementarity [45, 46, 47, 37]. In this case, we shall explore the contribution via the $\text{LB}\nu\text{B}$'s disappearance channel (DC); i.e. the transitions $\nu_\mu \rightarrow \nu_\mu$ and $\bar{\nu}_\mu \rightarrow \bar{\nu}_\mu$. Again, this might appear counter-intuitive, since DC is practically blinded (i.e. a $<1\%$ effect) to MO; as proved in **Appendix-B**. Instead, DC provides a complementary precise measurement of Δm_{32}^2 . This information unlocks a mechanism, to be described below, enabling the intrinsic MO sensitivity of JUNO to be enhanced by the external Δm_{32}^2 . This highly non-trivial synergy may yield a MO leading order role but introduces new dependences explored below.

Both JUNO and $\text{LB}\nu\text{B}$ analyse data in the 3ν framework so they can provide Δm_{32}^2 (or Δm_{31}^2) directly as output. The 2ν approximation leads to effective observables, such as $\Delta m_{\mu\mu}^2$ and Δm_{ee}^2 [45] detailed in **Appendix-C**. The $\text{LB}\nu\text{B}$ DC information precision on the Δm_{32}^2 measurement is limited by a δ_{CP} -driven ambiguity. The role of this ambiguity is small, but not fully negligible and will be detailed below. The dominant $\text{LB}\nu\text{B}$ -II's precision is today $\sim 2.9\%$ per experiments [48, 49]. The combined $\text{LB}\nu\text{B}$ -II global precision on Δm_{32}^2 is already $\sim 1.4\%$ [21]. Further improvement below 1.0% appears possible within the $\text{LB}\nu\text{B}$ -II era when integrating the full luminosities. An average precision of $\leq 0.5\%$ is reachable only upon the $\text{LB}\nu\text{B}$ -III generation. Instead, JUNO precision on Δm_{32}^2 is expected to be well within the sub-percent ($<0.5\%$) level [37].

The essence of the synergy is here described. Upon 3ν analysis, both JUNO and $\text{LB}\nu\text{B}$ experiments obtain two different values for Δm_{32}^2 . Since there is only one *true* solution, either NMO or IMO, the other solution is thus *false*. The standalone ability to distinguish between those two solutions is the *intrinsic* MO resolution power of each experiment. The key observation though is that the general relation between the true-false solutions is different for reactors and $\text{LB}\nu\text{B}$ experiments, as illustrated in Figure 3. For a given true Δm_{32}^2 , its false value, referred as $\Delta m_{32}^{2 \text{ false}}$, can be estimated, as shown in **Appendix C**. Regardless, all experiments must agree on the unique true Δm_{32}^2 solution. As a consequence, the corresponding JUNO ($\Delta m_{32}^{2 \text{ false}}_{\text{JUNO}}$) and $\text{LB}\nu\text{B}$ ($\Delta m_{32}^{2 \text{ false}}_{\text{LB}\nu\text{B}}$) false solutions will differ, if the overall Δm_{32}^2 precision allows their relative resolution. This false solution difference can be exploited as an extra dedicated discriminator characterised by the term

$$\Delta\chi_{\text{BOOST}}^2 \sim \left(\frac{\Delta m_{32}^{2 \text{ false}}_{\text{JUNO}} - \Delta m_{32}^{2 \text{ false}}_{\text{LB}\nu\text{B}}}{\sigma(\Delta m_{32}^2)_{\text{LB}\nu\text{B}}} \right)^2. \quad (1)$$

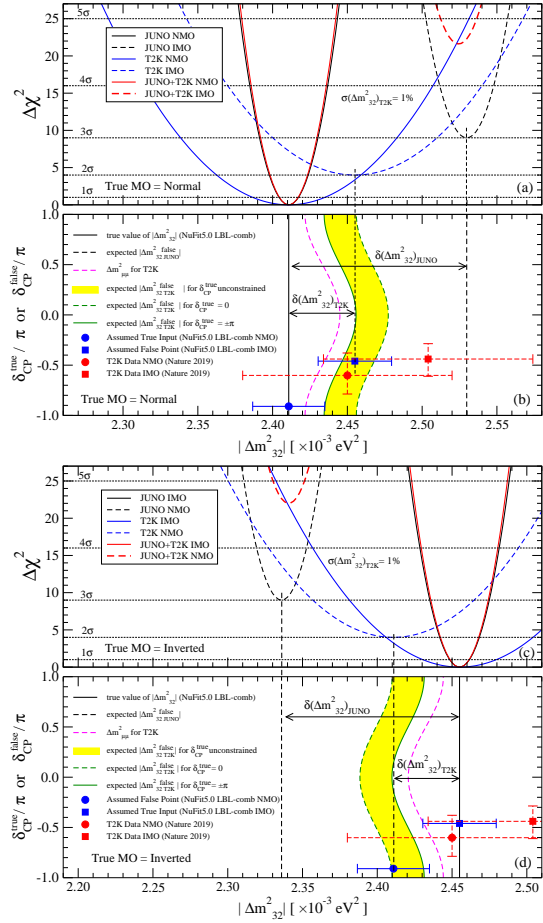


Figure 3: JUNO & $\text{LB}\nu\text{B}$ Mass Ordering Synergy. The behaviours of $\Delta\chi^2$ terms (parabolas) is shown as a function of $|\Delta m_{32}^2|$ for JUNO (black), T2K (or NOvA) and their enhanced combination (red). The $\Delta m_{32}^{2 \text{ true}}$ is fixed to the NuFit5.0 best value shown, in panels (a) and (c) for NMO and IMO. The extra gain in $\Delta\chi_{\text{BOOST}}^2$ discrimination numerically originates from the fact that the true $|\Delta m_{32}^2|$ solutions should match between JUNO (solid black vertical line) and $\text{LB}\nu\text{B}$ (solid blue vertical circle), hence the false solutions (dashed vertical lines) must differ. Panels (b) and (d) illustrate this origin. The relation between true-false Δm_{32}^2 solutions is different and complementarity for JUNO and $\text{LB}\nu\text{B}$ experiments. The difference is large ($\approx 1.5 \times \delta m_{21}^2$) for JUNO. Instead, $\text{LB}\nu\text{B}$ exhibits a smaller difference that modulates with δ_{CP} . So, the relative difference between $\Delta m_{32}^{2 \text{ false}}_{\text{JUNO}}$ and $\Delta m_{32}^{2 \text{ false}}_{\text{LB}\nu\text{B}}$ is maximal (minimal) for the δ_{CP} -conserving $\pm\pi$ (0) value. Hence, $\Delta\chi_{\text{BOOST}}^2$ depends on δ_{CP} and an ambiguity arises (yellow band) from the a priori different values of δ_{CP} for the true or false solutions. The T2K data (red points) contrasts the precision on $|\Delta m_{32}^2|$ now [50] as compared to needed scenarios $\leq 1.0\%$ scenario (blue points and parabolas). The precision of each contribution indicated by width of the parabolas, where JUNO is fixed to the nominal value [37].

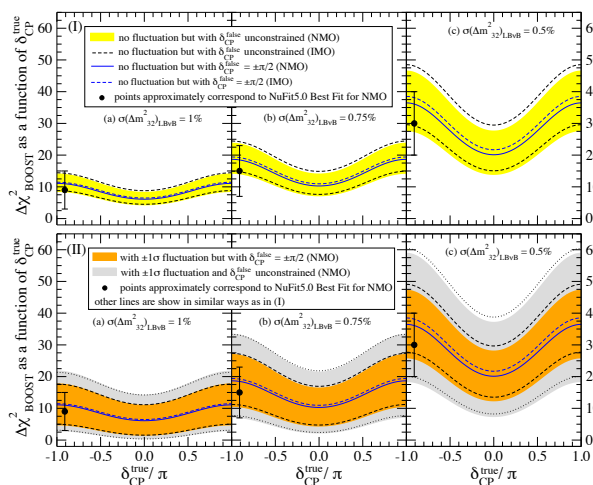


Figure 4: JUNO and $LB\nu B$ Mass Ordering Synergy Dependences. The isolated synergy boosting term obtained from the combining JUNO and $LB\nu B$ experiments is represented by $\Delta\chi^2_{\text{BOOST}}$, as defined in Eq. (1). $\Delta\chi^2_{\text{BOOST}}$ depends on the true value of δ_{CP} and Δm^2_{32} precision, where uncertainties are considered: 1.0% (a), 0.75% (b) and 0.5% (c). The $\Delta\chi^2_{\text{BOOST}}$ term is almost identical for both NMO and IMO solutions. Two specific effects lead the uncertainty in the a priori prediction on $\Delta\chi^2_{\text{BOOST}}$. (I) illustrates only the ambiguity of the CP phase (yellow band) and (II) includes the additional impact of the $\pm 1\sigma$ fluctuations of Δm^2_{32} , as measured by $LB\nu B$ (orange band). The JUNO uncertainty on Δm^2_{32} is considered. The grey bands shows when both effects were taken into account simultaneously. The mean value of the $\Delta\chi^2_{\text{BOOST}}$ term increases strongly with the precision on Δm^2_{32} . The uncertainties from CP phase ambiguity and fluctuation could deteriorate much of the a priori gain on the prospected sensitivities. The impact of Δm^2_{32} fluctuations dominates, while the δ_{CP} ambiguity is only noticeable for the best Δm^2_{32} precisions. The use of NuFit5.0 data (black point) eliminates the impact of the δ_{CP} prediction ambiguity while the impact of Δm^2_{32} remains as fluctuations cannot predict a priori. Today's favoured δ_{CP} maximises the sensitivity gain via the $\Delta\chi^2_{\text{BOOST}}$ term. When quoting sensitivities, we shall consider the lowest bound as the most conservative case.

This $\Delta\chi^2_{\text{BOOST}}$ term characterises the rejection of the false solutions (either NMO or IMO), including an explicit hyperbolic dependence on the overall precision on Δm^2_{32} . The derived MO sensitivity enhancement may be so strong that it can be regarded, and will be referred, as a potential *boost* effect in the MO sensitivity.

So, the JUNO- $LB\nu B$ boosting synergy exhibits four main features illustrated in Figure 4. First, there is a major increase of the combined MO sensitivity ($\Delta\chi^2_{\text{BOOST}} > 0$). This contribution is to be added to the intrinsic MO discrimination $\Delta\chi^2$ terms per experiment described in the previous sections. Second, a strong ex-

pected dependence on the precision of Δm^2_{32} is present, as shown in Eq. (1). The precision in Δm^2_{32} is typically dominated by the poorer $LB\nu B$ precision as compared to JUNO. Third, the unavoidable $\pm 1\sigma$ data fluctuations of Δm^2_{32} can have an important impact in the boosted MO sensitivity. And fourth, an explicit dependence on δ_{CP} manifests giving rise to an ambiguity. The two latter effects are mainly relevant for a priori predictions of $\Delta\chi^2_{\text{BOOST}}$ without data.

All these effects are quantified and explained in Figure 4. The possible fluctuations due Δm^2_{32} uncertainties and the δ_{CP} ambiguity could diminish much of the a priori boosting potential. These dependences are inherited by the complex phenomenology of $LB\nu B$, typically also suffering from a less precise outcome. The leading order effect is the uncertainty on Δm^2_{32} , referred as $\sigma(\Delta m^2_{32})_{LB\nu B}$. Three cases are explored in this work 1.0%, 0.75% and 0.5%, including the simultaneous impact of the non-negligible δ_{CP} ambiguity. This ambiguity arises from the possible different δ_{CP} phases obtained for the true and false solutions, as detailed in **Appendix C**. The main consequence is to limit the predictability of $\Delta\chi^2_{\text{BOOST}}$, even if the true value of CP phase was known. Its effect is not negligible when the $LB\nu B$ precision on Δm^2_{32} improves significantly ($\leq 0.5\%$), as shown in Figure 4. However, the direct use of $LB\nu B$ data bypasses some of the impact of this prediction limitation. This is why we adopt the NuFit5.0 latest global data, including the pertinent fluctuations. In this way, we are able to conservatively maximise the accuracy of our predictions to the most probable parameter-space, as favoured by the latest world neutrino data. This is particularly important to compute the most accurate $\Delta\chi^2_{\text{BOOST}}$ and hence the final MO determination significance. For the similar reason, our simplified formulation cannot easily account for the atmospheric data whose vast dynamic range in E/L demands a more complete treatment to be able to remain reasonably accurate.

In brief, when combining JUNO to the $LB\nu B$ experiments, the overall sensitivity works as if JUNO's intrinsic sensitivity gets boosted, via the external Δm^2_{32} information, as illustrated and quantified in Figure 5 as a function of the precision on Δm^2_{32} despite the sizeable impact of fluctuations. The $LB\nu B$ intrinsic AC contribution will be added, as shown in the next section. However, it is via the boosting that the DC information of the $LB\nu B$'s could play a major role in the overall MO sensitivity. However, this improvement cannot manifest without JUNO – and vice versa. For a average precision on Δm^2_{32} below 1.0%, even with fluctuations, the boosting effect can be large. A Δm^2_{32} precision as good as $> 0.7\%$ may be accessible by $LB\nu B$ -II while the $LB\nu B$ -

III generation is expected to go up to $\leq 0.5\%$ level.

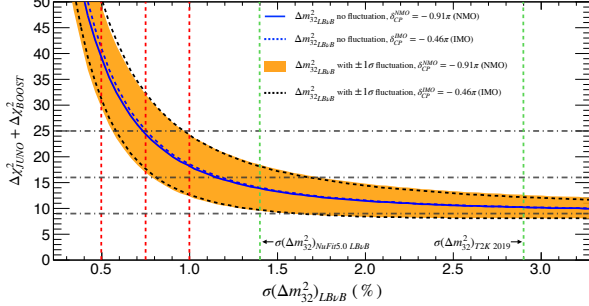


Figure 5: **JUNO Mass Ordering Sensitivity Boosting.** A major increase of JUNO intrinsic sensitivity ($\Delta\chi^2_{\text{JUNO}} \approx 9$) is possible upon the exploitation of the $\text{LB}\nu\text{B}$'s disappearance (DC) characterised by $\Delta\chi^2_{\text{BOOST}}$ depending strongly on the uncertainty of Δm_{32}^2 . Today's NuFit5.0 average $\text{LB}\nu\text{B}$ -II's precision on Δm_{32}^2 is $\sim 1.4\%$. A rather humble 1.0% precision is possible, consistent with doubling the statistics, if systematics allowed. Since NOvA and T2K are expected to increase their exposures by about factors of $\sim 3\times$ before shutdown, sub-percent precision may also be within reach. While, the ultimate precision is unknown, we shall consider a $\geq 0.75\%$ precision to illustrate this possibility. So, JUNO alone could yield a $\geq 4\sigma$ (i.e. $\Delta\chi^2 \geq 16$) MO sensitivity, at $\geq 84\%$ probability, within the $\text{LB}\nu\text{B}$ -II era. Fluctuations allowing, a 5σ potential may not be impossible. Similarly, JUNO may further increase in significance in order to resolve ($\geq 5\sigma$ or $\Delta\chi^2 \geq 25$) a purely vacuum oscillations MO measurement in combination with the $\text{LB}\nu\text{B}$ -III's Δm_{32}^2 information.

Since the exploited DC information is practically blinded to matter effects⁵, the boosting synergy effect remains dominated by JUNO's vacuum oscillations nature. This is why the sensitivity performance is almost identical for both NMO and IMO solutions, in contrasts to the sensitivities obtained from solely matter effects, as shown in Figure 2. This is specially noticeable for the case of atmospheric data. The case of T2K is particularly illustrative as its impact to MO resolution is via the boosting term mainly, given its small intrinsic MO information obtained by AC data. This combined MO sensitivity boost between JUNO and $\text{LB}\nu\text{B}$ (or atmospheric) is likely one of the most elegant and powerful examples so far seen in neutrino oscillations and it is expected to play a major role for JUNO (always needed) to yield a leading impact on the MO quest. In fact, this effect has already been considered by JUNO to claim its possible median 4σ potential [47, 37]; i.e. without the

Δm_{32}^2 fluctuations. Our results are fully consistent with those results, as described in **Appendix D**.

Simplified Combination Rationale

The combined MO sensitive of JUNO together with $\text{LB}\nu\text{B}$ -II experiments (NOvA and T2K) can be obtained from the independent additive of each individual $\Delta\chi^2$. Two contributions are expected: a) the $\text{LB}\nu\text{B}$ -II's AC, referred as $\Delta\chi^2(\text{LB}\nu\text{B-AC})$ and b) the combined JUNO and $\text{LB}\nu\text{B}$ -II's DC, referred as $\Delta\chi^2(\text{JUNO}\oplus\text{LB}\nu\text{B-DC})$. All terms were described in the previous sections⁶. Hence the combination can be represented as $\Delta\chi^2 = \Delta\chi^2(\text{JUNO}\oplus\text{LB}\nu\text{B-DC}) + \Delta\chi^2(\text{LB}\nu\text{B-AC})$, illustrated in Figure 6, where the orange and grey bands represent, respectively, the effects of the Δm_{32}^2 fluctuations and the CP-phase ambiguity. Figure 6 quantifies the MO sensitivity in significance (i.e. numbers of σ 's) obtained as $\sqrt{\Delta\chi^2}$ quantified in all previous plots. Again, both NMO and IMO solutions are considered for 3 different cases for the uncertainty of Δm_{32}^2 :

The $\Delta\chi^2(\text{LB}\nu\text{B-II-AC})$ Term: this is the intrinsic MO combined information, largely dominated by NOvA 's AC, as described in Figure 2. The impact of T2K ($\leq 2\sigma$) is very small, but in the verge of resolving MO for the first time, T2K may still help here. As expected, this $\Delta\chi^2$ depends on both θ_{23} and strongly on δ_{CP} , as shown in Figure 6, represented by the light green band. The complexities of possible correlations and systematics handling of a hypothetical NOvA and T2K combination are disregarded in our study and are considered integrated within the combination of the $\text{LB}\nu\text{B}$ -II term, now obtained from NuFit5.0. The full NOvA data is expected to be fully available by 2024 [49], while T2K will run until 2026 [48], upon the beam upgrades (T2K-II) aiming for HK.

The $\Delta\chi^2(\text{JUNO}\oplus\text{LB}\nu\text{B-DC})$ Term: this term can be regarded itself as composed of two contributions. The first part is the JUNO intrinsic information; i.e. $\Delta\chi^2 = 9 \pm 1$ units after 6 years of data-taking. This contribution is independent from θ_{23} and δ_{CP} , as shown in Figure 6, represented by the blue band. The second part is the JUNO boosting term, shown explicitly in Figure 4, including its generic dependences such as the true value of δ_{CP} . This term exhibits strong modulation with δ_{CP} and

⁵The measurement of Δm_{32}^2 depends slightly δ_{CP} , which is obtained via the AC information, itself sensitivity to matter effects.

⁶In this work, we use the terminologies, AC (appearance channel) and DC (disappearance channel) for simplicity but this does not mean that the relevant information is coming only from AC or DC, but that $\Delta\chi^2(\text{LB}\nu\text{B-AC})$ comes dominantly from $\text{LB}\nu\text{B}$ AC whereas $\Delta\chi^2(\text{JUNO}\oplus\text{LB}\nu\text{B-DC})$ comes dominantly from JUNO + $\text{LB}\nu\text{B}$ DC.

the uncertainty of Δm_{32}^2 , as illustrated in both Figures 4 and 5. The $\Delta\chi^2(\text{JUNO}\oplus\text{LB}\nu\text{B-DC})$ term strongly shapes the combined $\Delta\chi^2$ curves (orange). Indeed, this term causes the leading variation across Figure 6 for the different cases of the uncertainty of Δm_{32}^2 : a) 1.0% (top), which is easily reachable by LBνB-II, b) 0.75% (middle), which may still be reachable (i.e. optimistic) by LBνB-II and c) 0.5% (bottom), which is only reachable by the LBνB-III generation.

The combination of the JUNO along with both AC and DC inputs from LBνB-II experiments indeed appears on the verge of achieving the first MO resolved measurement with a sizeable probability. The ultimate significance of the combination is likely to mainly depend on the final uncertainty on Δm_{32}^2 obtained by LBνB experiments. The discussion of the results and implications, including limitations, is addressed in the next section.

Implications & Discussion

Possible implications arising from the main results summarised in Figure 6 deserved some extra elaboration and discussion for a more accurate contextualisation, including a possible timeline, as well as known limitations associated to our simplified approach. These are the main considerations:

1. MO Global Data Trend: today's reasonably high significance, a priori not far the level reached by the intrinsic sensitivities of JUNO or NOvA alone, is obtained by the most recent global analysis [21] favours NMO up to 2.7σ . This significance however lowers to 1.6σ without SK atmospheric data, thus proving their key value to the global MO knowledge today. The remaining aggregated sensitivity integrates over all other experiments. However, the global data preference is known to be somewhat fragile still between NMO and IMO solutions [17, 51, 21]. The reason behind is actually the corroborating manifestation of the alluded complementarity between LBνB-II and *reactors*⁷ experiments. Indeed, while the current LBνB data alone favours IMO, the match in Δm_{32}^2 measurements by LBνB and reactors tend to match better for the case of NMO, thus favouring this solution upon combination. Hence, the MO solution currently flips due to the reactor-LBνB data interplay. This might happen given the sizeable Δm_{32}^2 uncertainty fluctuations, as compared to the aforementioned scenario when JUNO is on. This effect is at the heart of the described boosting mechanism and has started manifesting earlier following the expectation a priori [45]. Hence,

this can be regarded as the first data-driven manifestation of the $\Delta\chi_{\text{BOOST}}^2$ effect.

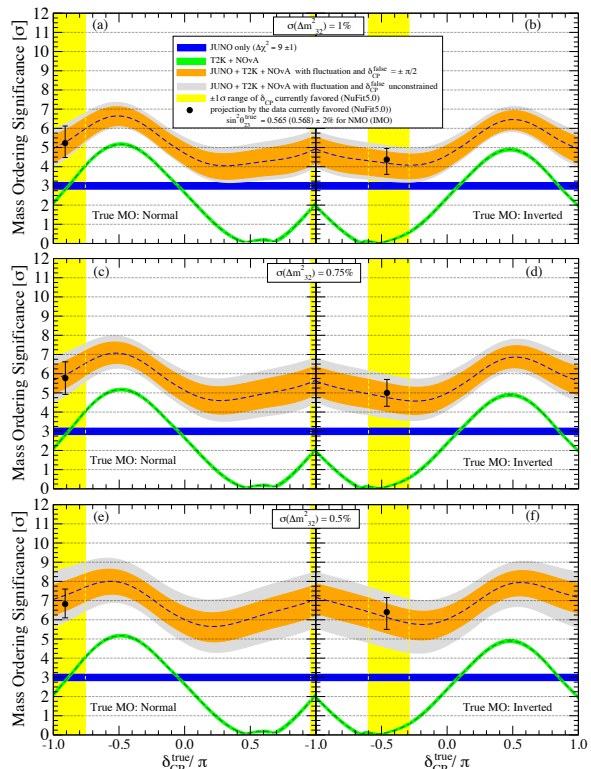


Figure 6: **The Combined Mass Order Sensitivity.** The combination of the MO sensitive of JUNO and LBνB-II is illustrated for six difference configurations: NMO (left), IMO (right) considering the LBνB uncertainty on Δm_{32}^2 to 1.0% (top), 0.75% (middle) and 0.5% (bottom). The NuFit5.0 favoured value is set for $\sin^2\theta_{23}$ with an assumed 2% experimental uncertainty. The intrinsic MO sensitivity are shown for JUNO (blue) and the combined LBνB-II (green), the latter largely dominated by NOvA. The JUNO sensitivity boosts when exploiting the LBνB's Δm_{32}^2 additional information via the $\Delta\chi_{\text{BOOST}}^2$ term, described in Figure 4 but not shown here for illustration simplicity. The orange and grey bands illustrate the boosting term prediction effects, respectively, the $\pm 1\sigma$ fluctuation of Δm_{32}^2 and the δ_{CP} ambiguity in addition. T2K impacts mainly via the precision of Δm_{32}^2 and the measurement of δ_{CP} . The combined sensitivity suggests a mean (dashed blue line) $\geq 4\sigma$ significance for any value of δ_{CP} even for the most conservative $\sigma(\Delta m_{32}^2) = 1\%$. However, a robust $\geq 5.0\sigma$ significance at 84% probability (i.e. including fluctuations) seems possible, should δ_{CP} and NMO remain favoured by data, as indicated by the yellow band and black point (best fit). Further improvement in the precision of Δm_{32}^2 translates into a better MO resolution potential.

⁷Before JUNO starts, the reactor experiments stand for Daya Bay, Double Chooz, RENO whose lower precision on Δm_{32}^2 is $\sim 2\%$.

2. Atmospherics Extra Information: we did not account for atmospheric neutrino input, such as the running SK and IceCube experiments. They are expected to add valuable $\Delta\chi^2$, though susceptible to the aforementioned θ_{23} and δ_{CP} dependences. This contribution is more complex to replicate with accuracy due to the vast E/L phase-space, hence we disregarded it in our simplified analysis. Its importance has long been proved by SK dominance of much of today’s MO information. So, all our conclusions can only be enhanced by adding the atmospheric missing contribution. Future ORCA and PINGU has the potential to yield extra MO information, while their combinations with JUNO data is being actively explored [52, 53] to yield full MO resolution.

3. Inter-Experiment Full Combination: a more complete strategy of data-driven combination between JUNO and LB ν B-II experiments will be beneficial in the future⁸. Ideally, this could be an official inter-collaboration effort to be able to carefully scrutinise the possible impact of systematics and correlations, including both experimentalists and phenomenologists. At this stage, we do not foresee a significant change in our findings by a more complex study, including the MO discovery potential here highlighted for the first time, due to the limitations of today’s data and knowledge.

For this reason, our approach did not aim to merely demonstrate the numerical yield of the combination between JUNO and LB ν B, but to illustrate and characterise the different synergies manifesting therein. So, our study was tailored to focus on the breakdown of all the relevant contributions in the specific and isolated cases of the MO sensitivity combination of the leading experiments. For example, the impact of the $\Delta\chi_{\text{BOOST}}^2$ was isolated while its effect is otherwise transparently accounted by a complete 3ν χ^2 formulation, such as done by NuFit5.0 or others similar analyses. Last, our study was tuned to the latest data in order to maximise the accuracy of the predictability, expected to be $\sim 0.5\sigma$ around the 5σ resolution threshold.

4. Hypothetical MO Resolution Timeline: one of the main observations upon this study is that the MO could be resolved ($\geq 5\sigma$), maybe even comfortably, by the JUNO, NO ν A and T2K combination. Considering today’s favoured δ_{CP} , the NMO solution discovery potential has a probability of $\geq 50\%$ ($\geq 84\%$) for a Δm_{32}^2 precision of up to 1.0% (0.75%). In the case of the more challenging IMO, the sensitivity may reach a mean of $\sim 5\sigma$ potential only if the Δm_{32}^2 uncertainty was as good as $\sim 0.75\%$. If so, still within the same time scale, the atmospheric data is expected to add up to enable a ro-

bust 5σ resolution for both solutions. If correct, this is likely to become the first fully resolved MO measurement tightly linked to the JUNO data timeline, as described in Figure 7, which sets the time to be around ~ 2028 . This possibility may be far from evident in today’s appreciation of the field.

Such a combined MO measurement can be regarded as a “hybrid” between vacuum and matter driven oscillations. In this context, JUNO and NO ν A are, unsurprisingly, the driving experiments. Despite holding little intrinsic MO information, T2K plays a key role by simultaneously a) boosting JUNO via its precise measurement of Δm_{32}^2 (the same as NO ν A) and b) aiding NO ν A by reducing the possible δ_{CP} ambiguity phase-space. This combined measurement relies on an impeccable 3ν data model consistency across all experiments. Possible inconsistencies may diminish the combined sensitivity.

Since our estimate has accounted for fluctuations (typically, up to $\sim 84\%$ probability), those inconsistencies should amount to $\geq 2\sigma$ effects for them to matter. Those inconsistencies may however be the first manifestation for new physics. Hence, this inter-experiment combination has an extra relevant role: to exploit the ideal MO binary phase-space solution to test for inconsistencies that may prove the way to possible discoveries beyond today’s standard picture. Other additional contributions, such as the aforementioned atmospheric data, are expected to reinforce the significance and the model consistency scrutiny potential here highlighted.

5. Readiness for LB ν B-III: in the absence of any robust model-independent for MO prediction and given its unique binary MO outcome, the articulation of at least two well resolved (i.e. $\geq 5\sigma$) measurements appears critical for the sake of redundancy and consistency test across the field. In the light of the unrivalled MO resolution power of DUNE, the articulation of another robust MO measurement may be considered as a priority to make the most of DUNE’s insight.

6. Vacuum versus Matter Measurements: since all experiments but JUNO are driven by matter effects, the articulation of a competitive and fully resolved measurement via only vacuum oscillations remains an unsolved challenge to date. Indeed, boosting JUNO sensitivity alone, as described in Figures 4 and 5, to $\geq 5\sigma$ remains likely impractical in the context of LB ν B-II, modulo fluctuations. However, this possibility is a priori numerically feasible in combination with the LB ν B-III improved precision, as shown in Figure 7. The potential major improvement in the Δm_{32}^2 precision, up to order 0.5% [29, 30], may prove crucial. Furthermore,

⁸During the final readiness of our work, one such a combination was reported [54] using a different treatment (excluding fluctuations). While their qualitative conclusions are consistent to our studies, there may still be numerical differences left to be understood.

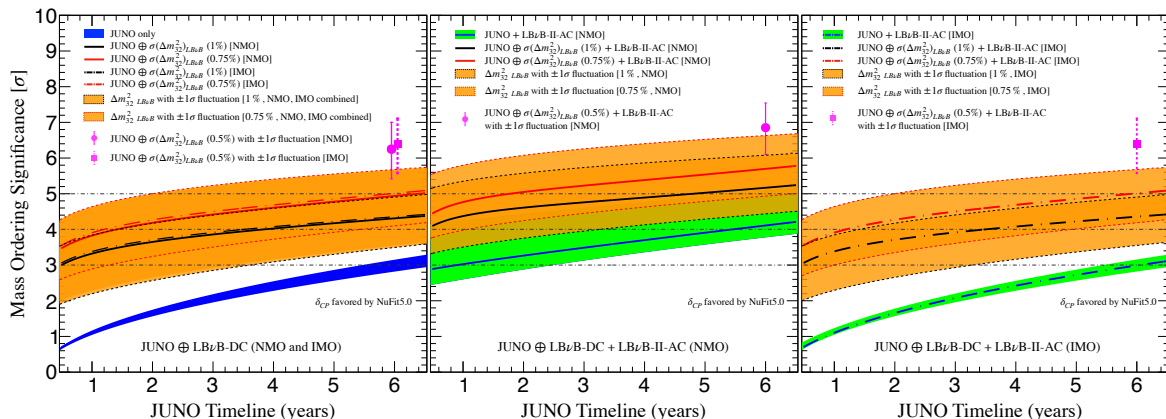


Figure 7: **Mass Order Sensitivity & Possible Resolution Timeline.** Since all the NOvA and T2K data are expected to be accumulated by ~ 2024 [49] and ~ 2026 [48], respectively, the timeline for the combined sensitivity follows the availability of the JUNO data. JUNO is expected to start by late 2022 reaching its statistically dominated nominal MO sensitivity (9 units of $\Delta\chi^2$) within ~ 6 years. We consider three possible scenarios: (left) JUNO boosted by the LBνB’s DC only (both NMO and IMO) and the JUNO combined to LBνB using both DC and AC, whose performance depends strongly on the solution: NMO (middle) and IMO (right). The evolution of the sensitivity depends largely on the boosting, as proved by considering three different Δm_{32}^2 uncertainties 1.0% (black line), 0.75% (red line) and 0.5% (magenta points) cases. The effect of Δm_{32}^2 fluctuations is indicated (orange bands), including that of the variance due to data favoured region for δ_{CP} (green band). The JUNO intrinsic (blue) and boosted sensitivities are almost independent from NMO and IMO solutions (left). This is almost identical to the IMO case (right), as the role of LBνB-II’s AC is negligible, thus driven by boosted effect only. In both cases, the mean significance is $\sim 5\sigma$ (red line), hence some additional atmospheric data ($\Delta\chi^2 \geq 7$ units) should suffice to reach a robust $\geq 5\sigma$, including fluctuations and degeneracies (i.e. $\geq 84\%$ probability). Should the solution be NMO though, as somewhat favoured by global data, a robust $\geq 5\sigma$ resolution ($\geq 84\%$ probability) may be comfortably feasible even for the lowest Δm_{32}^2 precision, thanks to the extra contribution by NOvA mainly. In the LBνB-III era though, the more precise Δm_{32}^2 could boost JUNO well above the 5σ level only using Disappearance Channel. This unique possibility goes well beyond the JUNO timeline; thus scaling is irrelevant, so data points are shown instead. In this era, JUNO data could prescind from any LBνB’s AC information, thus enabling a pure vacuum oscillation fully resolved MO measurement.

the comparison between two fully resolved MO measurements, one using only *matter effects* and one exploiting pure *vacuum oscillations* is foreseen to be one of the most insightful MO coherence tests. So, the ultimate MO measurements comparison may be the DUNE’s AC alone versus JUNO boosted by HK’s Δm_{32}^2 precision, thus maximising the depth of the MO-based scrutiny by their stark differences in terms of mechanisms, implying dependences, correlations, etc. The potential for a breakthrough exists, again, should a discrepancy manifest here. The expected improvement in the knowledge of δ_{CP} by LBνB-III experiments will also play an important role to facilitate this opportunity.

This observation implies that JUNO MO capability, despite its a priori humble intrinsic sensitivity, has the potential to play a critical role throughout the history of MO explorations. Indeed, the first MO fully resolved measurement is likely to depend on JUNO sensitivity (direct and indirectly), hence JUNO should maximise ($\Delta\chi^2 \geq 9$) or maintain its yield. However, JUNO’s ultimate aforementioned role may remain rather unaffected even by a small loss of performance, providing the overall sensitivity remains sizeable (e.g. $\Delta\chi^2 \geq 7$), as illustrated

in Figures 5 and 6. This is because JUNO sensitivity could still be boosted by the LBνB experiments via their precision on Δm_{32}^2 , thus sealing its legacy. There is no reason for JUNO not to perform as planned, especially given the remarkable effort for solutions and novel techniques developed for the control of spectral shape.

7. LBνB Running Strategy: since the role of these experiments to yield the maximal combined MO sensitivity is driven by both AC and DC derived informations, both channels should be considered when maximising the global MO sensitivities, as well as the usual optimisation based on δ_{CP} sensitivity. Indeed, as shown, the precision on Δm_{32}^2 could even play a more important role than the intrinsic MO resolution, based on the AC data. This is particularly crucial for T2K and HK due to their shorter baselines. So, forthcoming beam-mode running optimisation by the LBνB collaborations could, and likely should, consider that the neutrino mode is likely significantly benefit the DC outcome thanks to its larger signal rate and better signal-to-background ratio. For such considerations, our Figure 5 might offer the needed leading order guidance today.

Conclusions

Our here presented simplified proof-of-concept calculation, tuned to the latest world neutrino data via NuFit5.0, illustrates that the combined sensitivity of JUNO together with NOvA and T2K has the potential to yield the first resolved ($\geq 5\sigma$) measurement of Mass Ordering (MO). The timeline is expected to be around 2028, tightly linked to the JUNO schedule, since both NOvA and T2K data are expected to be available by 2026. Due to the absence of any a priori MO prediction and given its intrinsic binary outcome, we noted the benefit to the field to envisage at least two independent and well resolved ($\geq 5\sigma$) measurements. This is even more important in the light of the powerful outcome from the next generation of long baseline neutrino beams experiments. Such MO measurements could be exploited to over-constrain and test the standard oscillation model, thus opening for discovery potential, should unexpected discrepancies may manifest. The deepest phenomenological insight is however expected to be obtained by having two different and well resolved MO measurements based on either only matter effects and pure vacuum oscillations experimental methodologies. We here describe the feasible path to promote JUNO's MO measurement to reach a robust $\geq 5\sigma$ resolution level without compromising its unique vacuum oscillation nature. This potential depends on the next generation of long baseline neutrino beams disappearance channel ability to reach a precision of $\leq 0.5\%$ on Δm_{32}^2 .

Acknowledgment

Much of this work was originally developed in the context of our studies linked to the PhD thesis of Y.H. (APC and IJC laboratories) and to the scientific collaboration between H.N. (in sabbatical at the IJC laboratory) and A.C. Y.H. and A.C. are grateful to the CSC fellowship funding of the PhD fellow of Y.H. HN acknowledges CAPES and is especially thankful to CNPq and IJC laboratory for their support to his sabbatical. AC and LS acknowledge the support of the P2IO LabEx (ANR-10-LABX-0038) in the framework “*Investissements d’Avenir*” (ANR-11-IDEX-0003-01 – Project “NuBSM”) managed by the Agence Nationale de la Recherche (ANR), France. Our developments are framed within the *neutrino inter-experiment synergy* working group. We would like to specially thank the NuFit5.0 team (Ivan Esteban, Concha Gonzalez-Garcia, Michele Maltoni, Thomas Schwetz and Albert Zhou) for their kindest aid and support to provide dedicated information from their latest NuFit5.0 version. We also would like Concha Gonzalez-Garcia and Fumihiko Suekane for providing precious feedback on a short time scale and internal review of the original manuscript.

References

- [1] M.C. Gonzalez-Garcia and M. Yokoyama. Neutrino Masses, Mixing and Oscillation, in Review of Particle Physics. *To appear, PTEP*, 2020:083C01, 2020.
- [2] Hiroshi Nunokawa, Stephen J. Parke, and Jose W.F. Valle. CP Violation and Neutrino Oscillations. *Prog. Part. Nucl. Phys.*, 60:338–402, 2008. doi: 10.1016/j.pnpnp.2007.10.001.
- [3] B. Pontecorvo. Neutrino Experiments and the Problem of Conservation of Leptonic Charge. *Sov. Phys. JETP*, 26:984–988, 1968.
- [4] Ziro Maki, Masami Nakagawa, and Shoichi Sakata. Remarks on the unified model of elementary particles. *Prog. Theor. Phys.*, 28:870–880, 1962. doi: 10.1143/PTP.28.870.
- [5] P.A. Zyla et al. Review of Particle Physics. *To appear, PTEP*, 2020:083C01, 2020.
- [6] B.T. Cleveland, Timothy Daily, Jr. Davis, Raymond, James R. Distel, Kenneth Lande, C.K. Lee, Paul S. Wildenhain, and Jack Ullman. Measurement of the solar electron neutrino flux with the Homestake chlorine detector. *Astrophys. J.*, 496:505–526, 1998. doi: 10.1086/305343.
- [7] W. Hampel et al. GALLEX solar neutrino observations: Results for GALLEX IV. *Phys. Lett. B*, 447:127–133, 1999. doi: 10.1016/S0370-2693(98)01579-2.
- [8] J.N. Abdurashitov et al. Measurement of the solar neutrino capture rate with gallium metal. *Phys. Rev. C*, 60:055801, 1999. doi: 10.1103/PhysRevC.60.055801.
- [9] Q.R. Ahmad et al. Direct evidence for neutrino flavor transformation from neutral current interactions in the Sudbury Neutrino Observatory. *Phys. Rev. Lett.*, 89:011301, 2002. doi: 10.1103/PhysRevLett.89.011301.
- [10] S. Fukuda et al. Solar B-8 and hep neutrino measurements from 1258 days of Super-Kamiokande data. *Phys. Rev. Lett.*, 86:5651–5655, 2001. doi: 10.1103/PhysRevLett.86.5651.
- [11] K. Eguchi et al. First results from KamLAND: Evidence for reactor anti-neutrino disappearance. *Phys. Rev. Lett.*, 90:021802, 2003. doi: 10.1103/PhysRevLett.90.021802.
- [12] S.P. Mikheyev and A.Yu. Smirnov. Resonance Amplification of Oscillations in Matter and Spectroscopy of Solar Neutrinos. *Sov. J. Nucl. Phys.*, 42:913–917, 1985.
- [13] L. Wolfenstein. Neutrino Oscillations in Matter. *Phys. Rev. D*, 17:2369–2374, 1978. doi: 10.1103/PhysRevD.17.2369.

- [14] S.F. King. Neutrino mass models. *Rept. Prog. Phys.*, 67:107–158, 2004. doi: 10.1088/0034-4885/67/2/R01.
- [15] Amol S. Dighe and Alexei Yu. Smirnov. Identifying the neutrino mass spectrum from the neutrino burst from a supernova. *Phys. Rev. D*, 62:033007, 2000. doi: 10.1103/PhysRevD.62.033007.
- [16] Steen Hannestad and Thomas Schwetz. Cosmology and the neutrino mass ordering. *JCAP*, 11:035, 2016. doi: 10.1088/1475-7516/2016/11/035.
- [17] Ivan Esteban, M.C. Gonzalez-Garcia, Alvaro Hernandez-Cabezudo, Michele Maltoni, and Thomas Schwetz. Global analysis of three-flavour neutrino oscillations: synergies and tensions in the determination of θ_{23} , δ_{CP} , and the mass ordering. *JHEP*, 01:106, 2019. doi: 10.1007/JHEP01(2019)106.
- [18] P.F. de Salas, D.V. Forero, S. Gariazzo, P. Martinez-Mirav, O. Mena, C.A. Ternes, M. Trtola, and J.W.F. Valle. 2020 Global reassessment of the neutrino oscillation picture. ArXiv:2006.11237 [hep-ph].
- [19] F. Capozzi, E. Lisi, A. Marrone, and A. Palazzo. Current unknowns in the three neutrino framework. *Prog. Part. Nucl. Phys.*, 102:48–72, 2018. doi: 10.1016/j.pnpnp.2018.05.005.
- [20] The XXIX International Conference on Neutrino Physics and Astrophysics, Neutrino 2020, June 22 - July 2, 2020. <https://conferences.fnal.gov/nu2020/>, .
- [21] Ivan Esteban, M.C. Gonzalez-Garcia, Michele Maltoni, Thomas Schwetz, and Albert Zhou. The fate of hints: updated global analysis of three-flavor neutrino oscillations. ArXiv:2007.14792 [hep-ph]. Web: <http://www.nu-fit.org/?q=node/228>.
- [22] Mattias Blennow, Pilar Coloma, Patrick Huber, and Thomas Schwetz. Quantifying the sensitivity of oscillation experiments to the neutrino mass ordering. *JHEP*, 03:028, 2014. doi: 10.1007/JHEP03(2014)028.
- [23] Yu-Feng Li, Yifang Wang, and Zhi-zhong Xing. Terrestrial matter effects on reactor antineutrino oscillations at JUNO or RENO-50: how small is small? *Chin. Phys. C*, 40(9):091001, 2016. doi: 10.1088/1674-1137/40/9/091001.
- [24] M.H. Ahn et al. Indications of neutrino oscillation in a 250 km long baseline experiment. *Phys. Rev. Lett.*, 90:041801, 2003. doi: 10.1103/PhysRevLett.90.041801.
- [25] P. Adamson et al. Improved search for muon-neutrino to electron-neutrino oscillations in MINOS. *Phys. Rev. Lett.*, 107:181802, 2011. doi: 10.1103/PhysRevLett.107.181802.
- [26] N. Agafonova et al. Observation of a first ν_τ candidate in the OPERA experiment in the CNGS beam. *Phys. Lett. B*, 691:138–145, 2010. doi: 10.1016/j.physletb.2010.06.022.
- [27] D.S. Ayres et al. NOvA: Proposal to Build a 30 Kiloton Off-Axis Detector to Study $\nu_\mu \rightarrow \nu_e$ Oscillations in the NuMI Beamline, FERMILAB-PROPOSAL-0929, hep-ex/0503053. 3 2004.
- [28] K. Abe et al. The T2K Experiment. *Nucl. Instrum. Meth. A*, 659:106–135, 2011. doi: 10.1016/j.nima.2011.06.067.
- [29] Babak Abi et al. Deep Underground Neutrino Experiment (DUNE), Far Detector Technical Design Report, Volume II DUNE Physics. ArXiv:2002.03005 [hep-ex]. 2 2020.
- [30] K. Abe et al. Hyper-Kamiokande Design Report, arXiv:1805.04163 [physics.ins-det] . 5 2018.
- [31] K. Abe et al. Physics potentials with the second Hyper-Kamiokande detector in Korea. *PTEP*, 2018(6):063C01, 2018. doi: 10.1093/ptep/pty044.
- [32] Y. Fukuda et al. Evidence for oscillation of atmospheric neutrinos. *Phys. Rev. Lett.*, 81:1562–1567, 1998. doi: 10.1103/PhysRevLett.81.1562.
- [33] M. G. Aartsen et al. Determining neutrino oscillation parameters from atmospheric muon neutrino disappearance with three years of IceCube DeepCore data. *Phys. Rev. D*, 91(7):072004, 2015. doi: 10.1103/PhysRevD.91.072004.
- [34] Shakeel Ahmed et al. Physics Potential of the ICAL detector at the India-based Neutrino Observatory (INO). *Pramana*, 88(5):79, 2017. doi: 10.1007/s12043-017-1373-4.
- [35] Ulrich F. Katz. The ORCA Option for KM3NeT. ArXiv:1402.1022 [astro-ph.IM] . *PoS*, 2 2014.
- [36] M.G. Aartsen et al. Letter of Intent: The Precision IceCube Next Generation Upgrade (PINGU). ArXiv:1401.2046 [physics.ins-det]. 1 2014.
- [37] Fengpeng An et al. Neutrino Physics with JUNO. *J. Phys. G*, 43(3):030401, 2016. doi: 10.1088/0954-3899/43/3/030401.
- [38] Gian Luigi Fogli and E. Lisi. Tests of three flavor mixing in long baseline neutrino oscillation experiments. *Phys. Rev. D*, 54:3667–3670, 1996. doi: 10.1103/PhysRevD.54.3667.
- [39] D. Adey et al. Measurement of the Electron Antineutrino Oscillation with 1958 Days of Operation at Daya Bay. *Phys. Rev. Lett.*, 121(24):241805, 2018. doi: 10.1103/PhysRevLett.121.241805.
- [40] H. de Kerret et al. Double Chooz θ_{13} measurement via total neutron capture detection. *Na-*

- ture Phys.*, 16(5):558–564, 2020. doi: 10.1038/s41567-020-0831-y.
- [41] G. Bak et al. Measurement of Reactor Antineutrino Oscillation Amplitude and Frequency at RENO. *Phys. Rev. Lett.*, 121(20):201801, 2018. doi: 10.1103/PhysRevLett.121.201801.
- [42] A. Bandyopadhyay. Physics at a future Neutrino Factory and super-beam facility. *Rept. Prog. Phys.*, 72:106201, 2009. doi: 10.1088/0034-4885/72/10/106201.
- [43] Talk presented by Yue Meng at . The XXIX International Conference on Neutrino Physics and Astrophysics, Neutrino 2020, June 22 - July 2, 2020. <https://conferences.fnal.gov/nu2020/>, .
- [44] Angel Abusleme et al. TAO Conceptual Design Report: A Precision Measurement of the Reactor Antineutrino Spectrum with Sub-percent Energy Resolution. ArXiv:2005.08745 [physics.ins-det]. 5 2020.
- [45] Hiroshi Nunokawa, Stephen J. Parke, and Renata Zukanovich Funchal. Another possible way to determine the neutrino mass hierarchy. *Phys. Rev. D*, 72:013009, 2005. doi: 10.1103/PhysRevD.72.013009.
- [46] H. Minakata, H. Nunokawa, Stephen J. Parke, and R. Zukanovich Funchal. Determining neutrino mass hierarchy by precision measurements in electron and muon neutrino disappearance experiments. *Phys. Rev. D*, 74:053008, 2006. doi: 10.1103/PhysRevD.74.053008.
- [47] Yu-Feng Li, Jun Cao, Yifang Wang, and Liang Zhan. Unambiguous Determination of the Neutrino Mass Hierarchy Using Reactor Neutrinos. *Phys. Rev. D*, 88:013008, 2013. doi: 10.1103/PhysRevD.88.013008.
- [48] Talk presented by Patrick Dunne at The XXIX International Conference on Neutrino Physics and Astrophysics, Neutrino 2020, June 22 - July 2, 2020. <https://conferences.fnal.gov/nu2020/>, .
- [49] Talk presented by Alex Himmel at The XXIX International Conference on Neutrino Physics and Astrophysics, Neutrino 2020, June 22 - July 2, 2020. <https://conferences.fnal.gov/nu2020/>, .
- [50] K. Abe et al. Constraint on the matter–antimatter symmetry-violating phase in neutrino oscillations. *Nature*, 580(7803):339–344, 2020. doi: 10.1038/s41586-020-2177-0. [Erratum: *Nature* 583, E16 (2020)].
- [51] Kevin James Kelly, Pedro AN Machado, Stephen J Parke, Yuber F Perez Gonzalez, and Renata Zukanovich-Funchal. Back to (Mass-)Square(d) One: The Neutrino Mass Ordering in Light of Recent Data. ArXiv:2007.08526 [he-ph].
- [52] M.G. Aartsen et al. Combined sensitivity to the neutrino mass ordering with JUNO, the IceCube Upgrade, and PINGU. *Phys. Rev. D*, 101(3):032006, 2020. doi: 10.1103/PhysRevD.101.032006.
- [53] KM3NeT-ORCA and JUNO combined sensitivity to the neutrino mass ordering. Poster presented by Chau, Nhan. The XXIX International Conference on Neutrino Physics and Astrophysics. Neutrino 2020, June 22 - July 2, 2020. <https://conferences.fnal.gov/nu2020/>, .
- [54] CP violation and mass hierarchy with a combined sensitivity of T2K-II, NOvA and JUNO, poster presented by Ankur, Nath, et al., at The XXIX International Conference on Neutrino Physics and Astrophysics, Neutrino 2020, June 22 - July 2, 2020. <https://conferences.fnal.gov/nu2020/>, .
- [55] Keiichi Kimura, Akira Takamura, and Hidekazu Yokomakura. Exact formulas and simple CP dependence of neutrino oscillation probabilities in matter with constant density. *Phys. Rev. D*, 66:073005, 2002. doi: 10.1103/PhysRevD.66.073005.
- [56] Talk presented by Michael Baird at 40th International Conference on High Energy Physics (ICHEP2020), 28 July 2020 - 6 August 2020, Prague, 2020. <https://indico.cern.ch/event/868940/contributions/3817028/>, .
- [57] Atsuko Ichikawa, private communication.
- [58] Hisakazu Minakata, Hiroshi Nunokawa, Stephen J. Parke, and Renata Zukanovich Funchal. Determination of the Neutrino Mass Hierarchy via the Phase of the Disappearance Oscillation Probability with a Monochromatic $\bar{\nu}_e$ Source. *Phys. Rev. D*, 76:053004, 2007. doi: 10.1103/PhysRevD.76.079901. [Erratum: *Phys.Rev.D* 76, 079901 (2007)].

APPENDICES

A. Empirical Reproduction of the χ^2 Function for the LBνB-II Experiments

In this section, we shall detail how we computed the number of events for T2K and NOvA. For a constant matter density, without any approximation, appearance oscillation probability for given baseline L and neutrino energy E , can be expressed [55] as

$$\begin{aligned} P(\nu_\mu \rightarrow \nu_e) &= a_\nu + b_\nu \cos \delta_{\text{CP}} + c_\nu \sin \delta_{\text{CP}}, \\ P(\bar{\nu}_\mu \rightarrow \bar{\nu}_e) &= a_{\bar{\nu}} + b_{\bar{\nu}} \cos \delta_{\text{CP}} + c_{\bar{\nu}} \sin \delta_{\text{CP}}, \end{aligned} \quad (2)$$

where $a_\nu, b_\nu, c_\nu, a_{\bar{\nu}}, b_{\bar{\nu}}$ and $c_{\bar{\nu}}$ are some factors which depend on the mixing parameters ($\theta_{12}, \theta_{23}, \theta_{13}, \delta m_{21}^2$ and Δm_{32}^2), E and L . This implies that, even after taking into account the neutrino flux spectra, cross sections, energy resolution, detection efficiencies, and so on, which depend on neutrino energy, and after performing integrations over the true and reconstructed neutrino energies, the expected number of ν_e ($\bar{\nu}_e$) appearance events, N_{ν_e} ($N_{\bar{\nu}_e}$), for a given experimental exposure (running time) have also the similar δ_{CP} dependence as,

$$\begin{aligned} N_{\nu_e} &= n_0 + n_c \cos \delta_{\text{CP}} + n_s \sin \delta_{\text{CP}}, \\ N_{\bar{\nu}_e} &= \bar{n}_0 + \bar{n}_c \cos \delta_{\text{CP}} + \bar{n}_s \sin \delta_{\text{CP}}, \end{aligned} \quad (3)$$

where $n_0, n_c, n_s, \bar{n}_0, \bar{n}_c$ and \bar{n}_s are some constants which depend not only on mixing parameters but also on experimental setups. Assuming that background (BG) events do not depend (or depend very weakly) on δ_{CP} , the constant terms n_0 and \bar{n}_0 in Eq. (3) can be divided into the signal contribution and BG one as $n_0 = n_0^{\text{sig}} + n_0^{\text{BG}}$ and $\bar{n}_0 = \bar{n}_0^{\text{sig}} + \bar{n}_0^{\text{BG}}$, as an approximation.

In Table 2, we provide the numerical values of these coefficients which can reproduce quite well the expected number of events shown in the plane spanned by $N_{\nu_e}^{\text{obs}}$ and $N_{\bar{\nu}_e}^{\text{obs}}$, often called bi-rate plots, found in the presentations by T2K [48] and NOvA [49] at Neutrino 2020 Conference, for their corresponding accumulated data (or exposures). We show in the left panels of Figures 8 and 9, respectively, for T2K and NOvA, the bi-rate plots which were reproduced by using the values given in Table 2. Our results are in excellent agreement with the ones shown by the collaborations [48, 49].

The χ^2 function for the appearance channel (AC), for a given LBνB experiment, T2K or NOvA, which is based on the total number of events, is simply defined

as follows, for each MO,

$$\chi_{\text{LB}\nu\text{B}}^2 \text{ AC} \equiv \min_{s_{23}^2, \delta_{\text{CP}}} \left[\frac{(N_{\nu_e}^{\text{obs}} - N_{\nu_e}^{\text{theo}}(s_{23}^2, \delta_{\text{CP}}))^2}{N_{\nu_e}^{\text{obs}}} + \frac{(N_{\bar{\nu}_e}^{\text{obs}} - N_{\bar{\nu}_e}^{\text{theo}}(s_{23}^2, \delta_{\text{CP}}))^2}{N_{\bar{\nu}_e}^{\text{obs}}} + \chi_{\text{pull}}^2(\sin^2 \theta_{23}) \right], \quad (4)$$

where $N_{\nu_e}^{\text{obs}}$ ($N_{\bar{\nu}_e}^{\text{obs}}$) is the number of observed (or to be observed) ν_e ($\bar{\nu}_e$) events, and $N_{\nu_e}^{\text{theo}}$ ($N_{\bar{\nu}_e}^{\text{theo}}$) are the corresponding theoretically expected numbers (or prediction), and

$$\chi_{\text{pull}}^2(\sin^2 \theta_{23}) \equiv \left(\frac{\sin^2 \theta_{23}^{\text{true}} - \sin^2 \theta_{23}}{\sigma(\sin^2 \theta_{23})} \right)^2. \quad (5)$$

Note that the number of events in Eq. (4) include also background events.

	$n_0^{\text{sig}}/\bar{n}_0^{\text{sig}}$	$n_0^{\text{BG}}/\bar{n}_0^{\text{BG}}$	n_c/\bar{n}_c	n_s/\bar{n}_s
T2K ν NMO	68.6	20.2	0.2	-16.5
T2K $\bar{\nu}$ NMO	6.0	12.5	0.2	2.05
T2K ν IMO	58.1	20.2	0.7	-15.5
T2K $\bar{\nu}$ IMO	14.0	6.0	0.05	2.40
NOvA ν NMO	70.0	26.8	3.2	-13.2
NOvA $\bar{\nu}$ NMO	18.7	14.0	1.3	3.7
NOvA ν IMO	45.95	26.8	-3.25	-10.75
NOvA $\bar{\nu}$ IMO	26.2	14.0	-1.5	5.0

Table 2: **NOvA and T2K Oscillation Probability Empirical Parametrisation as of Neutrino 2020 Conference.** The numerical values of the factors appear in Eq. (3) are shown, which were adjusted to approximately agree with what have been presented by T2K [48] and NOvA [49]. These numbers correspond to the exposures of $2.0(1.6) \times 10^{21}$ protons on target (POT) for ν ($\bar{\nu}$) mode of T2K and $1.4(1.3) \times 10^{21}$ POT for ν ($\bar{\nu}$) mode of NOvA experiments. The 3 factors n_0^{sig}, n_c and n_s correspond to the case where $\sin^2 \theta_{23} = 0.55$ (0.57) for T2K (NOvA) and they scale as $n_0^{\text{sig}} \propto \sin^2 \theta_{23}$ and $n_c, n_s \propto \sin^2 2\theta_{23}$ as θ_{23} varies. The values of Δm_{32}^2 are fixed to $\Delta m_{32}^2 = 2.49(-2.46) \times 10^{-3}$ eV² for NMO (IMO) for T2K [48] and $\Delta m_{32}^2 = 2.40(-2.44) \times 10^{-3}$ eV² for NMO for NOvA [49, 56].

Using the number of events given in Eq. (3) with values of coefficients given in Table 2 we performed a fit to the data recently reported by T2K at Neutrino 2020 Conference [48] just varying $\sin^2 \theta_{23}$ and δ_{CP} and could reproduce rather well the $\Delta\chi^2$ presented by T2K in the same conference mentioned above, as shown in the right panel of Fig. 8. We have repeated the similar exercises also for NOvA and obtained the results, shown in the right panel of Fig. 9, which are reasonably in agreement

with what was presented by NOvA at the Neutrino 2020 Conference [49]. In the case of NOvA the agreement is slightly worse as compared to the case of T2K. We believe that this is because, for the results shown in Fig. 9, unlike the case of T2K, we did not take into account the θ_{23} constraint by NOvA (or we have set χ_{pull} in Eq. (5) equals to zero) as this information was not reported in [49].

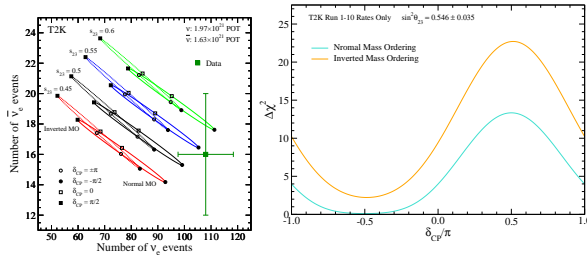


Figure 8: **Reproduction of T2K Bi-Rate and MO Sensitivity Results as of Neutrino 2020 Conference.** Left panel is the bi-rate plot which shows simultaneously the expected number of events for ν_e and $\bar{\nu}_e$ by varying continuously the values of δ_{CP} from $-\pi$ to π , indicated by the solid and dashed curves (ellipses) for 4 different values of $s_{23}^2 = \sin^2\theta_{23}$ indicated in the legend for the exposure of $2.0(1.6) \times 10^{21}$ POT for neutrino (anti-neutrino) mode. The point corresponding to the latest T2K data reported at Neutrino 2020 Conference [48] is indicated by the solid dark green square with 1σ error bars. Right panel shows the $\Delta\chi^2$ obtained by fitting the data using the χ^2 function given in Eq. (4).

We note that for this part of our analysis, we considered only the dependence of $\sin^2\theta_{23}$ and δ_{CP} and ignore the uncertainties of all the other mixing parameters as we are computing the number of events in an approximated way, as described above, by taking into account only the variation due to $\sin^2\theta_{23}$ and δ_{CP} with all the other parameters fixed (separately by T2K [48] and NOvA [49] collaborations) to some values which are close to the values given in Table 1.

In particular, we neglected the uncertainty of Δm_{32}^2 in the $\text{LB}\nu\text{B}$ AC part analysis when it is combined with JUNO plus $\text{LB}\nu\text{B}$ DC part analysis to obtain our final boosted MO sensitivities. Strictly speaking, Δm_{32}^2 must be varied simultaneously (in a synchronised way) in the χ^2 defined in Eq. (6) when it is combined with the χ^2 defined in Eq. (15). However, in our analysis, we simply add $\Delta\chi^2$ obtained from our simplified $\text{LB}\nu\text{B}$ AC simulation which ignored Δm_{32}^2 uncertainty, to the JUNO's boosted χ^2 (described in detail in the Appendix C). This can be justified by considering that $\sim 1\%$ level (or smaller) variations of Δm_{32}^2 only imply the similar (or

smaller) magnitude of variations in the appearance oscillation probabilities, which would be significantly smaller than the statistical uncertainties of $\text{LB}\nu\text{B}$ -II AC mode, which are expected to reach at most the level or $\sim 5\%$ or larger even in our future projections for T2K and NOvA.

For the MO resolution sensitivity shown in Figure 2 and used for our analysis throughout this work, we define the $\Delta\chi^2$ (labeled as $\Delta\chi_{\text{LB}\nu\text{B}}^{\text{AC}}$), as

$$\Delta\chi_{\text{LB}\nu\text{B}}^{\text{AC}}(\text{MO}) \equiv \pm \min_{\sin^2\theta_{23}, \delta_{\text{CP}}} \left[\chi_{\text{LB}\nu\text{B}}^{\text{AC}}(\text{IMO}) - \chi_{\text{LB}\nu\text{B}}^{\text{AC}}(\text{NMO}) \right], \quad (6)$$

where $+(-)$ sign corresponds to the case where the true MO is normal (inverted), and $\chi_{\text{LB}\nu\text{B}}^{\text{AC}}$ is computed as defined in Eq. (4) but with $N_{\nu_e}^{\text{obs}}$ replaced by the theoretically expected ones for given values of assumed true values of θ_{23} and δ_{CP} . In practice, since we do not consider the effect of fluctuation for this part of our analysis, $\chi_{\text{LB}\nu\text{B}}^{\text{AC}} \min = 0$ by construction for true MO.

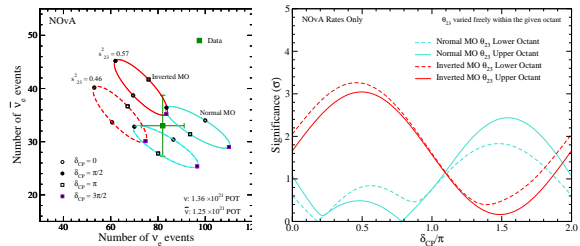


Figure 9: **Reproduction of NOvA Bi-Rate and MO Sensitivity Results as of Neutrino 2020 Conference.** Left panel is the bi-rate plot which shows simultaneously the expected number of events for ν_e and $\bar{\nu}_e$ by varying continuously the values of δ_{CP} from $-\pi$ to π , indicated by the solid and dashed curves (ellipses) for 4 different values of $s_{23}^2 = \sin^2\theta_{23}$ indicated in the legend for the exposure of $1.4(1.3) \times 10^{21}$ POT for neutrino (anti-neutrino) mode. The point corresponding to the latest NOvA data reported at Neutrino 2020 Conference [49] is indicated by the solid dark green square with 1σ error bars. Right panel shows the significance $\sqrt{\Delta\chi^2}$ obtained by fitting the data using the χ^2 function given in Eq. (4) but by setting $\chi_{\text{pull}}^2(\sin^2\theta_{23}) = 0$.

For simplicity, for our future projection, we simply increase by a factor of $3\times$ both T2K and NOvA exposures, to the coefficients given in Table 2 for both ν and $\bar{\nu}$ channels. This corresponds approximately to $8.0(6.4)\times 10^{21}$ POT for T2K $\nu(\bar{\nu})$ mode and to $4.1(3.8)\times 10^{21}$ POT for NOvA $\nu(\bar{\nu})$ mode, to reflect roughly the currently considered final exposures for T2K [57] ($\simeq 10 \times 10^{21}$ POT in total for ν and $\bar{\nu}$) and NOvA [56] ($\simeq 3.2 \times 10^{21}$ POT each for ν and $\bar{\nu}$). This approach

implies that our calculation does not consider future unknown optimisations on the ν ($\bar{\nu}$) mode running.

B. LBνB Disappearance MO Sensitivity

In the upper panel of Figure 10, we show the 4 curves of survival oscillation probabilities, $P(\nu_\mu \rightarrow \nu_\mu)$ and $P(\bar{\nu}_\mu \rightarrow \bar{\nu}_\mu)$ for NMO and IMO, which were obtained by using the best fitted parameters in NuFit5.0 given in Table 1 for the baseline corresponds to NOvA ($L = 810$ km) and with the matter density of $\rho = 2.8$ g/cm³. The NMO and IMO cases are shown, respectively, by blue and red colours whereas the cases for ν and $\bar{\nu}$ are shown, respectively, by solid thin and dashed thick curves. We observe that all of these 4 curves coincide very well with each other, so differences are very small. In the lower panel of the same Figure 10, we show the differences of these curves, between ν and $\bar{\nu}$ channels for both NMO and IMO, as well as between NMO and IMO for both ν and $\bar{\nu}$, as indicated in the legend. We observe that the differences of these oscillation probabilities are $\leq 1\%$ for the energy range relevant for NOvA.

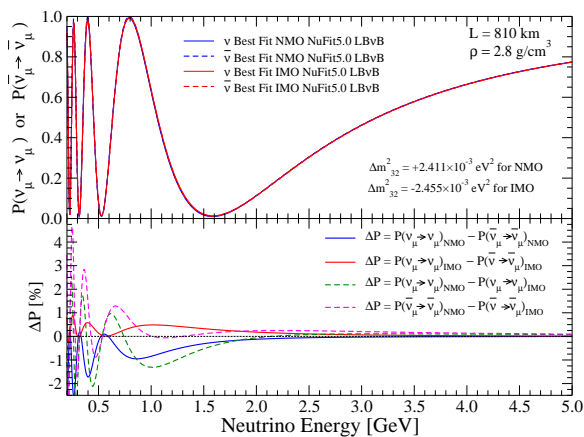


Figure 10: **LBνB Survival Probability Mass Ordering Dependence.** In the upper panel, the $\nu_\mu \rightarrow \nu_\mu$ and $\bar{\nu}_\mu \rightarrow \bar{\nu}_\mu$ survival probabilities computed by using the mixing parameters found in Table 1 are shown for NMO (solid and dashed red curves) and IMO (solid and dashed blue curves) as a function of neutrino energy, as indicated in the legend. In the lower panel, the differences of these probabilities are shown in percent.

Two points can be highlighted. First, the fact that the differences between neutrino and anti-neutrino are quite small implies that the matter effects are very small in these channels, hence determining MO by using matter effects based only on LBνB DC would be impossible. And second, the fact that the curves for

NMO and IMO agree very well implies that the absolute values of the effective mass squared differences, called $\Delta m_{\mu\mu}^2$, defined in Eq. (12) in Appendix D, which correspond to NMO and IMO cases, should be similar. Indeed, by using the values given in Table 1, we obtain $\Delta m_{\mu\mu}^2 = 2.422(-2.431) \times 10^{-3} \text{eV}^2$ for NMO (IMO) exhibiting a small $\sim 0.4\%$ difference. In other words, for each channel, ν and $\bar{\nu}$, there are two *degenerate* solutions, one corresponds to NMO and the other, to IMO, which give in practice the same survival probabilities. We stress that this degeneracy can not be resolved by considering LBνB experiment with DC alone.

C. Analytic Understanding of Synergy between JUNO and LBνB based experiments

In this section, we shall detail the relation between true and false Δm_{32}^2 solutions in the case of JUNO and LBνB, as they are different. This difference is indeed exploited as the main numerical quantification behind the $\Delta\chi_{\text{BOOST}}^2$ term.

C.1 JUNO Relation between True-False Δm_{32}^2

The $\bar{\nu}_e \rightarrow \bar{\nu}_e$ survival probability in vacuum can be expressed as [58]

$$P_{\bar{\nu}_e \rightarrow \bar{\nu}_e} = 1 - c_{13}^4 \sin^2 2\theta_{12} \sin^2 \Delta_{21} - \frac{1}{2} \sin^2 2\theta_{13} \times \left[1 - \sqrt{1 - \sin^2 2\theta_{12} \sin^2 \Delta_{21}} \cos(2|\Delta_{ee}| \pm \phi) \right], \quad (7)$$

where the notation $c_{ij} \equiv \cos \theta_{ij}$ and $s_{ij} \equiv \sin \theta_{ij}$ is used, and $\Delta_{ij} \equiv \Delta m_{ij}^2 L/4E$, L and E are, respectively, the baseline and the neutrino energy, and the effective mass squared difference Δm_{ee}^2 is given by [45]

$$\Delta m_{ee}^2 \equiv c_{12}^2 \Delta m_{31}^2 + s_{12}^2 \Delta m_{32}^2 = \Delta m_{32}^2 + c_{12}^2 \Delta m_{21}^2, \quad (8)$$

and ϕ is given by

$$\tan \phi = \frac{c_{12}^2 \sin(2s_{12}^2 \Delta_{21}) - s_{12}^2 \sin(2c_{12}^2 \Delta_{21})}{c_{12}^2 \sin(2s_{12}^2 \Delta_{21}) + s_{12}^2 \sin(2c_{12}^2 \Delta_{21})}, \quad (9)$$

where $\phi \simeq 0.36$ radian $\simeq 0.11\pi$ for $s_{12}^2 = 0.304$ and $\delta m_{21}^2 = 7.42 \times 10^{-5} \text{eV}^2$. The $+$ ($-$) sign in front of ϕ in Eq. (7) corresponds to the normal (inverted) mass ordering.

Upon data analysis, JUNO will obtain two somewhat different values of Δm_{32}^2 corresponding to NMO and IMO, which we call $\Delta m_{32 \text{ JUNO}}^2 \text{ NMO}$ and $\Delta m_{32 \text{ JUNO}}^2 \text{ IMO}$ where one of them should correspond (or closer) to the true solution. It is expected that by considering $\Delta_{ee}^{\text{NMO}} + \phi = \Delta_{ee}^{\text{IMO}} - \phi$, they are approximately related by

$$\Delta m_{32 \text{ JUNO}}^2 \text{ IMO} \simeq -\Delta m_{32 \text{ JUNO}}^2 \text{ NMO} - 2c_{12}^2 \delta m_{21}^2 - \delta m_\phi^2, \quad (10)$$

where the approximated value of δm_ϕ^2 can be estimated by choosing the average representative energy of reactor neutrinos (~ 4 MeV) as

$$\delta m_\phi^2 \equiv \frac{4E}{L} \phi \simeq 2.1 \times 10^{-5} \left(\frac{E}{4 \text{ MeV}} \right) \text{eV}^2. \quad (11)$$

We found that for a given assumed true value of $\Delta m_{32}^2 = 2.411 \times 10^{-3} \text{eV}^2$ (corresponding to NMO), we can reproduce very well the false value of $\Delta m_{32}^2 = -2.53 \times 10^{-3} \text{eV}^2$ (corresponding to IMO) obtained by a χ^2 fit if we use $E = 4.4$ MeV in Eqs. (10) and (11). The relation between true and false Δm_{32}^2 for JUNO is illustrated by the vertical black dashed and black solid lines in Fig. 3 (b) and (d).

C.2 LB ν B Relation between True-False Δm_{32}^2

It is expected that for LB ν B based experiments like T2K and NOvA whose L/E is adjusted to around the first oscillation maximal, such that $|\Delta_{31}| \sim |\Delta_{32}| \sim \pi/2$, only from the disappearance channel, $\nu_\mu \rightarrow \nu_\mu$ and $\bar{\nu}_\mu \rightarrow \bar{\nu}_\mu$, one could determine precisely the effective mass squared difference called $\Delta m_{\mu\mu}^2$ independent of the MO, which can be expressed, as a very good approximations, in terms of fundamental mixing parameters as [45],

$$\Delta m_{\mu\mu}^2 \equiv \Delta m_{32}^2 + (s_{12}^2 + \cos \delta_{\text{CP}} s_{13} \sin 2\theta_{12} \tan \theta_{23}) \delta m_{21}^2. \quad (12)$$

From this relation, one can extract two possible values of Δm_{32}^2 corresponding to two different MO as

$$\Delta m_{32}^2 \text{LB}\nu\text{B}^{\text{MO}} = +(-) |\Delta m_{\mu\mu}^2 - (s_{12}^2 + \cos \delta_{\text{CP}}^{\text{MO}} s_{13}^{\text{MO}} \sin 2\theta_{12} \tan \theta_{23}^{\text{MO}}) \delta m_{21}^2|, \quad (13)$$

where superscript MO implies either NMO or IMO, and + and - sign correspond, respectively, to NMO and IMO. Note that when the fit is performed assuming MO, the best fitted mixing parameters are, except for solar parameters θ_{12} and δm_{21}^2 , can be different. This relation can be rewritten as

$$\begin{aligned} \Delta m_{32}^2 \text{LB}\nu\text{B}^{\text{IMO}} &= -\Delta m_{32}^2 \text{LB}\nu\text{B}^{\text{NMO}} - \delta m_{21}^2 \{2s_{12}^2 + \sin 2\theta_{12} \\ &(\cos \delta_{\text{CP}}^{\text{NMO}} s_{13}^{\text{NMO}} \tan \theta_{23}^{\text{NMO}} + \cos \delta_{\text{CP}}^{\text{IMO}} s_{13}^{\text{IMO}} \tan \theta_{23}^{\text{IMO}})\} \\ &\simeq -\Delta m_{32}^2 \text{LB}\nu\text{B}^{\text{NMO}} - \delta m_{21}^2 \{2s_{12}^2 + \sin 2\theta_{12} \\ &\times s_{13} \tan \theta_{23} (\cos \delta_{\text{CP}}^{\text{NMO}} + \cos \delta_{\text{CP}}^{\text{IMO}})\}, \quad (14) \end{aligned}$$

where in the last line of the above equation, some simplifications were done based on the fact that best fitted values of $\sin^2 \theta_{13}$ and $\sin^2 \theta_{23}$ in recent global analysis [21] are similar for both MO solutions. By using the relation given in Eq. (14), for a given assumed true value of Δm_{32}^2 (common for all experiments) we obtain the yellow colour bands shown in Fig. 3 (b) and (d).

C.3 Boosting Synergy Estimation

The extra synergy for MO determination sensitivity by combining JUNO and LB ν B DC can be achieved thanks to the *mismatch* (or disagreement) of the fitted Δm_{32}^2 values for the wrong MO solutions between these two types of experiments. For the correct MO, Δm_{32}^2 values coming from different experiments should agree with each other within the experimental uncertainties but for those correspond to the wrong MO do not agree, which can be quantified and used to enhance the sensitivity as follows.

Following the procedure described in [47, 37], we simply try to add the external information on Δm_{32}^2 coming from LB ν B based experiments as a pull term as

$$\chi^2 = \chi_{\text{JUNO}}^2 + \left(\frac{\Delta m_{32}^2 - \Delta m_{32}^2 \text{NMO or IMO}}{\sigma(\Delta m_{32}^2) \text{LB}\nu\text{B}} \right)^2, \quad (15)$$

where χ_{JUNO}^2 implies the χ^2 function for JUNO alone computed in a similar fashion as in [37], $\sigma(\Delta m_{32}^2) \text{LB}\nu\text{B}$ implies the experimental uncertainty for Δm_{32}^2 to be achieved by LB ν B based experiments. As typical values, we consider 3 cases $\sigma(\Delta m_{32}^2) \text{LB}\nu\text{B} = 1, 0.75$ and 0.5% .

In order to take into account the possible fluctuation of the central values of the measured $\Delta m_{32}^2 \text{LB}\nu\text{B}$ we define the extra boosting $\Delta\chi^2$ due to the synergy of JUNO and LB ν B based experiments as the difference of χ^2 defined in Eq. (15) for normal and inverted MO as,

$$\Delta\chi_{\text{boost}}^2 \equiv \pm (\chi_{\text{IMO}}^2 - \chi_{\text{NMO}}^2), \quad (16)$$

where +(-) sign corresponds to the case where the true MO is normal (inverted). Note that in our simplified phenomenological approach (based on the future simulated JUNO data), for the case with no fluctuation, by construction, χ_{NMO}^2 (IMO) = 0 for NMO (IMO).

Suppose that we try to perform a χ^2 fit for the wrong MO. Let us first assume that $\sigma(\Delta m_{32}^2) \text{JUNO} \ll \sigma(\Delta m_{32}^2) \text{LB}\nu\text{B}$ and no fluctuation for simplicity (i.e. $\chi^2_{\text{true MO}} = 0$). The first term in Eq. (15), χ_{JUNO}^2 , forces to drive the fitted value of Δm_{32}^2 very close to the *false* one favoured by JUNO or $\Delta m_{32}^2 \text{JUNO}^{\text{false}}$ (otherwise, χ_{JUNO}^2 value increases significantly). Then the extra increase of χ^2 is approximately given by the second term in Eq. (15), with Δm_{32}^2 replaced by $\Delta m_{32}^2 \text{JUNO}^{\text{false}}$,

$$\begin{aligned} \Delta\chi_{\text{boost}}^2 &\sim \left[\frac{\Delta m_{32}^2 \text{JUNO}^{\text{false}} - \Delta m_{32}^2 \text{LB}\nu\text{B}^{\text{false}}}{\sigma(\Delta m_{32}^2) \text{LB}\nu\text{B}} \right]^2, \\ &\sim \left[\frac{\delta m_\phi^2 + 2\delta m_{21}^2 (\cos 2\theta_{12} - \sin 2\theta_{12} s_{13} \tan \theta_{23} \cos \delta_{\text{CP}})}{\sigma(\Delta m_{32}^2) \text{LB}\nu\text{B}} \right]^2 \\ &\sim 4, 9, 16, \text{ respectively, for } \delta_{\text{CP}} = 0, \pm\pi/2, \pm\pi, \quad (17) \end{aligned}$$

where the numbers in the last line were estimated for $\sigma(\Delta m_{32}^2)_{\text{LB}\nu\text{B}} = 1\%$. The case where $\delta_{\text{CP}} = \pm\pi/2$ and $\Delta\chi_{\text{boost}}^2 \sim 9$ can be directly compared with more precise results shown in Fig. 4(a), see the blue solid curve at $\delta_{\text{CP}}^{\text{true}} = \pm\pi/2$ which gives $\Delta\chi_{\text{boost}}^2 \sim 8$ which is in rough agreement. The expression in Eq. (17) is in agreement with the one given in Eq. (18) of [47] apart from the term δm_ϕ^2 which is not so large.

D. Formulation 3ν versus 2ν Models

In the previous discussions found in [47, 37], in order to demonstrate the boosting synergy effect between JUNO and LBνB experiments, the effective mass squared differences Δm_{ee}^2 and $\Delta m_{\mu\mu}^2$, defined respectively, in Eqs. (8) and (12) originally found in [45] were used. While we used these parameters in some intermediate steps of our computations, as described in Appendix C, we did not use these parameters explicitly in our combined χ^2 describing the extra synergy between JUNO and LBνB (DC) based experiments defined in Eq. (15), as well as in the final sensitivity plots presented in this paper.

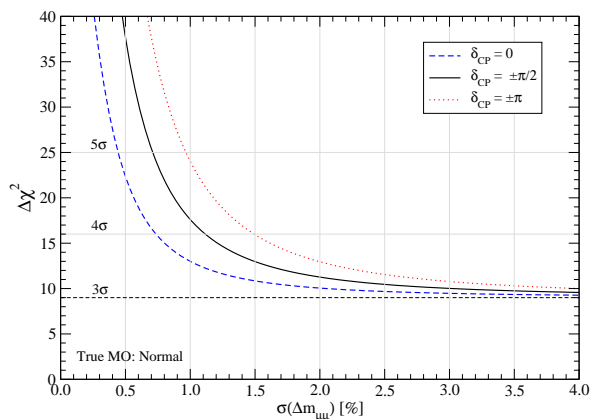


Figure 11: $\Delta\chi^2(\text{JUNO}\oplus\text{LB}\nu\text{B-DC})$ as a Function of the Precision of $\Delta m_{\mu\mu}^2$. Expected MO sensitivity to be obtained by JUNO with external information of $\Delta m_{\mu\mu}^2$ coming from LBνB experiments following the procedure described in [47, 37], are shown as a function of the precision of $\Delta m_{\mu\mu}^2$ for $\cos\delta_{\text{CP}} = \pm 1$ and 0. This plot is similar to Figure 7 in [47], once upgraded to the latest NuFit5.0 global data inputs. We observe that they are consistent with each other, if the curves for the δ_{CP} values of 0° (blue) and 180° (red) were interchanged, as a result of a minor typo in legend [47].

In order to check the consistency between our work and previous studies, we have explicitly verified that the results do not depend on the parameters to be used in the analysis and in the presentation of the final results

provided that that comparisons are done properly. In Figure 11, we show $\Delta\chi^2(\text{JUNO}\oplus\text{LB}\nu\text{B-DC})$ computed by using explicitly $\Delta m_{\mu\mu}^2$ (instead of using Δm_{32}^2) in our χ^2 analysis as done in [47, 37], as a function of the precision of $\Delta m_{\mu\mu}^2$. There is general good agreement with the result shown in Figure 7 of [47], if δ_{CP} curves for 0° and 180° were interchanged, as described in Figure 11.

8.3 Summary

The study of the MO synergy between JUNO and LB ν B experiments lead to two major conclusions:

- The combination of JUNO, NOvA and T2K may lead to the first resolved ($>5\sigma$) MO measurement by 2028, since JUNO is expected to start data taking in 2022 and accumulate 6 years statistics by 2028, and the NOvA and T2K data will be ready at that time. This a hybrid MO solution combining the JUNO intrinsic MO measurement, the NOvA and T2K intrinsic MO measurement from the appearance channel and the boosting synergy effect between JUNO and LB ν B disappearance channel via the high precision measurement of Δm_{32}^2 . In order to obtain a conservative and realistic estimation, the $\pm 1\sigma$ data fluctuations of Δm_{32}^2 and the ambiguity related to different δ_{CP} values for true and false MO solutions are taken into account. Furthermore the atmospheric neutrino data will further enhance the MO resolution, as it currently have a sizable contribution to today's MO knowledge via the Super-K experiment [56].
- A robust ($>5\sigma$) vacuum oscillations driven MO solution may be reachable by combining JUNO and LB ν B-III (e.g. Hyper-K) disappearance channel. This relies on the sub-percent precision measurement of Δm_{32}^2 from LB ν B-III by exploiting the aforementioned boosting synergy effect. The vacuum oscillations driven MO solution can be used to compare with the matter effects MO solution (likely by DUNE), yielding a ultimate MO scrutiny. Any unexpected discrepancy between the two resolved measurements may imply discovery potential.

My specific contributions to this MO synergy publication are:

(1.) The simulation of the JUNO Monte Carlo (MC) experiments (or virtual experiments). The JUNO MO sensitivity related studies are performed with the MC experiments by properly handling of the boosting synergy effect and data fluctuations.

(2.) The validation of the MC results with the analytical and numerical calculations. The JUNO MO sensitivity related studies including the intrinsic MO information, the MO boosting term and the data fluctuations are also performed with an analytical and numerical approach. Consistent results are obtained compared to the MC experiments study, thus yielding cross validation for the two approaches.

(3.) The MO sensitivity combination of JUNO and LB ν B according to the timeline of JUNO. The JUNO intrinsic MO sensitivity and the MO boosting term are estimated according to the JUNO time scale, and the intrinsic LB ν B-II MO sensitivity is added according to the current favored δ_{CP} range.

Conclusions

In the era of the high precision neutrino oscillation measurement, JUNO, as one of the most critical experiments, will contribute to the neutrino MO determination and the sub-percent precision measurement of half of all oscillation parameters (θ_{12} , Δm_{21}^2 and Δm_{32}^2). To achieve the high precision reactor neutrino oscillation measurement at JUNO, the most critical and challenging topic is the energy control including both the energy scale and the energy resolution.

The energy resolution stochastic component is designed to be better than $3\%/\sqrt{E}$. The energy scale and non-stochastic energy resolution, implying the energy detection systematics control, are required to be at sub-percent level, which are realized mainly through extremely careful detector design and dedicated detector response calibrations. Among the detector response effects, the readout charge response (or QNL) effect is particular important and challenging to control because of the largest charge dynamic range of JUNO's main readout system (LPMT) and the degeneracy between the QNL and almost all the other response effects.

Given the importance of the QNL control for the energy measurement, hence the high precision neutrino oscillation measurement at JUNO, this thesis is devoted to develop the novel Dual Calorimetry calibration technique to face this challenging topic. The Dual Calorimetry is designed by introducing the SPMT readout system, forming the energy estimator based on robust PE counting in addition to the main LPMT readout system which forms the energy estimator based on charge integration (through sophisticated waveform reconstruction). The Dual Calorimetry always implies the response comparison between the LPMT calorimetry and the SPMT calorimetry. Since the two systems are always exposed to the same events occurring in the LS, all the fully correlated response effects, i.e. the LS nonlinear response (LSNL), and the partially correlated effects, i.e. position nonuniform response (NU), can be canceled out or corrected. Thus the uncorrelated charge response effect (QNL) can be isolated experimentally. By exploiting the SPMT readout as the linear charge response reference for the LPMT readout, the QNL of the LPMT can be well controlled with the Dual Calorimetry.

Two methodologies of the Dual Calorimetry are developed in this thesis, i.e. DCC-laser and DCC-gamma. These two independent and complementary methods are the channel-wise implementations which exploit the SPMT system to calibrate directly the potential QNL of the LPMT at single channel level. DCC-laser exploits the unique advantage of the UV laser calibration source to achieve the maximal isolation the QNL effect, the full charge dynamic range coverage and all channels coverage. DCC-gamma exploits the advantage of radioactive (gamma) calibration sources to achieve the calibration of the target QNL related to the reactor neutrino signals. DCC-laser and DCC-gamma have complementary advantages, therefore, by merging them into one effective complete calibration scheme, the reactor neutrino induced QNL of the entire LPMT system can be significantly calibrated with several times up to one order of magnitude improvement.

Through the channel-wise QNL calibration, the calorimetry energy control can be improved significantly with the DCC. Specifically, the DCC directly contributes to the energy scale non-linearity (ESNL) control. The QNL induced ESNL bias can be restrained within 0.3%, and 0.1% level could be reachable. By calibrating the channel-wise QNL, the QNL induced nonuniform response bias can be well constrained to $\leq 0.1\%$ level. As for the energy resolution control with the DCC, the energy resolution deterioration caused by the QNL can be well confined to 1% level with the non-stochastic term below 1%. Therefore, by addressing the critical and challenging QNL calibration with the DCC, both the energy accuracy and precision can be significantly better controlled towards the designed goals, i.e. the sub-percent energy detection systematics control and 3% energy resolution at 1 MeV with $< 1\%$ non-stochastic term. Hence, the Dual Calorimetry ensures the necessary conditions for yielding the JUNO high precision reactor neutrino oscillation measurements.

Furthermore, the Dual Calorimetry could contribute to the systematics scrutiny and quantification through other possible implementations based on cosmogenic signals or neutrino oscillations which are worth exploring in the future. Meanwhile, it may be also worth exploring the possible higher order channel-wise DCC based on both data and MC. The precise energy resolution parameterization, especially for the non-stochastic component breakdown, is requisite upon the demonstration of the MC performance, the detector commissioning and running.

The Dual Calorimetry study during the thesis exhibits great potential to help achieving the high precision reactor neutrino oscillation measurements and is integrated into the baseline calibration strategy of JUNO. It contributes to a collaboration paper titled "*Calibration Strategy of the JUNO Experiment*" which has been submitted to arXiv [211]. A dedicated paper of the Dual Calorimetry containing most of the contents and results of this thesis is also under preparation.

The DCC performance depends on the hardware of the SPMT, especially the readout electronics providing the robust PE counting. Hence, some tests are completed during the thesis in order to validate the performance of the SPMT readout electronics for the Dual Calorimetry. The testing results indicate that the discriminator data stream and charge data stream can provide the redundant PE counting, charge and time information, thus enabling the Dual Calorimetry implementation. More collaboration effort is expected and ongoing to further address the SPMT readout performance.

Most of this thesis has been devoted to the Dual Calorimetry to ensure the best possible energy control (energy scale and energy resolution) being necessary to reach JUNO intrinsic $\sim 3\sigma$ MO measurement and sub-percent oscillation parameters measurement. Besides, the MO synergy study carried out during this thesis indicates the possible resolved ($\geq 5\sigma$) MO measurements by combining JUNO and LB ν B experiments. The combination of JUNO, NO ν A and T2K may lead to the first resolved MO measurement by 2028 by taking into account the intrinsic MO measurement of each experiment and the boosting synergy effect between JUNO and LB ν B. Furthermore, by combining JUNO and LB ν B-III (e.g. Hyper-K) disappearance channel, a vacuum oscillation driven MO solution may be reachable which can contribute to the ultimate MO scrutiny together with the matter effects MO solution (likely by DUNE). The MO synergy study contributes to a dedicated paper as presented in this thesis, which has been already submitted to arXiv [210] for imminent publication.

Conclusions

À l'ère de la mesure de l'oscillation des neutrinos de haute précision, JUNO, en tant que l'une des expériences les plus critiques, contribuera à la détermination de l'ordre de masse des neutrinos et à la mesure de la moitié de tous les paramètres d'oscillation (θ_{12} , Δm_{21}^2 et Δm_{32}^2) avec une précision sans précédent. Pour réaliser la mesure de l'oscillation des neutrinos du réacteur de haute précision à JUNO, le sujet le plus critique et le plus difficile est le contrôle de l'énergie, y compris l'échelle d'énergie et la résolution d'énergie.

Le composant stochastique de résolution d'énergie est conçu pour être meilleur que $3\%/\sqrt{E}$. L'échelle d'énergie et le composant non-stochastique de résolution d'énergie, impliquant le contrôle des erreurs systématiques sur l'énergie, doivent être au niveau inférieur à 1%, qui sont principalement réalisées grâce à une conception extrêmement soignée du détecteur et aux étalonnages dédiés de détecteur réponse. Parmi les effets de détecteur réponse, l'effet de charge réponse de lecture (ou QNL) est particulièrement important et difficile à contrôler en raison de la plus grande plage dynamique de charge du système de JUNO LPMT et de la dégénérescence entre le QNL et presque tous les autres effets de réponse.

Compte tenu de l'importance du contrôle QNL pour la mesure d'énergie, donc la mesure de l'oscillation des neutrinos à JUNO, cette thèse est consacrée au développement de la nouvelle technique d'étalonnage avec la Dual Calorimetry pour faire face à ce sujet difficile. La Dual Calorimetry est conçue en introduisant le SPMT système de lecture, formant l'estimateur d'énergie basé sur le PE comptage robuste en plus du LPMT système qui forme l'estimateur d'énergie basé sur l'intégration de charge. La Dual Calorimetry implique toujours la comparaison des réponses entre la LPMT calorimétrie et la SPMT calorimétrie. Puisque les deux systèmes sont toujours exposés aux mêmes événements dans le LS, tous les effets de réponse entièrement corrélés, i.e. la réponse non linéaire de LS (LSNL), et les effets partiellement corrélés, i.e. la réponse non uniforme sur la position (NU), peuvent être annulés ou corrigés. Donc, l'effet de réponse de charge non corrélé (QNL) peut être isolé expérimentalement. En exploitant le SPMT comme la référence de réponse de charge linéaire pour le LPMT, le QNL du LPMT peut être bien contrôlé avec la Dual Calorimetry.

Deux méthodologies de la Dual Calorimetry sont développées dans cette thèse, i.e. DCC-laser et DCC-gamma. Ces deux méthodes indépendantes et complémentaires sont les réalisations de la Dual Calorimetry par canal qui exploitent le SPMT système pour étalonner directement le potentiel QNL du LPMT au niveau d'un seul canal. Le DCC-laser exploite l'avantage unique de la UV laser source d'étalonnage pour obtenir une isolation maximale de l'effet QNL, la couverture de la plage dynamique de charge complète et la couverture de tous les canaux. Le DCC-gamma exploite l'avantage des sources d'étalonnage radioactives (gamma) pour réaliser l'étalonnage du QNL lié aux signaux des neutrinos de réacteur. Le DCC-laser et le DCC-gamma ont des avantages complémentaires. Par conséquent, en les fusionnant en un seul cadre d'étalonnage complet, la QNL induite par les neutrinos de réacteur de l'ensemble du LPMT système peut être considérablement étalonnée avec plusieurs fois jusqu'à un ordre de grandeur d'améliora-

tion.

Grâce à l'étalonnage de QNL par canal, le contrôle de l'énergie calorimétrique peut être considérablement amélioré avec le DCC. Plus précisément, le DCC contribue directement au contrôle de non-linéarité de l'échelle d'énergie (ESNL). Le biais de ESNL induit par la QNL peut être restreint à moins de 0.3%, et le niveau de 0.1% pourrait être atteint. En étalonnant la QNL par canal, le biais de réponse non uniforme induit par la QNL peut être bien contraint au niveau de $\leq 0.1\%$. En ce qui concerne le contrôle de la résolution d'énergie avec le DCC, la détérioration de la résolution causée par la QNL peut être bien confinée au niveau de 1% avec le terme non-stochastique inférieur à 1%. Donc, en abordant l'étalonnage de la QNL critique avec le DCC, l'exactitude et la précision de l'énergie peuvent être considérablement mieux contrôlées vers les objectifs conçus, i.e. le contrôle des erreurs systématiques sur l'énergie inférieures à 1% et la résolution d'énergie de 3% à 1 MeV avec le terme non-stochastique inférieur à 1%. Par conséquent, la Dual Calorimetry assure les conditions nécessaires pour obtenir les mesures d'oscillation des neutrinos de réacteur de haute précision à JUNO.

En outre, la Dual Calorimetry pourrait contribuer à l'examen minutieux et la quantification des erreurs systématiques par d'autres réalisations possibles basées sur des signaux cosmogéniques ou des oscillations des neutrinos qui méritent d'être explorées à l'avenir. Dans le même temps, il peut également valoir la peine d'explorer le DCC d'ordre supérieur basé sur les données et le MC. Le paramétrage précis de la résolution d'énergie, en particulier pour la décomposition des composants non-stochastiques, est requis lors de la démonstration des performances du MC et du fonctionnement du détecteur.

Les études de Dual Calorimetry pendant la thèse montrent un grand potentiel pour aider à réaliser la mesure de haute précision de l'oscillation des neutrinos de réacteur et elles sont intégrées dans la stratégie d'étalonnage de JUNO expérience. Ces études contribuent à un article de collaboration intitulé "*Calibration Strategy of the JUNO Experiment*" qui a été soumis à arXiv [211]. Un article dédié à la Dual Calorimetry contenant les contenus et résultats de cette thèse est également en préparation.

Les performances du DCC dépendent du matériel informatique de SPMT, en particulier la lecture électronique assurant le PE comptage robuste. Donc, certains tests sont effectués au cours de la thèse afin de valider les performances de la lecture électronique de SPMT pour la Dual Calorimetry. Les résultats des tests indiquent que le flux de données de discriminateur et le flux de données de charge peuvent fournir les informations redondantes de PE comptage, de charge et de temps, permettant la réalisation de la Dual Calorimetry. Plus d'efforts de la collaboration sont en cours pour améliorer les performances de la SPMT lecture.

La majeure partie de cette thèse a été consacrée à la Dual Calorimetry pour assurer le meilleur contrôle d'énergie possible (échelle d'énergie et résolution d'énergie) qui est nécessaire pour atteindre la mesure de $\sim 3\sigma$ MO intrinsèque et la mesure des paramètres d'oscillation de haute précision ($< 1\%$) à JUNO. Par ailleurs, les études de MO synergie réalisées au cours de cette thèse indiquent que le MO est possible résolu ($\geq 5\sigma$) en combinant les expériences JUNO et LB ν B. La combinaison de JUNO, NOvA et T2K peut conduire à la première MO mesure résolue d'ici 2028, en tenant compte de la mesure de MO intrinsèque de chaque expérience et de l'effet de synergie *boosting* entre JUNO et LB ν B. De plus, en combinant JUNO et le canal de disparition de LB ν B-III (par exemple Hyper-K), une MO solution dominée par l'oscillation sous vide peut être atteinte, ce qui peut contribuer à l'examen final de MO avec la MO solution dominée par les effets de matière (probablement par DUNE). Les études MO synergie contribuent à un article dédié tel que présenté dans cette thèse, qui a déjà été soumis à arXiv [210] pour publication imminente.

List of Figures

1.1	Elementary particles in the Standard Model	6
1.2	Solar neutrino spectra predicted by the SSM SFII-GS98 model	11
1.3	Fluxes of ^8B solar neutrinos measured by SNO (salt phase)	13
1.4	Solar (ν_e) neutrino survival probability with respect to the neutrino energy	13
1.5	The zenith angle distributions of atmospheric neutrino events in the Super-Kamiokande observation	15
1.6	Super-Kamiokande atmospheric neutrino L/E analysis	15
1.7	2σ confidence level region of θ_{23} and $\Delta m_{31(2)}^2$ for NMO and IMO with the latest results by 2020	16
1.8	1σ and 2σ allowed regions of δ_{CP} and $\sin^2 \theta_{23}$ for T2K and NOvA	18
1.9	Left: The ratio of the observed reactor $\bar{\nu}_e$ L/E spectrum to the expectation in absence of neutrino oscillation at KamLAND. Right: Allowed θ_{12} and Δm_{21}^2 regions (at 1σ , 90%, 2σ , 99%, and 3σ C.L.) for KamLAND data and solar neutrino data.	19
1.10	The θ_{13} measurements from Daya Bay (a), Double Chooz (b) and RENO (c). (d): 2σ confidence level region of θ_{13} and $\Delta m_{31(2)}^2$ for Daya Bay, Double Chooz and RENO	21
1.11	Illustration of the neutrino MO and unknown absolute mass scale	23
2.1	The JUNO experimental site	27
2.2	The reactor $\bar{\nu}_e$ disappearance (or survival) probability as a function of the neutrino energy	28
2.3	The reactor $\bar{\nu}_e$ energy spectrum at JUNO for no oscillation, oscillation NMO and IMO cases respectively	30
2.4	Spectra of the accidental, $^8\text{He}/^9\text{Li}$, fast neutron and $^{13}\text{C}(\alpha, n)^{16}\text{O}$ backgrounds	32
2.5	Illustration of the MO sensitivity in the reactor $\bar{\nu}_e$ energy spectrum at JUNO	34
2.6	The JUNO MO sensitivity ($\Delta\chi_{MO}^2$) contour as the function of the event statistics (luminosity) and the energy resolution	36
2.7	Energy non-linearity effect in the MO sensitivity	36
2.8	The estimated supernova neutrino event spectra with respect to the visible energy E_d at JUNO for a SN explosion at 10 kpc	39
2.9	The estimated solar neutrino spectra at JUNO	39
2.10	Left: proton decay signatures at JUNO for $p \rightarrow K^+ + \bar{\nu}$ channel. Right: 3σ sensitivity to the proton lifetime for $p \rightarrow K^+ + \bar{\nu}$ channel.	40
3.1	Schematic view of the JUNO detector	43
3.2	Illustration of the JUNO LS composition and the scintillation processes	44
3.3	Photos of the JUNO LPMTs and SPMT	45
3.4	The LPMT system readout scheme	46

3.5	The SPMT system readout scheme	48
3.6	Design of the UV laser source	49
3.7	Schematic of the calibration system	50
3.8	Schematic view of the Top Tracker and a TT wall	51
4.1	Residual QNL of the waveform reconstruction for a single channel in the FADC based electronics system of the Daya Bay experiment	55
4.2	The non-linearity defined in Ref.[188] to illustrate the importance of energy scale non-linearity control for the MO determination	55
4.3	The non-uniformity (NU) bias induced by the charge non-linearity	57
4.4	The LS response ratio between the LPMT and SPMT systems	58
4.5	The response ratio between a single LPMT and the SPMT system as the function of the source position along the detector radius	59
4.6	The response ratio between the LPMT and SPMT systems with respect to the electron source position along the detector radius	60
4.7	Detector level (or event-wise) QNL manifestation at JUNO in simulation	62
4.8	Particle dependent time profile	64
4.9	Position dependent time profile	64
4.10	Measured absorption length of each LS component and total absorption, superimposed with Rayleigh scattering length	65
4.11	LPMT and SPMT sensitivities on the "solar" oscillation parameters $\sin^2 \theta_{12}$ and Δm_{21}^2	68
5.1	UV laser wavelength spectrum in the JUNO laser system and LS emission spectrum when the LS is excited by the UV laser	72
5.2	Illustration of the DCC-laser	73
5.3	Response comparison between the single LPMT and the SPMT system	74
5.4	The linear region of the response relation between the single LPMT and the SPMT system	74
5.5	DCC-laser performance under the assumption of $\sim 10\%$ channel-wise QNL over 1~100 PE	76
5.6	DCC-laser performance under the assumption of $\sim 50\%$ channel-wise QNL over 1~100 PE	77
5.7	The particle and position dependent time profile impact on the QNL and the corresponding DCC-laser performance	79
5.8	Illustration of the DCC-gamma	81
5.9	The response relation between the single LPMT and the SPMT system while scanning the source position and scanning the radioactive source energy at each position	82
5.10	Response relations with the aligned SPMT responses	83
5.11	The SPMT one dimension NU map and the single LPMT one dimension NU map	85
5.12	Aligned response relation	85
5.13	DCC-gamma performance under the assumption of a $\sim 10\%$ QNL	86
5.14	Illustration of DCC-gamma challenge for calibrating two channels of which one is not reachable	88
5.15	DCC two stages strategy performance	90
5.16	SPMT QNL control through PE counting	92
5.17	LPMT QNL control through DCC with the $Pois(0)$ PE counting	93
5.18	SPMT QNL (channel-wise) control through $Pois(0)$ PE counting	95
5.19	Unbiased and biased Poisson distributions	96
5.20	Poisson statistics effect	98

5.21	PMT charge resolution effect	99
5.22	LPMT effective threshold effect	101
5.23	SPMT charge QNL effect	102
5.24	The single LPMT NU map (C_2 correction) effect	103
6.1	Liquid scintillator non-linearity for electrons, gammas and positrons . . .	107
6.2	Energy scale non-linearity for electrons with zero QNL, QNL at the de- tector center and QNL at the detector edge	108
6.3	QNL ($\sim 10\%$ channel-wise) impact on the ESNL and the control with DCC110	
6.4	QNL ($\sim 50\%$ channel-wise) impact on the ESNL and the control with DCC111	
6.5	NU calibration points at JUNO by assuming the azimuthal symmetry of the detector response	112
6.6	The JUNO detector NU response in the 2D r - θ plane	113
6.7	The QNL induced NU bias by an extreme case of $\sim 50\%$ channel-wise QNL	114
6.8	The DCC control for the QNL induced NU bias	114
6.9	Illustration of different contributions for the electron energy resolution at JUNO	115
6.10	QNL ($\sim 10\%$ channel-wise) impact on the energy resolution and the control with DCC	118
6.11	QNL (an extreme case of $\sim 50\%$ channel-wise) impact on the energy res- olution and the control with DCC	119
7.1	Prototype of the ABC board version 0	122
7.2	The typical pedestal distribution of one channel of the ABC board	124
7.3	Pedestal distributions for 128 channels of the ABC board	124
7.4	An example of the correlation between two different channels of the ABC board	125
7.5	Correlation matrix and correlation coefficient for 128 channels of the ABC board	126
7.6	A typical fine time distribution for one channel in the ABC	126
7.7	Time difference Δt_{ij} with channel 0 as the reference channel under the force trigger mode for 128 channels in the QDS	127
7.8	Three examples of the Δt_{ij} distribution	128
7.9	Pedestal stability during 16 days observation	129
7.10	Unexpected feature with high loading in QDS	130
7.11	Digital counting in the DDS in comparison with the charge measurement in the QDS	131
7.12	Time over threshold measurement in DDS for one channel	132
7.13	Time difference between the falling edge and the rising edge under the force-trigger mode in the DDS	133
7.14	Time difference Δt_{ij} with channel 0 as the reference channel under the force trigger mode for 128 channels in the DDS	133
7.15	The high trigger rate handling with the DDS for one channel	134

List of Tables

1.1	NuFit 5.0 global analysis of the neutrino oscillation parameters in the three neutrino framework	22
2.1	The efficiencies of the reactor $\bar{\nu}_e$ selection cuts, signal and background event rates per day at JUNO	33
2.2	Different contributions to the MO sensitivity	35
2.3	Current precision of neutrino oscillation parameters based on the state of the art knowledge by 2020	38
2.4	Expected precision of $\sin^2 \theta_{12}$, Δm_{21}^2 and $ \Delta m_{32}^2 $ at JUNO	38
3.1	LPMT (20-inch) specifications for MCP-PMT and Dynode PMT	46
3.2	JUNO SPMT (3-inch) specifications	47
3.3	The designed radioactive calibration sources for JUNO	49
4.1	The charge fraction in terms of the number of PE collected at the single PMT for the reactor $\bar{\nu}_e$ IBD events	61
4.2	$\sin^2 \theta_{12}$ and Δm_{21}^2 sensitivity with LPMT system and SPMT system . . .	67

Bibliography

- [1] H. Becquerel. Sur les radiations émises par phosphorescence. *Comptes-Rendus de l'Académie des Sciences*, 122 (1896) 420 (1896).
- [2] H. Becquerel. Sur les radiations invisibles émises par les corps phosphorescents. *Comptes-Rendus de l'Académie des Sciences*, 122 (1896) 501 (1896).
- [3] <https://www.nobelprize.org/prizes/physics/1903/summary/>.
- [4] <https://www.nobelprize.org/prizes/chemistry/1908/rutherford/facts/>.
- [5] J. Chadwick. Intensitätsverteilung im magnetischen spektrum der beta-strahlen von radium b+c. *Verhandlungen der deutschen Physikalischen Gesellschaft*, 16:383, 1914.
- [6] W. Pauli. Dear radioactive ladies and gentlemen. *Phys. Today*, 31N9:27, 1978.
- [7] E. Fermi. Tentativo di una teoria dei raggi beta. *Il Nuovo Cimento*, 11(1):1–19, 1934.
- [8] H. Bethe and R. Peierls. The neutrino. *Nature*, 133(3362):532–532, 1934.
- [9] C. L. Cowan, F. Reines, F. B. Harrison, H. W. Kruse, and A. D. McGuire. Detection of the free neutrino: a confirmation. *Science*, 124(3212):103–104, 1956.
- [10] G. Danby, J-M. Gaillard, K. Goulianos, L. M. Lederman, N. Mistry, M. Schwartz, and J. Steinberger. Observation of high-energy neutrino reactions and the existence of two kinds of neutrinos. *Physical Review Letters*, 9(1):36–44, 1962.
- [11] M. L. Perl et al. Evidence for anomalous lepton production positron-electron annihilation. *Physical Review Letters*, 35(22):1489–1492, 1975.
- [12] DONUT Collaboration. Observation of tau neutrino interactions. *Physics Letters B*, 504(3):218–224, 2001.
- [13] The ALEPH Collaboration, the DELPHI Collaboration, the L3 Collaboration, the OPAL Collaboration, the SLD Collaboration, the LEP Electroweak Working Group, the SLD electroweak, heavy flavour groups. Precision electroweak measurements on the z resonance. *Physics Reports*, 427(5-6):257–454, 2006.
- [14] S. Weinberg. A model of leptons. *Physical Review Letters*, 19(21):1264–1266, 1967.
- [15] Sheldon L. Glashow. Partial-symmetries of weak interactions. *Nuclear Physics*, 22(4):579–588, 1961.
- [16] A. Salam. Weak and electromagnetic interactions. *Proceedings Of The Nobel Symposium Held 1968 At Lerum, Sweden, Stockholm 1968*, pages 367–377, 1968.

- [17] Peter W. Higgs. Broken symmetries and the masses of gauge bosons. *Physical Review Letters*, 13(16):508–509, 1964.
- [18] G. S. Guralnik, C. R. Hagen, and T. W. B. Kibble. Global conservation laws and massless particles. *Physical Review Letters*, 13(20):585–587, 1964.
- [19] F. Englert and R. Brout. Broken symmetry and the mass of gauge vector mesons. *Physical Review Letters*, 13(9):321–323, 1964.
- [20] T. Asaka and M. Shaposhnikov. The ν MSM, dark matter and baryon asymmetry of the universe. *Physics Letters B*, 620(1-2):17–26, 2005.
- [21] R. N. Mohapatra et al. Theory of neutrinos: a white paper. *Reports on Progress in Physics*, 70(11):1757–1867, 2007.
- [22] https://en.wikipedia.org/wiki/standard_model.
- [23] B. Pontecorvo. Inverse beta processes and nonconservation of lepton charge. *JETP*, 34(1):247, 1958.
- [24] B. Pontecorvo. Neutrino experiments and the problem of conservation of leptonic charge. *JETP*, 53(5):1717, 1967.
- [25] Z. Maki, M. Nakagawa, and S. Sakata. Remarks on the unified model of elementary particles. *Progress of Theoretical Physics*, 28(5):870–880, 1962.
- [26] Super-Kamiokande Collaboration. Evidence for oscillation of atmospheric neutrinos. *Physical Review Letters*, 81(8):1562–1567, 1998.
- [27] SNO Collaboration. Direct evidence for neutrino flavor transformation from neutral-current interactions in the sudbury neutrino observatory. *Physical Review Letters*, 89(1), 2002.
- [28] KamLAND Collaboration. First results from KamLAND: Evidence for reactor antineutrino disappearance. *Physical Review Letters*, 90(2), 2003.
- [29] T2K Collaboration. Indication of electron neutrino appearance from an accelerator-produced off-axis muon neutrino beam. *Physical Review Letters*, 107(4), 2011.
- [30] Daya Bay Collaboration. Observation of electron-antineutrino disappearance at daya bay. *Physical Review Letters*, 108(17), 2012.
- [31] Double Chooz Collaboration. Indication of reactor electron antineutrino disappearance in the double chooz experiment. *Physical Review Letters*, 108(13), 2012.
- [32] RENO Collaboration. Observation of reactor electron antineutrinos disappearance in the RENO experiment. *Physical Review Letters*, 108(19), 2012.
- [33] E. Akhmedov. Quantum mechanics aspects and subtleties of neutrino oscillations. *arXiv:1901.05232*.
- [34] C. Giunti, C. W. Kim, and U. W. Lee. When do neutrinos really oscillate? quantum mechanics of neutrino oscillations. *Physical Review D*, 44(11):3635–3640, 1991.
- [35] E. K. Akhmedov and J. Kopp. Neutrino oscillations: quantum mechanics vs. quantum field theory. *Journal of High Energy Physics*, 2010(4), 2010.
- [36] L. Wolfenstein. Neutrino oscillations in matter. *Physical Review D*, 17(9):2369–2374, 1978.

- [37] S. P. Mikheyev and A. Yu. Smirnov. Resonant amplification of neutrino oscillations in matter and solar-neutrino spectroscopy. *Il Nuovo Cimento C*, 9(1):17–26, 1986.
- [38] F. Suekane. *Neutrino Oscillations*. Springer-Verlag GmbH, 2015.
- [39] P. C. de Holanda and A. Y. Smirnov. LMA MSW solution of the solar neutrino problem and first KamLAND results. *Journal of Cosmology and Astroparticle Physics*, 2003(02):001–001, 2003.
- [40] John N. Bahcall, Aldo M. Serenelli, and Sarbani Basu. New solar opacities, abundances, helioseismology, and neutrino fluxes. *The Astrophysical Journal*, 621(1):L85–L88, 2005.
- [41] Aldo M. Serenelli, W. C. Haxton, and Carlos Pena-Garay. Solar models with accretion. i. application to the solar abundance problem. *The Astrophysical Journal*, 743(1):24, 2011.
- [42] N. Vinyoles et al. A new generation of standard solar models. *The Astrophysical Journal*, 835(2):202, 2017.
- [43] F.L. Villante. ecCNO solar neutrinos: A challenge for gigantic ultra-pure liquid scintillator detectors. *Physics Letters B*, 742:279–284, 2015.
- [44] A. Serenelli. Alive and well: A short review about standard solar models. *The European Physical Journal A*, 52(4), 2016.
- [45] Raymond Davis, Don S. Harmer, and Kenneth C. Hoffman. Search for neutrinos from the sun. *Physical Review Letters*, 20(21):1205–1209, 1968.
- [46] GALLEX Collaboration. GALLEX solar neutrino observations: results for GALLEX IV. *Physics Letters B*, 447(1-2):127–133, 1999.
- [47] GNO Collaboration. GNO solar neutrino observations: results for GNO i. *Physics Letters B*, 490(1-2):16–26, 2000.
- [48] SAGE Collaboration. Results from SAGE (the russian-american gallium solar neutrino experiment). *Physics Letters B*, 328(1-2):234–248, 1994.
- [49] Kamiokande Collaboration. Solar neutrino data covering solar cycle 22. *Physical Review Letters*, 77(9):1683–1686, 1996.
- [50] Super-Kamiokande Collaboration. Measurements of the solar neutrino flux from super-kamiokande’s first 300 days. *Physical Review Letters*, 81(6):1158–1162, 1998.
- [51] SNO Collaboration. Electron energy spectra, fluxes, and day-night asymmetries of ^8B solar neutrinos from measurements with NaCl dissolved in the heavy-water detector at the sudbury neutrino observatory. *Physical Review C*, 72(5), 2005.
- [52] SNO Collaboration. Combined analysis of all three phases of solar neutrino data from the sudbury neutrino observatory. *Physical Review C*, 88(2), 2013.
- [53] Borexino Collaboration. Direct measurement of the ^7Be solar neutrino flux with 192 days of borexino data. *Physical Review Letters*, 101(9), 2008.
- [54] Borexino Collaboration. First evidence of pep solar neutrinos by direct detection in borexino. *Physical Review Letters*, 108(5), 2012.

- [55] Borexino Collaboration. First direct experimental evidence of cno neutrinos. *arXiv:2006.15115*, 2020.
- [56] I. Esteban et al. The fate of hints: updated global analysis of three-flavor neutrino oscillations. *arXiv:2007.14792*, 2020.
- [57] Super-Kamiokande Collaboration. Determination of solar neutrino oscillation parameters using 1496 days of super-kamiokande-i data. *Physics Letters B*, 539(3-4):179–187, 2002.
- [58] Particle Data Group. Review of particle physics. *Progress of Theoretical and Experimental Physics*, 2020(8), 2020.
- [59] Kamiokande-II Collaboration. Experimental study of the atmospheric neutrino flux. *Physics Letters B*, 205(2-3):416–420, 1988.
- [60] D. Casper et al. Measurement of atmospheric neutrino composition with the IMB-3 detector. *Physical Review Letters*, 66(20):2561–2564, 1991.
- [61] MACRO Collaboration. Matter effects in upward-going muons and sterile neutrino oscillations. *Physics Letters B*, 517(1-2):59–66, 2001.
- [62] Soudan 2 Collaboration. Measurement of the l/e distributions of atmospheric neutrinos in soudan 2 and their interpretation as neutrino oscillations. *Physical Review D*, 68(11), 2003.
- [63] Super-Kamiokande Collaboration. Evidence for an oscillatory signature in atmospheric neutrino oscillations. *Physical Review Letters*, 93(10), 2004.
- [64] Super-Kamiokande Collaboration. Measurement of the tau neutrino cross section in atmospheric neutrino oscillations with super-kamiokande. *Physical Review D*, 98(5), 2018.
- [65] Y. Nakajima. “superkamiokande.” talk at neutrino 2020 conference, june 22–july 2, 2020.
- [66] ANTARES Collaboration. ANTARES: The first undersea neutrino telescope. *Nuclear Instruments and Methods in Physics Research Section A: Accelerators, Spectrometers, Detectors and Associated Equipment*, 656(1):11–38, 2011.
- [67] IceCube Collaboration. The IceCube neutrino observatory: instrumentation and online systems. *Journal of Instrumentation*, 12(03):P03012–P03012, 2017.
- [68] IceCube Collaboration. Measurement of atmospheric neutrino oscillations at 6–56 GeV with IceCube DeepCore. *Physical Review Letters*, 120(7), 2018.
- [69] NuFit group. Nufit v5.0, <http://www.nu-fit.org/>.
- [70] K2K Collaboration. Indications of neutrino oscillation in a 250 km long-baseline experiment. *Physical Review Letters*, 90(4), 2003.
- [71] K2K Collaboration. Measurement of neutrino oscillation by the k2k experiment. *Physical Review D*, 74(7), 2006.
- [72] MINOS Collaboration. Observation of muon neutrino disappearance with the MINOS detectors in the NuMI neutrino beam. *Physical Review Letters*, 97(19), 2006.

- [73] MINOS Collaboration. Improved search for muon-neutrino to electron-neutrino oscillations in MINOS. *Physical Review Letters*, 107(18), 2011.
- [74] Thomas Carroll. "final long-baseline results from minos and minos+", talk at neutrino 2020 conference, june 22–july 2, 2020. (University of Wisconsin - Madison).
- [75] MINOS+ Collaboration. Precision constraints for three-flavor neutrino oscillations from the full minos+ and minos data set. *arXiv:2006.15208*, 2020.
- [76] MINOS Collaboration. Search for lorentz invariance and CPT Violation with the MINOS far detector. *Physical Review Letters*, 105(15), 2010.
- [77] MINOS Collaboration. Search for lorentz invariance and cpt violation with muon antineutrinos in the MINOS near detector. *Physical Review D*, 85(3), 2012.
- [78] OPERA Collaboration. Observation of a first $\nu\tau$ candidate in the opera experiment in the cngs beam. *Physics Letters B*, 691(3):138–145, 2010.
- [79] OPERA Collaboration. Final results of the OPERA experiment on $\nu\tau$ appearance in the CNGS neutrino beam. *Physical Review Letters*, 120(21), 2018.
- [80] T2K Collaboration. The t2k experiment. *Nuclear Instruments and Methods in Physics Research Section A: Accelerators, Spectrometers, Detectors and Associated Equipment*, 659(1):106–135, 2011.
- [81] T2K Collaboration. Constraint on the matter–antimatter symmetry-violating phase in neutrino oscillations. *Nature*, 580(7803):339–344, 2020.
- [82] T2K Collaboration. Observation of electron neutrino appearance in a muon neutrino beam. *Physical Review Letters*, 112(6), 2014.
- [83] Patrick Dunne. "latest neutrino oscillation results", talk at neutrino 2020 conference, june 22–july 2, 2020.
- [84] NOvA Collaboration. The NOvA technical design report. Technical report, 2007.
- [85] NOvA Collaboration. First measurement of neutrino oscillation parameters using neutrinos and antineutrinos by NOvA. *Physical Review Letters*, 123(15), 2019.
- [86] Alex Himmel. "new oscillation results from the nova experiment", talk at neutrino 2020 conference, june 22–july 2, 2020. (Fermilab).
- [87] KamLAND Collaboration. Reactor on-off antineutrino measurement with KamLAND. *Physical Review D*, 88(3), 2013.
- [88] I. Esteban et al. Global analysis of three-flavour neutrino oscillations: synergies and tensions in the determination of θ_{23} , δ_{CP} , and the mass ordering. *Journal of High Energy Physics*, 2019(1), 2019.
- [89] CHOOZ Collaboration. Limits on neutrino oscillations from the CHOOZ experiment. *Physics Letters B*, 466(2-4):415–430, 1999.
- [90] CHOOZ Collaboration. Search for neutrino oscillations on a long base-line at the CHOOZ nuclear power station. *The European Physical Journal C*, 27(3):331–374, 2003.
- [91] F. Boehm et al. Final results from the palo verde neutrino oscillation experiment. *Physical Review D*, 64(11), 2001.

- [92] Daya Bay Collaboration. Measurement of the reactor antineutrino flux and spectrum at daya bay. *Physical Review Letters*, 116(6), 2016.
- [93] Double Chooz Collaboration. Improved measurements of the neutrino mixing angle θ_{13} with the double chooz detector. *Journal of High Energy Physics*, 2014(10), 2014.
- [94] Seon-Hee Seo. New results from RENO and the 5 MeV excess. AIP Publishing LLC, 2015.
- [95] Daya Bay Collaboration. Measurement of the electron antineutrino oscillation with 1958 days of operation at daya bay. *Physical Review Letters*, 121(24), 2018.
- [96] P. F. de Salas et al. 2020 global reassessment of the neutrino oscillation picture. *arXiv:2006.11237*, 2020.
- [97] Francesco Capozzi et al. Addendum to “global constraints on absolute neutrino masses and their ordering”. *Physical Review D*, 101(11), 2020.
- [98] Thiago Bezerra. "new results from the double chooz experiment", talk at neutrino 2020 conference, june 22–july 2, 2020.
- [99] Jonghee Yoo. "reno", talk at neutrino 2020 conference, june 22–july 2, 2020.
- [100] JUNO Collaboration. Neutrino physics with JUNO. *Journal of Physics G: Nuclear and Particle Physics*, 43(3):030401, 2016.
- [101] DUNE Collaboration. Deep underground neutrino experiment (dune), far detector technical design report, volume ii: Dune physics. *arXiv:2002.03005*, 2020.
- [102] KM3Net Collaboration. Letter of intent for KM3net 2.0. *Journal of Physics G: Nuclear and Particle Physics*, 43(8):084001, 2016.
- [103] The IceCube-PINGU Collaboration. Letter of intent: The precision icecube next generation upgrade (pingu). *arXiv:1401.2046*, 2014.
- [104] Hyper-Kamiokande Collaboration. Hyper-kamiokande design report. *arXiv:1805.04163*, 2018.
- [105] ICAL Collaboration. Invited review: Physics potential of the ICAL detector at the india-based neutrino observatory (INO). *Pramana*, 88(5), 2017.
- [106] Stephen F. King. Neutrino mass and mixing in the seesaw playground. *Nuclear Physics B*, 908:456–466, 2016.
- [107] J. H. Christenson, J. W. Cronin, V. L. Fitch, and R. Turlay. Evidence for the 2π decay of the K^0 meson. *Physical Review Letters*, 13(4):138–140, 1964.
- [108] J. Schechter and J. W. F. Valle. Neutrinoless double beta decay in $SU(2) \times U(1)$ theories. *Physical Review D*, 25(11):2951–2954, 1982.
- [109] Michelle J. Dolinski, Alan W.P. Poon, and Werner Rodejohann. Neutrinoless double-beta decay: Status and prospects. *Annual Review of Nuclear and Particle Science*, 69(1):219–251, 2019.
- [110] KamLAND-Zen Collaboration. Search for majorana neutrinos near the inverted mass hierarchy region with KamLAND-zen. *Physical Review Letters*, 117(8), 2016.

- [111] KATRIN Collaboration. Improved upper limit on the neutrino mass from a direct kinematic method by KATRIN. *Physical Review Letters*, 123(22), 2019.
- [112] L. Gastaldo et al. The electron capture 163ho experiment echo: an overview. *Journal of Low Temperature Physics*, 176(5-6):876–884, 2014.
- [113] B. Alpert et al. HOLMES. *The European Physical Journal C*, 75(3), 2015.
- [114] M. P. Croce et al. Development of holmium-163 electron-capture spectroscopy with transition-edge sensors. *Journal of Low Temperature Physics*, 184(3-4):958–968, 2016.
- [115] A. Aguilar et al. Evidence for neutrino oscillations from the observation of electron antineutrinos in a muon antineutrino beam. *Physical Review D*, 64(11), 2001.
- [116] MiniBooNE Collaboration. A combined $\nu_{\mu} \rightarrow \nu_e$ and $\bar{\nu}_{\mu} \rightarrow \bar{\nu}_e$ oscillation analysis of the miniboone excesses. *arXiv:1207.4809*, 2012.
- [117] Carlo Giunti and Marco Laveder. Statistical significance of the gallium anomaly. *Physical Review C*, 83(6), 2011.
- [118] G. Mention et al. Reactor antineutrino anomaly. *Physical Review D*, 83(7), 2011.
- [119] K. N. Abazajian et al. Light sterile neutrinos: A white paper. *arXiv:1204.5379*, 2012.
- [120] Böser et al. Sebastian. Status of light sterile neutrino searches. *Progress in Particle and Nuclear Physics*, 111:103736, 2020.
- [121] S. F. King. Neutrino mass models. *Reports on Progress in Physics*, 67(2):107–157, 2003.
- [122] Amol S. Dighe and Alexei Yu. Smirnov. Identifying the neutrino mass spectrum from a supernova neutrino burst. *Physical Review D*, 62(3), 2000.
- [123] S. Hannestad and T. Schwetz. Cosmology and the neutrino mass ordering. *Journal of Cosmology and Astroparticle Physics*, 2016(11):035–035, 2016.
- [124] X. Qian and P. Vogel. Neutrino mass hierarchy. *Progress in Particle and Nuclear Physics*, 83:1–30, 2015.
- [125] Super-Kamiokande Collaboration. Atmospheric neutrino oscillation analysis with improved event reconstruction in super-kamiokande IV. *Progress of Theoretical and Experimental Physics*, 2019(5), 2019.
- [126] IceCube Collaboration. Determining neutrino oscillation parameters from atmospheric muon neutrino disappearance with three years of IceCube DeepCore data. *Physical Review D*, 91(7), 2015.
- [127] Yu feng Li, Yi fang Wang, and Zhi zhong Xing. Terrestrial matter effects on reactor antineutrino oscillations at JUNO or RENO-50: how small is small? *Chinese Physics C*, 40(9):091001, 2016.
- [128] H. Nunokawa, S. J. Parke, and R. Zukanovich Funchal. Another possible way to determine the neutrino mass hierarchy. *Physical Review D*, 72(1), 2005.
- [129] H. Minakata, H. Nunokawa, S. J. Parke, and R. Zukanovich Funchal. Determining neutrino mass hierarchy by precision measurements in electron and muon neutrino disappearance experiments. *Physical Review D*, 74(5), 2006.

- [130] Yu-Feng Li, Jun Cao, Yifang Wang, and Liang Zhan. Unambiguous Determination of the Neutrino Mass Hierarchy Using Reactor Neutrinos. *Phys. Rev. D*, 88:013008, 2013.
- [131] Liang Zhan, Yifang Wang, Jun Cao, and Liangjian Wen. Determination of the neutrino mass hierarchy at an intermediate baseline. *Physical Review D*, 78(11), 2008.
- [132] P. Vogel and J. Engel. Neutrino electromagnetic form factors. *Physical Review D*, 39(11):3378–3383, 1989.
- [133] P. Huber. Determination of antineutrino spectra from nuclear reactors. *Physical Review C*, 84(2), 2011.
- [134] Th. A. Mueller et al. Improved predictions of reactor antineutrino spectra. *Physical Review C*, 83(5), 2011.
- [135] Daya Bay Collaboration. Improved measurement of the reactor antineutrino flux at daya bay. *Physical Review D*, 100(5), 2019.
- [136] Double Chooz Collaboration. Double chooz θ_{13} measurement via total neutron capture detection. *Nature Physics*, 16(5):558–564, 2020.
- [137] RENO Collaboration. Observation of reactor antineutrino disappearance using delayed neutron capture on hydrogen at RENO. *Journal of High Energy Physics*, 2020(4), 2020.
- [138] P. Vogel and J. F. Beacom. Angular distribution of neutron inverse beta decay, $\nu e + p \rightarrow e + n$. *Physical Review D*, 60(5), 1999.
- [139] Y. Kino et al. Positron annihilation in liquid scintillator for electron antineutrino detection. *Journal of Nuclear and Radiochemical Sciences*, 1(2):63–68, 2000.
- [140] Daya Bay Collaboration. Measurement of electron antineutrino oscillation based on 1230 days of operation of the daya bay experiment. *Physical Review D*, 95(7), 2017.
- [141] Double Chooz Collaboration. Measurement of θ_{13} in double chooz using neutron captures on hydrogen with novel background rejection techniques. *Journal of High Energy Physics*, 2016(1), 2016.
- [142] A.A. Hahn et al. Antineutrino spectra from ^{241}Pu and ^{239}Pu thermal neutron fission products. *Physics Letters B*, 218(3):365–368, 1989.
- [143] K. Schreckenbach et al. Determination of the antineutrino spectrum from ^{235}U thermal neutron fission products up to 9.5 MeV. *Physics Letters B*, 160(4-5):325–330, 1985.
- [144] M.P. Decowski. Recent reactor anti-neutrino experiments. *Nuclear Physics B - Proceedings Supplements*, 138:250–256, 2005.
- [145] P. Vogel et al. Reactor antineutrino spectra and their application to antineutrino-induced reactions. II. *Physical Review C*, 24(4):1543–1553, 1981.
- [146] F. Capozzi, G. L. Fogli, E. Lisi, A. Marrone, D. Montanino, and A. Palazzo. Status of three-neutrino oscillation parameters, circa 2013. *Physical Review D*, 89(9), 2014.

- [147] G. L. Fogli et al. Global analysis of neutrino masses, mixings, and phases: Entering the era of leptonic CP violation searches. *Physical Review D*, 86(1), 2012.
- [148] David V. Forero, Rebekah Hawkins, and Patrick Huber. The benefits of a near detector for junos. *arXiv:1710.07378*, 2017.
- [149] D. Danielson et al. Reactor neutrino spectral distortions play little role in mass hierarchy experiments. *Physical Review D*, 99(3), 2019.
- [150] JUNO Collaboration. Tao conceptual design report: A precision measurement of the reactor antineutrino spectrum with sub-percent energy resolution. *arXiv:2005.08745*, 2020.
- [151] Stephen Parke and Mark Ross-Lonergan. Unitarity and the three flavor neutrino mixing matrix. *Physical Review D*, 93(11), 2016.
- [152] X. Qian, C. Zhang, M. Diwan, and P. Vogel. Unitarity tests of the neutrino mixing matrix. *arXiv:1308.5700*, 2013.
- [153] Amir N. Khan, Hiroshi Nunokawa, and Stephen J. Parke. Why matter effects matter for JUNO. *Physics Letters B*, 803:135354, 2020.
- [154] JUNO collaboration. Feasibility and physics potential of detecting ^8B solar neutrinos at junos. *arXiv:2006.11760*, 2020.
- [155] Pran Nath and Pavel Fileviez Pérez. Proton stability in grand unified theories, in strings and in branes. *Physics Reports*, 441(5-6):191–317, 2007.
- [156] Masaki Ishitsuka. "hyper-kamiokande", talk at neutrino 2020 conference, june 22–july 2, 2020. (Tokyo University of Science).
- [157] KamLAND Collaboration. Partial radiogenic heat model for earth revealed by geoneutrino measurements. *Nature Geoscience*, 4(9):647–651, 2011.
- [158] Borexino Collaboration. Comprehensive geoneutrino analysis with borexino. *Physical Review D*, 101(1), 2020.
- [159] J.B.Birks. *The Theory and Practice of Scintillation Counting*. Elsevier, 1964.
- [160] Daya Bay and JUNO collaborations. Optimization of the junos liquid scintillator composition using a daya bay antineutrino detector. *arXiv:2007.00314*, 2020.
- [161] H. Yang et al. Light attenuation length of high quality linear alkyl benzene as liquid scintillator solvent for the JUNO experiment. *Journal of Instrumentation*, 12(11):T11004–T11004, 2017.
- [162] D. Cao et al. Light absorption properties of the high quality linear alkylbenzene for the JUNO experiment. *Nuclear Instruments and Methods in Physics Research Section A: Accelerators, Spectrometers, Detectors and Associated Equipment*, 927:230–235, 2019.
- [163] Göttel Alexandre. "osiris - a 20 ton liquid scintillator detector as a radioactivity monitor for junos", poster at neutrino 2020 conference, june 22–july 2, 2020.
- [164] Wurm Michael. "osiris status", talk at 2nd junos international scientific committee meeting, 18 jan 2020, nanjing, junos internal docdb-5660.
- [165] T. Adam et al. JUNO Conceptual Design Report. *arXiv:1508.07166*, 2015.

- [166] P. Lombardi et al. Distillation and stripping pilot plants for the JUNO neutrino detector: Design, operations and reliability. *Nuclear Instruments and Methods in Physics Research Section A: Accelerators, Spectrometers, Detectors and Associated Equipment*, 925:6–17, 2019.
- [167] Zhonghua Qin, Alexander Olshevskiy, and Wei Wang. "status of 20-inch pmt instrumentation for the juno experiment", poster at neutrino 2020 conference, june 22–july 2, 2020.
- [168] M. Bellato et al. Embedded readout electronics r&d for the large pmts in the juno experiment. *arXiv:2003.08339*, 2020.
- [169] Garfagnini Alberto. Juno large pmt electronics and trigger status, juno internal docdb-4274.
- [170] Bei-Zhen Hu and Jilei Xu. The 3-inch pmts of the juno experiment, poster at neutrino 2018.
- [171] JUNO Small PMT group. "juno conceptual design report", juno internal docdb-3498.
- [172] Y. Zhang et al. Laser calibration system in JUNO. *Journal of Instrumentation*, 14(01):P01009–P01009, 2019.
- [173] Daya Bay Collaboration. A high precision calibration of the nonlinear energy response at daya bay. *Nuclear Instruments and Methods in Physics Research Section A: Accelerators, Spectrometers, Detectors and Associated Equipment*, 940:230 – 242, 2019.
- [174] JUNO Collaboration. Calibration strategy of the juno experiment, juno internal docdb-5922.
- [175] Yuanyuan Zhang et al. Cable loop calibration system for jiangmen underground neutrino observatory, juno internal docdb-6199.
- [176] G. L. Zhu et al. Ultrasonic positioning system for the calibration of central detector. *Nuclear Science and Techniques*, 30(1), 2019.
- [177] Y. H. Guo et al. Design of the guide tube calibration system for the JUNO experiment. *Journal of Instrumentation*, 14(09):T09005–T09005, 2019.
- [178] K. Feng et al. A novel remotely operated vehicle as the calibration system in JUNO. *Journal of Instrumentation*, 13(12):T12001–T12001, 2018.
- [179] C. Genster et al. Muon reconstruction with a geometrical model in JUNO. *Journal of Instrumentation*, 13(03):T03003–T03003, 2018.
- [180] K. Zhang et al. Muon tracking with the fastest light in the JUNO central detector. *Radiation Detection Technology and Methods*, 2(1), 2018.
- [181] T. Payupol et al. Shielding the earth magnetic field using spherical coils. *Journal of Physics: Conference Series*, 1144:012092, 2018.
- [182] C. Guo et al. The water system and radon measurement system of jiangmen underground neutrino observatory. *arXiv:1806.11105*.
- [183] H. Lu and E. Baussan and. The design of the JUNO veto system. *Journal of Physics: Conference Series*, 888:012088, 2017.

- [184] OPERA Collaboration. The OPERA experiment in the CERN to gran sasso neutrino beam. *Journal of Instrumentation*, 4(04):P04018–P04018, 2009.
- [185] D.A. Dwyer and T.J. Langford. Spectral structure of electron antineutrinos from nuclear reactors. *Physical Review Letters*, 114(1), 2015.
- [186] Liang Zhan, Yifang Wang, Jun Cao, and Liangjian Wen. Experimental requirements to determine the neutrino mass hierarchy using reactor neutrinos. *Physical Review D*, 79(7), 2009.
- [187] RENO Collaboration. Observation of energy and baseline dependent reactor antineutrino disappearance in the RENO experiment. *Physical Review Letters*, 116(21), 2016.
- [188] X. Qian, D. A. Dwyer, R. D. McKeown, P. Vogel, W. Wang, and C. Zhang. Mass hierarchy resolution in reactor anti-neutrino experiments: Parameter degeneracies and detector energy response. *Physical Review D*, 87(3), 2013.
- [189] F. Capozzi, E. Lisi, and A. Marrone. Neutrino mass hierarchy and electron neutrino oscillation parameters with one hundred thousand reactor events. *Physical Review D*, 89(1), 2014.
- [190] M. Grassi et al. Charge reconstruction in large-area photomultipliers. *Journal of Instrumentation*, 13(02):P02008–P02008, 2018.
- [191] Yongbo Huang et al. The flash adc system and pmt waveform reconstruction for the daya bay experiment. *Nuclear Instruments and Methods in Physics Research Section A: Accelerators, Spectrometers, Detectors and Associated Equipment*, 895:48–55, 2018.
- [192] Yu Xu. Machine learning application on waveform reconstruction in juno, juno internal docdb-4902.
- [193] Yaping Cheng. waveform fit template fit method, juno internal docdb-748.
- [194] G. Ranucci, A. Goretti, and P. Lombardi. Pulse-shape discrimination of liquid scintillators. *Nuclear Instruments and Methods in Physics Research Section A: Accelerators, Spectrometers, Detectors and Associated Equipment*, 412(2-3):374–386, 1998.
- [195] Wei-Li Zhong et al. Measurement of decay time of liquid scintillator. *Nuclear Instruments and Methods in Physics Research Section A: Accelerators, Spectrometers, Detectors and Associated Equipment*, 587(2-3):300–303, 2008.
- [196] Xiao-Bo Li et al. Timing properties and pulse shape discrimination of LAB-based liquid scintillator. *Chinese Physics C*, 35(11):1026–1032, 2011.
- [197] Y. Zhang. A complete optical model for liquid-scintillator detectors. *Nuclear Instruments and Methods in Physics Research Section A: Accelerators, Spectrometers, Detectors and Associated Equipment*, 967:163860, 2020.
- [198] M. Wurm et al. Optical scattering lengths in large liquid-scintillator neutrino detectors. *Review of Scientific Instruments*, 81(5):053301, 2010.
- [199] X. Zhou et al. Rayleigh scattering of linear alkylbenzene in large liquid scintillator detectors. *Review of Scientific Instruments*, 86(7):073310, 2015.

-
- [200] Yury Malyskin et.al. Status of oscillation parameters analysis, juno internal docdb-5488.
- [201] Anatael Cabrera et al. Spmt "solar" oscillation results, juno internal docdb-4960.
- [202] Hua-Lin Xiao et al. Study of absorption and re-emission processes in a ternary liquid scintillation system. *Chinese Physics C*, 34(11):1724–1728, 2010.
- [203] R. Dossi, A. Ianni, G. Ranucci, and O.Ju. Smirnov. Methods for precise photoelectron counting with photomultipliers. *Nuclear Instruments and Methods in Physics Research Section A: Accelerators, Spectrometers, Detectors and Associated Equipment*, 451(3):623 – 637, 2000.
- [204] Mariangela Settimo. Summary of the catiroc tests, juno internal docdb-3154.
- [205] Glenn Knoll. *Radiation detection and measurement*. Wiley, New York, 2000.
- [206] Selma Conforti. Catiroc datasheet, juno internal docdb-4730.
- [207] Cayetano Santos. <https://catiroc-test.pages.in2p3.fr/firmware/>.
- [208] Clement Bordereau. Abc v0 performances at cenbg, juno internal docdb-4225.
- [209] IceCube-Gen2 Collaboration and JUNO Collaboration Members. Combined sensitivity to the neutrino mass ordering with JUNO, the IceCube upgrade, and PINGU. *Physical Review D*, 101(3), 2020.
- [210] Anatael Cabrera et al. Earliest resolution to the neutrino mass ordering? *arXiv:2008.11280*, 2020.
- [211] JUNO Collaboration. Calibration strategy of the juno experiment. *arXiv:2011.06405*.